It Came From Outer Space: Position Reconstruction in the DEAP-3600 Dark Matter Detector

by

Navin Seeburn

Department of Physics

Royal Holloway, University of London

22nd January 2018

A thesis submitted to the University of London for the degree of Doctor of Philosophy

Declaration

I declare that this thesis and the work presented herein is entirely my own. Where I have consulted the work of others, this is always clearly indicated.

Signed:

Date:

Abstract

This thesis focuses on the determination of the position of events in the DEAP-3600 detector, a single phase, liquid argon dark matter direct detection experiment, which is currently taking its first year of data. The motivation for the existence of particle dark matter from prior research is outlined. The detector is described in detail as-built, along with the calibration systems and data acquisition equipment. The simulation of the detector is also described. The parameters of the simulated optical model are discussed, and their impact on the determination of event position is assessed. Work towards a more realistic detector simulation is discussed, showing agreement in basic variables important to reconstructing event position. The position reconstruction algorithms are described, and a method for improving one of the algorithms is developed which demonstrates better performance on known event source distributions. Timing information is also successfully implemented in position reconstruction, which will gain in importance as larger detectors are constructed. The position reconstruction is adapted to reconstruct an optical calibration source placed at a known location in the detector to within the error on the position of the source. The position reconstruction is then discussed as a means to calibrate the detector optical model using known source position distributions, and the performance of the more realistic detector simulation data is discussed. The reconstructed position and the surface alpha background, which position reconstruction is capable of rejecting, is then implemented in a profile likelihood ratio approach to a dark matter search analysis, in which, commonly, 90% C.L. upper limits are set on the spin-independent WIMP-nucleon scattering cross section. A preliminary upper limit setting analysis is then performed using a 220 day dataset and validated using an alternative analysis method.

Acknowledgements

Starting at the beginning, I first want to thank one Mr. Tom Beech, the physics teacher who tutored me, aged 16, grade E, and made physics irksomely fascinating in the kitchen-diner of my family home, and continued to do so in the labs at school for the next two years. I would also like to thank Dr. Rev. Gajdus, whose high expectations and devotion to teaching sparked a fascination with mathematics that will always be with me. I blame you two entirely.

Further along, I wish to thank Malcolm Fairbairn, who started in me an intense fascination with computational physics as my M.Sci. project supervisor. He sparked off a fascination with research that would guide me through these four years and, of course, put me in contact with Jocelyn and start this whole thing off.

I wish to unreservedly thank Jocelyn Monroe, my Ph.D. supervisor. You saw potential in me I did not know I had and, through relentless optimism and refusal to give up on me, made me realise it and surprise myself pretty much every day. Thank you for being the glass half full during these last four years, and a source of guidance and wisdom. You have bestowed on me an immeasurable amount of knowledge and experience, which is a gift for which I will always be grateful. May you continue to circumnavigate the globe.

I also wish to thank Joseph Walding, my advisor. Your guidance at every point in the last four years has been invaluable, and moreover thank you for your kindness, helping me out over a chat on an 8-hour layover at Toronto International. And thank you for introducing me to the wonder that is Lagavulin.

Thank you to Alistair Butcher, for being there since my very first year as an undergraduate at the King's College London Maxwell Society on Freshers' Week. Thank you

for bestowing mathematical wisdom, letting me bounce ideas off of you and understanding them, and for every time you humanised the PhD process and encouraged me to keep going. Thank you for being a comrade in arms, and, of course, for linearly interpolating those cubic splines.

I would like to thank the rest of my friends at Royal Holloway, for making this an unforgettable experience. Thank to Ben and Gabriela, for banding together with me to annihilate our first year coursework. To Mark Ward, whose Sheffield accent and fast friendship helped me settle in during my first culture-shocked weeks in Canada. To Nasim, for emotional support regarding the laserball and countless Skype conversations bestowing her wisdom about calibration data. To Franco, for comradeship, being an excellent room-mate in Sudbury, and teaching me about Italian hand expressions. To Asher, for teaching me about the world through Animal Fact Fridays and invaluable advice during the development of the last chapter of this thesis. And to the lot of you, for being the most intelligent and talented set of people I have ever worked with. Additionally I would like to thank my friends and collaborators at SNOLAB and the DEAP-3600 experiment, for being excellent colleagues, flatmates, and friends.

For all of this I owe an enormous debt of gratitude to my family. Thank you to my parents, Jean and Jay, for nodding, smiling and supporting me as I flew off on an adventure to the other side of the world to build a giant underground detector for something-or-other. Thank you for always giving me a shoulder to cry on at any hour of any day and raising me to work hard. None of this would have been possible without your support, care and delicious curry.

Thank you to my brother Kieran and his wife Lisa for love, support and catching me up on the films I missed over the last four years. Thank you for taking me in and caring for me. Thank you for emotional support and Hawaiian pizza, and for giving me the space and the means to put my life back together after the worst happened. I will never ever forget your generosity. To my entire family, live long and prosper.

Finally, and last but not least, I would especially like to thank you, the reader, for actually reading this.

Contents

1 Introduction **38**

1.1 Dark Matter Astrophysics 40

1.2 Dark Matter Candidates 48

1.2.1 Axions 48

1.2.2 WIMPs 51

1.3 Dark Matter Direct Detection 54

1.4 Detection Strategies 58

1.4.1 Backgrounds 59

1.4.2 Scintillator Detectors 63

1.4.3 Semiconductor Ionisation Detectors 66

1.4.4 Solid Cryogenic Bolometers 67

1.4.5 Superheated Liquid Detectors 68

1.4.6 Directional Detection 69

1.5 Scintillation in Liquid Noble Gases 70

1.5.1 Properties 71

1.5.2 Scintillation 72

1.5.3 Emission Timing 74

1.5.4 Recombination 76

1.5.5 Recoil Dependent Light Yield 77

1.5.6 Quenching 78

1.6 Conclusion 80

2 The DEAP-3600 Detector **81**

2.1 Overview . . . 81

2.2 Backgrounds . . . 83

2.2.1 ^{39}Ar . . . 83

2.2.2 Surface Alphas . . . 83

2.2.3 Neutrons . . . 87

2.3 The Inner Vessel . . . 89

2.3.1 Acrylic Vessel . . . 89

2.3.2 Light guides . . . 91

2.3.3 Resurfacing . . . 92

2.3.4 Filler blocks and reflectors . . . 93

2.3.5 Tetraphenyl Butadiene (TPB) deposition . . . 95

2.3.6 Photomultiplier Tubes (PMTs) . . . 97

2.4 Outer Components . . . 101

2.4.1 Magnetic Compensation . . . 102

2.4.2 Glovebox and Inner Neck . . . 103

2.5 Purification Systems . . . 104

2.5.1 Purification and Filling . . . 104

2.6 Detector Readout . . . 105

2.6.1 Front End . . . 106

2.6.2 Data Acquisition . . . 107

2.6.3 Digitiser and Trigger Module . . . 107

2.7 Calibration Systems . . . 109

2.7.1 Optical Calibration . . . 109

2.7.2 Radioactive Source Calibration . . . 117

2.8 Conclusion . . . 118

3 Simulation, Analysis and Optics **120**

3.1 Simulation . . . 120

3.1.1 Optical Model . . . 121

3.1.2 PMT Simulation . . . 126
3.1.3 DAQ Simulation . . . 127
3.2 Analysis . . . 128
3.2.1 Charge . . . 129
3.2.2 Data Quality . . . 129
3.2.3 F_{prompt} . . . 131
3.2.4 F_{maxpe} . . . 132
3.3 Optics Variation . . . 134
3.3.1 Argon . . . 135
3.3.2 TPB . . . 138
3.3.3 Acrylic . . . 143
3.4 Conclusion . . . 145

4 Position Reconstruction 147
4.1 Centroid . . . 147
4.2 ShellFit . . . 148
4.2.1 Charge Response Model . . . 148
4.2.2 Minimisation . . . 152
4.3 MBLikelihood . . . 155
4.4 UberShellFit . . . 156
4.4.1 TPB patch solid angle calculation . . . 156
4.4.2 Computational Efficiency . . . 158
4.4.3 Reparametrisation . . . 160
4.5 Time Reconstruction . . . 160
4.5.1 Position Dependence of Observed Time . . . 161
4.5.2 The Timing Model . . . 163
4.5.3 Reconstruction Model . . . 167
4.6 Performance . . . 174
4.6.1 ^{39}Ar . . . 174
4.6.2 Radial Resolution . . . 178

4.6.3 Surface Alpha Reconstruction . . . 184
4.7 Conclusion . . . 185

5 Calibration **187**
5.1 Optical Flask Calibration . . . 187
5.1.1 Reconstruction Adaptation . . . 188
5.1.2 Position Reconstruction of Commissioning Data . . . 196
5.1.3 Position Reconstruction of Laserball Simulations . . . 201
5.1.4 Comparison of Simulation to Data . . . 203
5.2 ^{39}Ar Radial Bias . . . 205
5.3 ^{22}Na Source Calibration . . . 212
5.3.1 Simulation . . . 212
5.3.2 Cut motivation and simulation comparison . . . 213
5.3.3 Reconstruction . . . 216
5.4 Conclusion . . . 218

6 Dark Matter Search **220**
6.1 Poisson Method . . . 221
6.2 Profile Likelihood Ratio Method . . . 224
6.2.1 Hypothesis Testing . . . 225
6.2.2 Likelihood Construction . . . 226
6.3 Model PDF Implementation . . . 227
6.3.1 WIMP Model . . . 227
6.3.2 ^{39}Ar Model . . . 228
6.3.3 Radial Model . . . 230
6.3.4 Alpha Model . . . 233
6.4 Operation . . . 237
6.4.1 Consistency checks . . . 237
6.5 Limit Calculation . . . 240
6.6 Conclusion . . . 242

List of Figures

1.1 Rotation velocity of celestial objects in galaxy NGC6503 vs their radial distance from the galactic centre, reaching a constant at high radius. Figure reproduced from Ref. [5]. 41

1.2 (a) The luminous matter from cluster 0024+1654. Image from W.N. Colley and E. Turner (Princeton University), J.A. Tyson (Bell Labs, Lucent Technologies) and NASA/ESA. (b) The matter distribution in cluster 0024+1654, inferred from luminous matter and gravitational lensing. Data from [10]. 42

1.3 A colourised image of the Bullet Cluster, which is an example of the remnant of two collided clusters with a clear separation between the matter and dark matter component. The reconstruction of gas from X-ray spectroscopy is shown in red, and the distribution of dark matter as indicated by gravitational lensing is shown in blue. X-ray image from Ref. [18]. Lensing map and optical background imaging from Ref. [15]. 43

1.4 μK fluctuations in the temperature spectrum of the CMB mapped vs direction of origin in a Mollweide projection with the galactic plane at the equator, as measured by Planck. The contributions from the dipole term and galactic plane emission have been subtracted. Plot reproduced from Ref. [20]. 44

1.5 Observed power spectrum $D_l^{TT} = l(l+1)\hat{C}_l$ from photon temperature two-point correlation function at angular scale l on top, and a residual between observation and ΛCDM model fit shown on bottom. D^{TT} notation is used by Planck to distinguish temperature (T) correlation function from photon polarisation measurements. Plot reproduced from Ref. [1]. . 46

1.6 Predictions of the primordial ^{4}He (top) and deuterium (bottom) abundances with varying baryon density ω_b. The green stripes represent the Planck prediction from Big Bang Nucleosynthesis with a 68% uncertainty on rates at which nuclear reactions take place, and on the neutron lifetime. Horizontal grey bands show observational bounds on helium from Ref. [23], and deuterium from Ref. [22] and Ref. [24]. The vertical red band represents the Planck constraint on ω_b [1]. Grey horizontal band show observation constraints from the listed authors, not listed here. Plot reproduced from Ref. [1]. 47

1.7 Axion to two photon coupling against axion mass for ADMX [32] and microwave cavity experiments from University of Florida (UF) [33], the Rochester-Fermilab-Brookhaven (RBF) experiment [34, 35], HAYSTAC [36] and ORGAN [37]. Current sensitivity of ADMX is shown in green. The parameter space bounded by the DFSZ and KSVZ models is shown as yellow band. Figure reproduced from Ref. [38]. 50

1.8 Summary of the axion to two photon coupling against axion mass parameter space, containing the region shown in Figure 1.7. Figure reproduced from Ref. [38]. 50

1.9 Spin dependent Helm form factor squared $F_{SI}^2(E_R)$ vs nuclear recoil energy E_R for He, Ne, Ar, Kr and Xe, assuming a 100GeV WIMP mass, skin thickness $s \simeq 0.9$fm, and parameters $a \simeq 0.52$fm and $c \simeq 1.23A^{1/3} - 0.6$fm fitted from muon scattering data [49]. 57

1.10 Differential rate in keV dR/dE_R vs WIMP recoil energy E_R, for Ne, Ar, Ge and Xe, assuming 30 GeV (dashed line) and 300 GeV (solid line) WIMP masses. Plot reproduced from Ref. [59]. 58

1.11 Summary of results at time of writing, showing spin independent (SI) WIMP-nucleon scattering cross section vs WIMP mass. 90% C.L. upper limits suggested by experiments are shown as curves. Signal regions suggested by experimental results are shown as oval shapes. The dashed orange line above the orange region corresponds to the sensitivity to WIMP cross sections required to observe atmospheric, supernova and ^{7}Be/^{8}B solar neutrinos. The yellow region represents the potential parameter space for observation of WIMPS under minimal SUSY. Reproduced from Ref. [38]. 59

1.12 Summary of results in 2017, showing spin independent (SI) WIMP-nucleon scattering cross section vs WIMP mass. Solid curves represent observed exclusion regions, and dashed curves represent projected exclusion regions. The DEAP-3600 4.44 day result is shown in solid blue. The 3 tonne-year projected exclusion curve as discussed in 1.4.2 is shown in dashed blue. Again, signal regions suggested by experimental results are shown as oval shapes. Reproduced from Ref. [3]. 60

1.13 Total flux of muon-induced neutrons at the rock-cavern boundary at each of the underground sites labelled. Reproduced from Ref. [60]. 61

1.14 Combined voltage traces vs time from two PMTs viewing nuclear (left, blue) and electronic recoils (right, red) in liquid argon, where PMTs observed between 80 and 99 photoelectrons per recoil event. Reproduced from Ref. [108]. 74

1.15 Nuclear recoil (higher F_{prompt}) band data taken using the AmBe source in DEAP-3600, with the WIMP search ROI shown as a black box. Reproduced from Figure 3a in Ref. [3]. 75

1.16 Quenching factor observed in vs nitrogen (a) and oxygen (b) contamination level in ppm, from contamination studies in WArP [120, 121]. Also shown in (b) is the raw surviving fraction, a ratio of light yield with oxygen contamination to light yield without, including effects other than quenching, discussed further in Ref. [121]. 79
1.17 Triplet lifetime vs nitrogen (a) and oxygen (b) contamination level in ppm, from contamination studies in WArP [120, 121]. 79
1.18 Measurement of variation in argon absorption length with contamination level of nitrogen, from contamination studies in WArP [120]. The band shown corresponds to 1σ boundaries on the measurement. 80

2.1 A rendered cutaway schematic of the DEAP-3600 detector. Rendered by Koby Dering. 82
2.2 The ^{220}Rn (left) and ^{222}Rn (right) decay chains, from ^{232}Th and ^{238}U respectively. Each isotope is shown above its half life (where a number of years is represented a, for annum). The energy of the ejected alpha is shown in red. Figure prepared by T. Pollmann [123]. 84
2.3 Schematic showing the locations of origin of surface alpha decay backgrounds. Schematic produced by T. Pollmann. 85
2.4 Distributions of energy deposited in the TPB layer by ^{210}Po decay products, as calculated in SRIM-2010 [122]. Simulation and plot produced by T. Pollmann. 85
2.5 Differential energy spectra for muon-induced neutrons emerging from rock faces at underground laboratory sites used for low-background detector physics. Histograms with 50 MeV wide bins show the energy spectra produced by simulations of neutrons in rock wall. Reproduced from Ref. [60]. 89
2.6 Photograph showing the fully bonded AV with light guides. 90

2.7 Measurement of attenuation length of TPB re-emission light against re-emission light wavelength using a spectrophotometer. The acrylic selected for the DEAP-3600 AV is the UV-absorbing (UVA) sample from Reynolds Polymer Technologies (RPT), shown in solid blue. The acrylic selected for the light guides is the Spartech UVA sample in dashed red. Figure prepared by V. Volkovo and M. Kuzniak in Ref. [128]. 91

2.8 Spectrometer measurement of the variation of the attenuation length of light guide acrylic with the incident light wavelength. Measured internally by P. Rau, figure prepared by M. Kuzniak. 92

2.9 Rendering showing the resurfacer apparatus as installed in the AV via the glovebox and AV neck. Rendered by Koby Dering. 93

2.10 Plot showing contributions to the predicted ^{210}Pb activity in acrylic with varying depth of acrylic removed. The contribution from radon decay daughter deposition on the surface is shown in blue; the contribution from radon diffused into the acrylic is shown in red; the upper limit from Ge detector assays of the acrylic bulk is shown in cyan. With the removed layer thickness predicted at 0.4 mm, the residual AV surface activity is dominated by the contribution from radon diffusion at $\sim$15 α/m^2/day. Plot produced by B. Cai and M. Boulay [129]. 94

2.11 a) Wrapping of the light guides and AV. The light guide is wrapped with reflective aluminised Mylar backed with black Tyvek and magnetic shields. The AV is wrapped with white specular reflecting Tyvek backed by 3 layers of light-proofing and a cushioning layer of Tyvek foam; b) a schematic of an installed filler block between the light guides, with supporting springs, prepared by K. Dering 95

2.12 Re-emission spectra at visible wavelengths for a 1.5 μm layer of TPB produced using vacuum-deposition. Different colours correspond to different wavelengths of incident light from a monochromator at 128 nm (the peak argon scintillation wavelength), 160 nm, 175 nm and 250 nm. The spectrum from illumination with 128nm light peaks at 425 nm. Reproduced from Ref. [130]. 96

2.13 Integrated fluorescence efficiency as a function of incident light wavelength for a 1.5 μm layer of TPB. Reproduced from Ref. [130]. 96

2.14 Photo showing the stainless steel TPB source, wrapped with a Watlow coil heater, and containing a copper crucible housing the TPB powder. Reproduced from Ref. [131]. 97

2.15 An exploded view rendering of a fully installed and constructed PMT mount. Rendering by Koby Dering. 98

2.16 Photographs showing the acrylic vessel: a) with all PMT mounts, copper collars and filler blocks installed, b) PMT cabling installed between two layers of polyurethane foam blocks. Photographed by Mark Ward. 99

2.17 PMT pulse timing distributions for prompt, late, double and early pulse types, with each distribution normalised to unit area under the curve. Pulse times are shown relative to the peak of the prompt PDF shown in blue. Reproduced from data in Ref. [136]. 100

2.18 A plot showing the magnetic field strength magnitude $|\vec{B}|$ and vertical component $\vec{B}_z$ in the vicinity of the DEAP-3600 vessel, as calculated with Radia [137, 138]. Also shown are three circles representing the approximate locations of the muon veto PMTs (blue), the steel outer vessel (red), and the AV PMTs (green). Includes the effects of the ambient magnetic field as measured on site, the magnetic compensation coils of MiniCLEAN, located next to DEAP-3600 in their final constructed locations. . 102

2.19 A schematic showing the apparatus within the AV neck. A cooling coil fed with liquid nitrogen is surrounded by a flow separator tube, which separates downward cold argon flow and upward warm argon flow together with flow guides at the bottom and top of the tube. A vacuum jacket is placed around the neck to reduce the heat load from the argon and the cabling in the outer vessel neck. Rendered by Koby Dering. 104

2.20 A rendering showing the AARF system installed on a light guide. Large arrows in red show an example of a possible light path from the AARF acrylic stub, reflected from the PMT and down the light guide towards the AV. Rendered by Koby Dering. 110

2.21 Prompt occupancy vs PMT angle from the AARF PMT. Occupancy is calculated as fraction of events for which a PMT sees 1 or more PE. Prompt occupancy only accepts PE from pulses detected within -24 ns and +44 ns of the DAQ trigger. PMTs are sorted in order or ascending angle to the AARF PMT. Two PMTs are disabled due to problems at time of data taking. Plot prepared by Berta Beltran. 111

2.22 A single PE (SPE) charge spectrum in pC for pulses within a 68 ns window. Vertical axis shows the number of pulses observed with a charge on the horizontal axis. Produced using the AARF on a PMT on the top ring of PMTS nearest the neck. Full waveform data was taken (without ZLE) with 15% occupancy in the AARF PMT. The fitted function, shown in blue, is described by equations 2.3-2.5. The pedestal Gaussian (grey dotted), single (green dotted) and multiple (pink and purple) PE contributions to the fit are shown under data (black with error bars). Shown below is the difference in between function and data. The function fits the data with a χ^2 per number of degrees of freedom at $\sim$1. Plot prepared by T. Pollmann, reproduced from Ref. [132]. 112

2.23 The variation of mean single PE charge with time for a group of 8 PMTs at the top of the detector. One representative PMT (no. 6, in red) is shown with the mean SPE charge determined from the AARF monitoring runs that occurred over this period, and error bars representing the parameter errors from the fit depicted in Figure 2.22. The time axis begins on 1st June 2016. A slight upward trend is observed for most PMTs over the course of the year depicted. Discontinuities in the mean SPE charge occur at times when the PMTs were powered down and back up. The environmental conditions changed a number of times, as depicted on the plot: Phase 1: AV under vacuum with TPB deposited and compensation coils on; Phase 2: in addition, water shielding tank is filled with chilled water; Phase 3: AV filled with argon gas at room temperature; Phase 4: Cool down phase with increasingly cold argon gas. Plot prepared by T. Pollmann. 114

2.24 The laserball driven by the 445 nm laser head, photographed during ex-situ testing by N. Fatemighomi. 115

2.25 Pulse time from every PMT measured relative to the start of the DAQ event waveform. Data was taken with the laserball at the centre of the detector, using the 445 nm laser diode. The pulse time has been corrected for SCB channel timing offsets, and timing offsets from varying PMT cable lengths for each channel. Plot prepared by F. La Zia. 115

2.26 Left: Relative efficiencies of the PMT array obtained by averaging the relative efficiencies obtained four data sets taken with the laserball at the centre of the detector, separated by rotation angle $\Delta\phi_{LB} = \pi/2$. Vertical axis is the number of PMTs with relative efficiency observed in each 0.02 wide bin. Right: A plot comparing the relative efficiencies obtained from the laserball data to those obtained from AARF data, where an efficiency of 1 is defined for a single PMT. Plots prepared by R. Mehdiyev. 116

2.27 a) A drawing showing the calibration tubes. Three vertical tubes, Cal A, B and E allow sources to be deployed close to the equator, and Cal F allows sources to be deployed at points around the detector, and close to the neck. b) A photograph showing the two gamma calibration racks on the left and the neutron calibration rack on the right. 118

3.1 Comparison of ray-traced simulated detector renderings to photographs of the as-built detector. The depictions show the detector before PMT installation, after the installation of filler blocks, and after closing the steel shell. Ray traced images from Ref. [140]. Photographs by Mark Ward and other collaboration members on shift. 122

3.2 A drawing showing the effect that a rough surface in the 'ground' surface model would have on the surface normal, deviating it by the angle $\theta = \hat{n} \cdot \hat{n}'/|\hat{n}||\hat{n}'|$. The condition $\hat{n} = \hat{n}'$ represents the 'polished' surface model. 123

3.3 Variation of the liquid argon refractive index (n) with wavelength (λ), as implemented in simulation. The curve in blue is reproduced from the extrapolation in Ref. [141]. 124

3.4 Variation of the liquid argon scattering length (l) with wavelength (λ), as implemented in simulation. The curve in blue is reproduced from the extrapolation in Ref. [141]. 125

3.5 Variation of the TPB scattering length (l) with wavelength (λ), as implemented in simulation. 126

3.6 Projection of F_{prompt} distribution for 80 PE electronic recoil events, plotted alongside effective model fit, as labelled. Red dashed line indicates the lower limit of the fit range. Brown and yellow lines represent the 90% and 50% nuclear recoil acceptance boundaries. (b) Comparison of electronic recoil data to model for 120-240 PE range, with 90% and 50% nuclear recoil acceptance indicated. Compares DEAP-1 projection (dashed) to improved effective model from DEAP-3600. Reproduced from Ref. [3]. . 132

3.7 Distribution of F_{maxpe} vs n_{SC} for a standard physics run. 133

3.8 Comparing the distribution of F_{prompt} vs n_{SC} for a standard physics run whilst (a) cutting on events with $F_{maxpe} > 0.2$, (b) allowing all F_{maxpe} values. 133

3.9 Comparing the ^{39}Ar F_{maxpe} distribution in simulation in cases where the argon scattering length is varied at values motivated in literature. Additionally, the effect of the introduction of a 10% absorption component in argon is shown, modelling the effect of impurities present in argon. 137

3.10 Comparing the ^{39}Ar F_{prompt} distribution in simulation in cases where the argon scattering length is varied at values motivated in literature. Additionally, the effect of the introduction of a 10% absorption component in argon is shown, modelling the effect of impurities present in argon. 137

3.11 Comparing the distribution of number of hit PMTs N_{hit} in simulation of ^{39}Ar where argon scattering length is varied at values motivated in literature. Additionally, the effect of the introduction of a 10% absorption component in argon is shown, modelling the effect of impurities present in argon. 138

3.12 Total charge observed over 10^6 laserball events in the 40 PMTs nearest the bottom of the detector. PMT IDs are in ascending order moving from the top of the detector to the bottom of the detector. The laserball is simulated at $z = -550$ mm using the 375 nm laser head. Simulations were performed with and without a hole of radius 142.5 mm in the TPB at the bottom of the detector. 139

3.13 Distributions of F_{maxpe} for 6×10^4 ^{39}Ar events, for varying TPB Rayleigh scattering lengths. 140

3.14 Distributions of F_{prompt} for 6×10^4 ^{39}Ar events, for varying TPB Rayleigh scattering lengths. 141

3.15 Distribution of the fraction of PE in each PMT relative to total PE in all PMTs, over all events. The laserball was simulated at $z = -550$ mm using the 375 nm laser head, fired 10^6 times, for varying TPB Rayleigh scattering lengths. 142

3.16 Distribution of the fraction of PE in each PMT relative to total PE in all non-AARF PMTs, over all events. The AARF was simulated at the light guide for PMT 229, fired 4×10^4 times, for varying TPB Rayleigh scattering lengths. The PMT IDs on the horizontal axis are sorted in order of increasing distance to the AARF PMT, where PMT ID 0 is the AARF PMT. 142

3.17 Distribution of the fraction of PE in each PMT relative to total PE in all non-AARF PMTs, over all events. The AARF was simulated at the light guide for PMT 229, fired 4×10^4 times, for varying light guide and AV attenuation lengths. The PMT IDs on the horizontal axis are sorted in order of increasing distance to the AARF PMT, where PMT ID 0 is the AARF PMT. 143

3.18 Distribution of the fraction of PE in each PMT relative to total PE in all non-AARF PMTs, over all events. The AARF was simulated at the light guide for PMT 229, fired 4×10^4 times, for varying attenuation lengths. The PMT IDs on the horizontal axis are sorted in order of increasing distance to the AARF PMT, where PMT ID 0 is the AARF PMT. 144

3.19 F_{maxpe} distributions from AARF simulations with varying AV and light guide acrylic attenuation lengths. 145

3.20 F_{prompt} distributions from AARF simulations with varying AV and light guide acrylic attenuation lengths. 146

4.1 A schematic depicting the solid angle Ω used to denote a point on the TPB, and the re-emission angle θ from the light guide normal. Event position vector is denoted $\vec{x}$ and distance between event and TPB point is denoted $|\vec{x}_{TPB} - \vec{x}|$. Acrylic vessel and light guide are not to scale. 150

4.2 Number of photons re-emitted by TPB per incident UV Photon, $W(\Omega,\vec{x})$, at any point in Ω on the TPB surface. Shown in the colour axis as a function of radial co-ordinate $|\vec{x}|$ of the event and the distance between the event position vector and the TPB re-emission position vector $|\vec{x}_{TPB}-\vec{x}|$ 150

4.3 Difference between polynomial fit of $W(\Omega,\vec{x})$ and bin content from the histogram shown in Figure 4.2, using the same bin boundaries. The set of empty bins in Figure 4.2 is shown here as a set of zero bins with no variation of bin content. 151

4.4 Probability $H(\theta_i(\Omega))$ that a photon re-emitted from a point on the TPB Ω produces a PE in a PMT i at a angle θ_i away from Ω. 152

4.5 Charge PDFs for n PE. When n>1, the distribution is described by the 1 PE double Polya distribution convolved with itself $n-1$ times. 154

4.6 Probability that a photon emitted from position $\vec{x}$ is observed in a PMT i at an angle $\theta_{ev,i}$ away from the position vector, relative to the centre of the detector. The probability is plotted against $\cos(\theta_{ev,i})$. 156

4.7 A schematic, not to scale, showing an example of the stripe orientation relative to the position vector $\vec{x}$ (vectors denoted in bold). The unit sphere is centred on the position vector $\vec{x}$ and stripe boundaries are circles with axes of symmetry parallel to $\vec{x}$. The circles are concentric on the point where $\vec{x}$ meets the TPB. Also shown is an example circle opening angle θ', defined such that $\cos(\theta')=1$ refers to a direction parallel to the position vector $\vec{x}$. 158

4.8 Number of PE observed per UV scintillation photon $\mu_i(\vec{x},1)$, vs event radius $R=|\vec{x}|$ normalised to the detector radius $R_0=851$ mm for varying $\cos(\theta_{ev,i})$ from $\cos(\theta_{ev,i})=-1$ (lowest curve) to $\cos(\theta_{ev,i})=1$ (highest curve). 159

4.9 Number of photons re-emitted by TPB per incident UV photon, $W(\Omega,\vec{x})$, at a point Ω on the TPB surface. Shown against the radial co-ordinate $|\vec{x}|$ of the event and the deviation angle between the event position vector and the TPB re-emission position vector. 160

4.10 Difference between polynomial fit of $W(\Omega,\vec{x})$ and bin content from the histogram shown in Figure 4.9, using the same bin boundaries. Shown against the radial co-ordinate $|\vec{x}|$ of the event and the deviation angle between the event position vector and the TPB re-emission position vector. 161

4.11 Radial co-ordinate $|\vec{x}|$ of the simulated event position vertex $\vec{x}$, vs time of flight t_{TOF} of photons from time of emission to time of arrival at a PMT photocathode. Colour axis: photons per histogram bin. Each simulated event is an instantaneous isotropic point source with the wavelength spectrum of argon scintillation. 162

4.12 Probability of observing a time of flight t_{TOF}. Events located at the centre of the detector are shown in blue, and events located near the surface of the detector are shown in green. Each event is an instantaneous isotropic point source with the wavelength spectrum of argon scintillation. 162

4.13 Probability of observing a time of flight t_{TOF} for the first photon observed in each PMT, for PMTs that observed 1PE (blue), 5PE (green), and 10PE (pink). Each event is an instantaneous isotropic point source with the wavelength spectrum of argon scintillation. 163

4.14 A summary of the time of flight from event to PMT. Note that in diagram notation, $t_{TOF} = t_{TOF,AV} + t_{TOF,LG} + t_{TOF,TPB}$, where $t_{TOF,TPB}$ is the time of flight in TPB, not shown. 164

4.15 An example of a PMT photocathode arrival time PDF (Cathode Time) for an instantaneous, isotropic 128 nm photon source. The distribution is fitted using the weighted sum of two gamma distributions, with $\chi^2/n_{dof} < 1$. 165

4.16 Schematic showing the angle $\theta_{ev,i}$ between event position vector and PMT position vector 168

4.17 Time offset, χ (colour axis), plotted against event vertex radial co-ordinate (normalised to $R_0 = 851$ mm) and cosine of the angle $\theta_{ev,i}$ shown in Figure 4.16. 168

4.18 Polynomial parameter, α (colour axis), plotted against event vertex radial co-ordinate (normalised to $R_0 = 851$ mm) and cosine of the angle $\theta_{ev,i}$ shown in Figure 4.16. 168

4.19 Exponential parameter, θ (colour axis), plotted against event vertex radial co-ordinate (normalised to $R_0 = 851$ mm) and cosine of the angle $\theta_{ev,i}$ shown in Figure 4.16. 169

4.20 Normalisation weighting parameter, N (colour axis), plotted against event vertex radial co-ordinate (normalised to $R_0 = 851$ mm) and cosine of the angle $\theta_{ev,i}$ shown in Figure 4.16. The two gamma distribution model is normalised to unity under the curve after summation of the two gamma distributions. 169

4.21 χ^2 per n_{dof} (colour axis), plotted against event vertex radial co-ordinate (normalised to $R_0 = 851$ mm) and cosine of the angle $\theta_{ev,i}$. 170

4.22 Single PMT arrival time PDFs showing modelled time of flight (t_{TOF}) to the PMT photocathode for every photon (blue) and first photon (green) in a PMT which observes 4 PE. 171

4.23 Photocathode arrival time PDF, comparing modelled time of flight (pink) to simulated photocathode time for simulated isotropic 128 nm photon sources (green) 173

4.24 PMT anode arrival time PDF, comparing the model of the sum of time of flight and PMT transit time (pink) to simulated anode arrival time for simulated isotropic 128 nm photon sources (green) 173

4.25 PMT anode arrival time PDF, comparing the model of the sum of scintillation emission time, time of flight and PMT transit time (pink) to simulated anode time for simulated ^{39}Ar β^- decays at 15 keV$_{ee}$ (green) 174

4.26 Probability of observing a reconstructed or simulated ^{39}Ar event at a radius $(R/R_0)^3$. A loose PE cut selects only those events which observed between 80 and 300 scintillation PE with afterpulsing removed. The blue distribution shows the simulated ^{39}Ar distribution after the cut. The reconstructed distribution for ShellFit is shown in green; UberShellFit is shown in pink; and MBLikelihood is shown in purple. The result of the centroid calculation is also shown in red. 175

4.27 The ratio of reconstructed to simulated ^{39}Ar events in a given bin in radius $(R/R_0)^3$. A loose PE cut selects only those events which observed between 80 and 300 scintillation PE with afterpulsing removed. The blue line at ratio = 1 depicts the scenario where reconstruction matches simulation perfectly. The reconstructed distribution for ShellFit is shown in green; UberShellFit is shown in pink; and MBLikelihood is shown in purple. The result of the centroid calculation is also shown in red. 176

4.28 Number of events reconstructed per bin in $(R_{rec}/R_0)^3$, shown in green and the fit to a Gaussian, shown in pink, for $R_{MC} = 595.7$ mm. 178

4.29 Number of events reconstructed per bin in $(R_{rec}/R_0)^3$, shown in green and the fit to a Gaussian, shown in pink, for $R_{MC} = 127.65$ mm. The Gaussian is a poor fit to the cubic radius distribution, which is truncated at $R_{rec} = 0$ and has an unphysical negative mean radius. 179

4.30 Number of events reconstructed per bin vs $(R_{rec} - R_{MC})$, shown in green and the fit to a Gaussian, shown in pink, for $R_{MC} = 127.65$ mm. 179

4.31 Number of events reconstructed per bin vs $(R_{rec} - R_{MC})$, shown in green and the fit to a Gaussian, shown in pink, for $R_{MC} = 595.7$ mm. The Gaussian is a poor fit to the event distribution which has asymmetric tails. 180

4.32 Radial resolution σ in mm for events simulated in 20 radial shells with radii R_{MC} distributed at equal spacing in radius between $R_{MC} = 0$ mm and $R_{MC} = 851$ mm. ShellFit is shown in green; UberShellFit is shown in pink; UberShellFit+Time is shown in yellow; and MBLikelihood is shown in purple. 181

4.33 Radial bias μ in mm for events simulated in 20 radial shells with radii R_{MC} distributed at equal spacing in radius between $R_{MC} = 0$ mm and $R_{MC} = 851$ mm. ShellFit is shown in green; UberShellFit is shown in pink; UberShellFit+Time is shown in yellow; and MBLikelihood is shown in purple. 181

4.34 The ratio of radial resolution σ to UberShellFit radial resolution σ_{USF} for events simulated in 20 radial shells with radii R_{MC} distributed at equal spacing in radius between $R_{MC} = 0$ mm and $R_{MC} = 851$ mm. UberShellFit+Time is shown in yellow and MBLikelihood is shown in purple. The pink line $\sigma/\sigma_{USF} = 1$ represents perfect agreement between UberShellFit and another reconstruction algorithm. 182

4.35 The ratio of radial bias μ to UberShellFit radial bias μ_{USF} for events simulated in 20 radial shells with radii R_{MC} distributed at equal spacing in radius between $R_{MC} = 0$ mm and $R_{MC} = 851$ mm. UberShellFit+Time is shown in yellow and MBLikelihood is shown in purple. The pink line $\mu/\mu_{USF} = 1$ represents perfect agreement between UberShellFit and another reconstruction algorithm. 182

4.36 The distribution of cubic reconstructed radius $(R_{rec}/R_0)^3$ for 2 million ^{210}Po alpha decays simulated in the TPB layer. ShellFit is shown in green; UberShellFit is shown in pink; UberShellFit+Time is shown in yellow; and MBLikelihood is shown in purple. 185

5.1 Argon scintillation wavelength spectrum, as recorded in simulation performed in each instance of ShellFit run during initialisation, before iterating over and reconstructing events. 188

5.2 Laserball emission wavelength spectrum, as recorded by M. Kuzniak using the 445 nm laser head and extrapolated to 375 nm laser head, shown in blue and green respectively. 189

5.3 Simulated photons per PE for isotropic point sources with wavelength distributions $P(\lambda) = \delta(\lambda - \lambda_{emit})$, at the argon scintillation wavelength $\lambda_{emit} = 128nm$ in purple and at the laserball laser head wavelengths $\lambda_{emit} = 375nm$ in green and $\lambda_{emit} = 445nm$. Note that the lowest photon per PE values correspond to the highest yields of PE per photon. 189

5.4 Number of photons re-emitted by TPB per incident UV photon, $W(\Omega, \vec{x})$ (colour axis), at any point Ω on the TPB surface. Shown against the radial co-ordinate $|\vec{x}|$ of the event and the deviation angle between the event position vector and the TPB re-emission position vector. Generated using the extrapolated 375 nm wavelength spectrum, analogously to Figure 4.9 in Section 4.4.3. 190

5.5 PE production probability $H(\theta_i(\Omega))$ at a re-emission angle θ. Generated using the extrapolated 375 nm wavelength spectrum, analogously to Figure 4.4 in Section 4.2.1. 191

5.6 PE production probability $H(\theta_i(\Omega))$ at a re-emission angle θ. Generated using the measured 445 nm wavelength spectrum, analogously to Figure 4.4 in Section 4.2.1. 191

5.7 Occupancy (colour axis) observed in a PMT in direction θ_i, ϕ_i relative to the laserball surface. This map is produced using a fitting routine designed by N. Fatemighomi. 192

5.8 Schematic illustrating the difference between the position of a PMT θ_i, ϕ_i in a co-ordinate system centred on the laserball, and the position of a PMT $\theta_{pmt,i}$, $\phi_{pmt,i}$ in a co-ordinate system centred on the centre of the detector. The laserball is translated downwards relative to the centre of the detector. Laserball, AV and PMT dimensions are not to scale. 193

5.9 Hit occupancy, or fraction (in %) of events in which a PMT sees 1 or more PE, vs the PMT ID of that PE. A cut is made such that only PE observed within a window at ±4 ns relative to the DTM trigger are considered. PMT IDs are arranged in order of vertical position, from the neck to the bottom of the detector with ascending PMT ID. The laserball is located at the centre of the detector, at a rotation $\phi_{LB} = 0$, and the laserball is illuminated using the 445 nm laser head. The distribution is fitted with a straight line, shown in blue. 193

5.10 PE occupancy, or PE per event per PMT, vs the PMT ID of that PE. No timing cut is applied. PMT IDs are arranged in order of vertical position, from the neck to the bottom of the detector with ascending PMT ID. The laserball is located at the centre of the detector, at a rotation $\phi_{LB} = 0$, and the laserball is illuminated using the 445 nm laser head. The distribution is fitted with a straight line in (a), shown in blue. The ratio of fitted occupancy to observed occupancy is shown in (b), where the blue line at ratio 1 represents perfect agreement between observed and fitted occupancy. . . 195

5.11 PE occupancy (colour axis) observed in a PMT in direction θ_i, ϕ_i relative to the laserball surface. No timing cut is applied. This map is produced using a fitting routine designed by N. Fatemighomi. 195

5.12 F_{prompt} plotted against the total observed PE from charge division. Colour axis is number of events per bin. The laserball is located at the centre of the detector, at a rotation of $\phi_{LB} = \pi/2$, and is illuminated using the 445 nm laser head. 197

5.13 F_{prompt} plotted against the total observed PE from charge division. Colour axis is number of events per bin. The laserball is located at the centre of the detector, at a rotation of $\phi_{LB} = \pi/2$, and is illuminated using the 445 nm laser head. 198

5.14 Reconstructed cubic radius distribution $(R/R_0)^3$, where $R_0 = 851$ mm is the AV-TPB boundary radius. The vertical axis is on a log scale. The laserball is located at the centre of the detector, at a rotation of $\phi_{LB} = \pi/2$, and is illuminated using the 445 nm laser head. 198

5.15 Laserball data reconstructed co-ordinate distributions in x, y and z. The laserball is located at the centre of the detector, at a rotation of $\phi_{LB} = \pi/2$, and is illuminated using the 445 nm laser head in (a) and the 375 nm laser head in (b). 199

5.16 Laserball data reconstructed co-ordinate distributions in x, y and z. The laserball is located 550 mm above the centre of the detector, at a rotation of $\phi_{LB} = \pi/2$, and is illuminated using the 445 nm laser head in (a) and the 375 nm laser head in (b). 199

5.17 Laserball data reconstructed co-ordinate distributions in x, y and z. The laserball is located 550 mm below the centre of the detector, at a rotation of $\phi_{LB} = \pi/2$, and is illuminated using the 445 nm laser head in (a) and the 375 nm laser head in (b). 199

5.18 Reconstructed co-ordinate distribution in x for laserball data. The reconstructed distribution is fitted with a Gaussian. The laserball is located at the centre of the detector, at a rotation of $\phi_{LB} = \pi/2$, and is illuminated using the 445 nm laser head. 200

5.19 Laserball simulation reconstructed co-ordinate distributions in x, y and z. The laserball is simulated at the centre of the detector, at a rotation of $\phi_{LB} = \pi/2$. The wavelength distribution from the 445 nm laser head is used in (a), and the distribution from the 375 nm laser head is used in (b). 202

5.20 Laserball simulation reconstructed co-ordinate distributions in x, y and z from simulation. The laserball is simulated 550 mm above the centre of the detector, at a rotation of $\phi_{LB} = \pi/2$. The wavelength distribution from the 445 nm laser head is used in (a), and the distribution from the 375 nm laser head is used in (b). 202

5.21 Laserball simulation reconstructed co-ordinate distributions in x, y and z from simulation. The laserball is simulated 550 mm below the centre of the detector, at a rotation of $\phi_{LB} = \pi/2$. The wavelength distribution from the 445 nm laser head is used in (a), and the distribution from the 375 nm laser head is used in (b). 203

5.22 Comparison of reconstructed z distributions from data and simulation. The laserball is located at the centre of the detector, at a rotation of $\phi_{LB} = \pi/2$. The simulated and real laserball are illuminated using the 445 nm laser head in (a), and the 375 nm laser head is used in (b). 204

5.23 Comparison of reconstructed z distributions from data and simulation. The laserball is located 550 mm above the centre of the detector, at a rotation of $\phi_{LB} = \pi/2$. The simulated and real laserball are illuminated using the 445 nm laser head in (a), and the 375 nm laser head is used in (b).204

5.24 Comparison of reconstructed z distributions from data and simulation. The laserball is located 550 mm below the centre of the detector, at a rotation of $\phi_{LB} = \pi/2$. The simulated and real laserball are illuminated using the 445 nm laser head in (a), and the 375 nm laser head is used in (b).204

5.25 Simulated PE occupancy, or PE per event per PMT, vs the PMT ID of that PE. No timing cut is applied. PMT IDs are arranged in order of vertical position, from the neck to the bottom of the detector with increasing PMT ID. The laserball is simulated at the centre of the detector, at a rotation of $\phi_{LB} = 0$. The wavelength distribution from the 445 nm laser head is used. The distribution is fitted with a straight line in (a), shown in blue. The ratio of fitted occupancy to observed occupancy is shown in (b), where the blue line at ratio 1 represents perfect agreement between observed and fitted occupancy. 205

5.26 Comparison of the distribution of F_{prompt} vs n_{SC} in ^{39}Ar simulation and data. Colour axis is number of events per bin. The effect of the prescale is clearly visible at high n_{SC}. 206

5.27 Comparison of the distribution of F_{maxpe} vs n_{SC} in ^{39}Ar simulation and data. Colour axis is number of events per bin. 206

5.28 Reconstructed cubic radius $(R_{rec}/R_0)^3$ distributions, normalised to the event radius R_0, comparing simulated ^{39}Ar (yellow) to data (pink) in the electronic recoil band. A simulation-data bias is visible on comparing the two. 207

5.29 The ratio of the probability of an event reconstructing at a given cubic radius $(R_{rec}/R_0)^3$ in data (pink) to the probability in simulation, as compared in Figure 5.28. A ratio at unity represents perfect agreement. 208

5.30 Reconstructed cubic radius $(R_{rec}/R_0)^3$ distributions, normalised to the event radius R_0, comparing the effects of changing the TPB thickness to 1, 2 and 4 μm, shown in (a) alongside the distribution from data. The distribution ratio of each modified simulation to the distribution from data is shown in (b). A ratio at unity represents perfect agreement. 209

5.31 Reconstructed cubic radius $(R_{rec}/R_0)^3$ distributions, normalised to the event radius R_0, comparing the effects of changing the argon Rayleigh scattering length to the E. Grace measured value at 57 cm, changing the TPB scattering length to the value favoured by Stolp *et. al.* [143] and both changes at once, alongside the distribution from data. The distribution ratio of each modified simulation to the distribution from data is shown in (b). A ratio at unity represents perfect agreement. 210

5.32 Comparing the agreement with data from the combination of the E. Grace measurement with the range of favoured TPB scattering lengths from the study by Stolp *et. al.* [143]. 211

5.33 Demonstration of the effect of using the new optical model in Chapter 3 in lookup tables, reconstructing ^{39}Ar data and simulation also using the new optical model. Distributions are in reconstructed cubic radius $(R_{rec}/R_0)^3$, normalised to the event radius R_0, comparing simulated ^{39}Ar (yellow) to data (pink) in the electronic recoil band. 211

5.34 Energy spectra for the electrons produced in ^{22}Na gamma interactions in argon, showing the products of Compton scattering, the photoelectric effect, ionisation from other electrons, and the reconstructed energy of these events 213

5.35 Energy spectra for gamma interactions in surrounding detector materials, showing the products of Compton scattering, the photoelectric effect, ionisation from other electrons, and the reconstructed energy of these events 214

5.36 The distribution of F_{prompt} in a simulation of a 333kBq ^{22}Na source, using a 16μs event window, and the DAQ trigger configuration used in in-situ data, compared to in-situ data. Data corresponding to argon scintillation (blue), acrylic Cerenkov (green) and the mixture of the two (pink) is produced by requiring that simulation tracking information records interaction in the argon. The source (yellow) and background (brown) data correspond to events in real data where the source is and is not present in Cal F respectively. 215

5.37 The distribution of F_{maxpe} in a simulation of a 333kBq ^{22}Na source, using a 16μs event window, and the DAQ trigger configuration used in in-situ data, compared to in-situ data. Data corresponding to argon scintillation (blue), acrylic Cerenkov (green) and the mixture of the two (pink) is produced by requiring that simulation tracking information records interaction in the argon. The source (yellow) and background (brown) data correspond to events in real data where the source is and is not present in Cal F respectively. 216

5.38 The distribution of scintillation PE n_{SC} in a simulation of a 333kBq ^{22}Na source, using a 16μs event window, and the DAQ trigger configuration used in in-situ data, compared to in-situ data. Data corresponding to argon scintillation (blue), acrylic Cerenkov (green) and the mixture of the two (pink) is produced by requiring that simulation tracking information records interaction in the argon. The source (yellow) and background (brown) data correspond to events in real data where the source is and is not present in Cal F respectively. 217

5.39 The reconstructed cubic radial distribution in a simulation of 1.27MeV gammas using the DAQ trigger configuration used in real data, compared to real data. 217

6.1 Scatter plot showing the distribution of 27 events in F_{prompt} and Q_{PE}, which pass the nominal cut flow from the first paper analysis. The events are thought to originate from a scintillation in the neck and are under investigation. 221

6.2 Zero event 90% C.L. upper limits on a spin-independent WIMP-nucleon scattering cross section vs WIMP mass, calculated using the Poisson method, using the original design specifications from the detector. For comparison, the same zero event limit with an 802.95 mm fiducial radius, and the 1, 2 and 3 event limits. 222

6.3 Zero event 90% C.L. upper limits on a spin-independent WIMP-nucleon scattering cross section vs WIMP mass, calculated using the Poisson method, using the original design specifications from the detector. Comparisons show the effect of lowering the PE threshold on the achieved sensitivity to lower scattering cross sections. 223

6.4 Mean and upper and lower error on F_{prompt} plotted vs Q_{PE}. Simulated and calculated by Shawn Westerdale for F_{prompt} for the DEAP-3600 first result, from data from SCENE and Regenfus *et. al.* [155]. 229

6.5 Projection of the WIMP PDF as implemented in the likelihood, in F_{prompt} vs Q_{PE}. The colour axis is in arbitrary units due to the use of FFT convolution, and the PDF is normalised internally in the algorithm. 229

6.6 Projection of the ^{39}Ar PDF as implemented in the likelihood, in F_{prompt} vs Q_{PE}. The colour axis is in arbitrary units due to the use of FFT convolution, and the PDF is normalised internally in the algorithm. 230

6.7 The variation of the observed radial bias μ normalised to the AV radius R_0, with the true cubic radius of the event $(R_{MC}/R_0)^3$. The distribution is fitted with a cubic polynomial. 232

6.8 The variation of the observed radial resolution σ normalised to the AV radius R_0, with the true cubic radius of the event $(R_{MC}/R_0)^3$. The distribution is fitted with a cubic polynomial. 232

6.9 A projection of the ^{39}Ar PDF in observed reconstructed radius R_{rec} and Q_{PE}, as implemented in the likelihood. The colour axis is in arbitrary units due to the use of FFT convolution, and the PDF is normalised internally in the algorithm. 233

6.10 The distribution of observed Q_{PE} for simulated ^{210}Po alphas emitted from the TPB bulk. The distribution is fitted with a three-component exponential which is implemented in the likelihood. The full energy deposition peak in TPB is observed above the fitted QPE range of $50 < Q_{PE} < 600$, and the DAQ trigger condition truncates the distribution below it. 235

6.11 The distribution of F_{prompt} observed from simulation of ^{210}Po alphas emitted from the TPB surface. The distribution is fitted with a Gaussian distribution which is implemented in the likelihood. 235

6.12 The two-component distribution of F_{prompt} observed from simulation of ^{210}Po alphas emitted from the AV inner 80 μm. The distribution is fitted with two Gaussian distributions separately, which are implemented in the likelihood. 236

6.13 The distribution of reconstructed radius, plotted as the radial distance inward from the AV boundary, $R_0 - R_{rec}$, for simulated ^{210}Po alphas emitted from the AV inner 80 μm. The distribution is fitted with a weighted sum of three half-Gaussian distributions, which is implemented in the likelihood. 236

6.14 Fitted light yield linear coefficient B distribution for 5000 pseudo-experiments generated and fitted using only the ^{39}Ar PDF and constraint terms. Only the B parameter is floated in the minimisation. 239

6.15 Fitted linear PE resolution coefficient B distribution for 1000 pseudo-experiments generated and fitted with the full likelihood model, including the ^{39}Ar side-band from data. Every nuisance parameter is floated in the minimisation. 239

6.16 The variation of the ROI lower boundary in F_{prompt} with Q_{PE}, together with a scatter plot showing the distribution of the 27 events in F_{prompt} and Q_{PE} from Figure 6.1. The boundary in F_{prompt} is chosen by choosing the value which maximises $s/(s+b)^{1/2}$, and does not exclude any of the 27 events. 241

6.17 Preliminary 90% C.L. upper limits on the spin-independent WIMP-nucleon scattering cross section. Grey crosses are obtained from a profile likelihood ratio analysis using a dataset containing 27 events which reconstruct in the ROI. The pink line is obtained using the Poisson method assuming zero background events, and the purple line is obtained using the Poisson method assuming 27 events. 241

List of Tables

1.1 A summary of the properties of four directional detection experiments currently undergoing R&D. Adapted from [95]. 70

1.2 Properties of liquid noble gases. Values from Ref. [97, 98]. Approximate price ranges from Ref. [99]. 71

2.1 A table summarising the contributions to the surface alpha background, the probability $P_{leak,ROI}$ that an alpha will reconstruct in the energy region of interest, and the implied tolerable limits for that leakage fraction. Alongside these are measurements from detector data and assays of detector materials. 86

2.2 Summary of the highest contributors to the neutron nuclear recoil background, the number of events per year expected from each component, and the number of events that enter an example WIMP region of interest. Region of interest is taken as an example defined by total observed PE in the region 120-240 PE (equivalent to 20-40 keV$_{ee}$ for a conservative light yield of 6 PE per keV$_{ee}$), and a nominal PSD parameter cut $0.6 < F_{prompt} < 0.8$. Components are listed in order of decreasing ROI events per year. Table reproduced from calculations in Ref. [125, 126, 127]. 88

5.1 A table summarising properties of six runs within the laserball dataset. . . 197

6.1 Summary of nuisance parameters and their constraint forms and parametrisation. A parameter with no symbol is constrained by a PDF of its value. A † denotes a parameter whose constraint encodes the amount of deviation from the measured value. A ‡ denotes a parameter whose constraint encodes the (positive or negative) number of measurement errors away from measurement that the parameter can be. 238

Acronyms

F_{maxpe} Ratio of highest q_{PE} observed in any PMT to total q_{PE} observed in the event.

F_{prompt} DEAP PSD parameter representing the ratio of prompt to late scintillation light, as defined generally in Section 1.5.3 and for DEAP-3600 in Section 3.2.3.

L_{eff} Quenching factor.

N_{hit} Number of PMTs which observed a pulse with a peak time within the event window.

R_0 The radius of the AV surface, nominally 851 mm.

n_{PE} PE count from Bayesian PE counting.

n_{SC} Scintillation PE count from Bayesian PE counting.

q_{PE} PE count from dividing the charge in each PMT by its fitted SPE charge.

AARF Acrylic and Aluminium Reflector and Fibre-optics.

ADU Analogue-to-digital converted units.

AV Acrylic vessel.

C.L. Confidence level.

DAQ Data acquisition (refers to DAQ apparatus).

DEAP Dark matter Experiment using Argon Pulse shape discrimination.

DEAP-1 DEAP prototype experiment.

DEAP-3600 DEAP experiment with a vessel that carries a maximum of 3600 kg of liquid argon.

DTM Digitiser and trigger module.

eV_{ee} Electronic equivalent recoil energy unit.

eV_r Nuclear recoil energy unit.

PE Photoelectron(s).

PMT Photomultiplier tube.

PSD Pulse shape discrimination.

RAT Reactor Analysis Tool.

ROI Region of interest.

SCB Signal conditioning board, as described in Section 2.6.1.

SD Spin Dependent, referring to a WIMP-nucleon scattering cross section.

SI Spin Independent, referring to a WIMP-nucleon scattering cross section.

SPE Single photoelectron.

TPB Tetraphenyl Butadiene.

V1720/V1740 High/low gain CAEN digitiser boards.

WIMP Weakly Interacting Massive Particle.

ZLE Zero length encoding, a digitiser board setting saving waveform blocks instead of full-waveform data..

Chapter 1

Introduction

Astrophysical observations and precision cosmology indicate that Standard Model baryons make up 4.72% of the mass-energy density of the universe, and that baryonic matter represents 16.5% of the matter density of the universe [1]. The remainder of that matter density is inferred from observation of the effects of its gravitational interaction with standard model particles in astrophysical observations of the early and present universe. Because it has not been observed to interact with Standard Model particles via the electromagnetic (or strong) force, or emit light, it is known collectively as dark matter. A candidate particle known as the Weakly Interacting Massive Particle (WIMP), which theoretically interacts with Standard Model particles and has a weak-scale interaction and mass, results in the correct matter density fraction and accounts for astrophysical observations. This motivates the search for an observation of a weak interaction by a) direct detection experiments observing the interaction with a target mass; b) creating the candidate in a collider experiments and observing its products; or c) indirect detection by observing its effects on emissions from astrophysical sources. The work in this thesis presents part of an effort to understand particle interactions in a direct detection experiment known as DEAP-3600 (Dark matter Experiment using Argon Pulse Shape Discrimination). The thesis focuses on efforts to determine the positions at which particle interactions occurred within in the detector.

The first chapter discusses the astrophysical evidence in favour of a dark matter component to the mass-energy density of the universe, and an alternative explanation for its

gravitational effects. The chapter then describes the candidates for a dark matter particle and summarises the techniques currently employed to detect these particles, with a focus on WIMPs. Chapter 1 closes by describing the physics of scintillation in liquid noble gases. The discussion focuses on argon, the target materialÂ and scintillator in DEAP-3600. Chapter 2 discusses the DEAP-3600 experiment, a single-phase liquid argon dark matter direct detection experiment based in Sudbury, Ontario in Canada [2]. The experiment has completed commissioning and published its first result on 4.44 live days of data [3] and at time of writing continues to take and analyse its first year of data. Chapter 2 also discusses the standard model particles that can mimic a WIMP signal in the detector and produce background events. Identification and reduction of background events increases the sensitivity of a detector to WIMP signal. The author contributed to construction of the detector and commissioning tasks, and operated the data acquisition throughout the life time of the experiment. Chapter 3 discusses the simulation and analysis software used in DEAP-3600, known as RAT (for Reactor Analysis Tool). The discussion also describes the common analysis quantities used in data analysis in future chapters. Chapter 3 then discusses the effect that the uncertainty on optical parameters used in the simulation have on the analysis variables on which position reconstruction depends. The author worked on updating the optical model in simulation to better reflect the results from data. Chapter 4 discusses the energy and position reconstruction algorithms employed in DEAP-3600 data analysis. The author redesigned the mathematical model describing light propagation to photomultiplier tubes in one position reconstruction algorithm called ShellFit. The author also reduced the CPU time of ShellFit such that it was capable of being implemented in the automated analysis. The author also developed a method to relate positions to the time-dependence of detector data in an addition to the existing position reconstruction model. The discussion in Chapter 4 concludes with an analysis of the effect of each change to the position reconstruction model on the performance of position reconstruction on simulations of background events. Chapter 5 discusses the use of calibration sources to assess the performance of position reconstruction, comparing data taken with the sources installed to the results of simulation of the sources and detector response. Chapter 6 dis-

cusses the role that position reconstruction plays in a dark matter search. The author developed a profile likelihood ratio analysis with Alistair Butcher, the original author of the software, and Shawn Westerdale. The author implemented the reconstructed event radial co-ordinate as a position and energy dependent PDF in the likelihood, as well as implementing background event PDFs from alpha decays at the detector surface, which the position reconstruction is capable of rejecting by reconstructing them at the surface and defining a radial cut away from the surface. The analysis is performed on a set of 27 events observed to pass the standard dark matter search cut flow at time of writing, and the result is verified using zero event and 27 event results set using the simpler Poisson method.

1.1 Dark Matter Astrophysics

This section outlines the evidence from astrophysics and cosmology that suggests that there exists a dark matter component in our universe.

The smallest scale at which dark matter has presented itself in astrophysical observation is at the galactic scale. Vera Rubin made observations of the Doppler shifts of celestial objects near the galactic plane in the Andromeda Nebula [4], and from these inferred their velocities.

The distribution of orbital velocity v against the object's distance from the galactic centre r is known as a rotation curve. Rubin observed that outside of the radial extent of Andromeda's luminous matter the orbital velocity of celestial objects is not related to r by the standard Newtonian orbital velocity, $v = (GM(r)/r)^{1/2}$, where $M(r)$ is the mass contained within r. Instead velocity becomes independent of r at high r, as shown in the observed rotation curve for galaxy NGC6503 [5] in Figure 1.1. The preferred explanation for this inconsistency is a spherical halo of non-luminous matter, or dark matter. The contribution a dark matter halo has to rotation velocities is shown as the dot-dashed line in Figure 1.1. Also shown is that the combination of the contribution from the dark matter curve and a contribution from cold gas reconciles the total rotational velocity, shown as a solid line, with the data. Rubin confirmed her observation in 1985 in a catalogue of

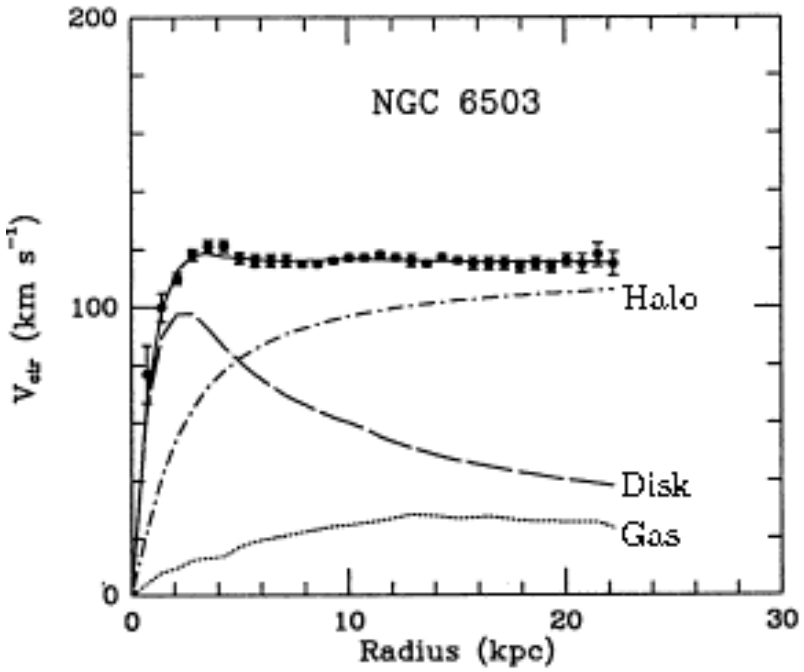

Figure 1.1: Rotation velocity of celestial objects in galaxy NGC6503 vs their radial distance from the galactic centre, reaching a constant at high radius. Figure reproduced from Ref. [5].

54 spiral galaxies in Ref. [6]. The catalogue of rotation curve observations now stands at over 1000 galaxies [7]. For a comprehensive review of the development of galactic rotation curve observation the reader is directed to Ref. [8].

Moving up in scale, hints of the requirement of dark matter were previously found in observations of galaxies in the Coma Cluster by Fritz Zwicky. He observed that the velocity dispersion $\sigma(v)$ of galaxies in the Coma Cluster was $\sigma(v) = 1019 \pm 360$ km s^{-1}, which implied that the mean density of the cluster was greater by a factor of 400 than that implied by luminous matter [9].

Gravitational lensing can be used to determine the mass and matter distribution of a galaxy cluster to infer the presence of dark matter. General relativity holds that in the vicinity of large gravitational potentials the local geometry is curved. Light propagating through such geometry has its trajectory altered, such that light from an object behind a large gravitational potential is curved around that potential, effectively acting as a lens. The extent of the deviation from its true position is dependent on the mass M_l of the lens, with the observed angular radius of deviation given by $\theta = ((4GM_lD_{lb})/(c^2D_lD_b))^{1/2}$, where $D_{l,b}$ are the distances between observer and either lens and background object, and

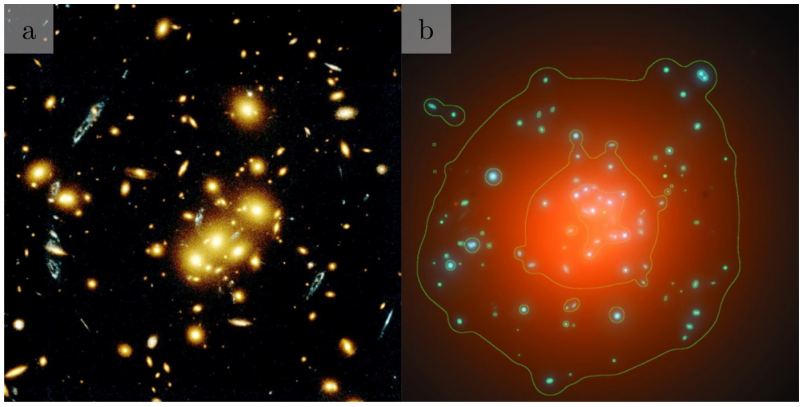

Figure 1.2: (a) The luminous matter from cluster 0024+1654. Image from W.N. Colley and E. Turner (Princeton University), J.A. Tyson (Bell Labs, Lucent Technologies) and NASA/ESA. (b) The matter distribution in cluster 0024+1654, inferred from luminous matter and gravitational lensing. Data from [10].

D_{lb} is the distance between lens and background object. Figure 1.2a shows the luminous matter from cluster 0024+1654 as white and yellow spots, most densely distributed at the centre of the image. A background quasar appears as several images in an arc shown in blue. Figure 1.2b shows the matter distribution in cluster 0024+1654. The luminous masses are shown in blue, alongside mass reconstructed from gravitational lensing of background objects, from lower mass in orange to higher mass in yellow. The overall matter distribution consists of a smooth background distribution, with spikes from the galaxies in the cluster. The matter distribution implied by lensing extends beyond the luminous matter of any individual galaxy in the cluster, inferring a non-luminous matter component that extends beyond the luminous extent of galaxies.

An alternative theory explaining rotation curve-based astrophysical evidence without inferring the existence of dark matter is that of modified Newtonian dynamics, or MOND [11]. In 1983, Milgrom proposed that Newtonian gravity should be reduced at small accelerations a. The parameter a_0 is the characteristic acceleration at which the modification applies. a_0 has been measured for a catalogue of 100 galaxies at $a_0 = 1.2 \times 10^{-10} ms^{-1}$ [12]. An interpolating function is applied $\mu(a/a_0)$ such that $a \to a\mu(a/a_0)$, which satisfies the classical case where $\mu(a/a_0) \to 1$ for $a \gg a_0$ and the modified case where $a \to a/a_0$ for $a \ll a_0$ and orbital velocity becomes constant at $v = (GMa_0)^{1/4}$. While MOND is capable of reproducing rotation curves of spiral galaxies within error [12], it

Figure 1.3: A colourised image of the Bullet Cluster, which is an example of the remnant of two collided clusters with a clear separation between the matter and dark matter component. The reconstruction of gas from X-ray spectroscopy is shown in red, and the distribution of dark matter as indicated by gravitational lensing is shown in blue. X-ray image from Ref. [18]. Lensing map and optical background imaging from Ref. [15].

under-predicts galactic cluster masses by a factor of 2 [13]. For a comprehensive account of the successes and difficulties of MOND the reader is directed to Ref. [13], and Chapter 6 of Ref. [14].

Another observation at the galactic cluster scale is that of the cluster 1E 0657-56, known as the Bullet Cluster, shown in Figure 1.3. The Bullet Cluster is the aftermath of the collision of two galactic clusters [15]. The red region in Figure 1.3 depicts X-ray emission from hot gas, from X-ray measurements using the Chandra X-ray Observatory; the blue region indicates the presence of dark matter reconstructed from gravitational lensing of background objects observed by the Hubble Space Telescope. Electromagnetic interactions between the gases in the two clusters caused the gas component to slow down, with a spatial offset with respect to stars and dark matter at the 8σ significance level [16]. The dark matter components passed through one another without interacting, which would cause the two components to slow and cluster, implying a small dark matter self-interaction cross section. Analysis of Chandra and Hubble observations of 72 galactic cluster collisions produced a 95% C.L. upper limit on the dark matter self-interaction cross section per unit dark matter mass at $\sigma_{DM}/m_{DM} \leq 0.47\text{cm}^2\text{g}^{-1}$ (95 C.L.) [17].

At a cosmological scale, further evidence for the existence of dark matter comes from observations of the Cosmic Microwave Background, or CMB, by the Wilkinson

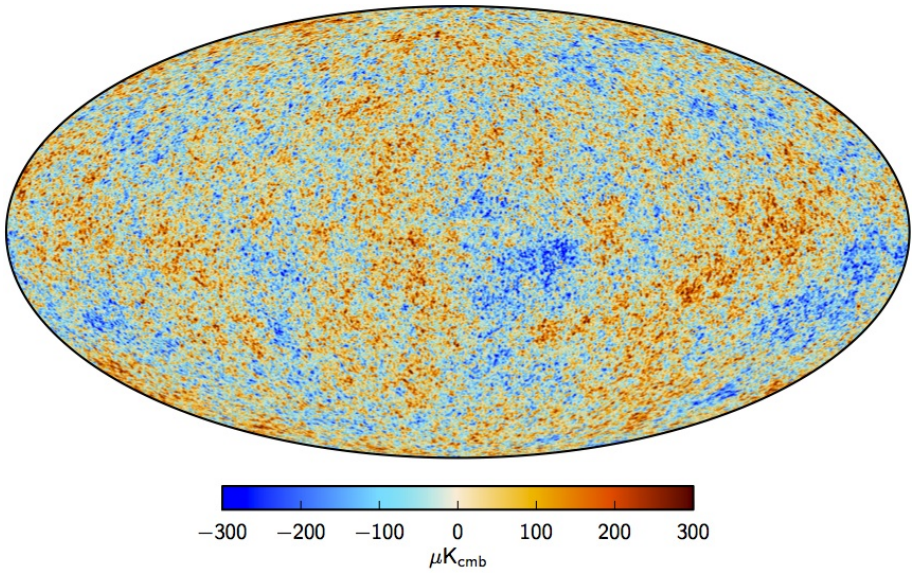

Figure 1.4: μK fluctuations in the temperature spectrum of the CMB mapped vs direction of origin in a Mollweide projection with the galactic plane at the equator, as measured by Planck. The contributions from the dipole term and galactic plane emission have been subtracted. Plot reproduced from Ref. [20].

Microwave Anisotropy Probe (WMAP) [19], and more recently by ESA's Planck mission [20]. The CMB is comprised of photons emitted from the surface of last scattering when photons decoupled and the opaque photon-baryon fluid became transparent. The CMB is observed to be isotropic, per the cosmological principle, which states that the matter distribution of the universe is isotropic and homogeneous in all directions. CMB photon energies are observed today to follow a black body spectrum with a temperature of T=2.726 K. Temperature fluctuations below the order of 10^{-5}K indicate the presence of small scale-invariant anisotropies in density at the time of photon decoupling. The competing forces of gravity from matter and radiation pressure from photons set up a multi-modal oscillation across the baryon-photon fluid whose shape depends on the matter-energy composition and geometry of the universe. For a comprehensive review of CMB theory the reader is directed to Ref. [21].

Figure 1.4 shows a Planck measurement of the temperature of photons in the CMB, after subtracting the contributions from the galactic plane and a dipole term produced by our motion in the universe. Using a spherical harmonics expansion one can map the

temperature fluctuation at a given point in the sky:

$$\Delta T(\theta,\phi) = \sum_{l=0}^{\infty} \sum_{m=-l}^{l} a_{lm} Y_{lm}(\theta,\phi) \tag{1.1}$$

where the Y_{lm} are spherical harmonics which form an orthonormal basis describing all possible oscillation shapes on a sphere. The a_{lm} form a set of independent random variables that characterise the amount and sign of fluctuation between points separated by an angular scale l, where $l \propto \theta^{-1}$. m indexes the different oscillation shapes which contribute to the total oscillation pattern, with $2l+1$ values of integer m per multipole value l. Assuming Gaussian temperature fluctuations, the expectation value of a_{lm} is $\langle a_{lm} \rangle = 0$, corresponding to no fluctuation. The amount of anisotropy for a given l is parametrised by taking the variance $\langle |a_{lm}|^2 \rangle$ of the set of $\{a_{lm}\}$ that could produce a theoretical fluctuation at an angular scale l. The variance of a_{lm} is related to the variance of the theoretical temperature fluctuations $\langle \Delta T^2(\phi,\theta) \rangle$ it produces by:

$$\langle \Delta T^2(\phi,\theta) \rangle = \sum_{l} \left(\frac{2l+1}{4\pi} \right) C_l, \text{ where } C_l = \left(\frac{1}{2l+1} \right) \sum_{m} \langle a_{lm} \rangle \tag{1.2}$$

C_l is the fluctuation amplitude at an angular scale l. Analogously, the *observed* power spectrum $\hat{C}_l$ is related to the observed temperature variance averaged over the entire sky (a 4π solid angle) by:

$$\frac{1}{4\pi} \int_{-1}^{1} \int_{0}^{2\pi} \Delta T^2_{obs}(\phi,\theta) d[\cos(\theta)] d\phi = \sum_{l} \left(\frac{2l+1}{4\pi} \right) \hat{C}_l, \text{ where } \hat{C}_l = \left(\frac{1}{2l+1} \right) \sum_{m} |a_{lm}| \tag{1.3}$$

The observed $\hat{C}_l$ summarises the information contained in a CMB temperature fluctuation map, and can be plotted vs l to produce an observed power spectrum. The power spectrum from the Planck 2015 result [1] is shown in Figure 1.5, plotted as $l(l+1)C_l$ vs l. The observed spectrum is compared to the best fit model from the Standard Model of Cosmology, or ΛCDM model (for cosmological constant Λ, and Cold Dark Matter), which fits the observed spectrum within error at $l > 30$, as shown on the residual plot at the bottom of 1.5. The measurement variance, known as the cosmic variance, is given by $\langle (C_l - \hat{C}_l)^2 \rangle = (2/2l+1)\, C_l^2$, which diverges and produces the larger error bars on measurements at $l < 10$.

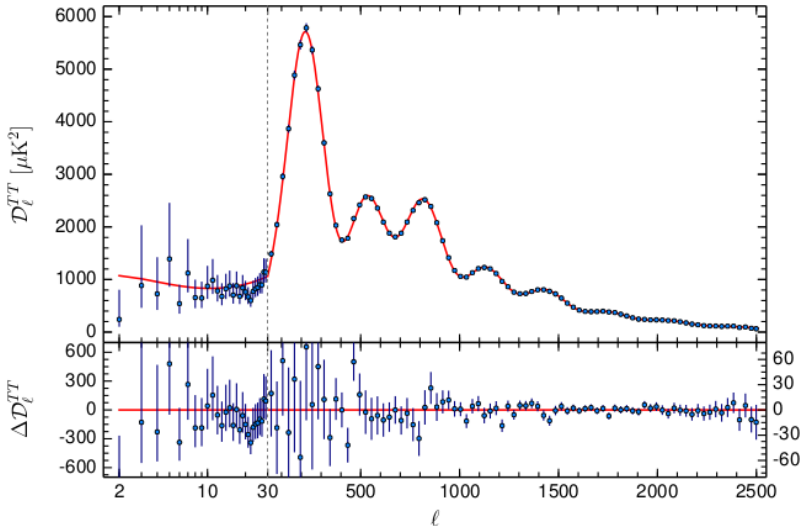

Figure 1.5: Observed power spectrum $D_l^{TT} = l(l+1)\hat{C}_l$ from photon temperature two-point correlation function at angular scale l on top, and a residual between observation and ΛCDM model fit shown on bottom. D^{TT} notation is used by Planck to distinguish temperature (T) correlation function from photon polarisation measurements. Plot reproduced from Ref. [1].

The locations and sizes of peaks and troughs in the oscillation pattern at $l > 30$ depend on parameters in the ΛCDM model [21], which are constrained by fitting the theoretical spectrum to the observed spectrum. Among the ΛCDM model parameters are mass-energy density parameters $\Omega = \rho/\rho_c$, which are defined as the fraction of the total mass-energy density ρ_c required for a universe with flat geometry where $\sum_i \Omega_i = 1$, and the reduced Hubble constant $h = H_0/(100 \text{ km s}^{-1} \text{ Mpc}^{-1})$. The first peak in the power spectrum depends on the age and geometry of the universe. The baryon density is inferred from the ratio of the second to first peaks, fitted at $\Omega_b h^2 = 0.02226 \pm 0.00023$ from Planck [1]. The total matter density Ω_m depends on the height of the third peak, fitted at $\Omega_m h^2 = 0.1426 \pm 0.0020$, or $6.4\Omega_b$ [1]. The best fit result also states a cold dark matter mass-energy density of $\Omega_c h^2 = 0.1186 \pm 0.002$, the remaining $5.4\Omega_b$ of missing mass-energy density in the universe [1].

A complementary constraint on the baryon density comes from estimating the primordial abundances of light elements formed in the radiation-dominated phase ∼1 s after the Big Bang. This is a process known as Big Bang Nucleosynthesis (BBN), which is reviewed comprehensively in Ref. [22]. As the universe expanded and cooled, and as temperatures dropped below the binding energies of nuclei, light elements began to form,

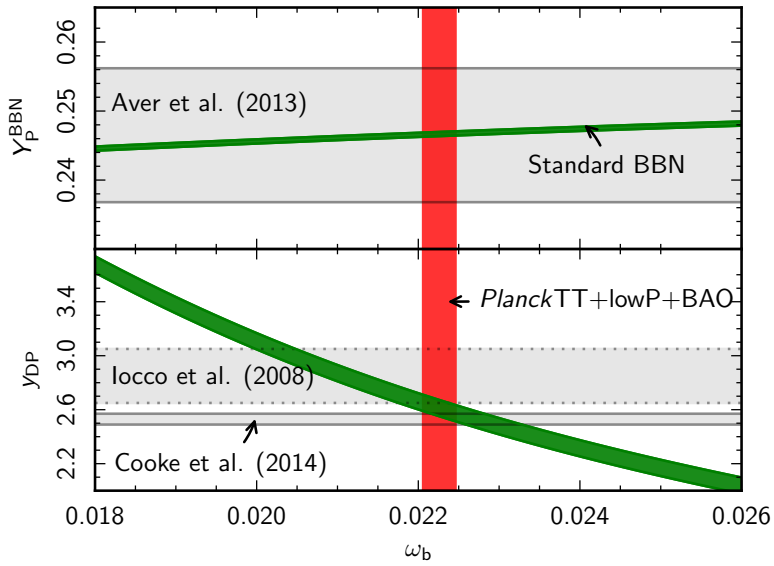

Figure 1.6: Predictions of the primordial ^{4}He (top) and deuterium (bottom) abundances with varying baryon density ω_b. The green stripes represent the Planck prediction from Big Bang Nucleosynthesis with a 68% uncertainty on rates at which nuclear reactions take place, and on the neutron lifetime. Horizontal grey bands show observational bounds on helium from Ref. [23], and deuterium from Ref. [22] and Ref. [24]. The vertical red band represents the Planck constraint on ω_b [1]. Grey horizontal band show observation constraints from the listed authors, not listed here. Plot reproduced from Ref. [1].

then their abundance froze out when the expansion rate exceeded the reaction rate, analogously to the WIMP freeze-out mechanism discussed later in Section 1.2.2. The element abundances depend on η, the photon to baryon (abundance) ratio, which determines the baryon mass-energy density parameter Ω_b. Predictions of the primordial helium and deuterium abundances from Ref. [1] are shown against Ω_b in the green bands in Figure 1.6. The constraint $\Omega_b h^2 = 0.02226 \pm 0.00023$ obtained from a fit of the ΛCDM model to Planck CMB data is shown in red [1]. Observational constraints on the abundances of helium from Ref. [23], and deuterium from Ref. [22] and Ref. [24] are shown as horizontal grey bands. Both deuterium constraints are consistent with the prediction from BBN, within the range of Ω_b fitted from CMB data [1].

1.2 Dark Matter Candidates

If dark matter is assumed to be one or more particle species like baryonic matter, it must have a specific set of properties in order to be consistent with astrophysical observations. It must be electrically neutral, else it might interact with or produce light. It must not emit photons, given that it does not collapse into the centres of galaxies it inhabits. It must also be gravitationally interacting and collisionless as required to explain, for example, the separation of dark and baryonic matter in Bullet Cluster. It must have a lifetime long enough that we cannot observe its decay. It must also exist as an approximately spherical halo as large as its host galaxies to explain the observations of galactic rotation curves and cluster velocities. It must be travelling at non-relativistic speeds, or it would prevent structure formation below the galactic cluster scale, and result in a smaller relic abundance than that which results from fits to the CMB power spectrum.

A set of theoretical particles have emerged that fit the above prescription, the most favoured two of which, axions and Weakly Interacting Massive Particles (WIMPs), are discussed in this section.

1.2.1 Axions

Axions are postulated as both a dark matter candidate and a solution to the strong CP problem. CP violation is observed in weak interactions, but not in quark interactions. In Quantum Chromodynamics (QCD), the CKM matrix M, which is measurable in flavour changing weak interactions, contains a CP violating phase $\theta \approx \mathscr{O}(1)$. One of the consequences of CP violation is an observable electron dipole moment (EDM) of the neutron given by $|d_n| \approx 10^{-16}\hat{\theta} e$cm, where e is the charge of the electron. Measurement of $|d_n|$ provides a value for the parameter $\hat{\theta} = \theta - |det(M)|$). In combination with a measurement for $|det(M)|$, the a measurement of $|d_n|$ provides a value for θ. Current measurements place the electron dipole moment at $|d_n| < 2.9 \times 10^{-26} e$ cm [25]. As a consequence, this implies an upper bound on the parameter $\hat{\theta} < 10^{-9}$. That the dipole moment $|d_n|$ and observable $\hat{\theta}$ should be so small in QCD is known as the strong CP problem.

The Peccei-Quinn solution [26, 27] makes $\hat{\theta}$ a dynamic variable, which can relax to

zero. This is achieved by introducing a spontaneously broken $U(1)_{PQ}$ symmetry, which necessitates a new Nambu-Goldstone boson, known also as the axion. Such a boson would be non-relativistic, with a mass m_A related to the symmetry breaking scale f_a by:

$$m_A \approxeq \frac{0.5957\text{meV}}{f_A/(10^{10}\text{GeV})} \tag{1.4}$$

Detection efforts focus on the detection of an axion-photon interaction, known as the Primakoff effect [28]. An axion-like particle in the DFSZ [29] and KSVZ [30] models has an axion to two photon decay width given by:

$$\Gamma_{A\to\gamma\gamma} = \frac{G_{A\gamma\gamma}^2 m_A^3}{64\pi} = 1.1\times10^{-24}s^{-1}\left(\frac{m_A}{\text{eV}}\right)^5 \tag{1.5}$$

Consequently an axion which has not decayed within the age of the universe has a mass of $m_A \lesssim 20$ eV. For a comprehensive review of axions and the strong CP problem the reader is directed to Peccei's summary of the topic in Ref. [31].

The axion detection experiment with leading sensitivity at time of writing is the Axion Dark Matter Experiment (ADMX). ADMX seeks to detect axions via their interaction with a magnetic field and consequent resonant production of microwave photons, in a high-Q (low loss) microwave cavity [32]. The current and projected sensitivity of the ADMX experiment to the axion to two photon coupling is shown in the lowest mass green band in Figure 1.7, alongside other microwave cavity experiments. The yellow band represents the parameter space bounded by the DFSZ and KSVZ models, much of which is unprobed at the time of writing, and the blue band is that shown in Figure 1.8.

Other limits are set by astrophysical observation, shown in the summary plot in Figure 1.8, which contains the region shown in Figure 1.7. The horizontal line labelled Horizontal Branch Stars represents the 95% C.L. upper limit from an analysis of stellar evolution in observations of globular clusters [39]. Also shown are the 3σ exclusion region from analysis of SN1987A data testing for axion-like particle conversion to gamma rays [40], and 95% C.L. limits from Fermi-LAT collaboration analysis of the gamma ray spectrum of NGC 1275 [41], and HESS collaboration analysis of the gamma ray spectrum of active galactic nucleus PKS 2155 [42]. For a summary of direct and astrophysical observation

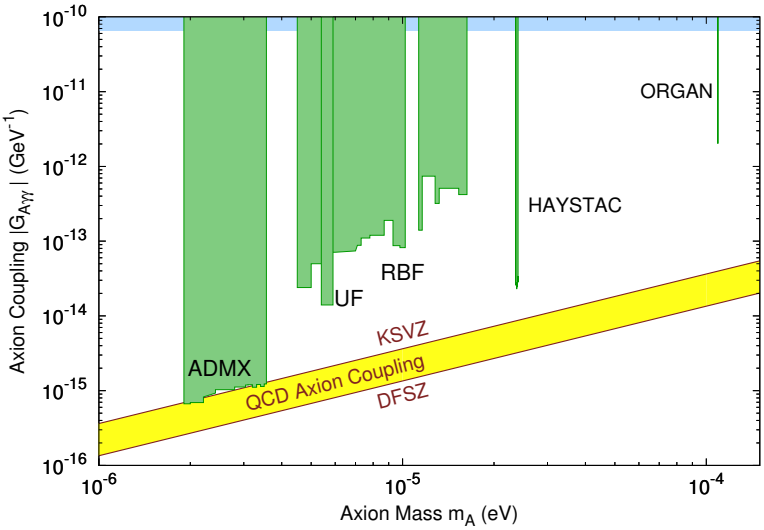

Figure 1.7: Axion to two photon coupling against axion mass for ADMX [32] and microwave cavity experiments from University of Florida (UF) [33], the Rochester-Fermilab-Brookhaven (RBF) experiment [34, 35], HAYSTAC [36] and ORGAN [37]. Current sensitivity of ADMX is shown in green. The parameter space bounded by the DFSZ and KSVZ models is shown as yellow band. Figure reproduced from Ref. [38].

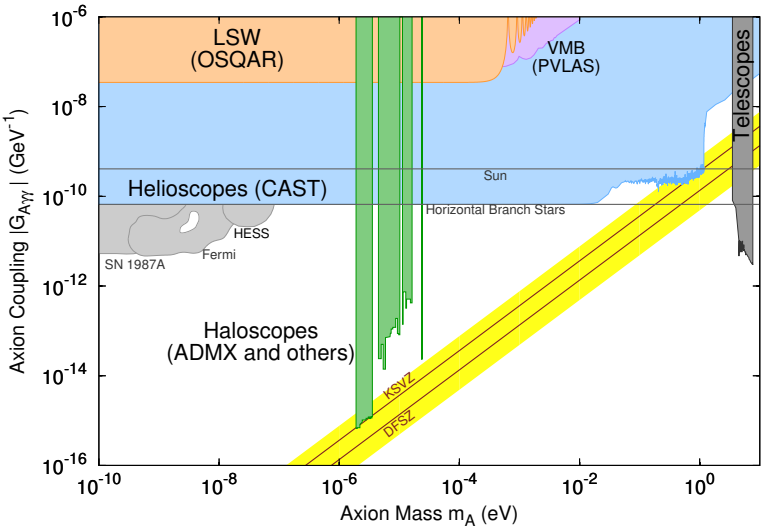

Figure 1.8: Summary of the axion to two photon coupling against axion mass parameter space, containing the region shown in Figure 1.7. Figure reproduced from Ref. [38].

efforts the reader is directed to Ref. [38].

1.2.2 WIMPs

The Weakly Interacting Massive Particle, or WIMP, denoted χ, is a class of candidate thought to interact weakly and gravitationally with Standard Model particles. It is also thought to be produced with an abundance consistent with the ΛCDM model, by means outlined below, following Section 7.1 of Ref. [14].

The WIMP has candidates which satisfy the conditions described at the beginning of this section. A popular candidate comes from supersymmetry (or SUSY). One of the predictions of the Minimal Supersymmetric Model (MSSM) is that each Standard Model particle has a supersymmetric superpartner with a half integer spin (S) difference but with the same baryon (B) and lepton (L) number. For a comprehensive review of SUSY, the MSSM and SUSY WIMP candidates, the reader is directed to Ref. [43]. A new quantity $R = (-1)^{3B+L+2S}$ gives $R = +1$ for Standard Model particles and $R = -1$ for sparticles. The value of R, known as R-parity, is conserved in every particle interaction. As a consequence of R-parity conservation a sparticle can only decay into other, lighter sparticles, meaning that the abundance at freeze out of the Lightest Supersymmetric Particle (LSP) must persist today. The favoured candidate considered by experimentalists is the lightest neutralino χ. It is comprised of the linear superposition of the zino, photino and two neutral higgsinos (superpartners of the Z^0, photon and Higgs doublet respectively), and is electrically neutral and stable. SUSY provides a means by which to cancel quadratic divergences in radiative (higher-order) corrections to the mass squared of the Higgs boson. This requires that the mass of the LSP (or any sparticle) $m_\chi \lesssim 1$ TeV.

WIMPs are created in the early universe from the annihilation of Standard Model particles, and vice versa, in thermal equilibrium. Production and annihilation took place at a rate $\Gamma = \langle \sigma_{ann} v \rangle n_{eq}$, where $\langle \sigma_{ann} v \rangle$ is the annihilation cross section averaged over the velocity distribution of WIMPs, and n_{eq} is the WIMP equilibrium number density. The time evolution of the number density n of a particle in thermal equilibrium is governed by

the Boltzmann equation:

$$\frac{dn}{dt} + 3Hn = -\langle \sigma_{ann} v \rangle (n^2 - n_{eq}^2) \tag{1.6}$$

where H is the Hubble constant. As the universe expanded it cooled. The expansion rate is given by the Hubble constant, which varies with temperature as $H(T) = 1.66 g_*^{1/2} T^2 / m_{pl}$, where g^* is the number of relativistic degrees of freedom, and $m_{pl} \simeq 10^{19}$ GeV is the Planck mass.

At high temperatures $T \gg m_\chi$, where m_χ is the WIMP mass, WIMPs were relativistic. The WIMP number density n varied with temperature as $n = N/R^3 \propto T^3$. Importantly, this means n_{eq} fell faster than H. At low temperatures $T \lesssim m_\chi$, the annihilation rate Γ fell exponentially with n_{eq}:

$$\Gamma \propto n_{eq} = g^* (m_\chi T / 2\pi) exp(-m_\chi / T) \tag{1.7}$$

The number of χ with enough kinetic energy to annihilate falls until $\Gamma \lesssim H$, at which point the χ falls out of equilibrium and annihilation ceases. The resulting relic abundance is fixed at today's value, a process known as freeze out. As $\Gamma \propto \langle \sigma_{ann} v \rangle$ the smaller the annihilation cross section the longer the fall in n_{eq} lasts before freeze out, and the smaller the resulting relic density.

From the above description, we can make an approximate calculation of the relic number density, following Ref. [44] (for a full derivation the reader is directed to Chapter 7.2 of Ref. [14]). Here subscripts f and 0 are used to denote values at the time of freeze out and today, respectively. The entropy density in the universe per co-moving volume remains constant as expansion continues, meaning $n_0/s_0 = n_f/s_f$, where $s_f \simeq 0.4 g_* T_f^3$. At freeze-out, $\Gamma = n_f \langle \sigma_{ann} v \rangle = H$, and $T_f \approxeq m_\chi / 20$. Dividing through by entropy, and rearranging:

$$\frac{n_0}{s_0} = \frac{n_f}{s_f} = \frac{H}{s_f \langle \sigma_{ann} v \rangle} \approxeq \frac{1.66 g_*^{1/2}}{0.4 g_* m_{pl} T_f \langle \sigma_{ann} v \rangle} \approxeq \frac{100}{m_\chi m_{pl} g_*^{1/2} \langle \sigma_{ann} v \rangle} \tag{1.8}$$

By taking the χ mass-energy density parameter $\Omega_\chi = \rho_\chi / \rho_c$, and substituting in the Planck mass m_{pl}, current entropy density $s_0 \simeq 4000 \text{cm}^{-3}$, and current critical density

$\rho_c \simeq 10^{-5} h^2 \text{GeVcm}^{-3}$, and noting that $\rho_\chi = m_\chi n_0$:

$$\Omega_\chi h^2 = \frac{m_\chi n_f}{\rho_c} \simeq \frac{3 \times 10^{-27} cm^3 s^{-1}}{\langle \sigma_{ann} v \rangle} \tag{1.9}$$

The result is approximately independent of WIMP mass. For a weak-scale interaction with a $m_\chi \sim 100$ GeV - 1 TeV WIMP, $\langle \sigma_{ann} v \rangle \sim \alpha^2 (100 GeV)^{-2} \sim 10^{-25}$, and the resulting value of $\Omega_\chi h^2 \sim 0.03$ is within an order of magnitude of the Planck observation [1] of $\Omega_c h^2 = 0.1186 \pm 0.002$. A similar argument from Section 10.3 of Ref. [14] states that the thermal relic mass-energy density of a WIMP follows:

$$\Omega_\chi \propto \frac{1}{\langle \sigma_{ann} v \rangle} \propto \frac{m_\chi^2}{g_\chi^4} \tag{1.10}$$

For a weak scale interaction with a $m_\chi \sim 100$ GeV - 1 TeV WIMP with coupling $g_\chi \sim g_{weak} \simeq 0.65$, $\Omega_\chi \sim 0.23$ [14]. The coincidence of the WIMP thermal relic density with the density parameter is known as the 'WIMP miracle', and strongly motivates the candidacy of the WIMP.

A WIMP may be detected in three ways. The direct detection of a WIMP scattering with a target nucleus in a detector is discussed in detail in the next section. Indirect detection techniques search for the Standard Model products of WIMP decay or annihilation in regions of high WIMP density. For example, the Large Area Telescope (LAT) on the Fermi Gamma-ray Space Telescope has observed an excess of 1-100 GeV gamma-rays from the galactic centre [45], which may be the product of WIMP annihilation [46]. Uncertainties in modelling of cosmic-ray source and interstellar emission distributions in the galactic centre propagate to large uncertainties on the excess itself, and the source of the excess has not been conclusively proven to be either baryonic or dark matter [47]. The debate is summarised by the Fermi-LAT collaboration in Ref. [45].

WIMPs may be created in collision events at accelerator experiments. The WIMP would leave the detector owing to its weak scale interaction cross section, leaving a signature which deviates from Standard Model predictions of missing energy and momentum. The reliance on missing energy provides poor mass resolution, nor can it prove the stability of the candidate beyond the extent of the detection apparatus. However, their

complementarity with other searches is important: collider experiments for example set more stringent upper limits than direct detection experiments in low WIMP mass regions, especially in the case of spin dependent interactions. For a comprehensive review of the outlook for WIMP detection at accelerators, the reader is directed to Ref. [48].

1.3 Dark Matter Direct Detection

In a direct detection experiment the aim is to observe a WIMP scattering with a target nucleus, by means described in Section 1.4. A detector can measure the WIMP energy spectrum, the annual modulation of the WIMP energy, or the directional dependence of the recoil. Each is described in this section, starting by describing the WIMP recoil energy spectrum.

The differential scattering rate per of keV of recoil energy E_R, kg of target mass, and day of exposure is given by [49]:

$$\frac{dR}{dE_R}(E_R) = \frac{\rho}{m_\chi m_A k} \int_{v_{min}}^{v_{esc}} v.f(\vec{v}, \vec{v_E}) \frac{d\sigma}{dE_R}(v, E_R) d^3v \tag{1.11}$$

where m_A is the target nucleus mass, $\vec{v}$ is the WIMP velocity relative to the target nucleus, v_{min} is the minimum WIMP velocity that can produce a recoil energy E_R, v_{esc} is the galactic escape velocity, and $d\sigma/dE_R$ is the differential scattering cross section. The differential scattering rate is dependent on the model for the WIMP velocity distribution $f(\vec{v})$ in the Milky Way halo, the WIMP density in the vicinity of Earth ρ, and a scattering differential cross section $d\sigma/dE_R$, which are described in this section.

The WIMP halo model is commonly described by the Standard Halo Model (SHM) as an isotropic, isothermal sphere with density $\rho(r) \propto r^{-2}$. The WIMP velocity distribution is given by a Gaussian (often called a Maxwellian), as $f(\vec{v}, \vec{v_E}) = exp(-(\vec{v} + v_E)^2/2v_0)$ [49]. The Gaussian is normalised by the constant k such that $k = 4\pi \int_{v_{min}}^{v_{esc}} f(\vec{v}, \vec{v_E}) v^2 dv$, and the distribution is truncated above the galactic escape velocity v_{esc}. From analysis of radial velocities of Milky Way stars from the RAVE survey [50], the 90% C.L. limits on v_{esc} place it within the range $498 < v_{esc} < 608$ km s $^{-1}$, with median velocity $\bar{v_{esc}} = 544 \pm 39$ km s $^{-1}$. The velocity distribution is also truncated below the minimum WIMP velocity

that can produce a recoil energy E_R:

$$v_{min} = \sqrt{\frac{m_A E_R}{2}} \frac{m_A + m_\chi}{m_A m_\chi} \tag{1.12}$$

The value $v_0 = \sqrt{3/2} v_c$ is the velocity dispersion, or Gaussian spread parameter $\sigma(v)$ of dark matter velocities. This is related to the galactic rotation velocity, $v_c = 220 \pm 20$ km s^{-1} [51].

The WIMP velocity distribution depends on the velocity of the Earth relative to the WIMP halo, which is described by $\vec{v_E} = \vec{u}_r + \vec{u}_s + \vec{u}_E$. The galactic rotation velocity at the radial position of the Sun with respect to the galactic centre is given by $\vec{u}_r = (0, v_c, 0)$. The SHM assumes a value of $v_c = 220 \pm 20$ km s^{-1} [51], but v_c has been shown to vary between 200 ± 20 km s^{-1} and 279 ± 33 km s^{-1} depending on calculation technique [52]. A signal in a detector sensitive to the direction of origin of the WIMP would find the WIMP recoil rate peaked for recoils parallel to the direction of motion of the Sun, which is towards the constellation Cygnus.

The velocity of the Sun relative to nearby stars is estimated at $\vec{u}_s = (11.1^{+0.69}_{-0.75}, 12.24^{+0.47}_{-0.47}, 7.25^{+0.37}_{-0.36})$ km s^{-1} from fitting the velocity distribution of nearby stars [53]. The velocity of the Earth relative to the Sun $\vec{u}_E$ cycles annually, meaning the Earth's velocity relative to the halo has a time dependence given by $v_E \simeq 244 + 15\sin(2\pi y)$ km s^{-1}, where y is the fraction of a year elapsed since the previous March 2nd. The velocity relative to the halo reaches a maximum on June 2nd, $|\vec{v}_E| = 258$ km s^{-1}, and a minimum on December 2nd, $|\vec{v}_E| = 229$ km s^{-1} with an 8% uncertainty on the mean velocity [49]. The observation of an annual recoil energy modulation that fits such a profile can be interpreted as evidence in favour that the recoil signal was WIMP-induced.

The differential rate is also dependent on a model for the local WIMP density. The SHM value $\rho_0 = 0.3$GeVcm^{-3} is used [54] in analyses that compare the sensitivities of different direct detection experiments. Numerical simulations and new data sets have highlighted cases that disagree with the SHM value. For example, NFW [55] and Einasto [56] density profiles have been shown to disagree with the SHM outside of error, stating $\rho_0 = 0.389 \pm 0.025$GeVcm^{-3} and $\rho_0 = 0.385 \pm 0.027$GeVcm^{-3} respectively [57]. For

a comprehensive summary of the uncertainty in astrophysical input parameters to the WIMP differential scattering rate the reader is directed to Ref. [54].

In general the scattering of a WIMP with a nucleon is described by the combination of vector, axial-vector, scalar, pseudo-scalar and tensor interactions with partons. In the non-relativistic limit the number of components reduces to only scalar spin-independent (SI) and axial vector spin-dependent (SD) interactions. The differential cross section for WIMP scattering with a target nucleus in Eq. 1.13 contains contributions from spin-independent and spin-dependent interactions:

$$\frac{d\sigma}{dE_R} = \frac{m_A}{2\mu_A^2 v^2}\left(\sigma_{0,SI}F_{SI}^2(E_R) + \sigma_{0,SD}F_{SD}^2(E_R)\right) \tag{1.13}$$

where $\mu_A = m_\chi m_A/(m_\chi + m_A)$ is the WIMP-nucleus reduced mass, σ_0 denotes a WIMP-nucleon scattering cross section at zero momentum transfer, $v = |\vec{v}|$ is the magnitude of the WIMP velocity relative to the target nucleus, and $F_{SI,SD}(E)$ are spin independent and spin dependent nuclear form factors, which are explained below. The spin independent zero momentum transfer cross section is described in Eq. 1.14 below:

$$\sigma_{0,SI} = \frac{4\mu_A^2}{\pi}\left(Zf_p + (A-Z)f_n\right)^2 = \frac{4\mu_A^2 f_p^2 A^2}{\pi} \tag{1.14}$$

For the spin independent contribution isospin conservation is assumed, which means that protons and neutrons have equal coupling f, and $f_p = f_n$. Z and A denote proton and mass numbers of the target nucleus, respectively. The dependence $\sigma_{0,SI} \propto A^2$ enhances the cross section for heavier targets.

The term $F(E)$ in Eq. 1.13 is the nuclear form factor, which models the interference of a WIMP interaction with multiple nucleons. At low momentum transfer, the scattering amplitudes of various nucleons add in phase and coherent scattering takes place. As the momentum transfer decreases, the de Broglie wavelength of the WIMP increases. As the de Broglie wavelength reaches the scale of the target nucleus, the interaction loses coherence and the scattering amplitude decreases. The Helm form factor [58] is typically used for $F(E)$, assuming that the nucleon distribution is the same as the nuclear charge distribution obtained from electron and muon scattering data. The model treats the nucleus

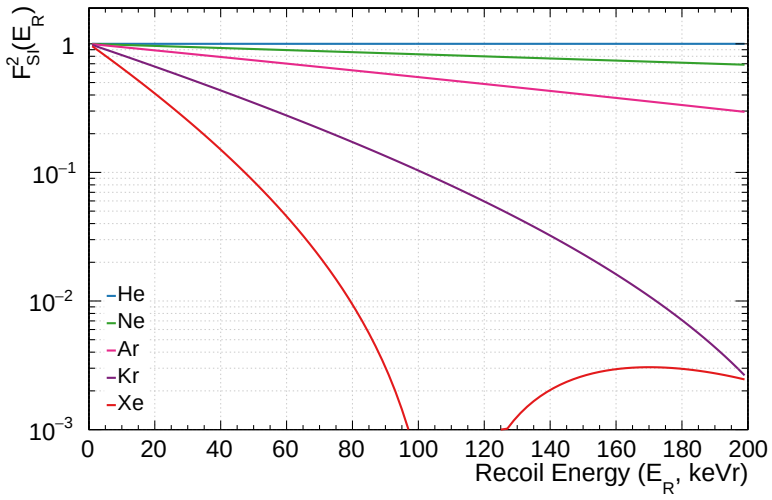

Figure 1.9: Spin dependent Helm form factor squared $F^2_{SI}(E_R)$ vs nuclear recoil energy E_R for He, Ne, Ar, Kr and Xe, assuming a 100GeV WIMP mass, skin thickness $s \simeq 0.9$fm, and parameters $a \simeq 0.52$fm and $c \simeq 1.23A^{1/3} - 0.6$fm fitted from muon scattering data [49].

as a uniform sphere of radius $R_0 = \sqrt{c^2 + (7/3)\pi^2 a^2 - 5s^2}$, with a finite skin thickness $s \simeq 0.9$ fm, and from fits to muon scattering data parameters $c \simeq 1.23A^{1/3} - 0.6$ fm and $a \simeq 0.52$ fm [49]. The form factor itself is given by:

$$F(E) = \frac{3j_1\left(R_0\sqrt{2m_A E_R}\right)}{R_0\sqrt{2m_A E_R}} \exp\left(-2m_A E_R s^2\right) \tag{1.15}$$

where m_A is the mass of the nucleus and $j_1(R_0\sqrt{(2m_A E_R)}$ is the first order spherical Bessel function. The form factor for the noble gases He, Ne, Ar, Kr and Xe is shown in Figure 1.9, which shows the loss of coherence and decrease in coherent scattering amplitude at high energy for each element.

The differential rate of WIMP-nucleus scatters observed in an experiment's energy units is parametrised by a detector response function $H(E_R, E_{du})$, which maps recoil energy E_R to detected energy E_{du}. Typically this will include an efficiency term for the linear conversion in detected energy per unit recoil energy, and a convolution with a Gaussian resolution function, which models the finite energy resolution of the detector. The observed differential rate [49] is thus $dR/dE_{du} = \int dE_R\,(dR/dE_R)\,H(E_R, E_{du})$. The differential rate dR/dE_R, in keV is shown in Figure 1.10 for recoils in Ne, Ar, Ge and Xe, and assuming 30 GeV (dashed line) and 300 GeV (solid line) WIMP masses. The parametri-

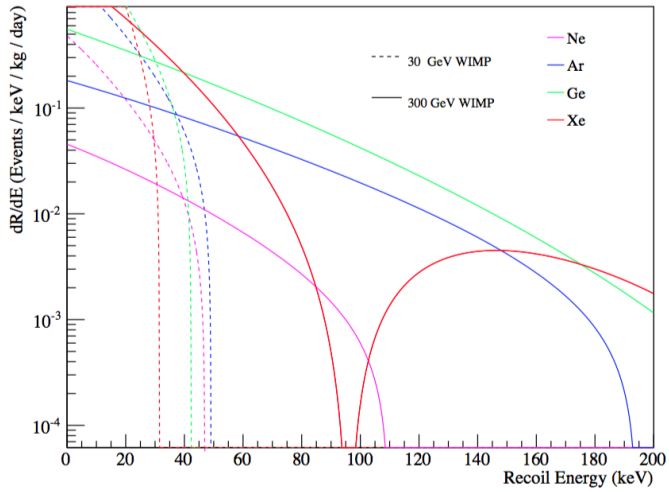

Figure 1.10: Differential rate in keV dR/dE_R vs WIMP recoil energy E_R, for Ne, Ar, Ge and Xe, assuming 30 GeV (dashed line) and 300 GeV (solid line) WIMP masses. Plot reproduced from Ref. [59].

sation described above is assumed in calculation of dR/dE_R from Equation 1.13. For low mass WIMPs the lightest elements are most sensitive, whereas at high mass the A^2 enhancement in $\sigma_{0,SI}$ is the dominant effect on the relative rates of the target elements.

1.4 Detection Strategies

A scattering WIMP will produce three types of detectable signal, depending on the material: thermal excitations, or phonons; ionisation from a recoiling charged ion or electron; and scintillation light, from excitation of the medium followed by relaxation and emission of light. Each direct detection experiment will use one or more of the three signal channels. An exception is the superheated fluid experiment, discussed in Section 1.4.5, which detects a recoiling nucleus by observing bubble nucleation and the acoustic signature that accompanies it.

A summary of recent signal regions and 90% C.L. upper limits on the SI WIMP-nucleon scattering cross section at varying WIMP masses is shown in Figure 1.11. Also shown are the observed signal regions assuming a WIMP signal for DAMA/LIBRA, discussed in Section 1.4.2, which are excluded by more stringent 90% C.L. upper limits, shown as exclusion curves at lower cross sections. The orange line corresponds to the neu-

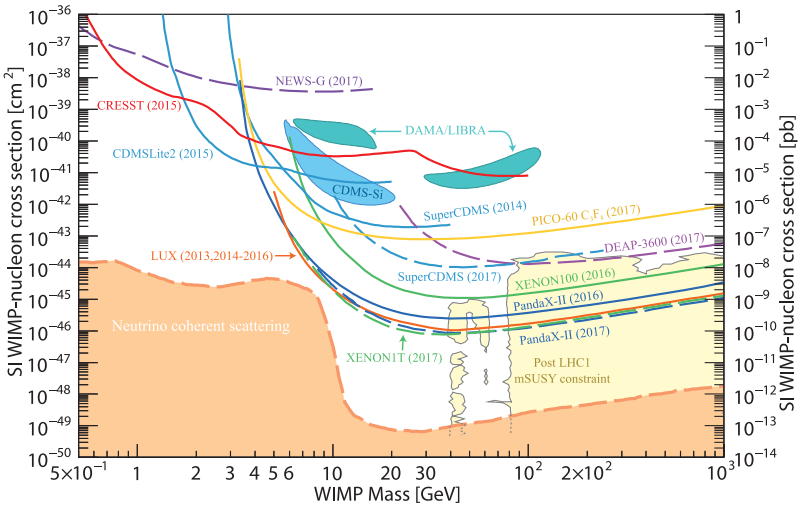

Figure 1.11: Summary of results at time of writing, showing spin independent (SI) WIMP-nucleon scattering cross section vs WIMP mass. 90% C.L. upper limits suggested by experiments are shown as curves. Signal regions suggested by experimental results are shown as oval shapes. The dashed orange line above the orange region corresponds to the sensitivity to WIMP cross sections required to observe atmospheric, supernova and ^{7}Be/^{8}B solar neutrinos. The yellow region represents the potential parameter space for observation of WIMPS under minimal SUSY. Reproduced from Ref. [38].

trino floor, the WIMP-nucleon scattering cross section at which energy spectra of WIMP recoils agree within uncertainty with that of atmospheric, supernova and ^{7}Be/^{8}B solar neutrinos combined. The projected sensitivities of next generation multi-tonne detectors, such as LZ and DARWIN, approach the neutrino floor. Directionality measurement is expected to be a useful technique in rejecting solar neutrino backgrounds as discussed in Section 1.4.6.

Another recent summary at time of writing is shown in Figure 1.12. The lowest observed 90% C.L. upper limits on the SI cross section comes from LUX and XENON1T, with the projected sensitivity from DEAP-3600 expected to be competitive at the same level as current limits, as discussed further in Section 1.4.2.

1.4.1 Backgrounds

As the WIMP interaction signal induces a recoil, any particle which can induce a recoil in the target medium at the same energies as a WIMP can mimic the WIMP and act as a background to low-background direct detection experiments. An overview of background

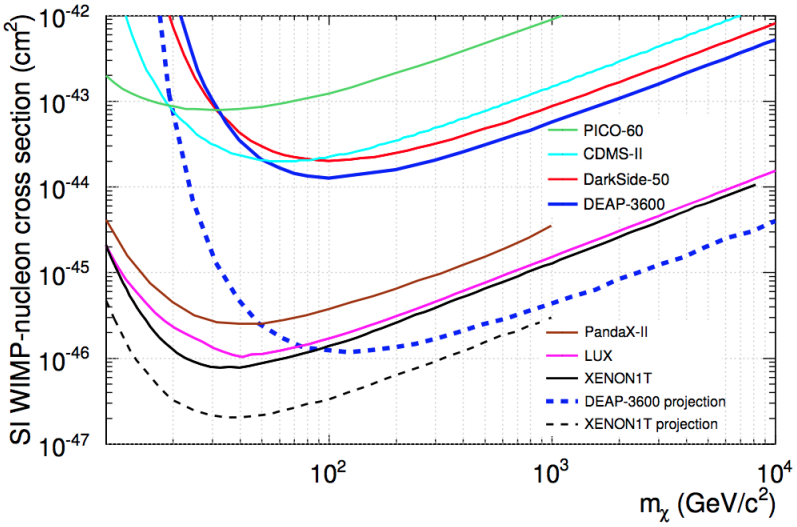

Figure 1.12: Summary of results in 2017, showing spin independent (SI) WIMP-nucleon scattering cross section vs WIMP mass. Solid curves represent observed exclusion regions, and dashed curves represent projected exclusion regions. The DEAP-3600 4.44 day result is shown in solid blue. The 3 tonne-year projected exclusion curve as discussed in 1.4.2 is shown in dashed blue. Again, signal regions suggested by experimental results are shown as oval shapes. Reproduced from Ref. [3].

sources to such experiments is presented here. The backgrounds to the DEAP-3600 experiment are discussed in detail in Section 2.2.

Particles scattering with the electron instead of the nucleus can cause the atom to recoil, known as an electronic recoil. Electronic recoils from charged particles and γ-rays are discriminated from nuclear recoils, from neutrons and WIMPs, by comparing the behaviour of each in more than one of the detection channels listed above, or by identifying a behaviour of the target medium. Specific examples are given in the following subsections as applicable to different detector types. The target media used in searches produce different charge and light yields to electronic and nuclear recoils with the same energy deposition, as explained in detail for noble gases in Section 1.5.5. As a result nuclear recoil energies are denoted in recoil energy units eV_r and electronic recoil energies are denoted in electronic equivalent energies eV_{ee}.

Neutrons form a source of nuclear recoil background. If they scatter once in the target medium they form an indistinguishable nuclear recoil background, which must be characterised and rejected in analysis. Event reconstruction which identifies multiple scatters at different locations and seperate times enables their discrimination from single scatters

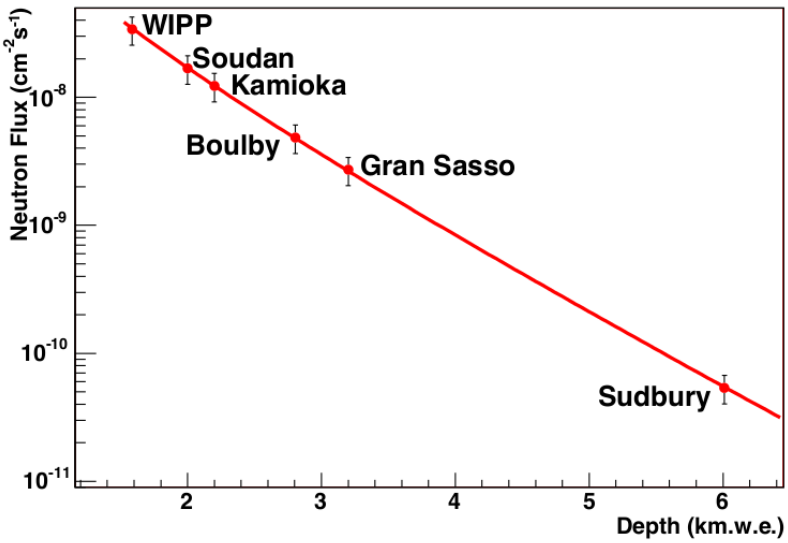

Figure 1.13: Total flux of muon-induced neutrons at the rock-cavern boundary at each of the underground sites labelled. Reproduced from Ref. [60].

and WIMPs. Cosmic ray muons are one source of neutrons through (μ,n) interactions. The muon flux is passively mitigated by constructing direct detection experiments in underground laboratories with rock overburden. The muon flux incident on a laboratory is inversely proportional to the amount of rock overburden above it, as shown for different underground laboratories in Figure 1.13. Low-background experiments will also actively mitigate the appearance of muons in data by surrounding the detector with water, and instrumenting the water with light detectors, such as photomultiplier tubes. A passing muon produces Cerenkov radiation in water, and events in which Cerenkov radiation is observed followed by a neutron scatter are tagged as background.

Radioactivity in materials surrounding the target medium is another source of background. Long lived unstable isotopes in the ^{238}U and ^{232}Th decay chains are present in materials due to their natural abundance from the formation of the Earth. Low-background experiments will mitigate radiogenic backgrounds by selecting and manufacturing materials with the lowest radioisotope content. For example, germanium counters are used to measure the rate and energies of gamma decays in each decay chain, and the contamination from daughters in each decay chain is estimated. Recoiling daughter nuclei from radioactive decay processes can emanate from the surfaces of detector components

into the target medium, which necessitates the use of a purification system in liquid and gas-based low-background detectors to cycle and remove such contaminants.

Alpha decays in laboratory and detector materials are a source of fast neutron flux induced by (α,n) interactions. The flux of neutrons originating from outside the detector is mitigated by shielding using materials containing nuclei with large neutron capture cross sections, such as water and acrylic, as discussed in Section 2.2. The α itself produces a low energy background by scattering multiple times below the surface of a material before inducing a recoil in the target medium, as discussed in detail in Section 2.2. Recoils from α particles may be reduced by using position reconstruction, identifying a region near to the detector surface where surface α backgrounds are most likely to reconstruct, and rejecting events that reconstruct in that region. The position rejection process is called fiducialisation, and the un-rejected region is known as the fiducial volume. γ-decays in the ^{238}U and ^{232}Th decay chains occur at energies up to 2.6 MeV. The γ background is also mitigated by shielding. The γ and surface β decays that reach the target medium may also be mitigated using electronic recoil discrimination.

The flux of neutrinos on the earth is potentially a source of background for low-background detectors, if coherent neutrino-nucleus scattering is observed. At recoil energies $\leq$30 keV for lighter nuclei such as carbon the flux of ^{7}Be and ^{8}B solar neutrinos is the dominant neutrino background for low mass WIMPs [61]. For example, 10^2 ^{8}B solar neutrino scattering events are expected per argon tonne-year per keV$_r$ at 1 keV$_r$, and argon has a recoil energy spectrum endpoint of 18.8 keV for solar neutrinos [62]. The background for higher mass WIMPs is dominated by supernova relic anti-neutrinos and atmospheric (anti-)neutrinos, the latter of which scatters in argon at a rate five orders of magnitude lower than the solar neutrino flux [62]. The combination of these backgrounds produce the “neutrino floor", defined as the WIMP-nucleon scattering cross section at which the energy spectra of WIMP and neutrino recoils agree within uncertainty. For example in xenon the energy spectrum for a WIMP of mass $m_\chi = 6$ GeV and SI WIMP-nucleon scattering cross section $\sim 5 \times 10^{-45}$ cm^2 matches the energy spectrum for ^{8}B neutrinos [63]. The neutrino floor is shown as a dashed orange line in Figure 1.11.

1.4.2 Scintillator Detectors

Solid Scintillator Detectors

Solid scintillator detection experiments use high purity inorganic scintillator crystals as their target. Photomultiplier tubes (PMTs) are used to detect scintillation from energy deposition in the crystal. The crystals are grown at sizes on the order of cm^3, and larger targets are constructed using arrays of scintillator crystals. Multiple targets are built this way to increase an experiment's combined target mass. One detector of this type is DAMA, a NaI detector based at the LGNS underground laboratory, which consisted of nine NaI targets of mass 9.7 kg, and took data over seven annual cycles. The experiment was then upgraded to DAMA/LIBRA, consisting of 25 NaI targets of mass 9.7 kg. DAMA/LIBRA collected 1.33 tonne-years of data over 14 annual cycles in combination with previous DAMA data. An oscillation in event rate was observed at 9.2σ C.L. for recoil energies of 2-4 keV_r, with a period of 0.996 ± 0.002 years and an amplitude of $1.9\pm0.2\%$ of the average rate [64]. Analysis of the uncertainty and modulation due to crystal temperature, WIMP flux, ambient pressure surrounding the crystals, radon background and electronics noise yielded that none of the effects investigated were large enough to be consistent with no rate modulation [65, 66]. From scattering with sodium, an SI cross section discovery region at 2×10^{-40} cm^2 is implied for WIMP masses (10-15) GeV. From scattering with iodine, an SI cross section at 2×10^{-41} cm^2 is implied for WIMP masses (6-20) GeV. These signal regions are excluded by other experiments as shown in Figures 1.11 and 1.12.

Liquid Noble Gas Detectors

Particle scattering in liquid noble gases produces detectable signals in the form of scintillation light and electrons from ionisation. Liquid nobles are transparent to their own scintillation light wavelength for the path lengths at present detector sizes, and scintillation is detected using PMTs. Scintillation in liquid nobles is discussed in Section 1.5. Ionisation electrons are detected by drifting them towards a gaseous region in a detector using a uniform electric field. In the gaseous region they produce light through scintilla-

tion and electroluminescence, which is detected by PMTs.

Single phase detectors use noble gases in the liquid phase and can collect only scintillation light. The detected scintillation timing profile is different for electronic and nuclear recoils as the energy loss per unit length dE/dx of the incident particle is larger in neutrons and WIMPs than electrons and gammas. The exploitation of the timing profile to discriminate between electronic and nuclear recoils is known as Pulse Shape Discrimination (PSD), which is described in more detail in Section 1.5.

XMASS is an example of a liquid xenon single phase detector based in the Gran Sasso National Laboratory, Italy, which consists of an 835 kg spherical target region surrounded by 642 PMTs. XMASS demonstrated a rejection of electron recoil events with energies between 4.8 keV$_{ee}$ and 7.2 keV$_{ee}$ by a factor of $7.7\pm1.1(\text{stat})^{+1.2}_{-0.6}(\text{sys})\times10^{-2}$, whilst retaining 50% nuclear recoil acceptance [67]. For electronic recoil energies between 9.6 and 12 keV$_{ee}$ the rejection factor at 50% nuclear recoil acceptance improves to $7.7\pm2.8(\text{stat})^{+2.5}_{-2.8}(\text{sys})\times10^{-3}$. Using 0.818 tonne-years of data and a nuclear recoil energy threshold of 4.8 keV$_r$, XMASS-1 set a 90 C.L. upper limit on the SI WIMP-nucleon scattering cross section of 3.2×10^{-41} cm^2 at a WIMP mass of 140 GeV [68].

DEAP-3600 is an example of tonne-scale liquid argon single phase detector with a 3263 kg target mass (originally 3600 kg) before fiducialisation, based in SNOLAB in Sudbury, Ontario, in Canada. With its first result DEAP-3600 has set the most stringent 90% C.L. upper limit on the SI WIMP-nucleon scattering cross section using argon, at 1.2×10^{-44} cm^2 for a 100 GeV WIMP mass, having seen no candidate events [3]. The limit, shown in solid blue in Figure 1.11, is set using a 9.87 tonne-day exposure, electronic recoil rejection leakage probability at $< 1.2\times10^{-7}$ events and a 64-132 keVr energy region of interest. Over three years of data taking with a 1000 kg fiducial mass and 48 keV$_r$ nuclear recoil energy threshold it is projected to reach a sensitivity to SI WIMP-nucleon scattering cross section of 10^{-46} cm^2 for a 100 GeV WIMP mass [2]. The DEAP-3600 projected 90% C.L. upper limit for 3 tonne-years of data taking is shown in dashed blue in Figure 1.12. The DEAP-3600 detector is described in Chapter 2.

In dual phase detectors the use of both liquid and gas additionally enables collection

of data from ionisation. Scintillation and ionisation signals are known as S1 and S2 respectively. Discrimination between electronic and nuclear recoils in dual phase detectors is performed using the ratio S1:S2. Multiple dual phase detectors have been constructed using the time projection chamber (TPC) format. A TPC consists of cylindrical target mass in the liquid phase with a layer of gas above it, a uniform electric field parallel to the cylindrical axis, and a layer of PMTs above and below the target mass. Electron time of flight relative to the initial scintillation time is used to locate the position of an event along the cylindrical axis, and PMTs are used to reconstruct position perpendicular to the axis.

LUX is an example of a xenon TPC constructed in the Sanford Underground Research Facility in the USA, with a 250 kg target mass. LUX set a 90% C.L. upper limit on the SI WIMP-nucleon scattering cross section limit at 2.2×10^{-46} cm^2 for a 50 GeV WIMP mass [69, 70]. LUX used a 332 live day exposure with 100 kg fiducial volume, and a nuclear recoil energy threshold of 3keV was set using the energy at which PSD has $\geq$50% nuclear recoil acceptance. Electronic recoil leakage into the WIMP PSD cut was observed to occur with an average 0.2% probability [69]. The combination of this with a previous 92 live day exposure allows LUX to set a 90% C.L. upper limit at 1.1×10^{-46} cm^2 for a 50 GeV WIMP mass [71]. XENON-1T is another TPC constructed in the Laboratori Nazionali del Gran Sasso in Italy. At time of writing, XENON1T has set the world-leading 90% C.L. upper limit on the SI WIMP-nucleon scattering cross section, at 7.7×10^{-47} cm^2 for a 35 GeV WIMP. XENON1T used 34.2 live day exposure using a 1042 ± 12 kg fiducial mass, in a 5-40 keV nuclear recoil energy region of interest. Thereafter the XENON-1T experiment is projected to reach a 90% C.L. upper limit on the SI WIMP-nucleon scattering cross section of 1.6×10^{-47} cm^2 at a 50GeV WIMP mass with a 2 tonne-year exposure, 1 tonne fiducial mass, 0.5% electronic recoil leakage at 50% nuclear recoil acceptance and a 4-50 keV nuclear recoil energy region of interest [72]. This is then projected to be exceeded by the LZ collaboration which follows LUX, whose SI sensitivity is projected to reach below 3×10^{-48} cm^2 at a 40 GeV WIMP mass, using a 5.6 tonne fiducial volume, the PSD rejection power observed in the 332 live day

LUX result, and a 6 keV$_r$ nuclear recoil energy threshold [69]. The LUX and XENON-1T observed limits are shown in Figure 1.11, and the LZ projected limit is shown in Figure 1.12.

1.4.3 Semiconductor Ionisation Detectors

Germanium detectors composed of n and p-type semiconductors are constructed to detect ionisation. The CoGeNT detector is an example of a p-type Ge experiment of mass 443 g, which took 3.4 years of data in the Soudan Underground Laboratory in a search for an annual modulation signal. The semiconductors are cooled to 77K using liquid nitrogen, which reduces thermal noise from the target mass, and the manufacture of high purity Ge reduces radiogenic backgrounds. The combination of these factors enabled the use of a low energy threshold of 0.5 keV [73]. The use of only ionisation disables nuclear and electronic recoil discrimination, but a high energy resolution enables the identification of backgrounds using the characteristic energy spectrum of each source, which enables background identification analyses in modulation searches [74]. CoGeNT observed a full-width half-maximum energy of 0.235 keV at 5.9 keV energy deposition [75]. In p-type semiconductors a dead surface layer shields the target from surface α and β decay products. The rise time of the signal is used to discriminate between recoils near the surface and those further into the target bulk, enabling fiducialisation to a fiducial volume of 330$\pm$30 g with a bulk contamination of 4.4% from surface events [75]. CoGeNT [73] observed an annual modulation consistent with the WIMP hypothesis at the 2.2σ level in an energy range of (0.5 - 2) keV$_{ee}$, but with an amplitude larger by a factor of 4-7 than expected by the WIMP hypothesis. The result implied a WIMP with an SI cross section of 2.5×10^{-41}cm^2 at 8 GeV WIMP mass. An updated analysis of the same data at recoil energies, focused on the separation of bulk and surface events below 1 keV$_{ee}$, now estimates that significance at below 1σ [76].

CDEX-1 is another example of a p-type Ge experiment, based at the China Jinping Underground Laboratory. CDEX-1 uses a 994 g target enclosed in a NaI scintillator and achieves a minimum energy threshold of 177 eV_{ee} at 50% nuclear recoil acceptance [77].

Using a 53.9 kg-day exposure with a fiducial volume (subtracting the dead surface layer regions) of 919 g and a 475 eV energy threshold CDEX-1 set a 90% C.L. upper limit on the SI WIMP-nucleon scattering cross section $< 10^{-42}$ cm^2 in the 6-20 GeV WIMP mass range [78]. The CDEX-1 result rules out the CoGeNT interpretation using the same target material as CoGeNT [77, 78].

1.4.4 Solid Cryogenic Bolometers

Cryogenic bolometers consist of a crystal with a thin coating of superconducting film cooled its phase transition temperature. Energy deposition produces an electronic or nuclear recoil in the crystal lattice which propagates as a phonon. The phonon is absorbed at the surface layer of the crystal and raises the temperature of the superconducting film. Temperature variation in the film is detected by measuring the variation in resistance that temperature change induces. The phonon transit time is used to differentiate between scattering in the surface and inner bulk of the crystal and select a fiducial volume. Collection of charge or scintillation light also allows the discrimination of electronic and nuclear recoils. Species that induce nuclear recoils deposit more energy per unit distance dE/dx and experience quenching (explained in Section 1.5.6), reducing their charge and scintillation yields per phonon compared to electronic recoils. Bolometers are operated in the mK regime, allowing O(GeV) WIMP mass searches with low thresholds at <keV.

CRESST-II is an example of a $CaWO_4$ bolometer instrumented with silicon-sapphire wafers, based in the Laboratori Nazionali del Gran Sasso in Italy [79]. CRESST-II uses 18 targets with a total mass of 5 kg, and achieved an energy threshold of 307.3$\pm$3.6 eV. Using a 52 kg-day exposure, CRESST-II set the most stringent 90% C.L. upper limit on the SI cross section 2×10^{-39} cm^2 at WIMP mass 1.7 GeV, and at WIMP masses of 0.5 GeV with an upper limit of 2×10^{-36} cm^2 [79]. The limit set in Ref. [79] does not exclude the region implied by a nuclear recoil excess reported by CRESST-II on 730 kg-days of exposure [80], which was consistent with WIMP masses of 11.6 GeV and 25.3 GeV with SI WIMP-nucleon scattering cross sections of 3.7×10^{-41} cm^2 and 2×10^{-42} cm^2 respectively.

Another example is EDELWEISS-III, an array of 8 Ge detectors based at Laboratoire Souterrain de Modane (LSM) [81]. EDELWEISS-III measures ionisation charge using electrodes mounted at the edge of each 800 g Ge crystal, which is fiducialised to a mean 625 g fiducial volume per crystal with a rejection factor for surface events at 4×10^{-5} above 15 keV recoil energies. The combination of ionisation and phonon information enables the rejection of electronic recoils by a factor of 6×10^{-6} at 90% nuclear recoil acceptance, independent of energy in the experiment energy range. Using thresholds of 2 keV and 1.5 keV at 70% trigger efficiency for the two halves of the detector array, EDELWEISS-III set a 90% C.L. upper limit on the SI WIMP-nucleon scattering cross section of 4.3×10^{-40} cm^{-2} for a 5 GeV WIMP and 4.3×10^{-44} cm^{-2} for a 20 GeV WIMP.

1.4.5 Superheated Liquid Detectors

Refrigerants superheated to just below their boiling point can be used as a target mass. Scattering induces a localised phase transition and nucleates a bubble if the energy transfer to the nucleus is above a threshold energy per unit volume for bubble nucleation. This means that a such detectors are operated as threshold detectors, without energy sensitivity. The threshold energy is tuned by adjusting the pressure and temperature of the liquid. The nucleation threshold makes these detectors uniquely insensitive low dE/dx species such as γ and β from surface impurity decays. A nucleation can be detected acoustically using piezoelectric transducers and optically using CCD cameras. The faster rise time of the acoustic emission from a larger, louder bubble created by surface αs is used to identify them [82, 83]. CCD cameras are used to image a bubble and determine its position with O(mm) precision, which is used to select a fiducial volume. The target is reset by compressing the liquid then decompressing it to below its vapour pressure, necessitating a delay between events. Two types of detector exist in this class: bubble chambers and droplet detectors. Bubble chambers contain unsuspended superheated liquids. Droplet detectors contain superheated droplets of the target material suspended in water and a cross-linked polymer, which acts to prevent boiling at the bubble interface which prolongs

the delay between events [84]. Fluorine is a common feature of target compounds, with unpaired protons and large expectation values for the proton spin, giving it an enhanced SD sensitivity [85].

The PICO collaboration have produced the most competitive detectors in this class at time of writing. The PICO-60 detector is based in SNOLAB, in Sudbury, Ontario, in Canada. PICO-60 used a 52 kg C_3F_8 target with a fiducial mass of 47±0.5 kg, achieving a threshold of 3.29 ± 0.09 keV, alpha cut efficiency at 99.6±0.5% and cut efficiency on neutron multiple scatters at 99.4±0.1%. Additionally, PICO calculate an expected 0.026±0.007 electronic recoils above threshold in their 30.0 live-day run. Using an exposure of 30.0 live-days PICO-60 set the leading 90% C.L. upper limit on the SD WIMP-proton scattering cross section with a minimum at 3.4×10^{-41} cm^2 for a 30 GeV WIMP mass [86]. The same result also implied a 90% C.L. upper limit on the SI WIMP-nucleon cross section with a minimum at 8×10^{-44} cm^2 for a 30 GeV WIMP mass, as shown in Figure 1.11.

1.4.6 Directional Detection

The measurement of a preferential recoil direction with respect to the trajectory of the Earth is made possible with directional detectors. When WIMP detector efforts reach a sensitivity to WIMP cross sections at which solar neutrino background is observed, directional measurement will also allow for rejection of the solar neutrino background by distinguishing the direction of the sun from the direction of the WIMP wind [87].

The main properties of four directional detection experiments are shown in Table 1.1. Currently detector designs utilise TPC technology with targets such as CF_4, CS_2 and ^{3}He in the gaseous phase. At low pressures <120 mbar, a 100 GeV WIMP with a velocity 220 km s^{-1} can induce a gas nucleus to recoil with a 1-2 mm path length [14, 88]. The target region is separated from an amplification region by a readout plane. The amplification region has a stronger electric field (in e.g. DRIFT) or higher pressure gas (in e.g. DMTPC), either of which induces avalanche amplification. Beyond the avalanche region the track can be read out directly by a charge-sensitive device such as a multi-wire proportional

Name	Volume (L)	Gas	P (mbar)	Threshold (keV)	Location	Ref.
DRIFT	800	CS_2 (73%), CF_4 (25%), O_2 (2%)	55	20	Boulby	[89, 90]
MIMAC	5.8	CF_4 (70%), CHF_3 (28%), C_4H_{10} (2%)	50	2	Modane	[88, 91]
NEWAGE	37	CF_4	100	50	Kamioka	[92]
DMTPC	1000	CF_4	40	20	SNOLAB	[93, 94]

Table 1.1: A summary of the properties of four directional detection experiments currently undergoing R&D. Adapted from [95].

counter (MWPC, e.g. in DRIFT) or pixel array (e.g. in NEWAGE) or electroluminescent proportional scintillation photons are directed by lenses to CCD cameras (e.g. in DMTPC).

The ionisation density increases with energy deposition per unit length dE/dx. Track dE/dx information is used to determine the recoil site on one end of the track. The readout plane provides (x,y) position reconstruction, whilst information on the track length along the TPC cylindrical axis is reconstructed from the arrival time of drifted ionisation charge. The track range is dependent on particle species, where species that produce an electronic recoil produce tracks that are an order of magnitude longer than nuclear recoils, independent of energy. Recoils from alphas are indistinguishable from nuclear recoils, driving background contamination requirements. Unpaired nucleons in CF_4 and ^{3}He enhance the sensitivity to spin-dependent interactions. The most stringent upper limit on the SD cross section from this type of detector comes from the DRIFT collaboration, but it is not competitive compared to results from cryogenic bolometers [96].

1.5 Scintillation in Liquid Noble Gases

This section begins by describing scintillation physics in liquid nobles, with a focus on liquid argon. The variation with recoil type of the emission timing profile and scintillation light yield is discussed and the effect that the recombination process has on each in scintillation is discussed.

Property	He	Ne	Ar	Kr	Xe
Atomic Number (Z)	2	10	18	36	54
Atomic Mass (A)	4.0	20.18	39.95	83.80	131.29
Boiling Point T_b at 1 atm (K)	4.22	27.1	87.3	119.74	165.0
Gas density at 1 atm, 298 K (g/l)	0.16	0.82	1.63	3.43	5.40
Gas density at 1 atm, T_b (g/l)	16.6	9.56	5.77	8.89	9.99
Liquid density at 1 atm, T_b (g/cm^3)	0.12	1.21	1.40	2.41	2.94
Peak Scintillation Wavelength (nm)	80	80	128	147	178
Singlet Time Const. τ_s	1 ns	<18 ns	7.0 ns	3 ns	4 ns
Triplet Time Const. τ_l	13 s	15.4 μs	1.5μs	111 ns	22 ns
Price USD/m^3 in 2004	4.20-4.90	60-120	2.70-8.50	400-500	4000-5000

Table 1.2: Properties of liquid noble gases. Values from Ref. [97, 98]. Approximate price ranges from Ref. [99].

1.5.1 Properties

As target materials the liquid noble gases present a number of advantages. A summary of the properties of noble gases is shown in Table 1.2. They have boiling points that are higher than, for example, the mK temperatures of cryogenic bolometers. Higher mass targets having higher boiling points and require less stringent cooling than the low mass targets. They are easily purified in the gaseous phase using charcoal traps and getters, as discussed in Chapter 2. The most popular targets, argon and xenon, have large A^2 enhancements that make them well-suited for high mass WIMP searches. The separation in singlet and triplet emission time constants, which are discussed in Section 1.5.3, is smaller in xenon than the lower mass liquid nobles, which makes it better suited to dual-phase detectors. Conversely, neon and argon are better suited to single-phase detectors using Pulse Shape Discrimination due to the larger separation of their time constants. As an example, the result from single phase xenon detection experiment XMASS quotes a rejection factor with 50% nuclear recoil acceptance of $7.7\pm2.8(\text{stat})^{+2.5}_{-2.8}(\text{sys})\times10^{-3}$ between 9.6 and 12 keV$_{ee}$, whereas the equivalent rejection factor at 90% nuclear recoil acceptance (a higher electronic recoil acceptance than the 50% nuclear recoil acceptance) from the DEAP-3600 first result is 1.2×10^{-7} [3] in the range 16-33 keV$_{ee}$. Most noble gases are cheap due to their natural abundance in air, with notable exceptions being krypton and xenon. Xenon is more expensive than argon by 2-3 orders of magnitude, which it more expensive to scale to larger detectors in the future.

Liquid nobles also have the advantage of a high light yield, defined as the number of photons emitted per unit energy transfer. This has been measured for nuclear recoils at $51.3^{+2.7}_{-2.5}$ photons/keV in liquid argon and $72.5^{+5.0}_{-4.4}$ photons/keV in liquid xenon [100]. Scintillation light from liquid nobles is also produced at too low an energy to stimulate further excitation of the medium, making liquid nobles transparent to their own scintillation light. For example, at the peak scintillation wavelength in liquid argon a photon has an energy of 9.7 eV, which is lower than the average energy required to produce a scintillation photon 19.5 ± 1 eV [100].

Intrinsic radioactive backgrounds can be a source of backgrounds in liquid nobles. Argon contains cosmogenically activated ^{39}Ar, which has a half life of 269 years and undergoes β^- decay with an endpoint energy of 565 keV. In liquid argon, ^{39}Ar decays at a rate of 1.01 Bq/kg [101], so when constructing larger detectors and running them with longer exposures an increased ^{39}Ar electronic recoil background is expected, which requires better PSD to mitigate it. In DEAP-3600, assuming a fiducial mass of 1 tonne of argon for three years, PSD must exclude events at a level better than 1 in 10^{10}. Likewise, commercially available Xenon contains the isotope ^{85}Kr at 20 ppt, which has a half life of 10.8 years, and β^- decays at a rate of 29 mBq/kg with an endpoint energy of 687 kg [102]. Purification of Xenon to a ^{85}Kr content of <3 ppt has been demonstrated, but will remain a problem as larger detectors are constructed [103].

1.5.2 Scintillation

Energy deposition from an incident particle induces a mixture of three processes to occur with atoms R: direct excitation forming excitons, denoted R^*; ionisation of an atom, denoted R^+; and elastic collision with other atoms, dissipating energy thermally. An deposition of energy E_{dep} results in the production of N_{ex} excitons and N_i ions:

$$E_0 = \frac{W}{f_n}(N_{ex} + N_i) \tag{1.16}$$

where W is the mean energy required to produce either an exciton or an ion. Both f_n and the ratio of excitons to ions N_{ex}/N_i depend on dE/dx, the energy loss per unit length of

the incident particle. The term f_n models the loss of energy to atomic motion and thermal dissipation. The Lindhard parametrisation [104] of f_n for an atom of atomic mass A and proton number Z is as follows:

$$f_n = \frac{kg(\varepsilon)}{1+kg(\varepsilon)}, \tag{1.17}$$

where k is the probability that members of the track collide, ε is proportional to E, and the form of $g(\varepsilon)$ is extracted from fitting to neutron scattering data in Ref. [49]. The latter are defined as follows:

$$k = 0.133Z^{2/3}A^{-1/2}, \tag{1.18}$$

$$g(\varepsilon) = 3\varepsilon^{0.15} + 0.7\varepsilon^{0.6} + \varepsilon \tag{1.19}$$

$$\varepsilon = 11.5Z^{-7/3}E(\text{ keV}), \tag{1.20}$$

where E is the integrated energy deposition along the path of the incident particle.

The excitons and ions form temporarily excited dimers or excimers, denoted R_2^*, in the singlet ($^1\Sigma_u^+$) and triplet ($^3\Sigma_u^+$) first excited states. An excimer then transitions to a repulsive ground state ($^3\Sigma_g^+$), emitting ultraviolet photons, and dissociates back to two atoms. For atoms undergoing direct excitation the process proceeds as follows:

$$R^* + R \rightarrow R_2^* \;\Rightarrow\; R_2^* \rightarrow R + R + h\nu \tag{1.21}$$

Scintillation from ions relies on recombination with an ionised electron to form an exciton with additional kinetic energy R^{**}, which dissipates that energy thermally via collisions with other atoms. Recombination will be explored further in Section 1.5.4, and occurs as follows:

$$R^+ + R \rightarrow R_2^+ \;\Rightarrow\; e^- + R_2^+ \rightarrow R^{**} + R \;\Rightarrow\; R^{**} + R \rightarrow R^* + R + \text{heat} \tag{1.22}$$

Thereafter scintillation proceeds as in the direct excitation case in Eq. 1.21. Each process can form excimers in either the singlet and triplet state. Relaxation from the singlet state is faster than from the triplet state, as the triplet state relaxation requires a forbidden spin flip, made possible by the mixing of the $^3\Sigma_u^+$ and $^1\Pi_u$ states by spin orbit coupling [105]. In liquid argon, the singlet and triplet states have lifetimes of τ_s=7$\pm$1 ns and τ_l=1.6$\pm$0.1

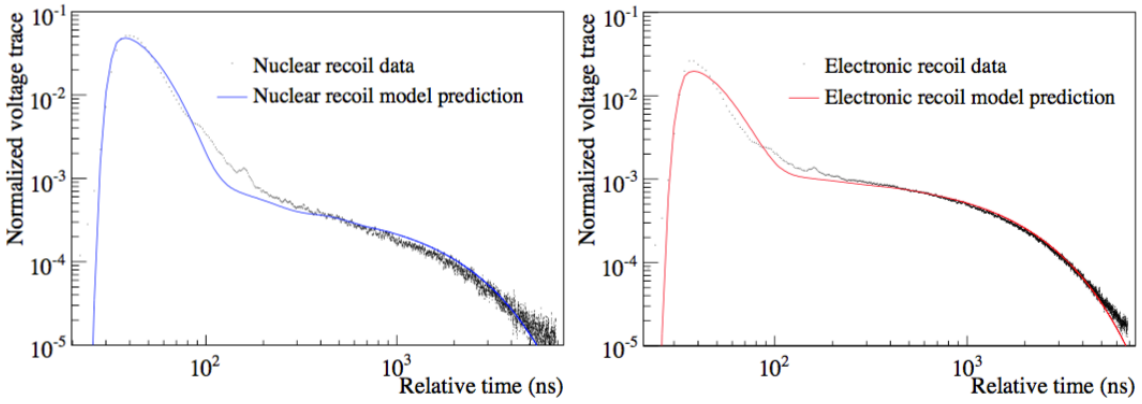

Figure 1.14: Combined voltage traces vs time from two PMTs viewing nuclear (left, blue) and electronic recoils (right, red) in liquid argon, where PMTs observed between 80 and 99 photoelectrons per recoil event. Reproduced from Ref. [108].

μs [98]. Spin orbit coupling is stronger for targets with higher atomic masses, which reduces the triplet lifetime. For example, the heavier noble xenon has a much faster triplet lifetime of 22±2 ns [98], compared to lighter neon and helium which have triplet lifetimes of 15.4±0.2 μs [106] and 13±2 s [107] respectively.

1.5.3 Emission Timing

The timing profile of scintillation from singlet and triplet excitations is described by the sum of two exponential distributions with lifetimes τ_s and τ_l as follows:

$$P_{scint}(t) = \frac{p_s}{\tau_s} exp\left(\frac{-t}{\tau_s}\right) + \frac{1-p_s}{\tau_l} exp\left(\frac{-t}{\tau_l}\right) \tag{1.23}$$

where $\tau_{s,l}$ are the short and long lifetimes and p_s is the fraction of light from singlet state excitation. Figure 1.14 shows voltage traces in two PMTs observing scintillation light from electronic and nuclear recoils in liquid argon, where the PMTs observed between 80 and 99 photoelectrons (PE) per recoil event. For the depicted data the study observed a best fit singlet fraction of p_s=0.279±0.010 for electronic recoils and $(1-p_s)$=0.702±0.010 for nuclear recoils [108]. The discrepancy at 80-300 ns is discussed in Ref. [108], attributing the spike at 150 ns to an electronics and cabling effect present in both datasets. Recombination is thought to be responsible for this difference, as described in the next subsection.

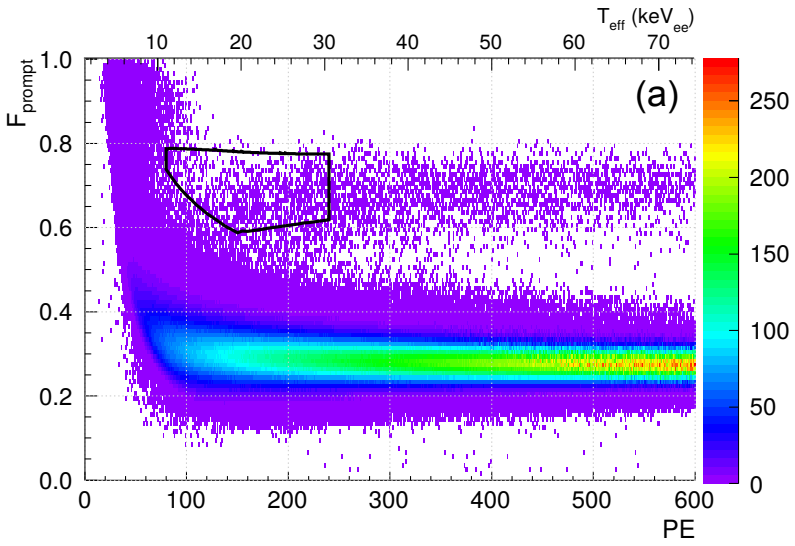

Figure 1.15: Nuclear recoil (higher F_{prompt}) band data taken using the AmBe source in DEAP-3600, with the WIMP search ROI shown as a black box. Reproduced from Figure 3a in Ref. [3].

The separation of lifetimes and difference in singlet fraction in the lighter noble gases enables discrimination between nuclear and electronic recoils using the ratio of singlet to triplet light, known as pulse shape discrimination [3, 67, 108, 109]. Commonly a variable F_{prompt} is defined which measures the ratio of PMT charge $Q(t)$ observed in a prompt window $t_0 < t < t_{pr}$ to that observed in a longer window $t_0 < t < t_{end}$:

$$F_{prompt} = \frac{\int_{t_0}^{t_{pr}} Q(t)dt}{\int_{t_0}^{t_{end}} Q(t)dt} \tag{1.24}$$

For example in the first result from DEAP-3600 $t_0 = -28$ ns, $t_{pr} = 150$ ns, and $t_{end} = 10\ \mu$s [3]. The distribution of F_{prompt} with total observed photoelectron count is shown in Figure 1.15 for scintillation in liquid argon in DEAP-3600 using an AmBe neutron source. The higher F_{prompt} band is produced by neutron scattering, producing nuclear recoils. The lower F_{prompt} band is produced by 4.4 MeV γ's from the AmBe source and β^- decays from the intrinsic ^{39}Ar background. The electronic and nuclear recoil bands converge for events at low energy. Preventing electronic recoil leakage into a chosen region of interest drives up the permissible energy threshold for liquid argon detectors compared to dual-phase detectors, particularly liquid xenon. F_{prompt} is discussed in more detail for argon and DEAP-3600 in Section 3.2.3.

1.5.4 Recombination

Recombination forms the dominant contribution to scintillation light, and has also been observed to affect the ratio of singlet to triplet state scintillation. It has been observed that under a 10 kVcm^{-1} electric field where the recombination electrons are drifted away, the scintillation light yield reduces by a factor of 3. The recombination fraction is estimated in [110] at (67±2)% for liquid argon and (74±2)% for liquid xenon. Likewise, under a 6 keVcm^{-1} field the ratio of singlet to triplet light from direct excitation in argon was observed to reduce to 0.045 compared to a ratio of 0.083 with no field [105].

The influence of recombination on the singlet to triplet ratio allows for discrimination between electronic and nuclear recoils using scintillation timing, as recombination is dependent on particle species and recoil type. The fraction of scintillation light from singlet state excitation for electrons, α and nuclear fission fragments in liquid argon has been observed at p_s=0.23, p_s=0.57 and p_s=0.75 respectively [98]. This behaviour is not well understood, but thought [111] to be characterised to first order by the linear energy transfer (LET), or dE/dx, of the incident particle. At high energies (>1 MeV) a particle incident upon the medium causes ionisation and excitation along its path, leaving a track of ions and excited atoms surrounded by ionisation electrons. Ionisation electrons propagate and either return to the track ions to recombine or interact with nearby atoms, a process known as thermalisation. Incident species with high dE/dx, which produce nuclear recoils, deposit higher ionisation density per unit distance than low dE/dx particles that produce electronic recoils, like electrons. A higher ionisation density produces stronger coulomb attraction and more recombination, which changes the singlet-triplet ratio. It is this effect that enables discrimination between electronic and nuclear recoils using scintillation timing. At the lower energies relevant for a dark matter search, the track reduces to a spherical region of ionisation surrounded by recombination electrons, but the dependence of ionisation density on dE/dx remains. For a comprehensive review of recombination which informed the above discussion, the reader is directed to Ref. [111].

1.5.5 Recoil Dependent Light Yield

From Ref. [112], the number of scintillation photons produced in scintillation by a nuclear recoil is given by:

$$n_{\gamma,\mathrm{nr}} = \frac{kg(\varepsilon)}{1+kg(\varepsilon)} f_l \frac{E_0}{W} \tag{1.25}$$

The additional quenching factor f_l introduces Birks' saturation, which models the prevention of photon emission from exciton through bi-excitonic quenching in regions of high excimer density produced by energy deposition, discussed in Section 1.5.6. From Ref. [113], Birks' Law states that the specific fluorescence per unit path length of an incident particle is given by:

$$\frac{dS}{dx} = \frac{A\frac{dE}{dx}}{1+kB\frac{dE}{dx}} \tag{1.26}$$

where A is the scintillation efficiency, k is given in Equation 1.17 and kB is the ionisation density during scintillation. Values of kB have been estimated in Ref. [114] at 1.12×10^{-3} MeV^{-1} g cm^{-2} for liquid neon, 7.40×10^{-5} MeV^{-1} g cm^{-2} for argon, and 2.02×10^{-3} MeV^{-1} g cm^{-2} for xenon. The quenching factor f_l appears in Birks' Law, given by Ref. [114]:

$$f_l = \frac{1}{1+kB\frac{dE}{dx}} \tag{1.27}$$

The observed scintillation light yield, defined as the number of photons N_{ph} emitted per unit energy E, differs between electronic and nuclear recoils. The reciprocal quantity $W_S = E/N_{ph}$ is defined as the energy transfer required to produce one photon in scintillation, thought of as a scintillation work function. Standardised measurements of the scintillation efficiency $L_{eff}(E)$ in a liquid noble at zero field are taken relative to the W_S value for scintillation from electronic recoils, from 122 keV γ-rays produced by cobalt source, denoted $W_{S,e}(122\mathrm{keV})$. For an observed $W_{S,nr}(E)$ value for a nuclear recoil, the scintillation efficiency is defined as $L_{eff}(E) = W_{S,e}(122\mathrm{keV})/W_{S,nr}(E)$.

In liquid argon L_{eff} has been observed to be constant at $L_{eff} = 0.25\pm0.02$ for nuclear recoils with energies between 20 and 250 keV [115]. A 6% variation in $0.235 < L_{eff} < 0.295$ for nuclear recoils with energies between 10.3 and 57.3 keV has been observed by SCENE [116]. When comparing electronic and nuclear recoil energies the suffix 'ee'

is appended to energy units to denote the electronic equivalent energy to certain nuclear recoil energy, suffix 'r', such that, for an energy in keV:

$$E\,[\mathrm{keV}_{ee}] = L_{eff} \times E\,[\mathrm{keV}_{r}] \tag{1.28}$$

For example, in liquid argon for $L_{eff} = 0.25$ a 15 keV_{ee} electronic recoil produces the same number of scintillation photons as a 60 keV_{r} nuclear recoil.

1.5.6 Quenching

There are multiple processes that can contribute to the reduction of the scintillation light yield due to quenching. One case has been mentioned previously, where the energy transferred to an atom during scattering produces neither ionisation nor excitation, and instead the atom transfers kinetic energy to other nearby atoms, heating the medium. Another is the scattering of two excited atoms in which one undergoes relaxation and ionises the other, in a process known as bi-excitonic quenching [117]:

$$R^{*} + R^{*} \rightarrow R + R^{+} + e- \tag{1.29}$$

As a result a process which would originally produce two scintillation photons from two excitons can only produce one photon though recombination with the ion. In the expression for the quenching factor f_l, Equation 1.27, the higher the density of excitons the more likely this is to occur, so the bi-excitonic quenching probability is enhanced in nuclear recoils, which have higher dE/dx.

Electrons can also escape recombination. They may thermalise after travelling far enough away from the region of ionisation density, characterised by the thermalisation length of electrons, measured at ~ 1.6 μm in liquid argon [118] and ~ 4.5 μm in liquid xenon [119].

Impurities can also affect the scintillation process. The effects of impurity on scintillation in argon have been studied by the WArP R&D program by deliberately introducing N_2 [120] and O_2 [121] contamination in a dual phase argon TPC. Figure 1.16 shows the light yield relative to zero additional contamination and contamination level in parts per

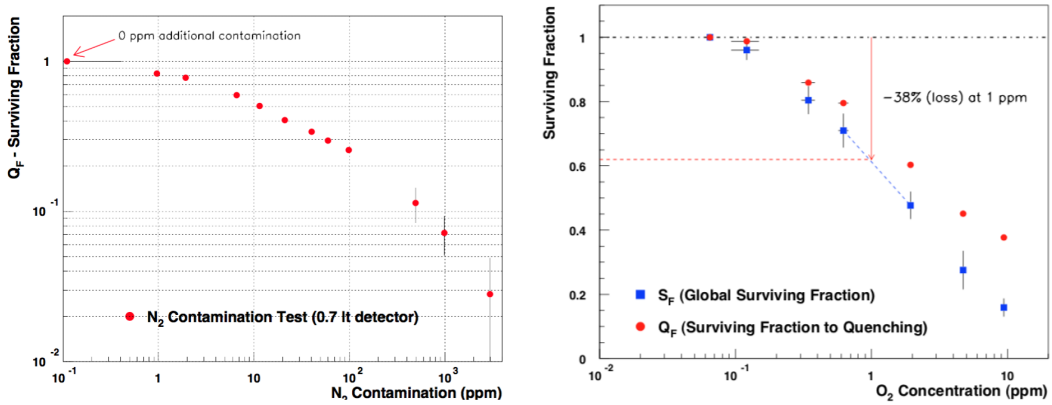

(a) (b)

Figure 1.16: Quenching factor observed in vs nitrogen (a) and oxygen (b) contamination level in ppm, from contamination studies in WArP [120, 121]. Also shown in (b) is the raw surviving fraction, a ratio of light yield with oxygen contamination to light yield without, including effects other than quenching, discussed further in Ref. [121].

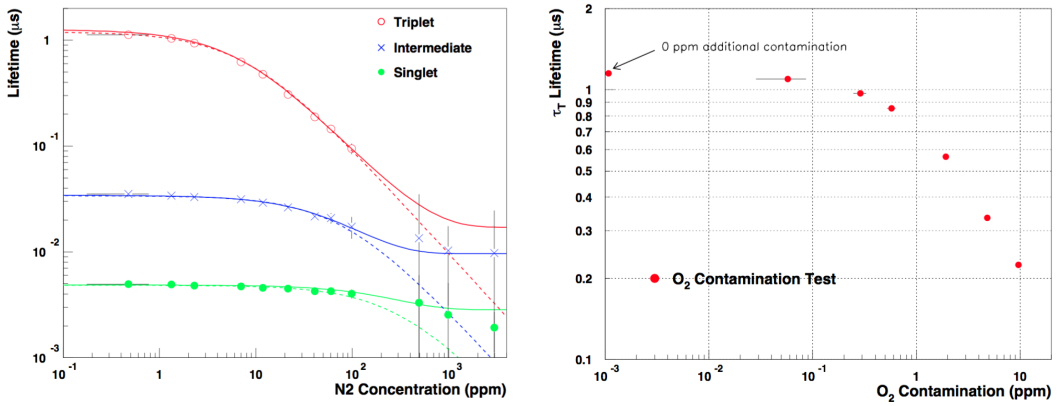

(a) (b)

Figure 1.17: Triplet lifetime vs nitrogen (a) and oxygen (b) contamination level in ppm, from contamination studies in WArP [120, 121].

million (ppm) of N_2 and O_2. This happens either by excited atoms transferring their excitation energy to the impurity or, in the case of electronegative impurities, recombination electrons being captured. Figure 1.17 shows the variation with contamination level of the observed triplet lifetime for contamination with O_2 and both singlet and triplet lifetime for contamination with N_2. Both singlet and triplet lifetimes are reduced with increased contamination, and the separation between the two component lifetimes converges. Figure 1.18 shows the variation in absorption length of scintillation light measured only for contamination with N_2. An increase in contamination level reduces the absorption length, increasing the absorption of scintillation light propagating a given distance.

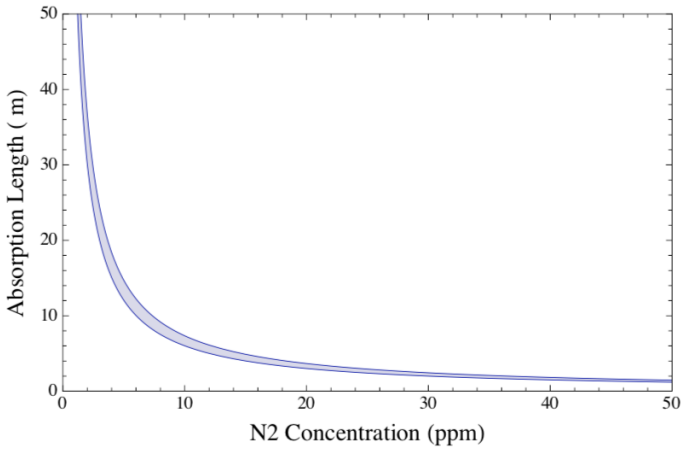

Figure 1.18: Measurement of variation in argon absorption length with contamination level of nitrogen, from contamination studies in WArP [120]. The band shown corresponds to 1σ boundaries on the measurement.

1.6 Conclusion

In this chapter, the principles of dark matter detection were introduced. The evidence from astrophysical observation and cosmology which suggests that there is a dark matter component to the universe was discussed. The theoretical motivation for two of the most popular and well-motivated candidates for particle dark matter were described. The principles of the direct detection of a WIMP candidate were outlined. The methods by which direct detection can take place using low-background detectors was also described, and a summary of recent detector efforts was given. The backgrounds that low-background detection efforts observe were also summarised. Focusing further on single phase, liquid noble detectors, of which the experiment described in this thesis is an example, the physics of scintillation in liquid nobles was discussed.

Chapter 2

The DEAP-3600 Detector

The aim of the DEAP-3600 experiment is to observe WIMPs producing nuclear recoils in its target mass. This chapter begins by providing an overview of the design of the detector in Section 2.1. In Section 2.2 the main particle sources which can mimic WIMP recoils in the detector, known as backgrounds, are summarised. In Sections 2.3-2.6 the components and construction of the detector are discussed. Particular emphasis is placed on the material optical properties which are important for event reconstruction. Following this in Section 2.7 the calibration systems are discussed.

2.1 Overview

DEAP-3600 is a single phase liquid argon scintillation detector, located 2.2 km underground at the SNOLAB facility in Sudbury, Ontario, in Canada. A schematic of the DEAP-3600 vessel is shown in Figure 2.1. Its target mass consists of 3263 kg of liquid argon contained within an acrylic vessel, or AV. As discussed in the previous chapter a recoil event in liquid argon produces scintillation light, with a peak wavelength of 128 nm, emitted isotropically. The inner surface of the AV is coated with a 3 μm layer of Tetraphenyl Butadiene (TPB), which is excited by argon scintillation light and isotropically emits visible light with a peak wavelength of 420 nm. The vessel is surrounded by 255 photomultiplier tubes (PMTs), where TPB re-emission photons produce photoelectrons (PE) through the photoelectric effect. The photoelectron signal is amplified by a

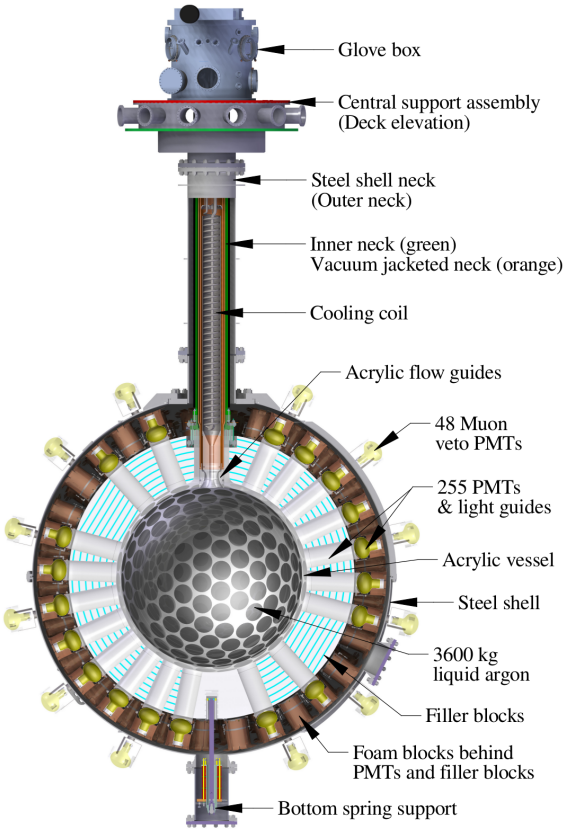

Figure 2.1: A rendered cutaway schematic of the DEAP-3600 detector. Rendered by Koby Dering.

dynode stack in the PMT and the resulting electronic signals are sent an electronic readout and data acquisition system.

The PMTs are mounted on the end of acrylic light guides. The PMTs and light guides are surrounded by layers of polystyrene and acrylic filler blocks and polyethylene foam blocks. The PMT layer is wrapped in a stainless steel mesh which constrains the inner vessel components in the event of an AV or component failure. The neck of the inner vessel allows argon to circulate through the purification systems, and a cooling coil in the inner neck cools argon injected into the vessel. The outer vessel separates the inner vessel from a cylindrical water tank 8 m in diameter. 48 PMTs mounted on the steel detect muon Cerenkov light in the water tank, enabling the rejection of cosmogenic neutrons, as described in the next section.

2.2 Backgrounds

The detector design, commissioning and analysis is motivated by the need for reduction of background standard model particle interactions, which produce signals that can mimic a WIMP nuclear recoil. Three major background sources are summarised here. To achieve <0.6 background event in three years of data, ^{39}Ar β^-, neutrons and alphas are each assigned a target of <0.2 events reconstructed in the energy region of interest and fiducial volume. Suppression of these backgrounds is crucial to the sensitivity of a dark matter search.

2.2.1 ^{39}Ar

The dominant source of electronic recoil backgrounds in liquid argon is the presence of the cosmogenically activated isotope ^{39}Ar which has a half life of 269 years, and produces β^- decays at a rate of 1.01 ± 0.1 Bq/kg [101], uniformly distributed throughout the detector, with an endpoint energy of 565 keV. A fiducial volume of 1000 kg of liquid argon, running for three years, will see 10^{11} such events. These background events produce electronic recoils, which pulse shape discrimination (PSD) is able to mitigate by a factor of 10^{-11} to satisfy the background target. This is elucidated in Section 1.5.3 on scintillation timing, which discusses F_{prompt}, the PSD parameter used in DEAP-3600.

2.2.2 Surface Alphas

Alpha decays are another background source which can produce scintillation in argon. The earth naturally contains radioactive isotopes with long lifetimes, which can contaminate detector materials during manufacture. For low-background experiments the ^{238}U and ^{232}Th decay chains are the most problematic, which contain a series of alpha and β decays accompanied by gamma radiation. For the highest energy alpha in either chain, simulations in SRIM-2010 [122] limit the alpha propagation range in AV acrylic to 80 μm. The alpha range means that surface alpha events are expected to originate from the inner 80 μm of the AV, and the 3 μm TPB layer.

Surface alpha backgrounds are compounded by radon, a noble gas present in air with

unstable isotopes ^{222}Rn and ^{220}Rn in the ^{238}U and ^{232}Th decay chains respectively. When ^{222}Rn decays in air the recoiling daughter isotopes can be deposited on a surface or diffuse into the surface itself. Either case results in the accumulation of ^{210}Pb further down the decay chain which has a half life of 22 years. Accumulated ^{210}Pb will decay to alpha-decaying ^{210}Po, which will be observed throughout the experiment. The radon decay chain is shown including alpha energies and half-lives in Figure 2.2.

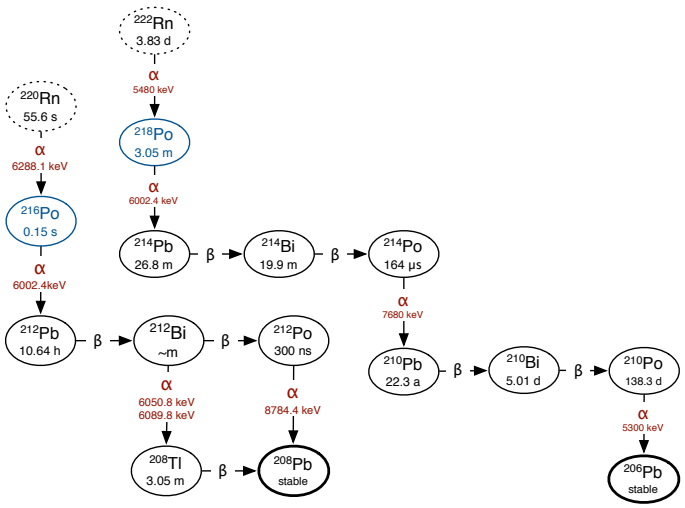

Figure 2.2: The ^{220}Rn (left) and ^{222}Rn (right) decay chains, from ^{232}Th and ^{238}U respectively. Each isotope is shown above its half life (where a number of years is represented a, for annum). The energy of the ejected alpha is shown in red. Figure prepared by T. Pollmann [123].

An alpha and recoiling daughter isotope are able to deposit energy and scintillate in different ways depending on where the decay takes place, as depicted in Figure 2.3. In case (a) the full alpha decay energy is deposited in argon. In cases (b) and (c) the decay of an isotope occurs in the TPB and on the argon-TPB interface. The combination of alpha scintillating in TPB and daughter scintillating in argon, case (b), produces less light than the opposite in case (c). The alpha is the more energetic of the pair of products, and the scintillation light yield of alphas in TPB is lower at 882±210 photons/MeV [124] than argon, which has a maximum scintillation light yield of $51.3^{+2.7}_{-2.5}$ photons/keV [100]. The low light yield in TPB also produces low energy events in case (d), where an alpha propagates through the TPB from a decay either on the acrylic-TPB boundary, or in the acrylic.

The result of a SRIM-2010 [122] simulation of ^{210}Po decays in the TPB layer, cases

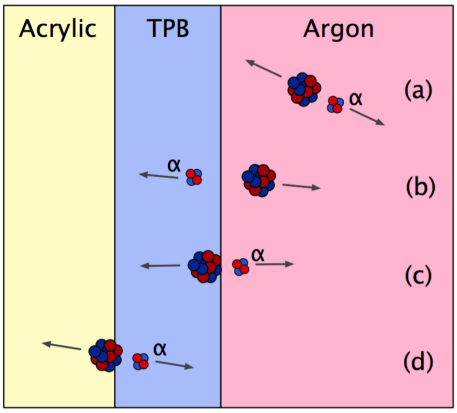

Figure 2.3: Schematic showing the locations of origin of surface alpha decay backgrounds. Schematic produced by T. Pollmann.

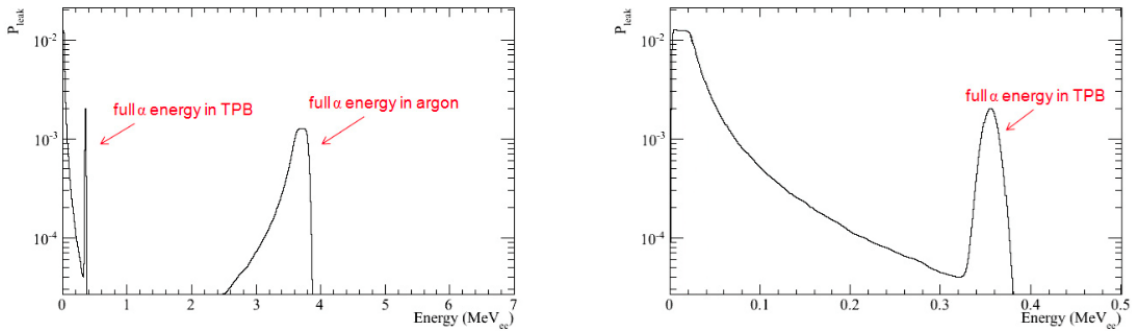

Figure 2.4: Distributions of energy deposited in the TPB layer by ^{210}Po decay products, as calculated in SRIM-2010 [122]. Simulation and plot produced by T. Pollmann.

(b) and (c) above, are shown in Figure 2.4. Each plot shows the probability of observing a scintillation light yield that corresponds to a given recoil energy in liquid argon, which includes TPB scintillation light. Alphas that enter the acrylic, in the reverse of case (d), scatter and produce no more light. Alphas that scatter in both TPB and acrylic produce the spectrum of low energies below the peak which corresponds to full energy deposition in TPB.

The alpha background from surface deposition and diffusion is controlled during manufacture and detector assembly by controlling material exposure to air, as elucidated in Section 2.3. The deposition component is entirely removed and the diffusion component partially removed using a sanding robot, which is discussed in Section 2.3.3. In addition a fiducial cut is made to reject events whose positions are reconstructed near the surface. The original design specification states a 1T fiducial mass of radius 550 mm at the centre

Location	Chain	$P_{leak,ROI}$ (%)	Limit μBq/(kg or m^2)	Limit (ppt)	Measurement μBq/(kg or m^2)
AV 80μm	^{238}U	0.39	2.9	0.23	3.7
	^{232}Th	0.39	3.9	0.95	5.3
	^{210}Po	0.39	23.2	8.2×10^{-9}	31
AV surface	^{210}Po	5.75×10^{-4}	15.1	-	2.2×10^{2}
TPB	^{238}U	6.51	5.7	0.46	$<4.33\times10^{3}$
	^{232}Th	6.13	8.8	2.2	$<1.69\times10^{3}$
	^{210}Po	7.19	42.0	1.5×10^{-8}	1.34×10^{3}
TPB (manufacturer)	-	-	-	-	0.15
TPB surface	^{210}Po	12.1	0.04	-	<310

Table 2.1: A table summarising the contributions to the surface alpha background, the probability $P_{leak,ROI}$ that an alpha will reconstruct in the energy region of interest, and the implied tolerable limits for that leakage fraction. Alongside these are measurements from detector data and assays of detector materials.

of the detector, assuming a position reconstruction radial resolution at the surface given by a Gaussian with resolution $\sigma = 100$ mm.

Table 2.1 summarises probabilities $P_{leak,ROI}$ that a given alpha reconstructs in a 20-40 keV$_{ee}$ region of interest (ROI). These probabilities are calculated using GEANT4 simulations of ^{238}U, ^{232}Th decay chains and out-of-equilibrium ^{210}Po in the detector, originating in acrylic and TPB, in the bulk material and on surfaces. To satisfy the upper limit of 0.2 surface events in three years, ^{238}U, ^{232}Th and ^{210}Po from each location are each given a conservative upper limit of $N_{UL} = 0.01$ events in the ROI in three years. The figures below assume that the fraction of events that leak into the fiducial volume is $P_{leak,fid} = 1.35 \times 10^{-3}$, or 3σ in from the surface. This corresponds to a tolerable upper limit of $N = N_{UL}/P_{leak,fid} < 7.4$ surface events in three years in the region of interest and fiducial volume.

Also shown in Table 2.1 is the implied tolerable contamination limit R from each source, in μBq/kg and parts per trillion (ppt) for bulk material and μBq/m^2 for surfaces, alongside measurements of each. Each rate upper limit R in μBq/kg is calculated from $P_{leak,ROI}$ according to $R = N/(m_i t n P_{leak,ROI})$. Here $N < 7.4$ surface events, $n = 8$, 5.99, 1 is the number of alphas in the ^{238}U, ^{232}Th, and ^{210}Pb chains respectively, t = 3 years, and $m_{AV} = 0.864$ kg for an 80 μm AV layer, $m = 0.031$ kg for 3 μm of TPB and $m_{TPB,S} = 9$ m^2 is the area of the TPB surface. All of the stated measurements are from assays of

samples taken from the material used in the detector, made using a germanium counter, with the exception of the ^{210}Po content on the AV and TPB surface.

The TPB surface ^{210}Po content is taken from measurement of the TPB used in a prototype detector, DEAP-1. A more stringent result on the bulk contamination is set in assays of the TPB used in DEAP-3600 performed by the manufacturer. The AV content is taken as the sum of intrinsic content from assays of the AV acrylic and the estimated component from radon diffusion into the surface after resurfacing. This is discussed in Section 2.3.3.

Improvements to position reconstruction of surface events increase the tolerable contamination upper limit required to see <0.2 events in our fiducial volume and ROI. Our measured contamination exceeds our tolerable limits assuming $P_{leak,fid} = 1.35 \times 10^{-3}$, which makes the identification of surface backgrounds in data and performance of position reconstruction of paramount importance in meeting the background budget.

2.2.3 Neutrons

When neutrons scatter in argon they produce nuclear recoils that have the same scintillation timing as a WIMP, which makes them indistinguishable by PSD. The dominant neutron background sources are summarised here.

As a consequence of the presence of intrinsic ^{238}U and ^{232}Th chain isotopes in laboratory and detector materials, radiogenic neutrons are produced from (α,n) interactions and spontaneous fission, with energy spectra that extend up to 10 MeV and peak energies at $\sim$2 MeV. The radiogenic neutron background is mitigated by placing shielding material around the argon target, which absorbs or scatters the neutron. In acrylic, a 1 MeV neutron has a mean free path of $\sim$2.2 cm, from total scattering cross sections of 4.24 barns in hydrogen, 2.58 barns in carbon and 8.15 barns in oxygen [125]. The combination of a 5 cm thick AV and 55 cm light guide and filler block layer ensures that radiogenic neutrons can scatter or be absorbed before reaching the argon. Components closest to the argon are thus the most likely to produce a radiogenic neutron that produces a nuclear recoil in argon. The neutron yields of the highest contributing components near the argon are listed in Table 2.2. The highest yield of these is produced from PMT glass, which is not

Component	Material	Yield	Events/year	ROI Events/year
PMTs	Borosilicate Glass	3.7×10^{-5} n/s/Bq	63400	3.432
Filler Block	Polyethylene foam	6.5×10^{-6} n/s/Bq	173	0.468
Water (μ,n)	Water	2.04×10^{-10} n/s/g	2187.34	0.146
Rock wall (α,n)	Norite	4400 n/d/cm^2	20181597	0.081
Rock wall (μ,n)	Norite	5.4×10^{-11} n/d/cm^2	18.72	0.052
Light guides	Acrylic	2.4×10^{-6}	510	0.038

Table 2.2: Summary of the highest contributors to the neutron nuclear recoil background, the number of events per year expected from each component, and the number of events that enter an example WIMP region of interest. Region of interest is taken as an example defined by total observed PE in the region 120-240 PE (equivalent to 20-40 keV$_{ee}$ for a conservative light yield of 6 PE per keV$_{ee}$), and a nominal PSD parameter cut $0.6 < F_{prompt} < 0.8$. Components are listed in order of decreasing ROI events per year. Table reproduced from calculations in Ref. [125, 126, 127].

optimised for radiopurity.

The flux of cosmic ray muons can also produce neutrons through (μ,n) interactions. Muon induced neutrons have an energy spectrum that extends up to several GeV, shown for different common low-background laboratories in Figure 2.5. SNOLAB has the lowest muon flux of those shown, having the highest rock overburden in which muons may scatter before reaching the laboratory. The largest target masses for a muon incident on SNOLAB are the laboratory rock wall and water tank. The flux of muon induced neutrons from the rock wall has been calculated at 5.4×10^{-11} s^{-1}cm^{-1} using simulations of rock wall neutron interactions in Ref. [60]. The production rate in water was also calculated at 2.04×10^{-14} s^{-1}g^{-1}, assuming 340 tonnes of water [126]. The resulting muon flux in one live year is also summarised in Table 2.2, assuming no rejection from the water veto. The high neutron scattering cross section in hydrogen means that water also shields the detector from the external neutron flux. This shielding is at its thinnest at the top of the detector, and the highest rock (α,n) neutron leakage rate originates from this area. The veto PMTs on the steel shell may capture Cerenkov light from a passing muon such that recoils in argon which coincide with a passing muon may be rejected, but only if the muon passes through the tank before interacting.

Also shown in Table 2.2 is the number of events per year detected in liquid argon from each source, using a GEANT4 simulation of the detector which is described in the next chapter. It assumes a nominal region of interest cut of 120-240 PE (equivalent to

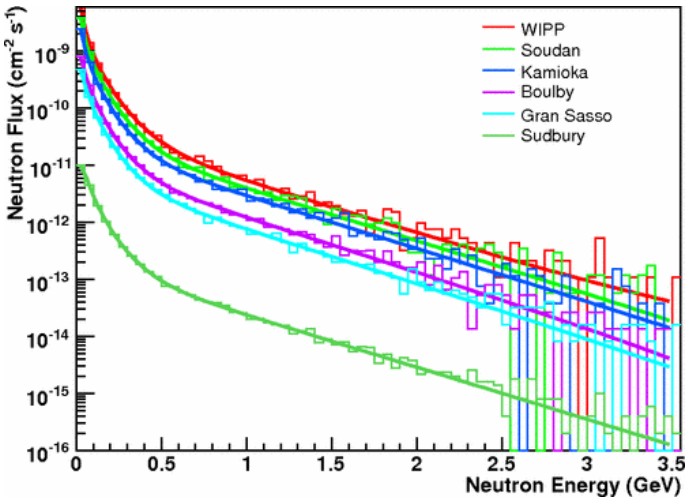

Figure 2.5: Differential energy spectra for muon-induced neutrons emerging from rock faces at underground laboratory sites used for low-background detector physics. Histograms with 50 MeV wide bins show the energy spectra produced by simulations of neutrons in rock wall. Reproduced from Ref. [60].

20-40 keV$_{ee}$ for a conservative light yield of 6 PE per keV$_{ee}$ from early studies) and a nominal PSD parameter cut $0.6 < F_{prompt} < 0.8$ to select nuclear recoils. Fiducialisation with position reconstruction is able to further reduce the neutron flux by a factor of ~ 14, using a 1T spherical fiducial mass of radius 550 mm at the centre of the detector [126].

2.3 The Inner Vessel

Construction of the inner vessel was completed with the sealing of the steel shell in March 2015. In this section the construction of the inner vessel is discussed. The discussion includes the optical properties of those components which argon scintillation and TPB excitation light encounter whilst propagating to the PMTs, as relevant to simulation and event reconstruction.

2.3.1 Acrylic Vessel

The acrylic vessel consists of a large spherical vessel with an inner surface diameter of 851 mm, of minimum surface thickness 5 cm. An opening of radius 12.75 cm at the top of the vessel connects to an acrylic neck, producing the AV's overall flask shape. The AV is shown in Figure 2.6.

Figure 2.6: Photograph showing the fully bonded AV with light guides.

The acrylic vessel was cast from distilled poly(methyl methacrylate), or PMMA, by Reynolds Polymer Technologies (RPT), Thailand, in 5 slices, a bottom cap, a top cap and the neck. The outer surface of the vessel and neck was milled to a <0.2 mm precision using a 5-axis CNC mill at the University of Alberta, producing stubs on which light guides were bonded. Due to constraints from the mine shaft dimensions the top cap, neck and light guides were transported into SNOLAB and bonded there. The pieces were bonded together by injecting acrylic between components. The AV and light guides were annealed at 80-85 °C after every bonding stage to minimise light loss due to inhomogeneity at the bond sites.

Radon levels were kept to 1 Bqm^{-3} throughout polymer formation. The total exposure of the AV to radon in SNOLAB air was controlled during annealing, as SNOLAB air has a radon activity measured at 10 Bqm^{-3}. The inside of the AV was kept overpressure with surface air with an expected purity of 1 Bqm^{-3} during AV bonding, and then sealed overpressure with nitrogen until resurfacing. From the total exposure of the AV to radon a concentration of 5×10^{-6} ppt of ^{210}Pb was estimated to be present in the acrylic surface at the time of resurfacing.

TPB re-emission light propagating through the AV is expected to travel a minimum of 5 cm before reaching a light guide. Spectrometer attenuation length measurements of a 1

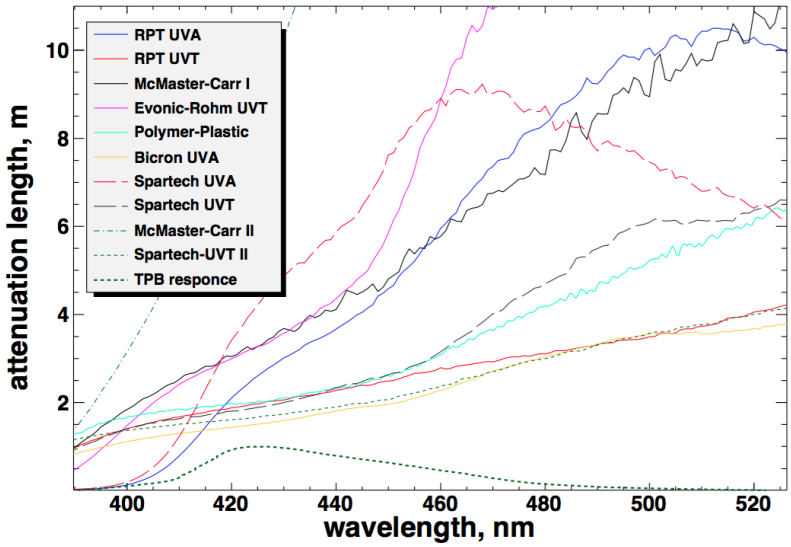

Figure 2.7: Measurement of attenuation length of TPB re-emission light against re-emission light wavelength using a spectrophotometer. The acrylic selected for the DEAP-3600 AV is the UV-absorbing (UVA) sample from Reynolds Polymer Technologies (RPT), shown in solid blue. The acrylic selected for the light guides is the Spartech UVA sample in dashed red. Figure prepared by V. Volkovo and M. Kuzniak in Ref. [128].

m thick sample of the UV-absorbing (UVA) acrylic used in the AV have been made, shown in Figure 2.7. The blue curve shows the variation of the attenuation length with incident light wavelength in the UVA sample from RPT. Also shown is the wavelength spectrum of TPB re-emission light, in arbitrary units. The attenuation length of light at the peak TPB emission wavelength in UVA acrylic manufactured by RPT is 3.5 m from Figure 2.7. The expectation value for the attenuation length weighted by the TPB emission spectrum is calculated at $3.9^{+0.5}_{-0.3}$ m in Ref. [128]. Both estimated attenuation lengths are two orders of magnitude higher than the AV thickness.

2.3.2 Light guides

The light guides are acrylic cylinders of radius 9.5 cm and length 45.6 cm, made from Spartech UV-absorbing (UVA) acrylic. Spectrometer measurements of the attenuation length of a 1 m long cylindrical sample of light guide acrylic were made by the collaboration, shown in Figure 2.8. The sample was annealed at 85°C, to mimic the expected treatment of the real light guides.

The light guide acrylic has an attenuation length measured by the collaboration at

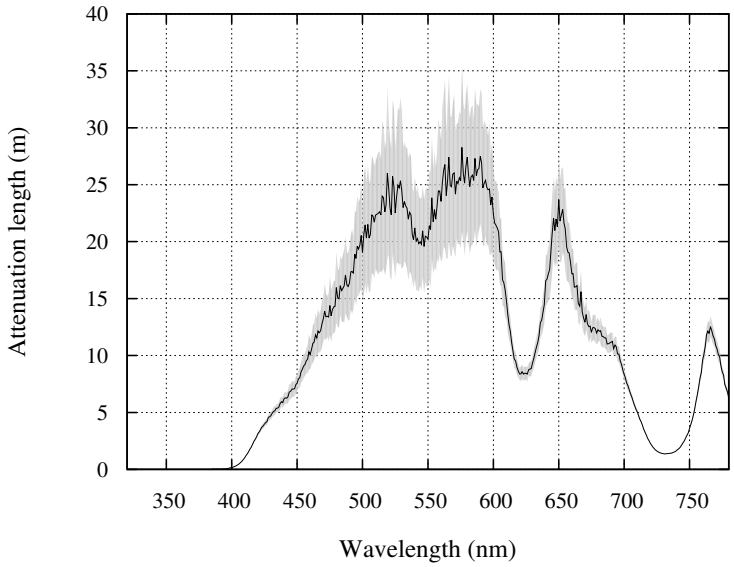

Figure 2.8: Spectrometer measurement of the variation of the attenuation length of light guide acrylic with the incident light wavelength. Measured internally by P. Rau, figure prepared by M. Kuzniak.

6.157±0.595 m for 440 nm light. The light guide side surfaces are wrapped with a 100 μm layer of Mylar (made from Polyethylene Terephthalate, or PET), prepared by Astral Technology Unlimited. The Mylar was sputter coated with a 100 nm thick layer of aluminium with impurity content estimated at 10 parts per million. The coating has a reflectance estimated at 92% of incident light from simulation. The aluminium reflects light exiting the radial surface of the light guide, and towards the PMT. A layer of black Tyvek wrapped around the Mylar layer additionally prevents light from entering the light guides from outside of them, and completes the light guide preparation. A set of wrapped light guides are shown in Figure 2.11a.

2.3.3 Resurfacing

A layer of the inner surface of the AV was removed using a sanding robot known as the resurfacer, which was developed and built at Queen's University, Ontario. The resurfacer is shown in Figure 2.9. The central support column supports a tilt arm which rotates in both θ and ϕ relative to the neck, driven by two stepper motors from outside of the vessel. The resurfacer operated in a spiral pattern from $\theta = 0$ to $\theta = \pi$ and returning,

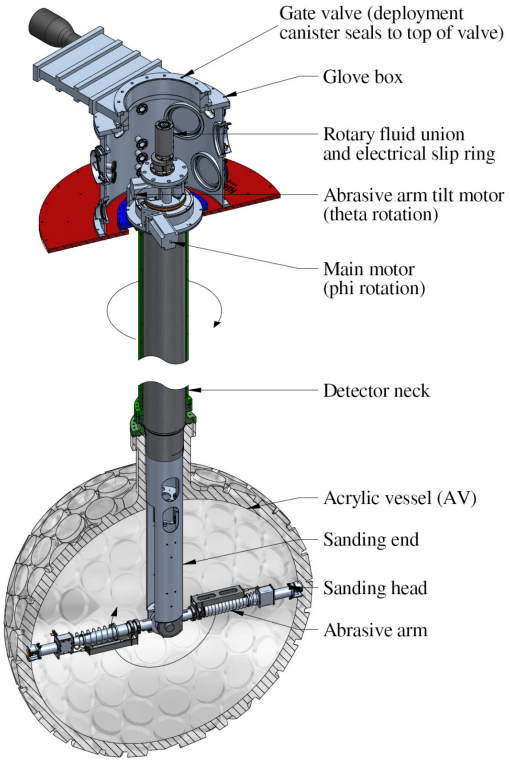

Figure 2.9: Rendering showing the resurfacer apparatus as installed in the AV via the glovebox and AV neck. Rendered by Koby Dering.

whilst rotating in ϕ. After each pass the pattern was rotated to a new position in ϕ, in order to prevent the build-up of systematic sanding anomalies.

During resurfacing the AV was kept under constant purge with nitrogen gas, degassed such that the radon content of nitrogen was below 10 mBqm^{-3}. Figure 2.10 shows the variation of the expected residual rate of ^{210}Pb events from acrylic with the depth of acrylic removed, assuming the starting estimation of 5×10^{-6} ppt from radon diffusion. Over the course of 200 hours of sanding 0.4 mm of acrylic surface was removed, leaving a surface alpha rate from ^{210}Pb of $\sim$15 α/m^2/day from radon diffusion from Figure 2.10.

2.3.4 Filler blocks and reflectors

Opaque filler blocks between the light guides complete the layer of neutron shielding buffer material between the PMTs and the argon. The filler blocks are made of layers of polystyrene foam and polyethylene. The latter also provides thermal insulation between

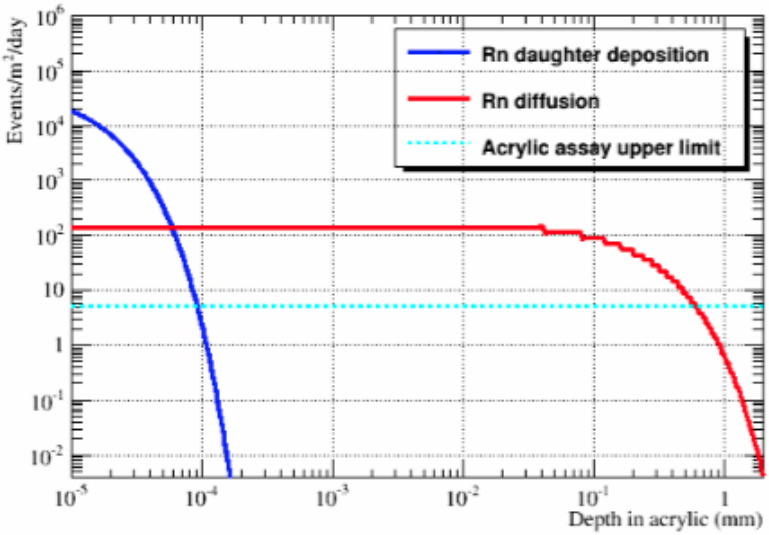

Figure 2.10: Plot showing contributions to the predicted ^{210}Pb activity in acrylic with varying depth of acrylic removed. The contribution from radon decay daughter deposition on the surface is shown in blue; the contribution from radon diffused into the acrylic is shown in red; the upper limit from Ge detector assays of the acrylic bulk is shown in cyan. With the removed layer thickness predicted at 0.4 mm, the residual AV surface activity is dominated by the contribution from radon diffusion at $\sim$15 α/m^2/day. Plot produced by B. Cai and M. Boulay [129].

the argon and PMTs. A schematic of an installed filler block is shown in Figure 2.11b. Select filler blocks are instrumented with temperature sensors at the innermost, middle, and outermost layers, for continuous monitoring of the AV temperature during detector operation. Additionally polyurethane foam blocks are placed between the PMTs to prevent the PMTs and cabling from heating their surroundings. In the gaps between the light guides the AV is wrapped with 4 layers of Tyvek as shown in Figure 2.11a. The purpose of each of the 4 layers is as follows:

- White Tyvek paper provides diffuse internal reflectance when light exits the AV between light guides.
- A white woven Tyvek layer behind it provides additional reflective coverage in the event of gaps forming as materials move during cooling.
- A black Tyvek layer connected to the light guide Tyvek ensures that no light can enter from outside the AV.

- The outermost layer of white polyethylene cushions the AV from the forces exerted by the filler blocks.

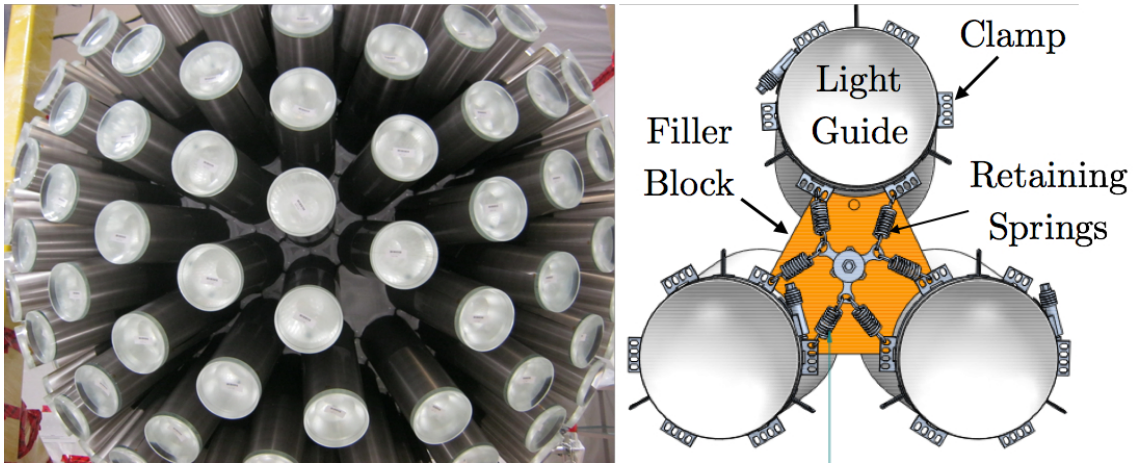

Figure 2.11: a) Wrapping of the light guides and AV. The light guide is wrapped with reflective aluminised Mylar backed with black Tyvek and magnetic shields. The AV is wrapped with white specular reflecting Tyvek backed by 3 layers of light-proofing and a cushioning layer of Tyvek foam; b) a schematic of an installed filler block between the light guides, with supporting springs, prepared by K. Dering

2.3.5 Tetraphenyl Butadiene (TPB) deposition

TPB is the wavelength shifter used to convert argon scintillation light to visible light to which the PMTs are sensitive. When TPB absorbs argon scintillation light, de-localised electrons in phenyl groups in the molecule are excited, which then de-excite and emit photons isotropically. This means that light will travel both outwards, in the direction of the acrylic light guides and PMTs, and inwards towards the detector. The re-emission wavelength spectrum is shown to be independent of incident light wavelength for wavelengths near and including the peak argon scintillation wavelength as shown in Figure 2.12. The re-emission spectrum peaks at 425 nm. The ratio of incident to emitted light intensity or fluorescence efficiency from the surface at 128 nm is 1.2, as shown in Figure 2.13.

TPB was deposited on the AV surface using a spherical stainless steel source of diameter 11 cm, made of 316 stainless steel. The steel sphere is perforated with 20 equidistant holes of diameter 14 mm. The source is shown in Figure 2.14. A copper crucible inside the steel ball held the TPB powder, which was heated to above its sublimation tempera-

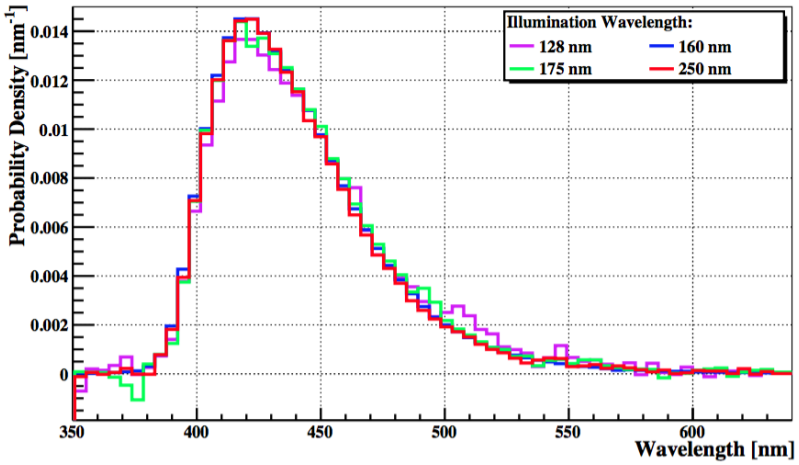

Figure 2.12: Re-emission spectra at visible wavelengths for a 1.5 μm layer of TPB produced using vacuum-deposition. Different colours correspond to different wavelengths of incident light from a monochromator at 128 nm (the peak argon scintillation wavelength), 160 nm, 175 nm and 250 nm. The spectrum from illumination with 128nm light peaks at 425 nm. Reproduced from Ref. [130].

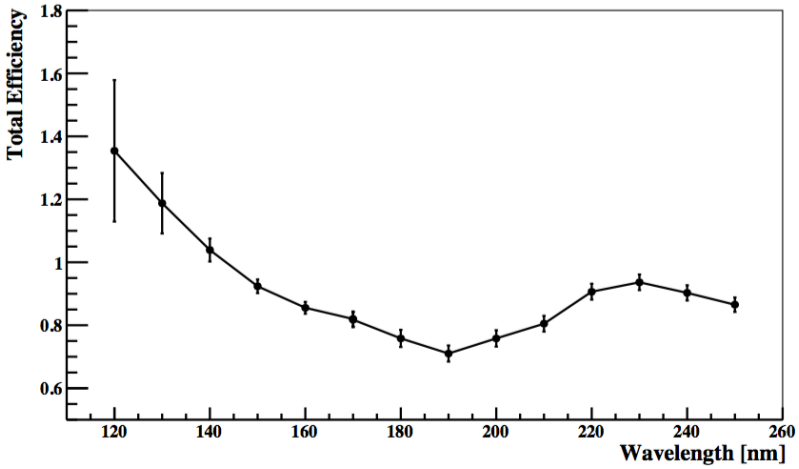

Figure 2.13: Integrated fluorescence efficiency as a function of incident light wavelength for a 1.5 μm layer of TPB. Reproduced from Ref. [130].

ture at 208 °C using a Watlow coil heater wound around the stainless steel surface. Before deployment the stainless steel was ultrasonically cleaned and passivated using citric acid, and both steel source and copper crucible were baked in a vacuum chamber at 210 °C, before being transported to the underground facility in two layers of radon diffusion-resistant material.

The source entered the detector on a 4 m long 0.75 inch diameter stainless steel pipe, with the detector under vacuum at 10^{-6} mbar. A first deployment without TPB evapo-

Figure 2.14: Photo showing the stainless steel TPB source, wrapped with a Watlow coil heater, and containing a copper crucible housing the TPB powder. Reproduced from Ref. [131].

rated and removed water absorbed into the AV surface. TPB was deposited in a further two deployments. Overall 29.4±0.2 g of TPB powder was deposited on the AV surface, resulting in a 3±0.02 μm coating, assuming a uniform thickness [131]. The TPB thickness was confirmed using an Inficon Front Loaded Quartz Deposition monitor placed at the neck of the vessel. Prior testing on acrylic plates placed 85 cm from the source imply that the method produces a coating which is uniform within a 20% variation, and this was verified by reproducing the coating in a smaller spherical test vessel.

2.3.6 Photomultiplier Tubes (PMTs)

The PMTs are the light sensitive part of the detector. Light incident on the photocathode of a PMT produces electrons through the photoelectric effect. The electrons propagate to a dynode under the influence of an electric field, which imparts enough additional kinetic energy to stimulate secondary emission in the dynode. This process repeats in a cascade over multiple dynodes, and a wired anode collects the electronic current.

Mounted on the end of each light guide is a Hamamatsu R5912 high quantum efficiency (HQE) PMT with a peak quantum efficiency of 35% at 400 nm (compared to 25% for a standard R5912). The PMTs are operated at voltages between 1500 V and 1900 V, matched such that the PMTs have a mean charge from a single photoelectron of 9.47 pC, with an RMS variation of 0.12 pC [132].

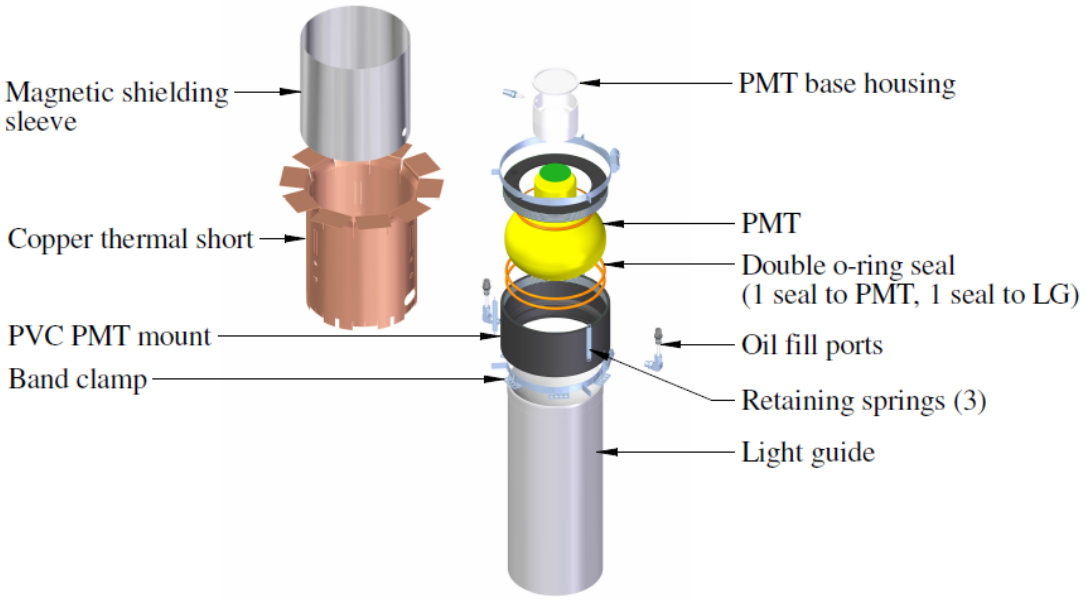

Figure 2.15: An exploded view rendering of a fully installed and constructed PMT mount. Rendering by Koby Dering.

Each PMT is attached to a light guide using a mounting assembly, shown in Figure 2.15. The gap between the PMT glass and light guide face is filled with silicone oil of viscosity 1000 cSt, with a refractive index of 1.403 specified in Ref. [133]. This minimises reflections when light encounters boundaries with acrylic and PMT glass, which have refractive indices of 1.501 [134] and 1.458 [135] respectively for 440 nm light. The PMTs are connected to cables which power the PMTs and return low voltage signal from the PMTs to the electronics discussed in Section 2.6. The AV is shown with a complete set of PMTs installed and with all cables and foam blocks installed in Figure 2.16.

The PMTs used in DEAP-3600 were studied using a 532 nm pulsed laser by T. Caldwell *et. al.* in Ref. [136]. The time dependent current of each pulse is described by either a double or triple log normal pulse shape (82% and 18% of pulses respectively):

$$I_{PMT}(t) = Q\sum_{i=1}^{n}\frac{N_i}{(2\pi)^{1/2}t\sigma_i}\exp\left[\frac{-ln(t/\tau_i)^2}{2\sigma_i^2}\right] \tag{2.1}$$

For each component i, the τ_i are the mean arrival time of an electron at the anode; σ_i are the root mean squared arrival time; and N_i are normalisation factors controlling the relative size of each term, such that $\sum_{i=1}^{n} N_i = 1$; and $n = 2,3$ is the number of terms for a

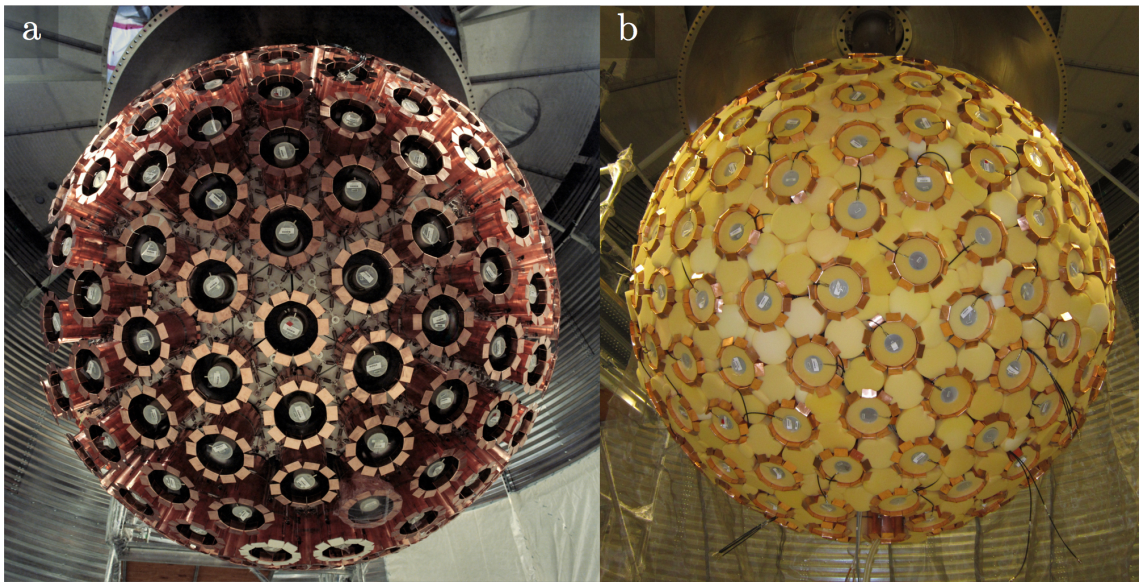

Figure 2.16: Photographs showing the acrylic vessel: a) with all PMT mounts, copper collars and filler blocks installed, b) PMT cabling installed between two layers of polyurethane foam blocks. Photographed by Mark Ward.

double and triple log normal pulse shape respectively. Q is the total charge of the pulse, described by an analytic function fitted to the charge distributions of single and multiple PE pulses. The function parameters are determined using data from the AARF in-situ optical calibration source as discussed in Section 2.7.1.

Photoelectron production processes produce a set of pulse types observed in Ref. [136], listed below. The characteristic timing distribution the four pulse types is shown in Figure 2.17, relative to the peak of the prompt timing distribution shown in blue.

Prompt The result of a simple cascade from dynode to dynode towards the anode (blue curve at -18<t<24 ns). The pulse has a charge Q described by the model discussed in Section 2.7.1. The mean transit time from photocathode to first dynode has been measured at 25.26 ns. Occurs for 91.2% of photoelectrons produced at the photocathode.

Late Occurs when a photoelectron elastically scatters off the first dynode in the chain, travelling backwards before being accelerated again towards the first dynode by the electric field in the PMT (green curve at t>24 ns). The timing distribution is peaked at twice the measured mean transit time, or 50.52 ns, and the pulse has the same

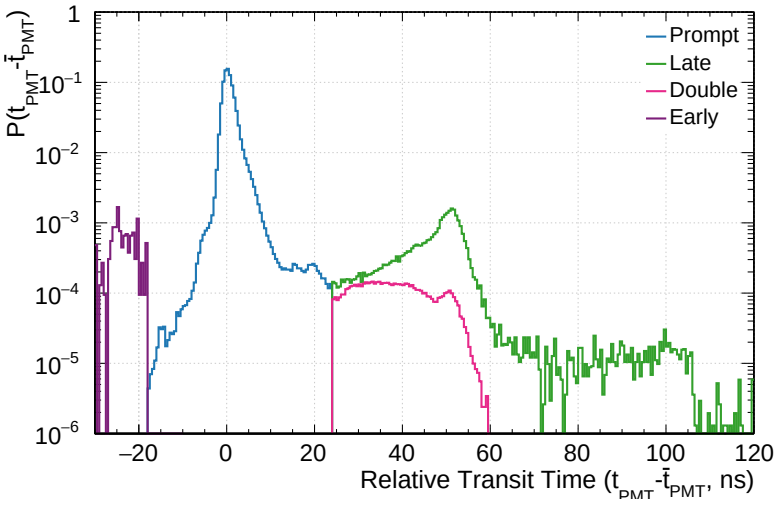

Figure 2.17: PMT pulse timing distributions for prompt, late, double and early pulse types, with each distribution normalised to unit area under the curve. Pulse times are shown relative to the peak of the prompt PDF shown in blue. Reproduced from data in Ref. [136].

charge Q as a prompt charge. Occurs for 3.2% of photoelectrons produced at the photocathode.

Double Occurs when a photoelectron at the first dynode inelastically recoils away from the first dynode in the chain, producing a first photoelectron and returning after being accelerated towards the dynode to produce a second photoelectron (pink curve at t>24 ns). The two photoelectrons produce two pulses with charges Q_i that sum to the prompt charge, $\sum_{i=1}^{2} Q_i = Q$. The first pulse timing distribution follows the prompt distribution and the second pulse time is distributed with a peak at 50.52 ns, or twice the mean transit time. Occurs for 5.5% of photoelectrons produced at the photocathode.

Early When a photon passes the photocathode and PMT glass without interacting. The photon then creates a photoelectron directly at the first dynode earlier than the prompt peak by approximately the mean transit time (purple curve at $-30 < t < -10.5$ ns). The cascade takes place as usual, but over fewer dynodes, resulting in a pulse with a smaller charge than a prompt pulse. Occurs for 1.2% of photoelectrons which reach a PMT photocathode. The other 98.8% produce prompt, late and

double pulses.

Afterpulsing The result of a photoelectron ionising residual gas in the vacuum inside a PMT. The positive ions move towards the photocathode under the influence of the electric field and produce photoelectrons. Afterpulses are detected several microseconds after prompt pulses, with small charges Q_i which satisfy $\sum_{i=1}^{n_{AP}} Q_i = Q$ for n_{AP} afterpulses.

Dark Pulses The result of thermal electron emission at the photocathode. These occur uniformly distributed in time, at a rate of 500 Hz, with the same charges Q as a prompt charge.

Additionally the neck is wrapped with four bundles of wavelength-shifting optical fibres with a peak absorption wavelength of 430 nm and a peak re-emission wavelength of 476 nm. The fibres cover the first 10 cm above the point where the neck meets the AV, and are connected to four Hamamatsu High Quantum Efficiency R7600-300 PMTs. The assembly is used to observe light produced by alphas near to or inside of the neck.

2.4 Outer Components

The outer vessel consists of two hemispheres made of 304 stainless steel bolted together at the equator, and a steel neck. Subject to the same mine shaft size constraints at the AV, this steel shell was fabricated in 6 pieces at All-Weld in Toronto, and welded together underground. The steel shell encapsulates the acrylic vessel and its exterior components, including the neck, ensuring light and water tightness, and is supported by the support frame of the deck constructed above it. Between the steel shell and PMT layer is placed a porous stainless steel mesh, which physically constrains components in the event of AV failure, and a space between the mesh and shell is purged with radon-filtered nitrogen gas to prevent electrical arcing between PMT connectors leading to PMT breakdown.

The water tank measures 8 m in diameter and is made of galvanized steel lined with a vinyl lining. It is filled with ultra-pure water (UPW) from on-site purification systems. On the exterior of the steel shell is mounted a set of 48 veto PMTs, which detect Cerenkov

light in water from cosmic ray muons. The water provides neutron shielding from radiogenic and cosmogenic neutrons, as discussed in Section 2.2 on backgrounds.

2.4.1 Magnetic Compensation

The presence of magnetic fields across a PMT can reduce its collection efficiency, and thus observed light yield in PE per unit energy. In the presence of a magnetic field a photoelectron emitted from a PMT photocathode will deviate from its path to and miss the first dynode. A photoelectron emitted from one dynode can also deviate from its path and miss the next dynode.

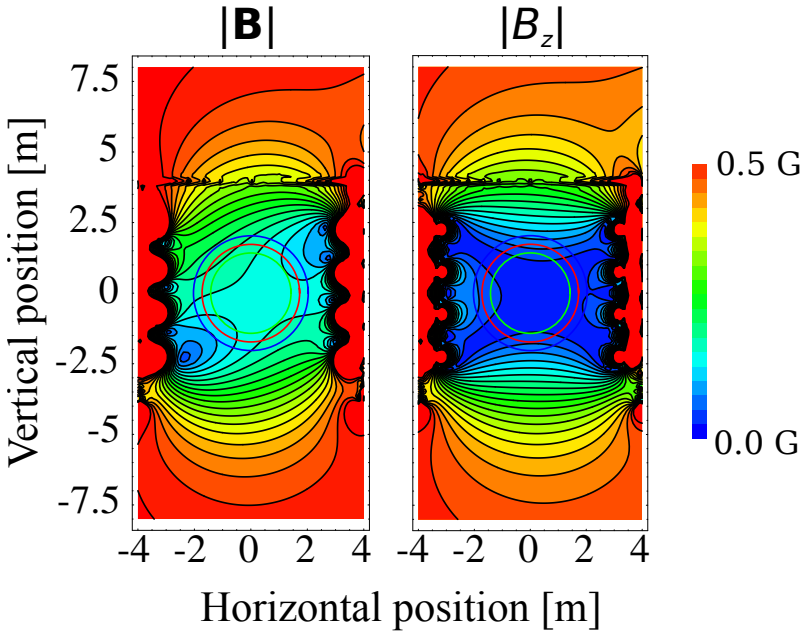

Figure 2.18: A plot showing the magnetic field strength magnitude $|\vec{B}|$ and vertical component $\vec{B}_z$ in the vicinity of the DEAP-3600 vessel, as calculated with Radia [137, 138]. Also shown are three circles representing the approximate locations of the muon veto PMTs (blue), the steel outer vessel (red), and the AV PMTs (green). Includes the effects of the ambient magnetic field as measured on site, the magnetic compensation coils of MiniCLEAN, located next to DEAP-3600 in their final constructed locations.

The magnitude and vertical component of the earth's magnetic field in the vicinity of DEAP-3600 is shown in Figure 2.18, as calculated using Radia [137, 138], with the location of the AV PMTs included for reference in green. The vertical $\vec{B}_z$ is compensated for using active magnetic compensation. Four identical submersible compensation coils are suspended from the water tank at elevations of z=±750 mm and z=±2250 mm relative to

the detector equator. A current is run through them to generate a compensating magnetic field. The resulting field cancellation reduces the collection efficiency loss in PMTs due to from 25% to 2%.

The horizontal $\vec{B}_{x,y}$ components of the earth's magnetic field are compensated for using passive shielding. Finemet foil shields are wrapped around the PMT mounts and light guides as shown in Figure 2.15, which reduce the collection efficiency loss from 2% to 1%.

2.4.2 Glovebox and Inner Neck

Access to the inside of the AV is provided by the glovebox, which is connected to the top of the AV neck, as shown in Figure 2.9 in Section 2.3.3. The glovebox ensures that the detector is never open to laboratory air. When deploying materials to and from the detector the glovebox space is purged with degassed nitrogen and evacuated before accessing the AV. A deployment canister is mounted on the glovebox when various sources are lowered into the AV before the installation of the neck inner components (which obstruct access). After the deployment of the resurfacer, internal calibration sources, TPB source and the inner neck components, only argon from the purification systems was transferred to and from the AV via the neck.

A cross section of the final neck configuration is shown in Figure 2.19. The outer neck is surrounded by a vacuum jacket to prevent heat transfer between warm outer vessel nitrogen in the steel shell and cold argon. Within the neck acrylic flowguides direct the flow of purified cool argon gas and liquid downwards towards the AV, and the flow of warm gaseous argon up towards the process systems. The two flows are separated by a combination of the flow guides and a flow separator tube. Inside the flow separator tube, cool argon gas flows downwards past a cooling coil located at the centre of the neck. The cooling coil consists of a stainless steel pipe with a vertical vacuum jacketed straight section surrounded by a bare coiled section. Liquid nitrogen is fed in through the straight section, and flows up the bare coiled section as it is warmed by argon outside the coil. The liquid nitrogen is stored in a separate storage dewar cooled using three Sterling

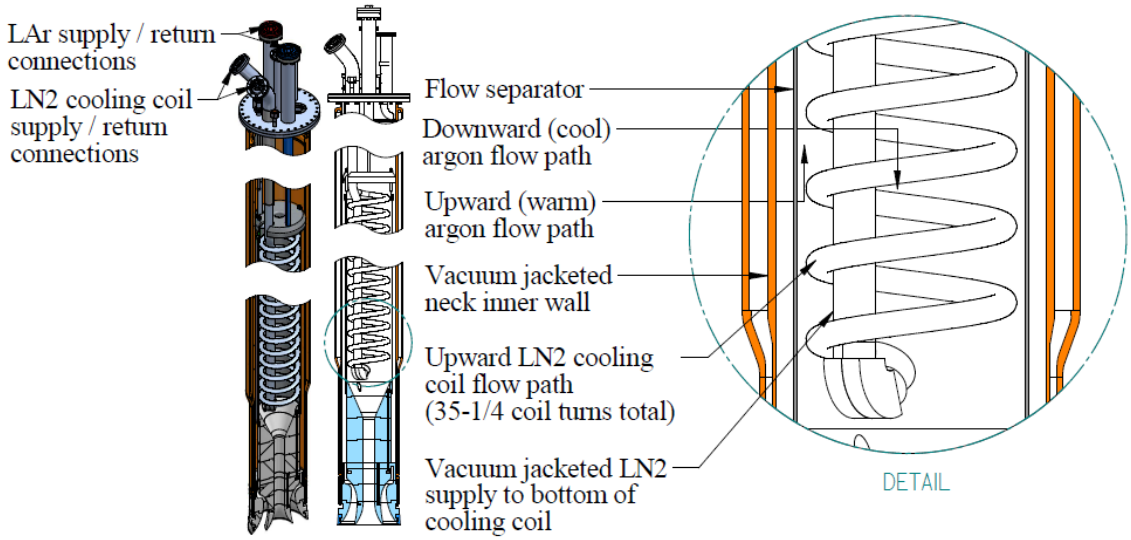

Figure 2.19: A schematic showing the apparatus within the AV neck. A cooling coil fed with liquid nitrogen is surrounded by a flow separator tube, which separates downward cold argon flow and upward warm argon flow together with flow guides at the bottom and top of the tube. A vacuum jacket is placed around the neck to reduce the heat load from the argon and the cabling in the outer vessel neck. Rendered by Koby Dering.

Electronics 1 kW cryocoolers. Warm argon gas returned from the AV flows up on the outside section of the flowguides, and at the top of the assembly steel flowguides can redirect the argon down the inner flowguide to be cooled, or the argon can be extracted to the purification systems to be purified, as described in the next section.

2.5 Purification Systems

The purification systems are designed to ensure the argon in the AV has a nominal electronegative impurity content of < 1 ppb, and a radon activity of ≤ 5 μBq. The effects that impurities can have on liquid nobles are discussed in Section 1.5.6.

2.5.1 Purification and Filling

The purification systems perform two types of filtration in two stages, listed below. Before purification, argon gas is heated to $\sim$300 K using a coil heater around a stainless steel heating unit. Afterwards, argon is cooled using a stainless steel condenser column containing liquid nitrogen. The argon is pumped through the systems using a KNF Neuberger

double diaphragm pump. The purification stages are described below:

Getter This is the contaminant removal stage - a reactive metal bonds with contaminant dimers and hydrocarbons incident on its surface. A SAES Mega-Torr PS5-MGT15 hot metal getter is used, which reduces contaminants to a level of < 1 ppb, and has a lifetime of 1 year of continual use, which is above the requirement for full running.

Charcoal filter This is the radon removal stage. The argon is cooled from 300K to 100K using a copper-wrapped coil with its base in liquid nitrogen, and passed downwards through a column containing 610 g of activated charcoal sandwiched between layers of steel wool, which holds it in place. A steel mesh and 50 μm filter prevents charcoal dust from exiting the radon trap. The argon is purified to a radon activity of ≤ 5 μBq.

The vessel was filled with liquid argon to its final fill level in October 2016. The first attempt at this fill failed upon liquid argon reaching the AV neck. It became apparent that the seals used in the flange that connects the acrylic vessel neck to the steel neck became colder than their operating temperatures and failed. Nitrogen in the steel shell was allowed to enter the AV, contaminating the argon at a level too high to filter out in the process systems. On heating and extracting the contaminated argon, the seal was verified to have closed. The second attempt filled to a final fill level $z = 551 \pm 30$ mm above the AV equator in September 2016. At 300 mm below the neck opening, the final fill level is far enough below the AV neck to prevent the same seals from reopening. The detector at the time of writing is filled with 3256.59 ± 111.91 kg of liquid argon.

2.6 Detector Readout

The detector readout is arranged in three separate components: the front end system, the data acquisition (DAQ) system and the digitiser and trigger module (DTM).

2.6.1 Front End

The purpose of the front end system is to provide and control the high voltage power supply to the PMTs, and direct the PMT output to digitisers via a set of signal conditioning boards (SCBs). There are 26 SCBs in total, 22 connected to the HQE R5912's, and another 4 connected to the water veto PMTs, with 12 channels per board (and 1 PMT per channel).

The high voltage supply is controllable via the DAQ computers. Automated controls increase the supply voltages up to the nominal PMT voltages when switching them on, and gradually decrease supply voltages when switching them off. The supply voltages are configured such that the PMTs have uniform gains of 10^7. Their uniformity is verified in calibration data as described in Section 2.7. Automated monitoring software shuts down a PMT if its observed pulse rate is observed to exceed 10^5 Hz.

The SCBs broaden the PMT signal in time by convolving the time dependent PMT current $I_{PMT}(t)$ with an exponential distribution:

$$I_{SCB}(t) = I_{PMT}(t) * \frac{1}{A}\left(\frac{t}{\tau}\right)^2 \exp\left(\frac{-t}{\tau}\right) \tag{2.2}$$

The constants $A = 1.0$ and $\tau = 4$ ns for SCB signals sent to V1720s and $A = 0.9$ and $\tau = 14$ ns for signals sent to V1740s. The V1720s have a faster sample rate than the V1740s and require less signal broadening to produce an equivalent number of samples per pulse as the V1740s, as elucidated in the next subsection.

The broadening from convolution increases the number of digitiser samples recording the rising edge of the pulse, which in turn enables pulse finding and charge estimation in analysis to take place over more samples. The signal is duplicated upon output from the SCBs: by default, the pulse is sent to a high gain CAEN V1720 digitiser board. The highest possible signal amplitude in the V1720 is 4096 ADU (analogue-to-digital units), and the baseline is set to 3900 ADU below the maximum amplitude, above which the signal is clipped. If a pulse height is observed that is high enough to cause clipping to occur in a V1720, it is outputted to lower gain CAEN V1740 digitiser boards, with the signal amplitude attenuated by an order of magnitude.

2.6.2 Data Acquisition

The digitiser boards consist of 32 CAEN V1720s with 8 channels each, reading out at a sample rate of 250 MS/s (megasamples per second), and 5 CAEN V1740s with 64 channels each, with sample rates of 65 MS/s. Both boards have a 12 bit resolution resulting in the maximum signal amplitude of $2^{12} = 4096$ ADU per sample. For comparison, a single PE pulse in a V1720 has an average pulse height of 50 ADU, so this bit depth allows for $\sim$82 coincident PE in a single pulse before clipping will occur in that channel. Each board has firmware that controls the readout of its buffers to 5 computers, with 4 computers dedicated to processing V1720 data, and another dedicated to processing V1740 data.

Both the V1720 and V1740 can read out full waveform data, but the V1720s also feature zero-length encoding (ZLE). ZLE functions in the same way as an analogue noise gate: the board begins transferring its buffers to the DAQ at any time a PMT signal intensity crosses a threshold above the signal baseline for an adjustable number of samples. A noise pulse has a mean height of 1.2 ADU, so the start threshold is set to 5 ADU above the baseline. The board then ceases reading out its buffers any time the signal intensity drops below a decay threshold for an adjustable number of samples, set as the same as the start threshold. Before and after each threshold 20 additional baseline samples (80 ns in 4 ns samples) are also read out to capture the pulse occasionally undershooting the baseline. For each ZLE block the boards record the charge in ADU above threshold, and block time information, and send this alongside block ZLE waveforms to the DAQ computers, where a software event builder merges the event data into a single event to be saved to file. The use of ZLE reduces the size of an event's output to the DAQ by an order of magnitude compared to full waveform output.

2.6.3 Digitiser and Trigger Module

The purpose of the digitiser and trigger module (DTM) is to decide when the digitisers should read out their buffers. The digitisers are synchronised with the 62.5 MHz master clock on the DTM, and records the event's clock time when triggered. The DTM logic is

adjustable by user and software: in every case it accepts input from a number of trigger sources and sends trigger output signals via Nuclear Instrumentation Module (NIM) outputs to a number of digitisers to send on the data in their buffers. It can also skip events periodically to accept one event per a user-configurable variable called the prescale factor. For example, a prescale factor of 10 means that only 10% of events are recorded.

In practice, the main types of trigger source used on the experiment are as follows:

Minimum Bias Triggers upon encountering a total signal intensity above a configurable threshold for a configurable number of bins, summed over a single SCB (analogue sum, or ASUM), or over any number of SCBs up to the entire set (sum of analogue sum, or ASUMSUM). Used for data taking during commissioning and optical calibration.

Periodic Generates a repeating set of triggers, either regularly spaced in time or with spaces between events according to an exponential distribution, mimicking the timing structure of scintillation events. Used for the study of pile up events and to control optical calibration sources, where a regular periodic trigger simultaneously instructs the optical calibration source to output light and the digitisers to read out their buffers.

External Triggers based on a signal connected to a NIM input on the DTM from, for example, synchronised calibration sources. In the case of the veto PMTs, a single V1740 connected to the veto PMTs sends a signal via NIM output to the DTM when more than eight veto PMTs see light simultaneously, which provides the coincidence trigger from the water veto during physics data taking.

PPG A further pulse pattern generator (PPG) board produces a regular set of pulses distributed to a test channel on each SCB, which duplicates the pulse in each SCB channel. This is used to monitor the behaviour of the SCBs and digitisers independent of the state of any individual PMT.

Physics An online software trigger is used for physics data taking, described below.

The online physics trigger is designed to prescale events for which there is a high expected background rate, whilst not prescaling on WIMP-like events. Prescale factors are set according to the observed photoelectron count, and the ratio of the charge observed in a short window to that in a long window, $F_{prompt} = Q_{short}/Q_{long}$. Typical window sizes are 177.2 ns and 3101 ns respectively. The $F_{prompt} < 0.5$ region is prescaled to reduce the $^{39}Ar\ \beta^-$ rate read by the DAQ. Events with $F_{prompt} > 0.5$ near the energy region of interest are recorded 100% of the time. Low energy events far below the region of interest are discarded, and high energy events far above the region of interest are prescaled. The DAQ trigger settings that are used in analysis in later chapters are summarised in Section 3.1.3, alongside their analogues in the simulated DAQ.

2.7 Calibration Systems

The calibration systems are divided into two separate types: internal optical calibration sources and external radioactive decay sources. The optical calibration sources use controlled light at known positions and wavelengths to parametrise the response of the PMTs and the detector optics, which informs our simulation and event reconstruction. This is performed repeatedly as changes to the detector occur with time during commissioning and as slow changes are observed in stable conditions during data taking. Radioactive sources are used to produce nuclear and electronic recoils within the detector's active volume, such that the response to both can be monitored over time. In addition, both types of calibration system can be used to quantify and monitor the performance of position and energy reconstruction.

2.7.1 Optical Calibration

The AARF System

The acrylic and aluminium reflector and fibre-optics (AARF) system is used to inject light into the detector during dedicated runs over the lifetime of the detector. The AARF system assembly is shown in Figure 2.20. Light from a 435 nm LED is directed along

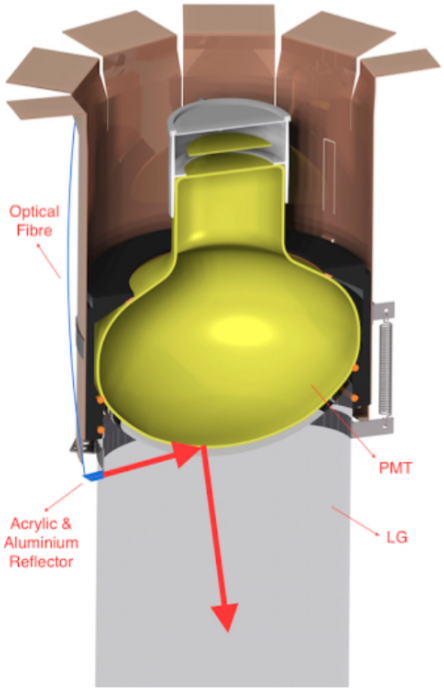

Figure 2.20: A rendering showing the AARF system installed on a light guide. Large arrows in red show an example of a possible light path from the AARF acrylic stub, reflected from the PMT and down the light guide towards the AV. Rendered by Koby Dering.

fibre optic cables into 20 light guides uniformly distributed about the detector, and into 2 opposite sides of the neck. The fibre is bonded to an acrylic stub, which is bonded to the acrylic. In the case of a light guide 80% of LED light is observed in the AARF PMT, and the remaining 20% is reflected from the PMT glass into the detector.

The LED is driven by a pulse generator which pulses at a rate of 1 kHz. The data acquisition trigger module is synchronised with the pulse generator to ensure that data is read out as light pulses are generated and that each light pulse is a separate event. Only PMTs pulses that are observed between -24 ns and +44 ns relative to the AARF trigger are accepted.

The intensity of the AARF is described using the occupancy in the PMTs which are non-adjacent to the AARF light guide. The occupancy of a PMT is defined as the fraction of events for which 1 or more photoelectron is observed in that PMT. The AARF was operated at intensities which correspond to mean occupancies of 5% and 15% in non-AARF PMTs.

The occupancy in each PMT for a 5% occupancy AARF run is shown in Figure 2.21 as

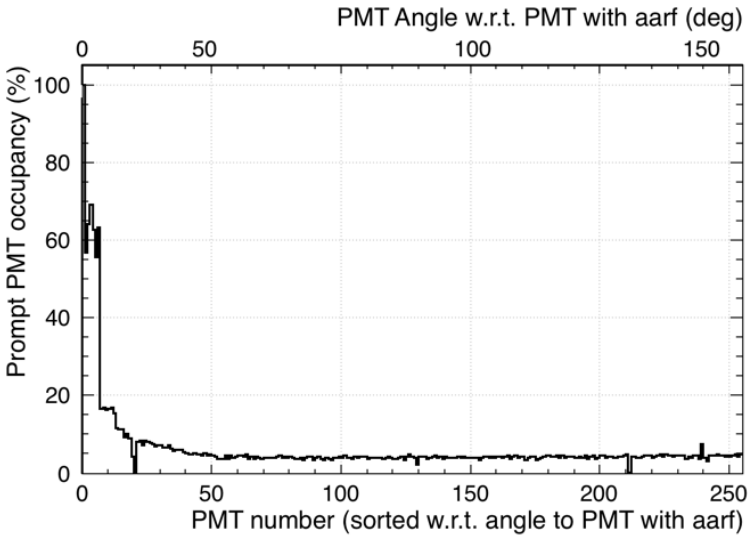

Figure 2.21: Prompt occupancy vs PMT angle from the AARF PMT. Occupancy is calculated as fraction of events for which a PMT sees 1 or more PE. Prompt occupancy only accepts PE from pulses detected within -24 ns and +44 ns of the DAQ trigger. PMTs are sorted in order or ascending angle to the AARF PMT. Two PMTs are disabled due to problems at time of data taking. Plot prepared by Berta Beltran.

a function of the angle between that PMT and the AARF PMT. Occupancy is observed to decrease in PMTs at higher angles away from the AARF PMT, reaching an approximately constant 5%. In 5% occupancy runs, on average only a single photoelectron per hit PMT is observed in PMTs furthest from the AARF.

Single PE Charge Calibration

The AARFs are used to record and model the single PE charge distributions of the PMTs, as described by the collaboration in Ref. [132]. The result of this calibration is summarised as follows.

PE multiplication at each dynode in the chain is a Poisson process. PE production from the first dynode is a sequence of Poisson processes with fluctuating rates, due to incomplete collection and multiplication of the primary PE produced by the photocathode. A sequence of Poisson processes is described by a Polya distribution, which approaches a Gamma distribution for many produced PE.

An example single PE charge spectrum as measured using the AARFs is shown in Figure 2.22. The SPE charge distribution is obtained by fitting to the data using the sum

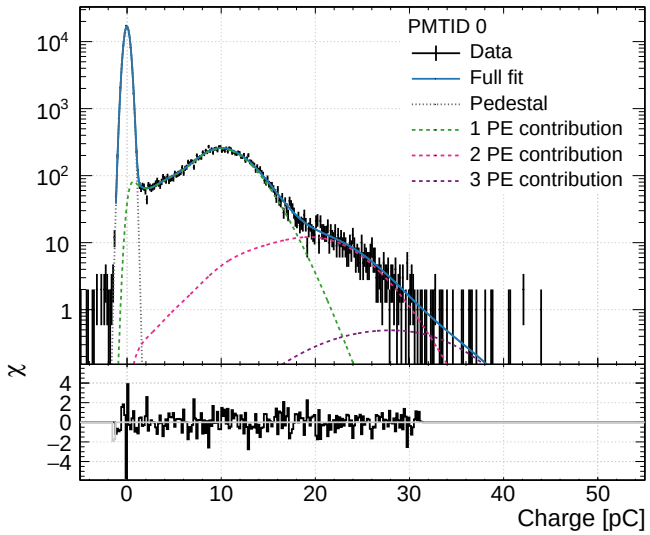

Figure 2.22: A single PE (SPE) charge spectrum in pC for pulses within a 68 ns window. Vertical axis shows the number of pulses observed with a charge on the horizontal axis. Produced using the AARF on a PMT on the top ring of PMTS nearest the neck. Full waveform data was taken (without ZLE) with 15% occupancy in the AARF PMT. The fitted function, shown in blue, is described by equations 2.3-2.5. The pedestal Gaussian (grey dotted), single (green dotted) and multiple (pink and purple) PE contributions to the fit are shown under data (black with error bars). Shown below is the difference in between function and data. The function fits the data with a χ^2 per number of degrees of freedom at $\sim$1. Plot prepared by T. Pollmann, reproduced from Ref. [132].

of two Polya distributions and an exponential term. The first Polya distribution models charge produced by the primary PE reaching the first dynode. The second models charge due to the primary PE from the photocathode reaching the second dynode and producing incomplete electron multiplication. An exponential term describes the photoelectron scattering on a dynode multiple times, such as in the double pulse as explained in Section 2.3.6. The total single PE charge distribution model is given by:

$$\text{SPE}(q) = \eta_1 \text{Gamma}(q;\mu,b) + \eta_2 \text{Gamma}(q;\mu f_\mu, b f_b) + \begin{cases} \eta_3 l e^{-ql} & \text{for } (q < \mu) \\ 0 & \text{for } (q > \mu) \end{cases} \quad (2.3)$$

where η describes the amplitude of each component such that the distribution is normalised to 1. The parameter μ is the mean, and b controls the width, of the first gamma distribution. The μf_μ and $b f_b$ in the second gamma distribution are relative to μ and b, controlled by the f terms which are floated in the fit. The gamma distribution in this

notation is given by:

$$\text{Gamma}(q;u,b) = \frac{1}{b\mu\Gamma(1)}\left(\frac{q}{b\mu}\right)^{\frac{1}{b}-1}\exp(\frac{-q}{b\mu}) \tag{2.4}$$

The full fit also includes the noise pedestal: a Gaussian function to account for charge fluctuations from electronics noise in PMTs that see zero PE. The charge observed in a PMT that observes n PE is the sum of a charge drawn randomly from the pedestal and n charges drawn randomly from SPE charge model SPE(q). Thus the charge distribution for n PE is given by SPE(q) convolved n times with the pedestal function Ped(q). The total charge distribution observed in a PMT that observed a mean λ PE over a set of AARF events is fitted using the sum of a set of n PE components weighted by the Poisson probability of seeing n PE given a mean PE λ observed in each hit PMT:

$$\begin{aligned} f(q) =& B\cdot[A\cdot\text{Ped}(q)+\text{Poisson}(1,\lambda)\cdot\text{Ped}(q)\otimes\text{SPE}(q) \\ &+\text{Poisson}(2,\lambda)\cdot\text{Ped}\otimes\text{SPE}(q)\otimes\text{SPE}(q)+\ldots] \end{aligned} \tag{2.5}$$

where the noise pedestal normalisation A is floated in the fit alongside the parameters in SPE(q).

The variation with time during commissioning of the mean single PE charge μ in the AARF PMTs closest to the neck of the AV is shown in Figure 2.23. The mean single PE charge increased as the detector cooled during commissioning and filling and has since stabilised after the fill in the conditions under which physics data is taken.

AARF data is collected monthly and the parameters from the function fitted to the data each month are stored in a CouchDB database. The charge model in simulation is also updated to match the measurement from data. Charge-based position reconstruction algorithms can use single photoelectron charge distributions as part of their model as discussed in Chapter 4. The position reconstruction automatically accounts for the variation of the parameters of the single photoelectron model with time by requesting them from the database.

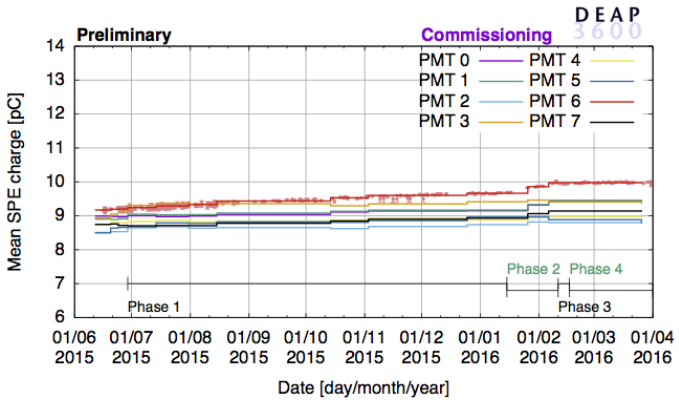

Figure 2.23: The variation of mean single PE charge with time for a group of 8 PMTs at the top of the detector. One representative PMT (no. 6, in red) is shown with the mean SPE charge determined from the AARF monitoring runs that occurred over this period, and error bars representing the parameter errors from the fit depicted in Figure 2.22. The time axis begins on 1st June 2016. A slight upward trend is observed for most PMTs over the course of the year depicted. Discontinuities in the mean SPE charge occur at times when the PMTs were powered down and back up. The environmental conditions changed a number of times, as depicted on the plot: Phase 1: AV under vacuum with TPB deposited and compensation coils on; Phase 2: in addition, water shielding tank is filled with chilled water; Phase 3: AV filled with argon gas at room temperature; Phase 4: Cool down phase with increasingly cold argon gas. Plot prepared by T. Pollmann.

The Laserball

The laserball was deployed once after the deposition of the TPB source. The laserball consists of a laser head attached to a fibre, which terminates at an acrylic stub light guide within a PerFluoroAlkoxy plastic flask containing 50 μm glass beads suspended in silicone gel. The flask as shown in Figure 2.24 is designed to emit pulses of UV light isotropically after repeated light scattering within the silicone gel. The laser is driven using a Hamamatsu PLP-10 picosecond light pulse generator and a set of laser diode heads that emit at 375 nm and 445 nm. The data acquisition trigger module is again synchronised with the pulse generator to ensure that data is read out as light pulses are generated, and that each light pulse is a separate event. The distribution of peak times of pulses in PMTs relative to the trigger time is shown in Figure 2.25, with a total range of 3.5 ns.

During deployment the laserball was attached to a support assembly, and suspended at an adjustable height within the AV. The laserball was deployed within the AV after TPB deposition, with the AV filled with N_2 gas at 20.28 PSIA to prevent the propagation to the TPB surface of recoiling daughters from the decay of radon on the laserball flask

Figure 2.24: The laserball driven by the 445 nm laser head, photographed during ex-situ testing by N. Fatemighomi.

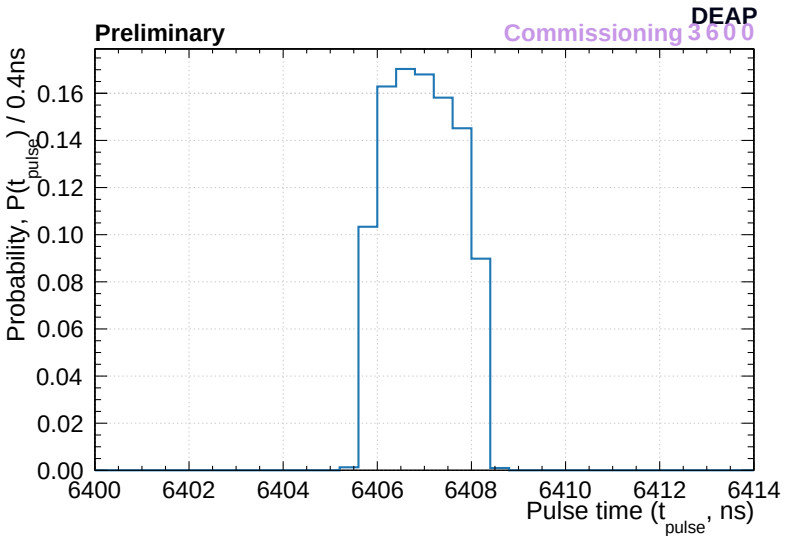

Figure 2.25: Pulse time from every PMT measured relative to the start of the DAQ event waveform. Data was taken with the laserball at the centre of the detector, using the 445 nm laser diode. The pulse time has been corrected for SCB channel timing offsets, and timing offsets from varying PMT cable lengths for each channel. Plot prepared by F. La Zia.

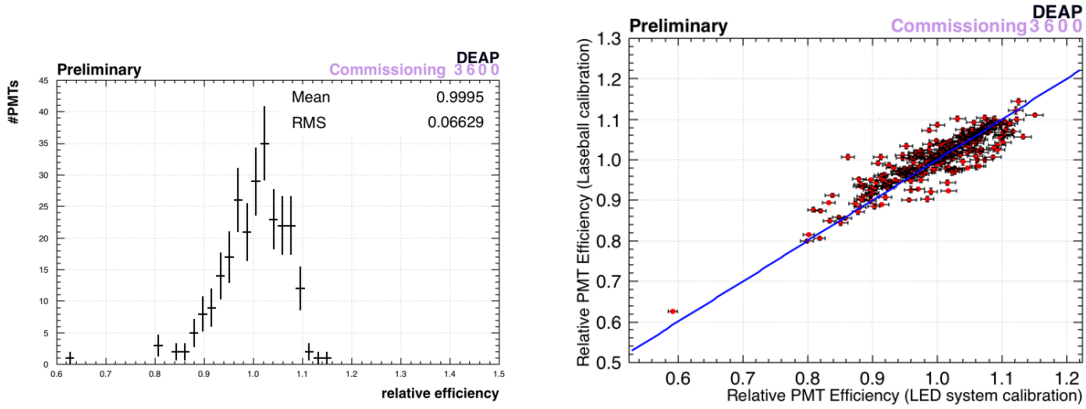

Figure 2.26: Left: Relative efficiencies of the PMT array obtained by averaging the relative efficiencies obtained four data sets taken with the laserball at the centre of the detector, separated by rotation angle $\Delta\phi_{LB} = \pi/2$. Vertical axis is the number of PMTs with relative efficiency observed in each 0.02 wide bin. Right: A plot comparing the relative efficiencies obtained from the laserball data to those obtained from AARF data, where an efficiency of 1 is defined for a single PMT. Plots prepared by R. Mehdiyev.

material. Data was taken with the laserball placed at the centre of the $x-y$ plane, at three elevations of $z = 0$ mm and $z = \pm 550$ mm relative to the equator of the detector, and rotated to four positions separated by rotation angle $\Delta\phi_{LB} = \pi/2$. The error on each elevation is estimated at ± 50 mm, and the error on each rotation is estimated at $\pm 8^{\circ}$.

The laserball data was used to estimate and correct for timing offsets between recorded PMT pulse times. Channel-to-channel timing offsets are produced in 8 ns intervals by the SCB electronics. The variation in PMT cable length produced variable offsets for different PMTs around the detector. The offset was measured using the laserball at $z = 0$ mm such that the transit time, and distance to every PMT, of photons leaving the laserball surface is equal. The pulse time distribution that is corrected by subtracting the offsets is shown in Figure 2.25. The width of the pulse time distribution is 3.5 ns.

The laserball was also used to calculate the relative variation in PE production efficiency due to the combination of PMT collection efficiency and individual light guide optical effects. The laserball was placed at the centre of the detector. The variation in occupancy with PMT ID was recorded, and fitted with a straight line, an example of which is shown in Figure 2.26. PMT ID's are indexed from the PMT closest to the neck to the PMT furthest from the neck with increasing ID number. The efficiency is recorded as

the ratio of observed occupancy to the fitted line, and averaged over four rotated positions of the laserball separated by rotation angle $\Delta\phi_{LB} = \pi/2$. Mean relative efficiencies measured using the laserball are shown in Figure 2.26. These efficiencies are recorded and applied in simulation, and compensated for in position reconstruction as discussed in Chapter 4. Importantly the laserball is the only calibration source placed at a known location within the AV, so it can be used to demonstrate that the position reconstruction functions correctly, as discussed in Chapter 5.

2.7.2 Radioactive Source Calibration

The radioactive sources are deployed periodically over the course of the commissioning of the detector and during stable running, in order to calibrate the energy reconstruction, pulse timing and position reconstruction in the detector. Two sources are used to this end: an AmBe neutron source, which produces WIMP-like nuclear recoils; and a ^{22}Na gamma source, which produces electronic recoils.

A ^{22}Na gamma source is used to produce electronic recoils in argon for calibration of the energy resolution of the detector, which at time of writing is estimated to undergo gamma decay at a rate of 333 kBq. The source emits a 1.27 MeV photon, which is of sufficiently high energy to be detected in the argon after scattering in intermediate materials. The positron from the ^{22}Na β^+ decay annihilates with a nearby electron in the source to produce two 511 keV photons in opposite directions, which are detected and used for tagging of a decay event.

The gamma source is placed at the centre of a cylindrical stainless steel canister, which houses on either side a tagging system composed of two 8.5 mm thick scintillator crystals, made of Cerium-doped Lutetium Yttrium Orthosilicate (LYSO), and behind each a compact Hamamatsu R9880U PMT. Two cable housings either side of the canister enclose the PMT cables and a steel umbilical attached to the canister which ensures that any force applied on the cabling is exerted on the canister, not the PMT or its connection.

A 74 MBq AmBe neutron source is used to produce nuclear recoils. The ^{241}Am undergoes alpha decay. The alpha undergoes alpha capture in a ^{9}Be nucleus, which stimulates

neutron production and creates an excited ^{12}C. The excited ^{12}C de-excites to produce a 4.4 MeV photon. The neutron source is placed at the centre of a cylindrical steel canister. On either side of the source is a 51 mm thick NaI scintillator crystal, in front of a 38 mm ETL 9102 PMT. The PMT detects scintillation in NaI from the 4.4 MeV photon which is used to tag a neutron decay.

The sources are deployed into the calibration tubes shown in the drawing in Figure 2.27. The neutron source is deployed into three vertical tubes, Cal A, B and E, which are at closest to the steel shell at the equator. The gamma source is deployed into Cal F, which is mounted on rails attached to the steel shell and which crosses over at the neck.

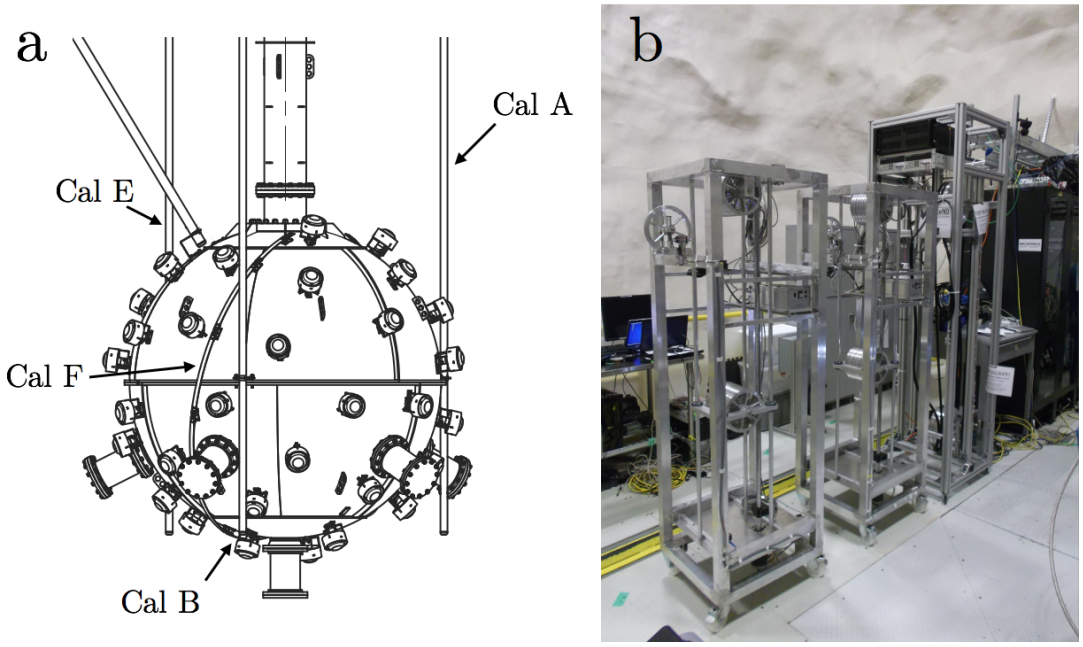

Figure 2.27: a) A drawing showing the calibration tubes. Three vertical tubes, Cal A, B and E allow sources to be deployed close to the equator, and Cal F allows sources to be deployed at points around the detector, and close to the neck. b) A photograph showing the two gamma calibration racks on the left and the neutron calibration rack on the right.

2.8 Conclusion

The design of the DEAP-3600 detector was motivated by background reduction, which is achieved through material selection, preparation and handling during construction and commissioning. The content in this chapter provides an overview of the detector as a

whole and the backgrounds the detector is designed to mitigate. The remainder of background mitigation is performed in analysis, and the success of that undertaking is dependent on a detailed simulation of the detector. In the case of the alpha backgrounds, position reconstruction is of paramount importance, and accurate position reconstruction relies heavily on detector simulation. That simulation is described in the next chapter.

Chapter 3

Simulation, Analysis and Optics

This chapter discusses the simulation of the DEAP-3600 detector. The simulation and analysis software is described. The PMT electronics and DAQ simulation is described, which produces data which mimics real detector data. The analysis variables from event reconstruction which are used in later analysis are also described. The detector optical model is then discussed, which the reconstruction model relies on to model the effect that the variation of the position of a point-like scintillation event has on the response of the PMT charge readout. The effect of variation of the optical model on those parameters which affect the variation of PMT charge with position is discussed, using simulation and data from the AARF calibration source and uniform ^{39}Ar background.

3.1 Simulation

In this section, the detector simulation is discussed. The Reactor Analysis Tool, or RAT, software package has been adapted for use in simulation and analysis in DEAP-3600. RAT was originally designed by Stanley Seibert for spherical liquid scintillator experiments instrumented with PMTs. A generic open-source version is available at Ref. [139]. The software package provides a framework which enables Monte Carlo simulation of a detector and data analysis to take place in the same software and in the same instance. The software also provides a command-line interface which can be scripted.

RAT uses GEANT4 to simulate the geometry of the detector as-built, using a plain-

text JSON-like table structure as a macro file to interface with GEANT4 geometry classes. Material and optical properties are encoded in the same way. Any geometric, optical or material property of the detector can be changed by the user in a single line in a RAT script as necessary. Particle and particle-material interactions are then handled in GEANT4. The simulated detector is shown compared to the detector as constructed in Figure 3.1. The top images compare the AV and light guides without PMTs and filler blocks installed. The middle images compare the AV with PMTs, copper shorts and filler blocks installed. The bottom image compares the steel shell in simulation with the AV enclosed, without calibration tubes, to the detector before the water tank was filled with water.

3.1.1 Optical Model

There are two aspects of the optical simulation that must be elucidated to inform the discussion ahead. The first of these is that Rayleigh scattering length and attenuation length are treated analogously, according to the Beer-Lambert Law. The Beer-Lambert law states that for light incident on a material boundary the probability of finding a photon that has not undergone scattering at a depth x into the material is given by $P(x) = exp(-x/l)$. The scattering or attenuation length l in a simulated material determines the distance at which a fraction $1/e$ of propagating photons will have passed without scattering or being absorbed. The user specifies a wavelength-dependent l and the probability that a particle will scatter or be absorbed.

The second is the way in which light propagates at the boundary between materials. Two surface types are used in simulation. The 'polished' surface type performs specular reflection and refraction according to Snell's law and models an ideal, completely smooth surface. The 'ground' surface type incorporates a model of diffuse reflection from a rough surface. For each interaction with a boundary the surface normal is modified by a uniformly distributed deviation angle θ as shown in Figure 3.2 with a maximum angle to the normal of $(1-a) \times \pi/2$, where the constant a is a scaling factor set by the user. The 'ground' model reduces to the 'polished' model for $a = 1$.

The scintillation process in liquid argon is performed using a class in RAT which in-

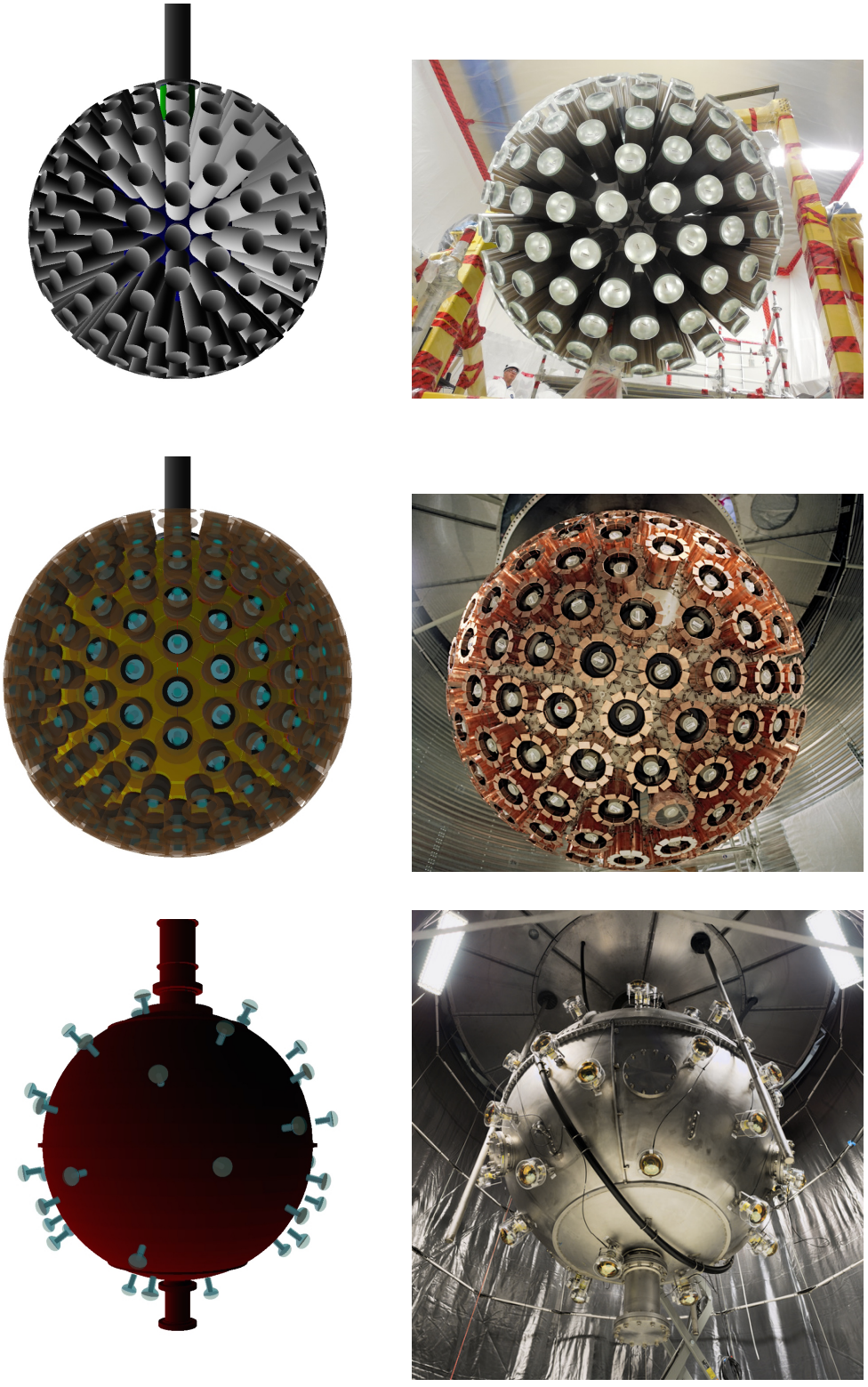

Figure 3.1: Comparison of ray-traced simulated detector renderings to photographs of the as-built detector. The depictions show the detector before PMT installation, after the installation of filler blocks, and after closing the steel shell. Ray traced images from Ref. [140]. Photographs by Mark Ward and other collaboration members on shift.

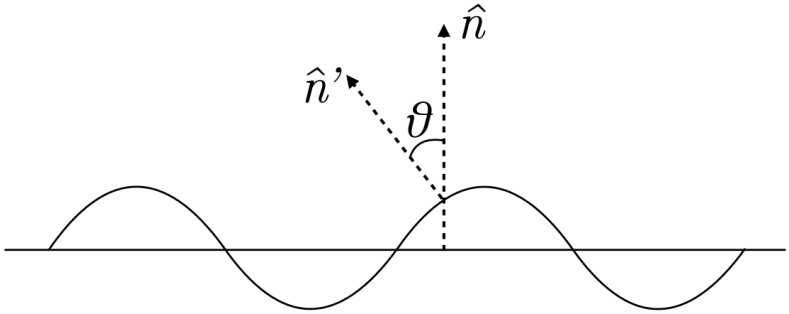

Figure 3.2: A drawing showing the effect that a rough surface in the 'ground' surface model would have on the surface normal, deviating it by the angle $\theta = \hat{n} \cdot \hat{n}'/|\hat{n}||\hat{n}'|$. The condition $\hat{n} = \hat{n}'$ represents the 'polished' surface model.

terfaces with GEANT4, according to the scintillation model described in Section 1.5.2. Because the scintillation light yield is dependent on dE/dx, the simulation tracks energy loss with each GEANT4 step of the track of a particle propagating in the medium. The scintillation photon yield is then calculated after the track has terminated according to the model outlined in Section 1.5.5, and scintillation photons are simulated. Energy dependent quenching is implemented according to the SCENE measurement in Ref. [116], with a quenching factor varying from $L_{eff} = 0.235$ at 10.3 keV$_r$ to $L_{eff} = 0.295$ at 57.3 keV$_r$. Photon emission timing is simulated according to the liquid noble scintillation timing PDF as described in Section 1.5.3. The double exponential relative weightings and time constants are implemented according to the values obtained in Table 2 in Ref. [108]. The wavelength-dependent refractive index of liquid argon is implemented in simulation as the curve shown in Figure 3.3. The curve uses the extrapolation to lower wavelengths in Ref. [141] from liquid data in the range 361.2-643.9 nm in Ref. [142], with $n = 1.45 \pm 0.07$ at 128 nm [141]. The wavelength-dependent Rayleigh scattering length model is implemented in simulation as the curve shown in Figure 3.4. The scattering length model also uses the extrapolation in Ref. [141], with $l = 55 \pm 5$ cm at the triple point at 87 K for $\lambda = 128$ nm light [141].

Scintillation photons propagate to the TPB layer and are absorbed and re-emitted via a TPB wavelength-shifting process implemented using a RAT interface class. When the wavelength shifting process occurs the incident photon is terminated, and a re-emission photon is generated with wavelength drawn randomly from the wavelength spectrum mea-

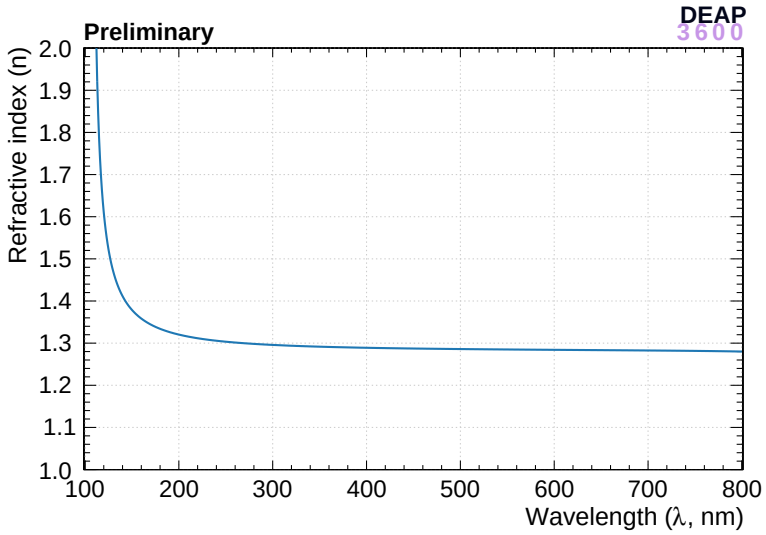

Figure 3.3: Variation of the liquid argon refractive index (n) with wavelength (λ), as implemented in simulation. The curve in blue is reproduced from the extrapolation in Ref. [141].

surement in Ref. [130] shown in Figure 2.13 in Section 2.3.5. The TPB coating is simulated as a uniform 3 μm spherical layer on the AV inner surface based on the calculation in Ref. [131] and the observation that a test deposition using the same apparatus in a smaller prototype spherical vessel produced a uniform coating with no macroscopic features. This may not be true in the larger DEAP-3600 vessel, and the optical calibration systems will be used to measure any non-uniformity the TPB layer may exhibit. The sanded surface model is implemented for the Ar-TPB and TPB-acrylic interfaces. The TPB scintillation yield of 882$\pm$210 photons/MeV from the measurement in Ref. [124] is implemented in simulation. The TPB re-emission timing PDF is implemented as a double exponential, with weightings and time constants implemented from measurement in Ref. [108].

A recent measurement by Stolp *et. al.* [143] estimates that the Rayleigh scattering length in TPB is within the range $2-3$ μm, and the best fit scattering length was observed at 2.75 μm. At time of writing it is the only measurement of its kind. The Stolp measurement uses a light yield correction to account for differences between the observed light yield from the apparatus and that in simulation. The difference is attributed to the surface roughness model in the GEANT4 simulation used during the study, where the TPB-air and TPB-substrate surfaces are modelled as a perfectly smooth surface, and cause transmitted light to leave the surface at angles not detected by the apparatus. Studies comparing the

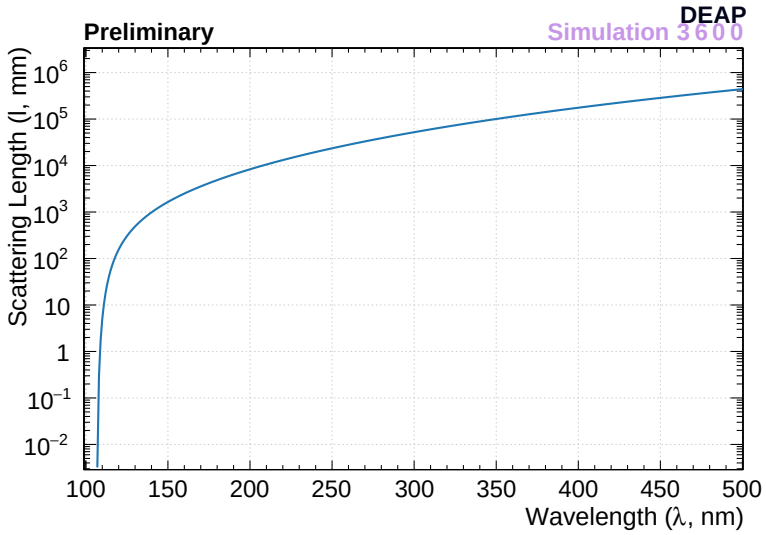

Figure 3.4: Variation of the liquid argon scattering length (l) with wavelength (λ), as implemented in simulation. The curve in blue is reproduced from the extrapolation in Ref. [141].

DEAP-3600 simulation to data observed a best fit scattering length of 3.73 μm for 440 nm light. The wavelength-dependent TPB scattering length implemented in simulation is shown in Figure 3.5. From this curve for light with the peak AARF wavelength of 435 nm the scattering length in TPB is 3.57 μm, and for light with the peak laserball wavelengths of 375 nm and 445 nm the scattering lengths in TPB are 2.04 μm and 3.89 μm respectively. Before the Stolp measurement took place, the TPB scattering length was set to 1 μm at all wavelengths as a place-holder. The simulation is compared to data for varying TPB scattering lengths in Section 3.3.

Re-emission photons are propagated through the acrylic before they reach a PMT photocathode. Based on bench-top measurement of acrylic samples [128] the acrylic is modelled as having negligible Rayleigh scattering, and any scattering is modelled as absorption. The simulation uses the wavelength-dependent attenuation length in AV acrylic as measured using a spectrometer in Ref. [128], shown in Figure 2.7 in Section 2.3.1. At the TPB wavelength spectrum peak the AV acrylic attenuation length is 3.5 m, more than an order of magnitude higher than the $>$ 5 cm AV thickness. The wavelength-dependent attenuation length of light guide acrylic is implemented as shown in Figure 2.8 in Section in 2.3.1, as measured using a spectrometer by P. Rau for the collaboration. At 440 nm the light guide acrylic attenuation length is measured at 6.157$\pm$0.595 m, again an order

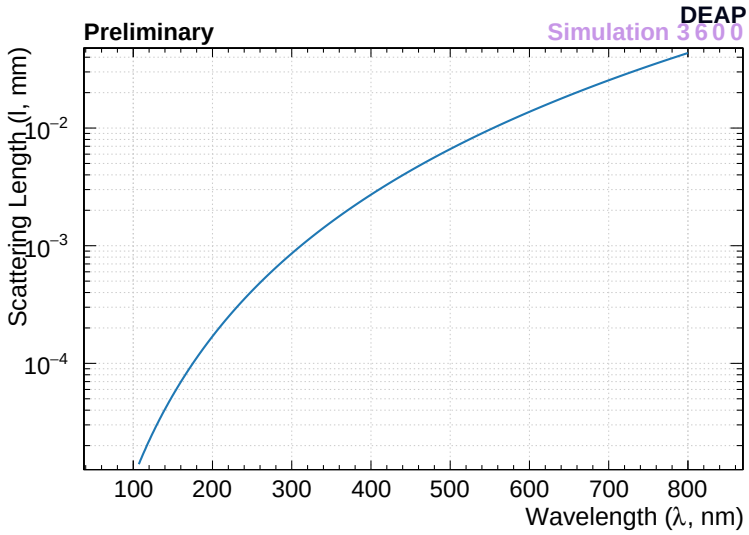

Figure 3.5: Variation of the TPB scattering length (l) with wavelength (λ), as implemented in simulation.

of magnitude higher than the light guide length of 45.6 cm. At the PMT end of the light guide the PMT geometry is simulated without the gap filled with silicone oil which is present on the detector as built.

3.1.2 PMT Simulation

When a photon reaches a PMT photocathode it is terminated and the PMT simulation is performed. The simulation of PMT photoelectron dynamics is handled separately by a RAT class according to the characterisation of the HQE R5912 PMTs in Ref. [136], discussed in Section 2.3.6. Photoelectrons are created and reach the dynode at a mean 25.26 ns later. The pulse timing is calculated by selecting the pulse type according to the probability of prompt, late, double and early pulses occurring. The pulse time is then offset by a time drawn from the pulse type's transit time PDF as shown in Figure 2.17 in Section 2.3.6.

The light guides and PMTs are each assumed to have exactly the same geometry, and optical and electronic properties. In situ measurements of the light guide and PMT efficiencies using the laserball and AARF system, described in Section 2.7.1, are implemented in simulation as changes to the photoelectron production efficiency in each PMT.

The time-dependent PMT current of the pulse is implemented using the double and

triple log normal model from Ref. [136], described in Section 2.3.6. The overall charge of a single PE pulse is drawn from the single PE charge distribution with parameters obtained using the AARF system, as described in Ref. [132] and Section 2.7.1. The measured variation in single PE charge from PMT to PMT is implemented in the single PE charge model in simulation. Noise pulses are distributed uniformly in time as a Poisson process, with pulse charges drawn from the single PE charge distribution.

3.1.3 DAQ Simulation

The DAQ simulation is designed to have the same properties as the real DAQ as described in Section 2.6. The waveforms from the PMT simulation are passed to the SCB simulation. The SCB response is modelled using a fast Fourier transform convolution with the PMT waveform according to Equation 2.2 in Section 2.6.1. The electronic waveforms are passed to classes which simulate the V1720s and V1740s and digitise the waveform using the same 4 ns bin width as the digitisers. Likewise, the ZLE feature in the V1720s is simulated such that ZLE blocks can be saved. Like the in-situ digitisers, the digitised ZLE blocks or full waveforms are saved in a ROOT file in the same tree structure which is filled by the real DAQ during data-taking.

The DTM simulation extends to a trigger simulation that behaves analogously to the real trigger. Simulated trigger settings are implemented that use the same charge thresholds and trigger timing responses as the real DAQ. The physics trigger is simulated analogously to the real physics trigger. The simulation begins at the generation of the primary particle in the event, such that events from the laserball and AARF, whose triggers are synchronised with pulse generators, are simulated by triggering on events which observe 1 or more PE. Trigger settings used in the analysis of real and simulated data in later chapters are summarised below. Each setting is indexed by a number in parentheses, used by the DAQ operator during data taking.

AARF run External trigger using NIM input from AARF pulse generator. ZLE waveforms in a 16 μs event window. In simulation the AARF pulses at beginning of MC event and the DAQ triggers on observing >0.5 PE.

Physics run Physics trigger, using ZLE waveforms in a 16 μs event window. Trigger on observing >23 PE in any given 144 ns. Prescales events which observe > 140 PE in 144 ns prompt window and $F_{prompt} < 0.5$ by factor 100. Prescale events which observe >1628 PE and any F_{prompt} by factor 1000. In simulation an analogous trigger setting is implemented with the same window lengths and F_{prompt} boundaries, but without the use of prescale factors.

^{22}Na physics run Used in conjunction with ^{22}Na source. Trigger on observing > 23 PE in any given 177.12 ns. Prescale all events by a factor 15, irrespective of energy and require $F_{prompt} < 0.5$. In simulation an analogous trigger setting is implemented, without the prescale factor.

3.2 Analysis

RAT can accept as an input raw waveforms in ROOT files from either the simulated or real DAQ and perform analysis on them interchangeably. For real detector data, once waveform data exists in the RAT data structure in a ROOT file, RAT analysis is automatically performed on a cluster computing platform. RAT analysis is compartmentalised into a set of event processors ordered into a dependence hierarchy, with low-level processors such as calibration and pulse finding, followed by higher level-processors which depend on pulse charge and time information, such as position reconstruction.

The pulse finding depends on calibrated constants such as channel-to-channel timing offsets produced by the DAQ and electronics, which are calibrated using pulse information. The data processing solves this problem by performing pulse finding twice, once for calibration, and once for final processing. The variables produced in subsequent higher level processing that are relevant for position reconstruction and analysis in this and subsequent chapters are discussed here.

3.2.1 Charge

The reconstructed charge in a PMT depends on pulse finding and charge calculation. Pulse finding is performed using a derivative pulse finding algorithm, which takes as its input raw waveforms and produces pulse objects containing timing and charge information. The pulse finding also identifies multiple overlapping pulse shapes which appear in >10 PE pulses, and identifies PE times within the pulse with sub-ns precision.

The charge in each PMT is calculated by integrating the charge above baseline in each pulse found by the pulse finder. A hit PMT is counted as a PMT which observed a pulse with a peak time within the event window. The number of hit PMTs is referred to as N_{hit}. The PE count produced by dividing the charge in each PMT by its fitted single PE charge is referred to as q_{PE}. In the first result the light yield using q_{PE} is quoted at $7.36^{+0.61}_{-0.52}$(fit systematics)$\pm$0.22(SPE systematics) PE/keV$_{ee}$ [3] where, the first errors are produced by the light yield fit and the second are produced by the error on the single photoelectron charge fit. In simulation the light yield using simulated PE is 7.1 PE/keV$_{ee}$, which is within the error on the stated result. An alternative PE count estimate comes from Bayesian single PE counting. Bayesian PE counting is described in Ref. [144]. An after-pulse tagging processor has been developed which, when tested using simulated afterpulsing can reproduce the number of simulated non-afterpulsing PE to within 0.05% error. The PE count in a PMT from Bayesian PE counting is referred to as n_{PE}. The Bayesian PE count with afterpulsing PE removed is referred to as n_{SC}, as afterpulsing removal leaves only scintillation PE. Particularly strong afterpulsing in a given PMT can bias position reconstruction towards that PMT, and in position reconstruction analysis in subsequent chapters the variable n_{SC} is used as the default PE count variable.

3.2.2 Data Quality

A number of cut constants are stored which are used to prevent pathological events being observed in a dataset. The common list of cuts used are listed below.

Trigger Sources The trigger distinguishes between different trigger types, and sets flags accordingly. An example of a non-physics trigger event which appears in physics

data is the periodic trigger which fires the pulse-pattern generator (PPG) at 56 Hz and records such events for DAQ calibration. These are cut by only selecting events with physics trigger flags.

DAQ cuts Another set of cuts is made such that the analysis is not run on pathological events. Examples include events which trigger too soon after a PPG event, PPG events themselves, events where a pulse is observed surrounded by an abnormal baseline, and events where the DAQ was busy and suppressing digitiser readout.

Sub-event cuts Another processor monitors for multiple increases in pulse rates in an event window which are indicative of the pile-up of events from different light sources. Each event is referred to as a sub-event. The selection of events with only one sub-event removes such pathologies.

Trigger time cut The calibrated trigger time in an event is defined as the peak of the pulse charges in the event, summed over all PMTs. This occurs at an average of 2500 ns after the start of the event window. Earlier trigger times occur when a previous event piles up in a new event window, and later trigger times occur due to pileup later in the window. The cut $2350 < t < 2650$ ns is used to catch pileup that is left undetected by the sub-event cut.

Previous trigger time A minimum 20 μs is required between the starts of two event windows, to prevent light from a previous event contaminating a next event. The time offset is 13.3 times longer than the triplet time constant in argon scintillation, and 11.6 triplet time constants later than the average previous calibrated trigger time.

Pulses before trigger time A cut requiring 2 or fewer pulses in the first 1600 ns of the event window (900 ns before the event peak) also removes pileup from previous events.

Neck veto PMTs Events in which the neck veto PMTs observed a pulse are cut. This removes events which originate near or inside the neck, such as alpha scintillation and ^{39}Ar in gaseous argon.

Top two PMT rows The top two rows of PMTs are above the liquid argon level and observe events which occur near the liquid surface and in the gaseous argon. A cut is made on events which see a fraction >0.069 of the total PE in the event in the top two rings of PMTs.

Gaseous argon Events which reconstruct above the fill level are removed from the dataset by cutting 50 mm below the estimation for the fill level for that run, which is lower than the 30 mm uncertainty on the fill level estimation.

3.2.3 F_{prompt}

F_{prompt} is a measure of the ratio of scintillation light which emitted from the fast component of the argon scintillation time profile to that emitted from both the fast and slow components. The variable has already been introduced in Section 1.5.3, and the discussion is continued here in more detail. Prompt $t_0 < t < t_{pr}$ and longer $t_0 < t < t_{end}$ time windows are defined, and F_{prompt} is given by:

$$F_{prompt} = \frac{\int_{t_0}^{t_{pr}} Q(t)dt}{\int_{t_0}^{t_{end}} Q(t)dt} \tag{3.1}$$

where $Q(t)$ is the total charge seen in an event at a given time t in the event window. The window parameters $t_0 = -28$ ns, $t_{pr} = 150$ ns, and $t_{end} = 10$ μs relative to the calibrated trigger time are chosen to maximise the separation between the electronic and nuclear recoil bands [3]. A projection of the electronic recoil band data at 80PE from Ref. [3] is shown in Figure 3.6a. In the grey curve in Figure 3.6a an 11-parameter PE-dependent empirical model is fitted to F_{prompt} for ^{39}Ar electronic recoil data shown in blue. The model describes the probability PSD(q_{PE},F_{prompt}) of observing an F_{prompt} at a given q_{PE}, given by [3]:

$$\text{PSD}(q_{PE}, F_{prompt}) = \Gamma(\bar{F}_{prompt}(q_{PE}), b(q_{PE})) \otimes \text{Gaus}(F_{prompt}; \sigma(q_{PE})) \tag{3.2}$$

where $b(q_{PE}) = a_0 + a_1/q_{PE} + a_2/q_{PE}^2$, $\sigma(q_{PE}) = a_3 + a_4/q_{PE} + a_5/q_{PE}^2$ and the mean F_{prompt} is given by $\bar{F}_{prompt} = a_6 + a_7/(q_{PE} - a_8) + a_9/(q_{PE} - a_{10})^2$, and the parameters a_{0-10} are varied in the fit. The model agrees with data with $\chi^2/n_{dof} = 1.068$, and is

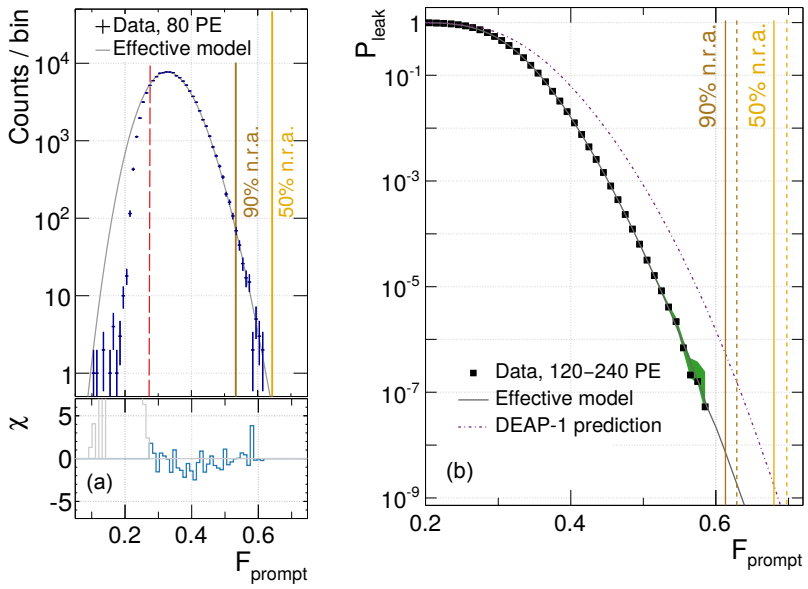

(a) (b)

Figure 3.6: Projection of F_{prompt} distribution for 80 PE electronic recoil events, plotted alongside effective model fit, as labelled. Red dashed line indicates the lower limit of the fit range. Brown and yellow lines represent the 90% and 50% nuclear recoil acceptance boundaries. (b) Comparison of electronic recoil data to model for 120-240 PE range, with 90% and 50% nuclear recoil acceptance indicated. Compares DEAP-1 projection (dashed) to improved effective model from DEAP-3600. Reproduced from Ref. [3].

implemented in the analysis in Chapter 6. In Figure 3.6b the same model is compared in grey to electronic recoil data in black, observed with $120 < q_{PE} < 240$, the nominal PE region of interest from the detector design specification. In both Figures 3.6a and b the solid brown vertical line corresponds to 90% nuclear recoil acceptance, and the yellow vertical line corresponds to 50% nuclear recoil acceptance. The conservative projection from the prototype DEAP-1 detector [145] is shown in dashed lines in Figure 3.6b, and is outperformed by the DEAP-3600 result. This motivated the move to an 80 PE threshold for the result in Ref. [3].

3.2.4 F_{maxpe}

The F_{maxpe} variable is the ratio of the highest PE count observed in any PMT to the total PE observed in the event, calculated using q_{PE}. The number of PE per emitted photon from a low energy, point-like scintillation event is proportional to the solid angle

subtended by the light guide with respect to the emission vertex. Events at the centre of the AV are expected to be observed as a uniform PE count (with Poisson fluctuation) in each PMT. For the same event near the TPB surface the nearest light guide has the largest solid angle and observes the most PE as a proportion of the total PE observed in the event. On this basis, F_{maxpe} is a measure of how surface-like an event is, with discrimination power for events which happen outside of the argon, for example in the AV and TPB.

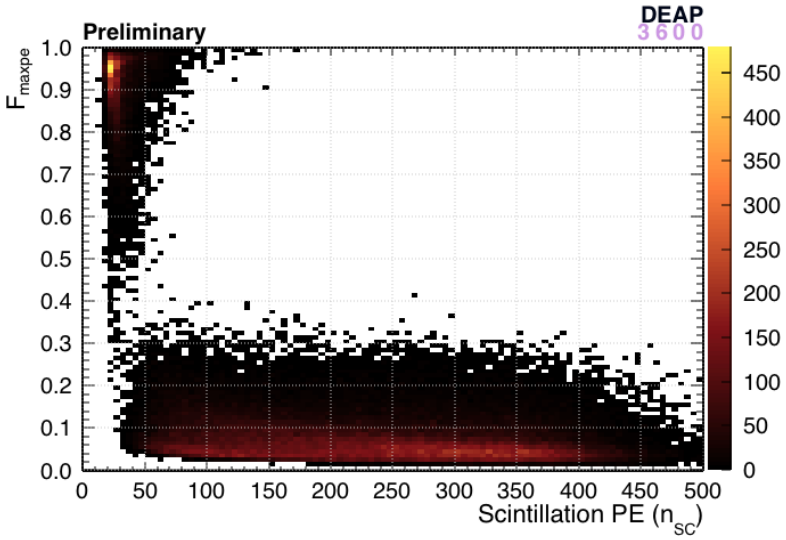

Figure 3.7: Distribution of F_{maxpe} vs n_{SC} for a standard physics run.

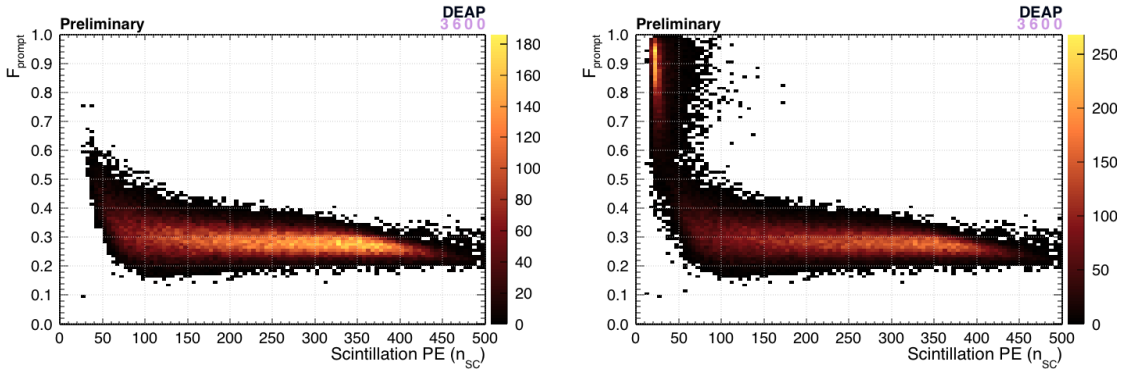

(a) (b)

Figure 3.8: Comparing the distribution of F_{prompt} vs n_{SC} for a standard physics run whilst (a) cutting on events with $F_{maxpe} > 0.2$, (b) allowing all F_{maxpe} values.

Figure 3.7 shows the distribution of F_{maxpe} for events in a physics data set which pass the data quality cuts discussed previously. The electronic recoil band occupies the region $F_{maxpe} < 0.2$, as would nuclear recoils. The vertical band at low N_{SC} at $F_{maxpe} > 0.4$ corre-

sponds to Cerenkov radiation in the acrylic vessel. A stringent cut on data at $F_{maxpe} > 0.2$ is made to isolate argon recoils. Figure 3.8 compares the distributions of F_{prompt} with n_{SC} using the same cuts, with (a) and without (b) the F_{maxpe} cut. The proximity of Cerenkov radiation to its closest PMT also makes a Cerenkov event have high F_{prompt} and F_{maxpe}, and the corresponding band is removed using an F_{maxpe} cut. A position reconstruction cut using $R_{rec} < 800$ mm using the position reconstruction algorithm MBLikelihood as in Ref. [3] removes the events at $F_{prompt} > 0.7$ and $F_{prompt} \simeq 0.1$. MBLikelihood is discussed further in Chapter 4.

3.3 Optics Variation

The position reconstruction algorithms described in the next chapter use an analytic model of the variation in charge and time of pulses in PMTs with the position of the light emission vertex. The models are fitted to the results of the simulation described above. Uncertainty on the measurements that informed the optical model in simulation can affect the model used in reconstruction.

In this section the effect of the variation of optical parameters on the observation of differences in PE count in PMTs is discussed. Those optical parameters are chosen which most affect the propagation of scintillation or re-emission photons in argon, TPB and acrylic. The optical model in simulation is at time of writing being optimised to match the data. The changes which most affect position reconstruction are explored here. The discussion is revisited in Section 5.2, when the effect of optical parameter changes on the position reconstruction is explored.

The optical parameters which most affect position reconstruction are those which affect the paths of photons from the scintillation emission vertex to the TPB, and those that affect the paths of TPB re-emission photons to the PMTs. Each changes the PE pattern observed across the PMTs because it changes the probability that a photon reaches a certain PMT instead of any other, and produces a PE. By contrast, parameters such as light yield and scintillation quenching factor affect the total number of PE observed in all PMTs. The PE count in each PMT is changed by the same factor, so total observed PE

cannot bias the position reconstruction in the same way.

In simulation, the estimated fill level $z_{fill} = 551$ mm is used. For ^{39}Ar β^- decay simulations electrons are distributed uniformly in liquid argon with energies according to the ^{39}Ar beta distribution truncated at 50 keVee. The physics trigger specified above is used in the DAQ simulation and the cut flow in Section 3.2.2 is applied. A loose region of interest cut is made at $80 < n_{SC} < 300$. Data and simulation from ^{39}Ar events is most sensitive to changes in the optical properties of liquid argon. The AARF calibration source was simulated using the same AARF location as in an AARF dataset taken after the completion of the second fill, at PMT ID 229. The simple trigger was simulated as discussed above. An AARF intensity was chosen to approximately match the PE count in the simulation to the data. The AARF calibration source is the closest calibration source to the TPB and the light guide and AV acrylic, and data and simulation from the AARF are more sensitive to TPB and acrylic optics than any other source. The laserball calibration source was simulated at the $z = -550$ mm position using the 375 nm laser head, and is compared to data taken with laserball deployed using the same laser head, at the same location and rotation. The $z = -550$ mm position is the closest the laserball was placed to the TPB surface and furthest it was placed from the neck. Light at the peak wavelength of 375 nm is absorbed and re-emitted by the TPB, and is also transmitted with a < 50 cm attenuation length in the AV (see Figure 2.7). As a consequence simulation and data from the laserball are sensitive to changes in the TPB and acrylic optical properties.

3.3.1 Argon

In the simulation of liquid argon the Rayleigh scattering length is a parameter with large uncertainty associated with it. The probability that Rayleigh scattering occurs at a given photon path length in the argon determines its path length and point of intersection with the TPB, which changes the probability that a PMT will observe a PE (from the associated TPB re-emission observed in the PMTs). Frequent scattering from a small scattering length will affect light paths and thus position reconstruction in situations where the light propagates distances on the same order of magnitude as the scattering length.

The extrapolation of scattering length by Seidel [146] yields a value of 90±31.5 cm at $\lambda = 128$ nm. There is tension between the Seidel value and a previous measurement performed near the triple point, at 87.15 K, performed by Ishida [147]. The Ishida measurement yielded a value for the scattering length of argon at 66 ± 3 cm. A new calculation by E.Grace [141] suggests that the scattering length in argon near the triple point, at 87 K, is 55 ± 5 cm. E. Grace also measured the scattering length at Royal Holloway, obtaining a scattering length at 57 ± 4 cm, which agrees with her calculation within error and is closer to the Ishida measurement than the Seidel extrapolation. Before the E. Grace measurement and extrapolation the Seidel value was used in simulation. The effect that varying the scattering length has on F_{maxpe} and F_{prompt} is discussed below.

The measurement from ArDM using comparison of simulation to data yielded an attenuation length of 52.1 ± 10 cm (error stated for a 100 PE threshold in Ref. [148]), assuming the scattering length from the Grace calculation. In Ref. [148] the observed attenuation is attributed to a possible absorption component in argon, owing to the presence of impurities which reduce the observed scattering length. The effect that the introduction of attenuation at this scale has on F_{maxpe} and F_{prompt} is also discussed below.

Sixty thousand ^{39}Ar events were simulated as specified above. The argon Rayleigh scattering length was varied using the Seidel (green), Ishida (purple) and Grace (pink) values. A nominal 10% chance of absorption (and 90% chance of Rayleigh scattering) in the simulated scattering process is applied to the Grace measurement in order to compare the effect of absorption in conjunction with a low Rayleigh scattering length relative to the Ishida value, as shown in yellow. The resulting F_{maxpe} and F_{prompt} distributions, normalised to unit area under the curve, are shown in Figures 3.9 and 3.10. Also shown in Figure 3.11 are the distributions of number N_{hit} of hit PMTs, which observed 1 or more PE. Alongside these the distributions from data are shown in blue. A relaxed $F_{maxpe} < 0.4$ cut is made such that the F_{maxpe} distribution is not truncated.

In the case of F_{prompt} the varied distributions reproduce the simulated distributions at $F_{prompt} > 0.16$. The simulated F_{prompt} distributions reproduce the data distribution with an offset of 0.01 observed in the peak of the simulated distributions. In the case of

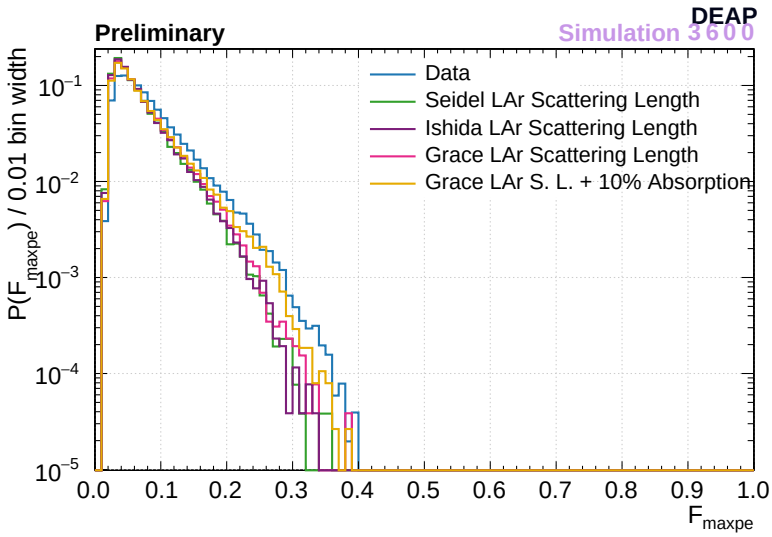

Figure 3.9: Comparing the ^{39}Ar F_{maxpe} distribution in simulation in cases where the argon scattering length is varied at values motivated in literature. Additionally, the effect of the introduction of a 10% absorption component in argon is shown, modelling the effect of impurities present in argon.

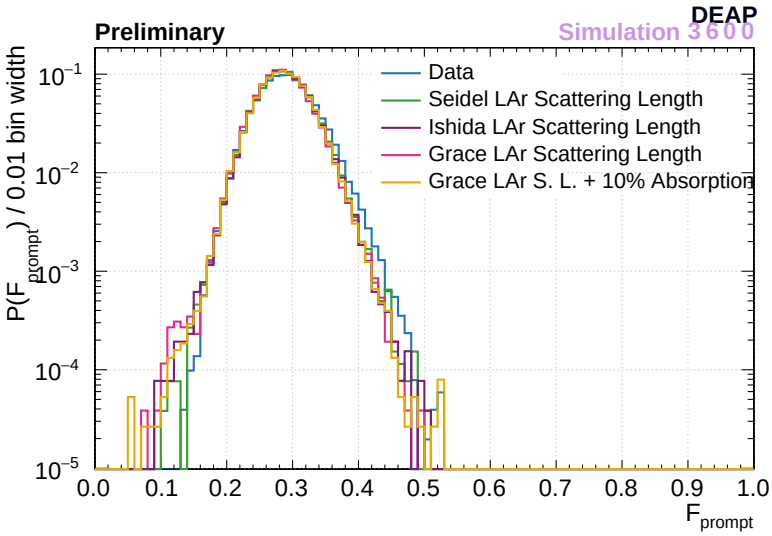

Figure 3.10: Comparing the ^{39}Ar F_{prompt} distribution in simulation in cases where the argon scattering length is varied at values motivated in literature. Additionally, the effect of the introduction of a 10% absorption component in argon is shown, modelling the effect of impurities present in argon.

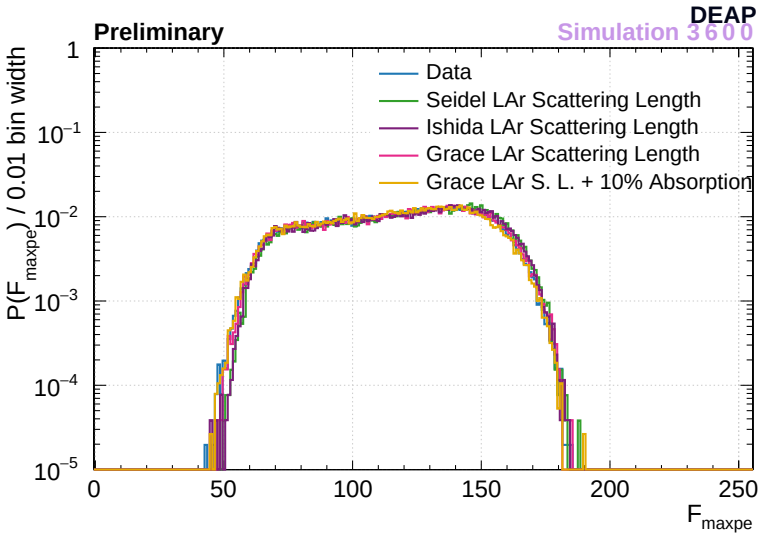

Figure 3.11: Comparing the distribution of number of hit PMTs N_{hit} in simulation of ^{39}Ar where argon scattering length is varied at values motivated in literature. Additionally, the effect of the introduction of a 10% absorption component in argon is shown, modelling the effect of impurities present in argon.

F_{maxpe} the simulated distributions reproduce the data distribution with a peak offset of 0.01, and are unable to reproduce the larger tail observed in data. Introducing absorption induces a small bias towards higher F_{maxpe}, but introduces a distribution shape which is not observed in data and no evidence of such contamination has been observed in data. In the case of N_{hit} the simulated distributions reproduce the data distribution to within 10% of the data curve. The above indicates that, despite the uncertainty associated with the scattering length, the scattering length does not affect charge and timing in a manner which produces offsets in charge and timing analysis parameters. The effect on position reconstruction is revisited in Section 5.2.

3.3.2 TPB

Non-uniformity

In the simulation the TPB layer is assumed to be a uniform spherical shell, whereas as constructed the TPB thickness is likely non-uniform. Possible effects are the thicker deposition of TPB at the bottom of the detector than the top because gravity shifts propagating TPB downwards, and small scale variation in thickness from the stochastic nature of the

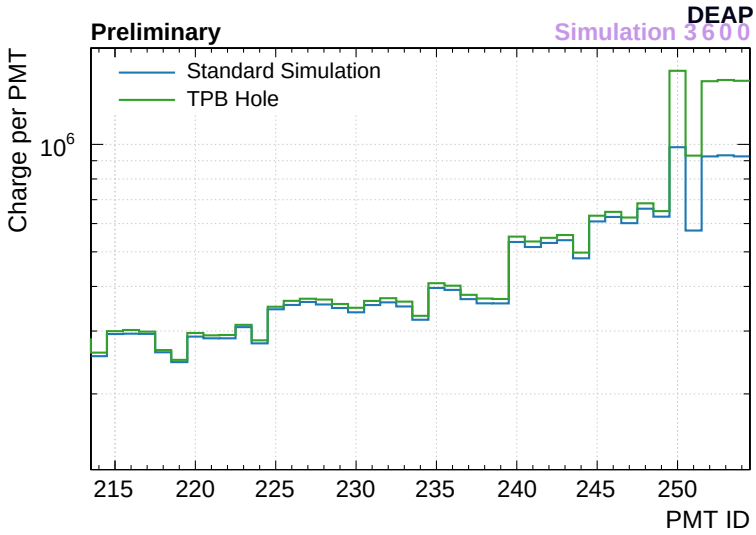

Figure 3.12: Total charge observed over 10^6 laserball events in the 40 PMTs nearest the bottom of the detector. PMT IDs are in ascending order moving from the top of the detector to the bottom of the detector. The laserball is simulated at $z = -550$ mm using the 375 nm laser head. Simulations were performed with and without a hole of radius 142.5 mm in the TPB at the bottom of the detector.

deposition process. To illustrate the most extreme effect of local variation, a circular hole in the TPB surface was simulated at the bottom of the detector, exposing the acrylic underneath. The hole has a radius of 142.5 mm, equivalent to 1.5 light guide radii, and is not centred on any one PMT.

The laserball calibration source was simulated as specified above, firing 10^6 times. The total q_{PE} observed in the 40 lowest PMTs on the detector z axis over all events is shown in Figure 3.12. Note that PMT IDs are ordered from top-most ($+z$, ID=0) to bottom-most ($-z$, ID=254). Charge is observed in the bottom-most PMTs from re-emission light from the closest TPB outside of the hole as well as 375 nm light transmission. The difference between a full layer and a hole is observed as a 51% increase in charge in the bottom-most 5 PMTs nearest the hole. If observed, this effect would bias a charge-based position reconstruction. Thickness variation will be characterised in the future in uniformity studies performed using the laserball calibration source. No compelling evidence for TPB non-uniformity has yet been observed.

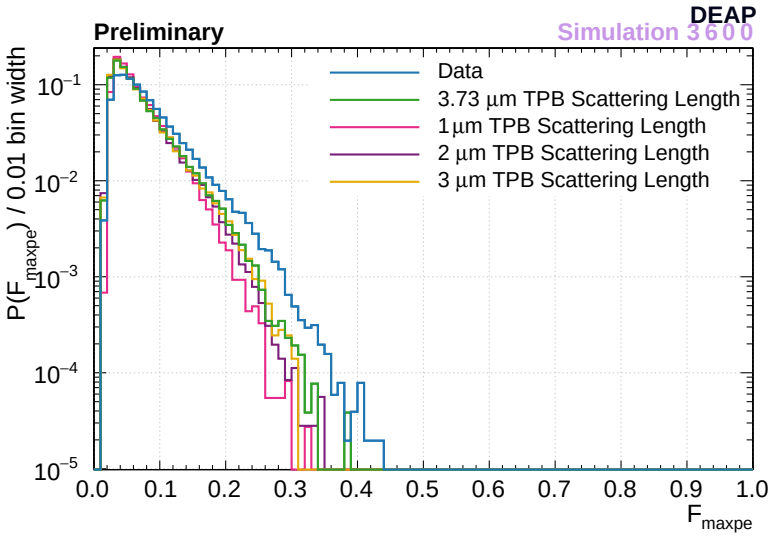

Figure 3.13: Distributions of F_{maxpe} for 6×10^4 ^{39}Ar events, for varying TPB Rayleigh scattering lengths.

Rayleigh scattering length

Rayleigh scattering in TPB affects the path of re-emission light. A shorter scattering length results in a more diffuse emission pattern of re-emission light from the TPB. This means that PMTs adjacent to the PMT facing a re-emission site become more likely to observe the emitted photon. Conversely a longer scattering length means that the PMT facing the re-emission site is more likely to observe the emitted photon than adjacent PMTs. This suggests that position reconstruction using charge information will be affected by the TPB scattering length, and this effect is explored further in Section 5.2.

Sixty thousand ^{39}Ar events were simulated for varying scattering lengths in TPB in the range 1-3μm, in 1 μm increments, and using the 3.73 μm scattering length. The resulting F_{prompt} and F_{maxpe} distributions, normalised to unit area under the curve, are shown in Figures 3.13 and 3.14. In every simulated case the F_{prompt} distribution peak is offset from the data distribution peak by 0.02. No deviation from the distribution produced by the 3.73 μm scattering length optics is observed in the 2-3 μm range. However reducing the scattering length 1 μm produces a deviation in the lower tail, reducing the tail position in F_{prompt} by 0.02 at $F_{prompt} > 0.14$. Conversely the higher tail position increases in F_{prompt} with increasing scattering length. This implies that pulse timing is not affected

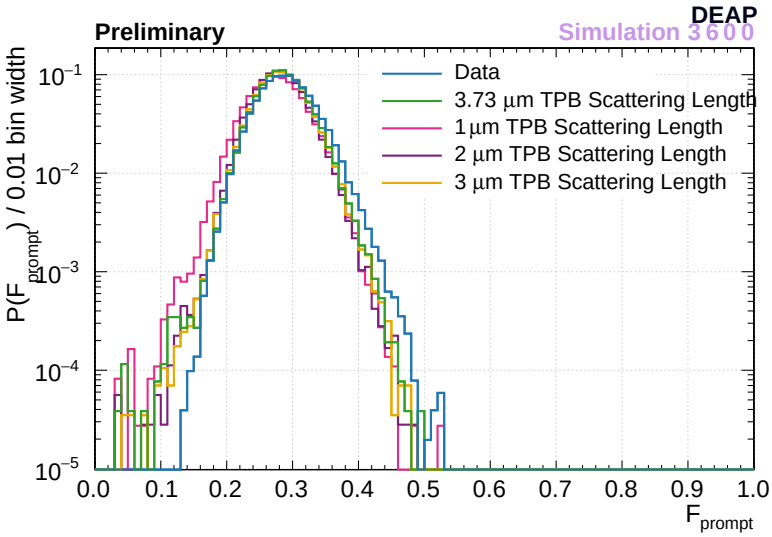

Figure 3.14: Distributions of F_{prompt} for 6×10^4 ^{39}Ar events, for varying TPB Rayleigh scattering lengths.

when considering variation of the scattering length at ≥ 2 μm in the range considered. Decreasing the scattering length to <2 μm produces a bias towards lower F_{maxpe} in the high tail. The scattering lengths 2-3 μm widen the distribution towards the distribution observed in data, with increasing bias observed with increasing scattering length.

The same scattering length variation was repeated in simulations of the laserball as specified above, fired 10^6 times per simulation. Light from the 375 nm laser which is incident on the TPB is absorbed and re-emitted. The fraction of PE observed in each PMT per total PE in all PMTs is shown against PMT ID in Figure 3.15. The scattering length variation was also repeated in simulations of 4×10^4 AARF pulses per scattering length. The fraction of PE in each PMT per total PE in all non-AARF PMTs is shown in Figure 3.16, with the PMT IDs sorted by increasing angle to the AARF PMT (where PMT ID 0 is the AARF PMT). The AARF PMT is not included in the calculation as the AARF saturates the AARF PMT.

The shorter the scattering length, the higher the probability of scattering per unit path length in the TPB and the more PE are distributed among the PMTs further from either light source. Conversely, for longer scattering lengths the charge distribution is more strongly peaked in the PMTs closest to the AARF, or PMTs nearest the laserball at the bottom of the detector. For this reason, the TPB scattering length is expected to affect a

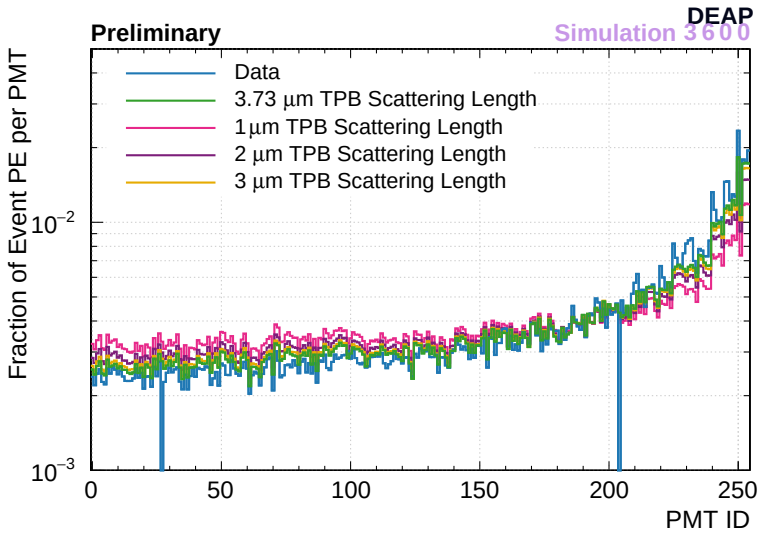

Figure 3.15: Distribution of the fraction of PE in each PMT relative to total PE in all PMTs, over all events. The laserball was simulated at $z = -550$ mm using the 375 nm laser head, fired 10^6 times, for varying TPB Rayleigh scattering lengths.

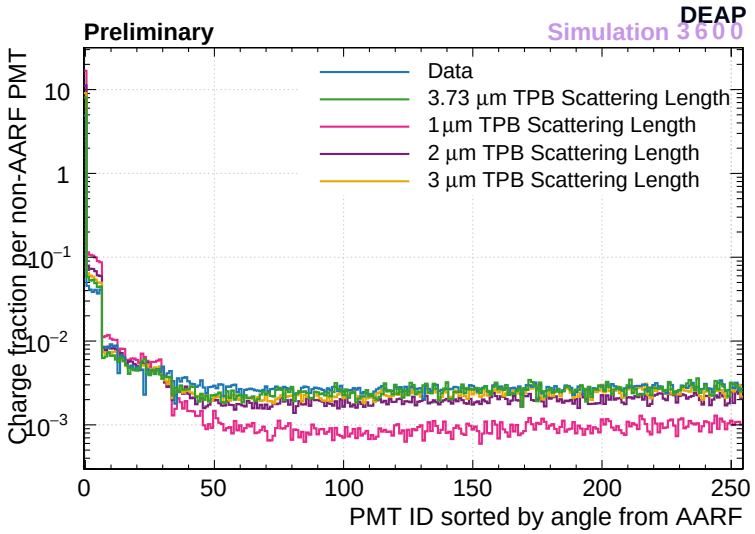

Figure 3.16: Distribution of the fraction of PE in each PMT relative to total PE in all non-AARF PMTs, over all events. The AARF was simulated at the light guide for PMT 229, fired 4×10^4 times, for varying TPB Rayleigh scattering lengths. The PMT IDs on the horizontal axis are sorted in order of increasing distance to the AARF PMT, where PMT ID 0 is the AARF PMT.

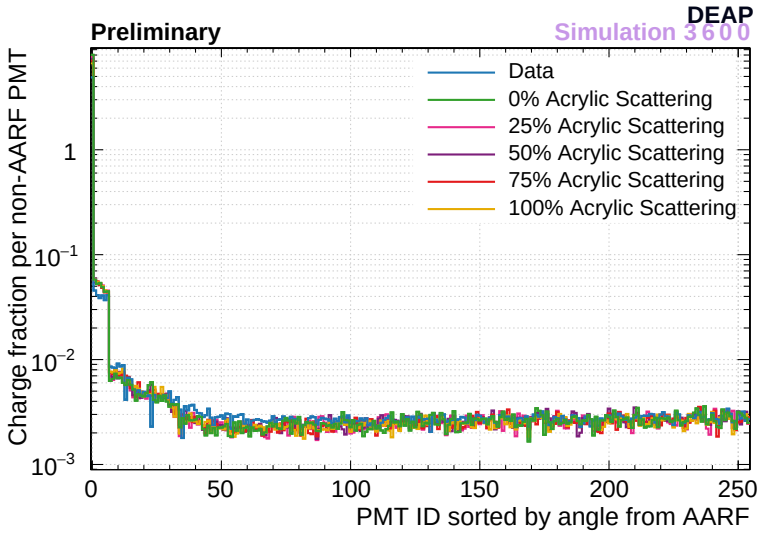

Figure 3.17: Distribution of the fraction of PE in each PMT relative to total PE in all non-AARF PMTs, over all events. The AARF was simulated at the light guide for PMT 229, fired 4×10^4 times, for varying light guide and AV attenuation lengths. The PMT IDs on the horizontal axis are sorted in order of increasing distance to the AARF PMT, where PMT ID 0 is the AARF PMT.

charge based position reconstruction. This is discussed further in Section 5.2.

3.3.3 Acrylic

Simulated photons in the light guide and AV acrylic are assumed to undergo attenuation, not Rayleigh scattering. The effect that introducing a non-zero Rayleigh scattering component in acrylic would have on the simulation is discussed here. The ratio of scattering to absorption was varied in 25% increments up to 100% in simulation. 4×10^4 AARF flashes were generated per simulation. The distributions of PE in each PMT per total PE in all non-AARF PMTs is shown in Figure 3.17 against PMT ID, sorted by increasing angle from the AARF PMT.

The introduction of scattering in the acrylic in simulation has no effect on the distribution of charge as a fraction of total charge across the PMTs, meaning that a scattering component in the acrylic would not bias position reconstruction. This is because as discussed in Section the absorption length for light with the peak 405 nm wavelength is 20 cm in the AV acrylic, longer than the 5 cm thickness of the acrylic. Likewise, the absorption length at 405 nm is 3 m in the light guides, which are of length 95 cm.

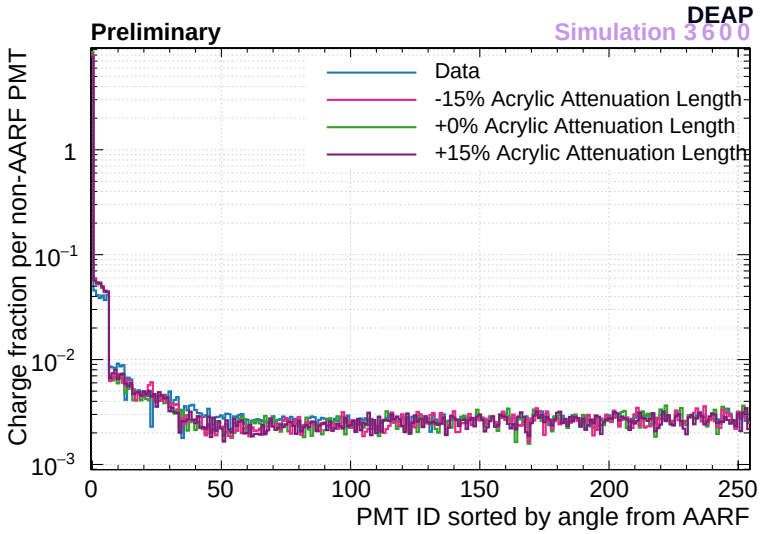

Figure 3.18: Distribution of the fraction of PE in each PMT relative to total PE in all non-AARF PMTs, over all events. The AARF was simulated at the light guide for PMT 229, fired 4×10^4 times, for varying attenuation lengths. The PMT IDs on the horizontal axis are sorted in order of increasing distance to the AARF PMT, where PMT ID 0 is the AARF PMT.

Considering the attenuation length itself, the uncertainty on the bench-top measurement of the light guide attenuation length that is implemented in simulation has a 15% error at 440 nm. The measured attenuation length in the AV and light guide acrylic was varied by $\pm 15\%$ of the measured value at all wavelengths. 4×10^4 AARF flashes were generated for each simulated attenuation length. The distributions of PE in each PMT per total PE in all non-AARF PMTs against PMT ID is shown in Figure 3.18, with PMT ID listed in order of increasing distance from the AARF PMT. The resulting distributions of F_{maxpe} and F_{prompt} are shown for simulation in Figures 3.19 and 3.20. The numerator of the F_{maxpe} ratio is the AARF PMT, which is saturated by the AARF. The data curve is omitted in F_{maxpe} because saturation makes comparison with data difficult to interpret. The data curve is omitted in F_{prompt} for that same reason, because the majority of the charge in time is also observed in the AARF PMT. The saturation model is however consistent between different simulations. The AARF laser is operated at an intensity which ensures that saturation is not observed in any of the non-AARF PMTs.

The variation of attenuation length has no effect on the distribution of charge between PMTs in a given event. As a consequence the acrylic scattering length will have little effect on position reconstruction. The variation of the attenuation length also has no

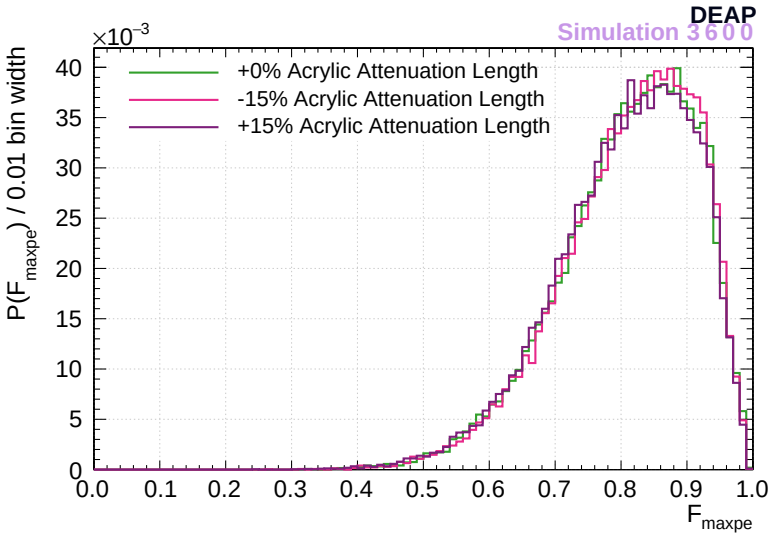

Figure 3.19: F_{maxpe} distributions from AARF simulations with varying AV and light guide acrylic attenuation lengths.

effect on the F_{prompt} distribution, demonstrating little effect on event pulse timing. The effects of attenuation length variation are instead observed in F_{maxpe}. In this case the increased attenuation length at +0% and +15% biases the peak in F_{maxpe} to lower values. This is because as the mean path length of a photon from emission to a PMT without being absorbed increases, photons are able to access a set of PMTs at wider angles to the AARF light guide more frequently. The inverse is true of a decreased attenuation length. A decreased attenuation length biases the F_{maxpe} peak to higher values. The effect on F_{maxpe} is much slighter than that from Rayleigh scattering length in TPB.

3.4 Conclusion

The simulation of the DEAP-3600 detector using the RAT software was discussed in this chapter. The optical information and measurements which are implemented in simulation of scintillation and re-emission photons were described. The DAQ simulation was discussed; the simulated analogues to real DAQ trigger types used in this and later chapters were discussed. Analysis in RAT was described, and the variables used in this and later chapters were discussed. The ^{39}Ar, laserball and AARF calibration sources were used to explore the effect variations in the optical model have on scintillation and re-emission

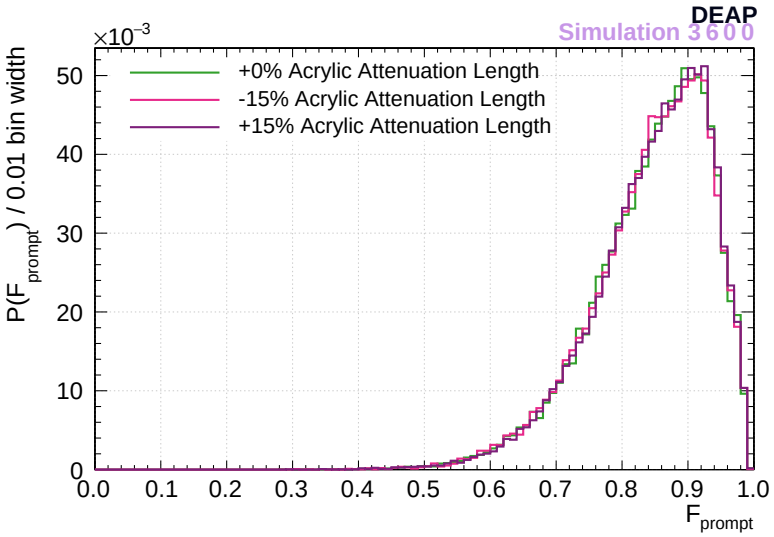

Figure 3.20: F_{prompt} distributions from AARF simulations with varying AV and light guide acrylic attenuation lengths.

photons. Emphasis was placed on those optical parameters which have the most potential to most affect position reconstruction. Rayleigh scattering in TPB was identified as having the largest effect on the distribution of charge among PMTs as a function of distance from the light source. The discussion included the set of optical parameters which most affect position reconstruction and the agreement between data and simulation. The parameters of the current standard optical model were discussed, which uses the Seidel argon Rayleigh scattering length and a 1 μm TPB scattering length independent of wavelength. An experimental model with modified argon and TPB scattering length was discussed, and the extent to which the new optical model matches the data was discussed. At time of writing those optical parameters which have negligible effects on position reconstruction are currently being optimised for energy calibration and background studies. As a result a discussion of the effect of the new optical model on position reconstruction is deferred to Chapter 5.

Chapter 4

Position Reconstruction

Position reconstruction in a scintillation-only detector instrumented with PMTs relies on the comparison of a PMT position and charge model with real PMT positions and charges, or photoelectron (PE) counts. There are two methods by which position reconstruction based on observed charge takes place in DEAP-3600. The first, centre of charge calculation, is described in the next section. The second is based on the minimisation of a Poisson likelihood comparing observed PMT charges with a model for predicting theoretical PMT charges for a hypothesised number of photons emitted from a given position, described in detail in the sections that follow.

The author's work on a maximum likelihood algorithm called ShellFit is described. Improvements to the geometric model used to produce predicted charges during minimisation are discussed, in an updated version of ShellFit called UberShellFit. The addition of time information to the UberShellFit charge likelihood is also discussed. The maximum likelihood algorithm MBLikelihood is also described. The algorithms are then benchmarked using the ^{39}Ar background uniformity and resolution as well as ^{210}Po decays in TPB.

4.1 Centroid

Centre of charge calculation uses a simple model of the detector which is only aware of the positions of the PMTs in the PMT array. An event position is calculated using an

analogy to a many body centre of mass calculation, instead weighted by the number of photoelectrons Q_i observed in each PMT i for an array of N_{PMT} PMTs with positions $\vec{x}_{PMT,i}$:

$$\vec{x} = \frac{\Sigma_{i=1}^{N_{PMT}} (Q_i)^a \vec{x}_{PMT,i}}{\Sigma_{i=1}^{N_{PMT}} (Q_i)^a} \tag{4.1}$$

where the exponent a is a hyperparameter. The default value is set as $a = 2$, which yields the ^{39}Ar uniformity observed in Section 4.6.1 of this chapter. This calculation has the advantage over minimisation algorithms of being computationally inexpensive and capable of reconstructing events that occurred outside of the argon, such as Cerenkov emission, but favours simplicity over accuracy. The disadvantage of this method is that it only uses PMT position, and does not model any of the physical and optical properties of the detector materials between the scintillation event vertex and PMTs, unlike the likelihood methods described in the next sections.

4.2 ShellFit

ShellFit is a position reconstruction algorithm which performs a maximum likelihood fit to observed charges by varying three position parameters $\vec{x}$, and the number of photons N_{UV} emitted by the event it reconstructs. The model the algorithm uses to predict theoretical charges given a position is described in this section.

4.2.1 Charge Response Model

During position reconstruction, a maximum likelihood algorithm compares a position-dependent charge response model to charges measured in photomultiplier tubes (PMTs) on the detector in order to determine the position of origin of a light-producing event. A small GEANT4 Monte Carlo simulation is run before event processing, modelling as a set of analytic functions the position dependence of the charge response a given PMT at its position relative to the event. Thereafter, the algorithm evaluates values from these functions during event reconstruction. The GEANT4 simulation includes optical properties of the materials in the detector informed by measurement, and a full simulated geometry of

the detector as included in RAT. As the optical model is updated with new measurements, and as the simulated detector geometry changes to reflect the as-built detector geometry, the charge response model can be updated by the user. The charge response model used in ShellFit is outlined in detail in the following subsections. Simulation in this chapter uses the current standard optical model.

Position Dependent Detector Response Model

During initialisation, 10^6 photons are simulated, isotropically distributed in direction, at increasing radii from the centre of the acrylic vessel (AV), with wavelengths randomly distributed according to the wavelength spectrum of argon scintillation. The simulation is used to measure the variation of two properties of light propagation in the detector:

1. The number of photons per incident UV photon $W(\Omega,\vec{x})$ re-emitted by the TPB, for a given position of origin $\vec{x}$ of the incident photon and point on the TPB within solid angle Ω with respect to the centre of the spherical scintillator volume.

2. The probability $H(\theta_i(\Omega))$ that a photon re-emitted from a point Ω on the TPB will produce a PE in a PMT i at an angle θ_i away from the re-emission point.

The re-emission and detection probabilities, $W(\Omega,\vec{x})$ and $H(\theta_i(\Omega))$, are extracted from simulation using tracking information. The $\Omega,\vec{x}$ dependence of $W(\Omega,\vec{x})$ is parametrised using two position measurements: the radial co-ordinate of the position of origin of the photon, $|\ \vec{x}\ |$, relative to the centre of the detector, and the vector distance from the initial position of the generated photon to the point of incidence on the TPB, $|\ \vec{x}_{TPB}-\vec{x}\ |$. This is elucidated in Figure 4.1. This parametrisation assumes that the variation of the observed charge distribution with distance to the TPB is spherically symmetric; that is, that it can be rotated to apply to a given PMT without loss of realism. A histogram recording the number of photons re-emitted by TPB per UV photon is produced, binned in $|\ \vec{x}\ |$ and $|\ \vec{x}_{TPB}-\vec{x}\ |$, as shown in Figure 4.2. The fraction recorded in the histogram is calculated by dividing the bin contents of two histograms, the numerator counting photons re-emitted at a point $\vec{x}_{TPB}$ on the TPB, the denominator those photons whose initial momentum vectors intersect with the TPB at a point $\vec{x}_{TPB}$, binned by $|\ \vec{x}\ |$ and $|\ \vec{x}_{TPB}-\vec{x}\ |$.

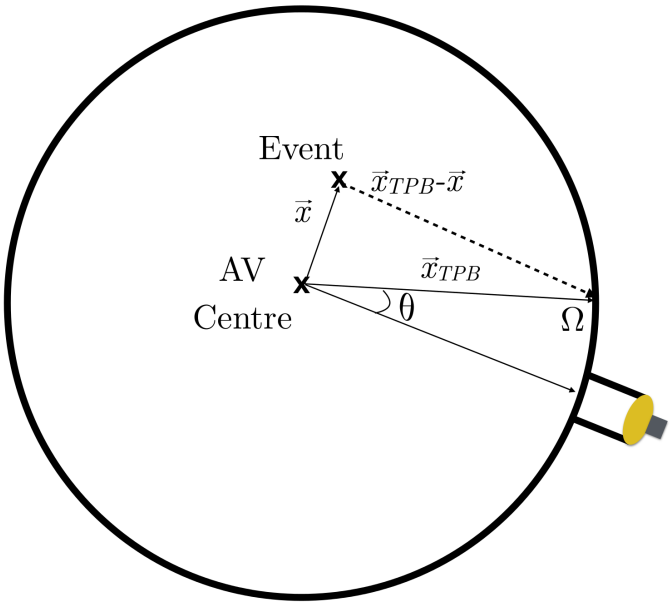

Figure 4.1: A schematic depicting the solid angle Ω used to denote a point on the TPB, and the re-emission angle θ from the light guide normal. Event position vector is denoted $\vec{x}$ and distance between event and TPB point is denoted $|\,\vec{x}_{TPB}-\vec{x}\,|$. Acrylic vessel and light guide are not to scale.

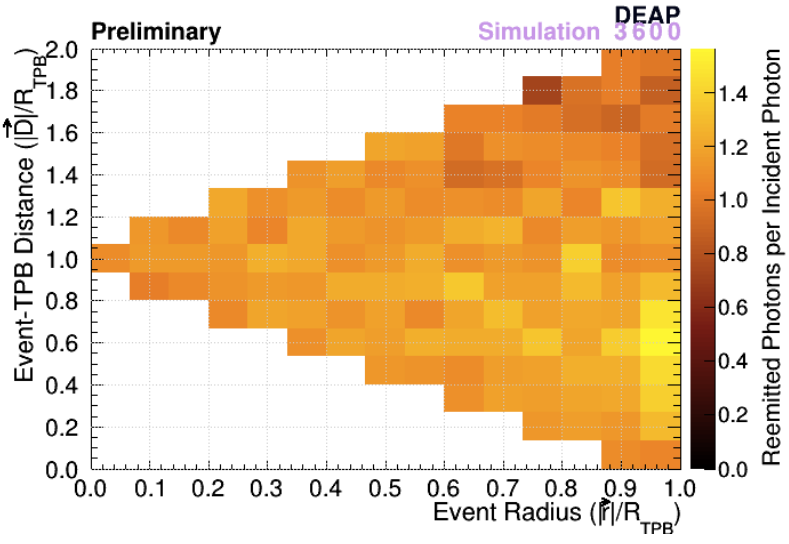

Figure 4.2: Number of photons re-emitted by TPB per incident UV Photon, $W(\Omega,\vec{x})$, at any point in Ω on the TPB surface. Shown in the colour axis as a function of radial co-ordinate $|\,\vec{x}\,|$ of the event and the distance between the event position vector and the TPB re-emission position vector $|\,\vec{x}_{TPB}-\vec{x}\,|$

.

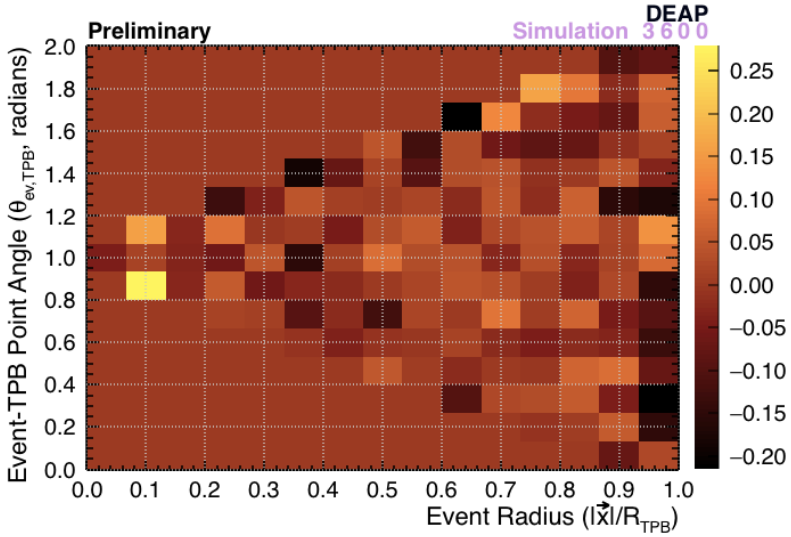

Figure 4.3: Difference between polynomial fit of $W(\Omega,\vec{x})$ and bin content from the histogram shown in Figure 4.2, using the same bin boundaries. The set of empty bins in Figure 4.2 is shown here as a set of zero bins with no variation of bin content.

Configurations where photons are likely to be reflected and then re-emitted elsewhere are observed as deviations below and above 1, and losses due to absorption by detector materials will lower this ratio. Deviations above 1 occur for events close to the TPB surface, and below 1 for events far from the TPB surface. The histogram is then fitted using a 2D polynomial. The difference between fit value and histogram bin content is shown in Figure 4.3. The fit performs consistently, with $\chi^2/n_{dof} \approx 0.9$, and is retained for later use in the minimisation stage.

Likewise, the probability $H(\theta_i(\Omega))$ is recorded as a histogram as a function of angle $\theta_i(\Omega)$, shown in Figure 4.4, and fitted with a third order spline after smoothing using the Kernel Density Estimation functions supplied by ROOT. Assuming homogeneity of the detector geometry near each PMT, the same function is applied to all PMTs regardless of their position. The result shows an angular distribution favouring the forward direction, towards the nearest PMT, and a low but non-zero contribution for backwards re-emission towards $\theta_i = \pi$.

The quantities $W(\Omega,\vec{x})$ and $H(\theta_i(\Omega))$ are used to compare the charge response model to detector response data during the minimisation process by predicting a PE count $\mu_i(\vec{x},N_{UV})$ in each PMT i, for a hypothesised position and number of UV photons N_{UV} emitted by the

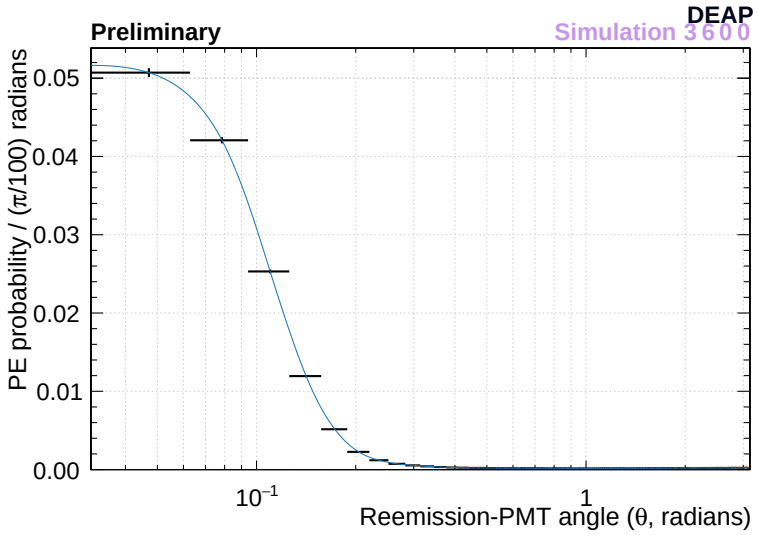

Figure 4.4: Probability $H(\theta_i(\Omega))$ that a photon re-emitted from a point on the TPB Ω produces a PE in a PMT i at a angle θ_i away from Ω.

source. The predicted charge in each PMT is calculated as a weighted mean over a grid of four-sided patches on the TPB surface, indexed j, weighted by the solid angle $\Omega_{patch,j}$ subtended by each patch of TPB relative to $\vec{x}$:

$$\mu_i(\vec{x}, N_{UV}) = N_{UV} \frac{\sum_j W(\Omega_j, \vec{x}) H(\theta_i(\Omega_j)) \Omega_{patch,j}}{\sum_j \Omega_{patch,j}} \tag{4.2}$$

The patch solid angle calculation is discussed in detail in Section 4.4.1.

4.2.2 Minimisation

Charge Types

During event processing, ShellFit accepts charge information from a set of PMTs as its input, in the form of a set of photoelectron (PE) counts. At time of writing it has running modes that correspond to two PE counting methods: Bayesian PE counting and charge division.

The input is arranged in three arrays, each containing N_{PMTs} entries:

1. Boolean listing whether each PMT was ”hit”: that it saw 1 PE or greater
2. The number of PE in each PMT from the Bayesian PE counting algorithm, with afterpulsing removed

3. The charge divided by the mean single PE charge for each PMT (charge division)

ShellFit uses a combination of item 1 and either 2 or 3 as part of the calculation of a likelihood, as outlined below. The default setting is to use PE counts with afterpulsing removed, from the Bayesian PE counting algorithm. For the rest of this and subsequent chapters, unless otherwise specified, this default is used.

Negative Log Likelihood Minimisation

For a hypothesised event with position $\vec{x}$ and number of emitted UV photons N_{UV}, the minimisation process evaluates a negative log likelihood function. The likelihood $\mathscr{L}_{Q,i}$ compares the set of predicted mean PE counts $\mu_i(\vec{x}, N_{UV})$, with the set of observed PE counts $\vec{Q}_i$ for each PMT i:

$$\mathscr{L}_{Q,i}(\vec{x}, N_{UV} \mid Q_i) = \begin{cases} Pois(0 \mid \mu_i) & \text{for } Q_i = 0 \\ P(Q_i \mid \mu_i) & \text{for } Q_i > 0 \end{cases} \tag{4.3}$$

The term $P(Q_i \mid \mu_i)$ takes on two forms, depending on the type of PE count under consideration. Using PE counts $\{n_{PE,i}\}$ or $\{n_{SC,i}\}$ from the Bayesian PE counting algorithm:

$$P(n_{PE,i} \mid \mu_i) = Pois(n_{PE,i} \mid \mu_i) \tag{4.4}$$

Using PE counts from charge division:

$$P(Q_i \mid \mu_i) = \sum_n P_n(Q_i \mid \mu_i) \tag{4.5}$$

$$\text{where } P_n(Q_i \mid \mu_i) = \begin{cases} P(Q_i \mid n) \times Pois(n \mid \mu_i) & \text{for } 1 < n < 15 \\ P(Q_i \mid n) \times Gaus(n \mid \sqrt{\mu_i}) & \text{for } n > 15 \end{cases},$$

$$n \in \mathbb{Z}^+ \text{ and } P(Q_i \mid n) > 10^{-4}$$

Using PMT charge in pC, $\{Q_{pC,i}\}$, the probability $P(Q_i \mid \mu_i) = P(Q_{pC,i} \mid n)$ is given by a double Polya function convolved with itself $N_{PE} - 1$ times, examples of which are shown for 1-8 PE in Figure 4.5. Combining each PMT likelihood over all PMTs, the result is a likelihood function comparing predicted charge to observed charge in every

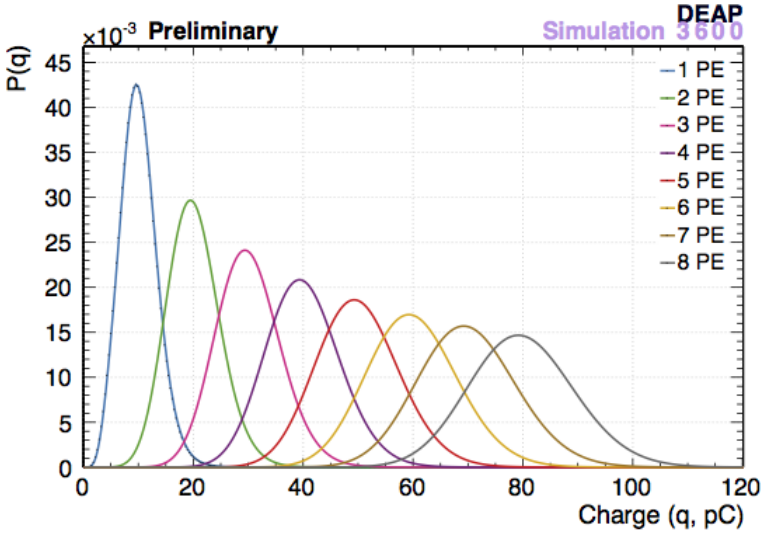

Figure 4.5: Charge PDFs for n PE. When n>1, the distribution is described by the 1 PE double Polya distribution convolved with itself $n-1$ times.

PMT:

$$\mathscr{L}(\vec{x}, N_{UV}) = \prod_{i=1}^{N_{PMTs}} \mathscr{L}_{Q,i}(\vec{x}, N_{UV} \mid Q_i) \tag{4.6}$$

where N_{PMTs} is the number of PMTs on the detector. The likelihood is converted to a negative log likelihood (NLL), which is minimised to find maximum likelihood estimators for position $\vec{x}$ and emitted photon count N_{UV} using MIGRAD, the gradient descent algorithm in the Minuit package.

As a starting point in the available parameter space a seed position and UV photon count is required. Initially, the UV photon count is calculated proportionally to the total PE count in the event, $N_{UV,init} = n_{photons/PE} \sum_i Q_i$, where $n_{photons/PE}$ is calculated from the ratio of emitted UV photons to observed PE in the simulation described in the previous subsection. The initial value for N_{UV} is either fixed or allowed to float during minimisation. For each event, a likelihood is computed for each of a coarse grid of positions uniform across the entire detector and numbers of UV photons uniformly distributed in the range $(0.75 \times N_{UV,init}) < N_{UV,grid} < (1.25 \times N_{UV,init})$. The set of parameters that yields the smallest log likelihood is chosen as the starting position for minimisation, near which the global minimum in the parameter space may reside. The result of subsequent minimisation in MIGRAD is saved to the RAT data structure.

4.3 MBLikelihood

The Mikhael Batygov likelihood fitter, or MBLikelihood, also minimises a per-PMT Poisson likelihood model comparing estimated charge to observed charge. The model used to relate position to charge also relies on a simulation, in this case performed separately prior to event processing. A simulation of 2×10^5 ^{40}Ar recoils is generated for each of 20 discrete radii, at positions along straight lines originating at the centre of the detector, along the positive x (North in the laboratory) and y (West) axes, and along the z axis both positive (up) and negative. 200 recoils are simulated for each of the 80 positions, and high photon counts are achieved by distributing the process across multiple CPUs on a grid computing system. Typically $\mathcal{O}(10^3)$ CPUs are used, resulting in a much higher photon count used in lookup generation than ShellFit (and UberShellFit, discussed in the next section). Three sets of quantities are saved from simulation: the radial co-ordinate of each event vertex $|\vec{x}|$ relative to the centre of the detector; the angle between each PMT i and each event vertex, $\arccos(\vec{x}\cdot\vec{x}_i/(|\vec{x}||\vec{x}_i|)) = \theta_{ev,i}$; and the number of PE produced in a PMT i per photon produced in scintillation. For each discrete radius the distribution of simulated PE per photon per PMT i vs $\theta_{ev,i}$ is smoothed using Kernel Density Estimation. A subset of the resulting distributions are shown in Figure 4.6. The contribution of the gaussian kernels used is most visible in the highest radius yellow and brown curves. During reconstruction a cubic spline is created in PE per photon per PMT vs radial co-ordinate for each PMT at a given $\theta_{ev,i}$ to interpolate between the 20 radii.

A prediction for the charge observed in each PMT is then taken as $\mu_i(\vec{x},N_{UV}) = N_{UV}\mu_{ph,i}$, where N_{UV} is the number of photons emitted from the event vertex. A joint Poisson likelihood of the form seen in Equations 4.3 and 4.4 is constructed:

$$\mathscr{L}(\vec{x},N_{UV}) = \prod_{i=1}^{N_{PMTs}} \text{Pois}(Q_i \mid \mu_i) \tag{4.7}$$

where Q_i is the observed charge in each PMT, with Bayesian single PE count and PE from charge division used interchangeably. MBLikelihood uses a custom in-line minimisation routine using gradient descent to minimise the joint likelihood and writes the resulting $\vec{x}$ and N_{UV} to the RAT data structure.

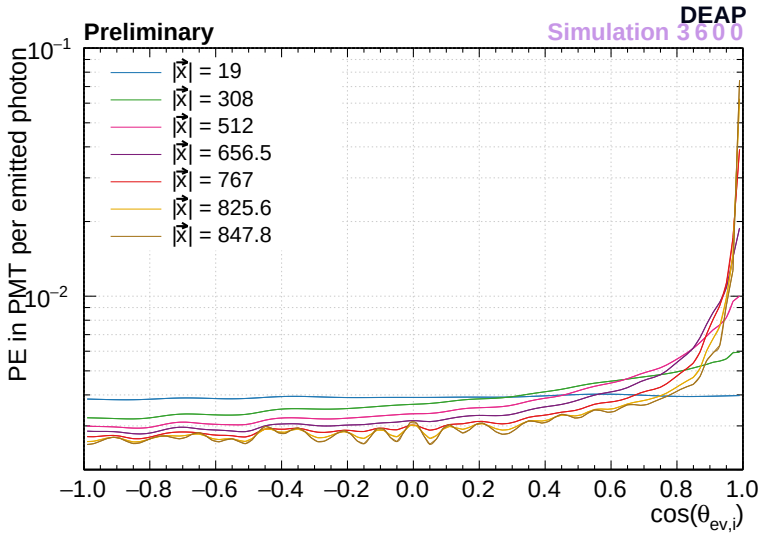

Figure 4.6: Probability that a photon emitted from position $\vec{x}$ is observed in a PMT i at an angle $\theta_{ev,i}$ away from the position vector, relative to the centre of the detector. The probability is plotted against $\cos(\theta_{ev,i})$.

4.4 UberShellFit

This section discusses a new version of ShellFit, called UberShellFit. UberShellFit addresses problems ShellFit has with the calculation of TPB geometry and slow performance which are described here. The result of these changes is discussed in Section 4.6.1.

4.4.1 TPB patch solid angle calculation

In ShellFit, calculation of the solid angle weighted mean PE μ produced in a PMT for an event at a hypothesised position $\vec{x}$, is performed by assuming the TPB is a sphere and separating it into rectangular patches from two regions. A circular region centred on the PMT axis and extended to encompass neighbouring light guides covers models TPB re-emission close to the PMT; the remaining TPB surface models other re-emission from across the detector. Each surface patch is assumed to have an area A_{patch} calculated by dividing the entire region's area on the TPB sphere by the number of patches. The patch positions $\vec{x}_{patch}$ are modelled by randomly sampling an isotropically distributed set of points in each region, and the solid angle each patch subtends with respect to $\vec{x}$ is

calculated as follows:

$$\Omega_{patch} = \arcsin\left(\frac{A_{patch} \times \cos(\theta_{dev})}{|\, x_{patch}\,|^2 + A_{patch}}\right) \tag{4.8}$$

where θ_{dev} is the deviation angle between $\vec{x}_{patch}$ and the patch position relative to the event position, $\vec{x}_{patch} - \vec{x}$. The $\cos(\theta_{dev})$ term approximates the effect of the patch solid angle becoming smaller for events at larger angles to the normal of the patch.

The $\cos(\theta_{dev})$ approximation fails as the event approaches to within half the longest side length of the centre of the patch, at which point rotating to large angles to the normal moves the event closer to the patch. The patch solid angle approaches zero for the approximation, whereas the actual patch solid angle approaches 2π, and the approximation under-predicts PE from these patches. This is a problem for surface events, which must be reconstructed very close to the TPB surface. In addition, the sum of all such patches on a TPB sphere $\sum_i \Omega_{patch,i} \neq 4\pi$.

The problem described above is alleviated by a more exact solid angle calculation. A new calculation of the TPB patches consists of a set of four-sided stripe segments on the TPB surface. Circular stripes are drawn on the unit sphere centred on the position vector $\vec{x}$ with axes of symmetry parallel to $\vec{x}$. The stripes are concentric on the point $|\, \vec{x}_{TPB}\,|\, \hat{x}$ where the unit position vector $\hat{x} = \vec{x}/\,|\, \vec{x}\,|$ meets the TPB. An example of the stripe orientation on the unit sphere around the position vector is shown in Figure 4.7, not to scale. Those stripes are then segmented into square patches on the unit sphere. The stripe width is uniform in $\cos(\theta')$ (see Figure 4.7) and the segment length is uniform in ϕ', where $\cos(\theta') = 1$ corresponds to the direction parallel to the position vector $\vec{x}$. Using a fixed segmentation on the unit sphere ensures that as the event approaches the TPB surface, the patches on the TPB surface that are closer to the event become smaller and the patches further away become larger. This ensures a higher resolution model for PMTs nearer to the event where $W(\Omega, \vec{x})$ and $H(\theta_i(\Omega))$, and thus $\mu_i(\vec{x}, N_{UV})$, undergo the fastest changes and require the most detail about angular variation from the model.

The solid angle of each patch is calculated using the analytic function for the solid angle of a circle for an observer on the axis of symmetry of the circle. For a stripe with

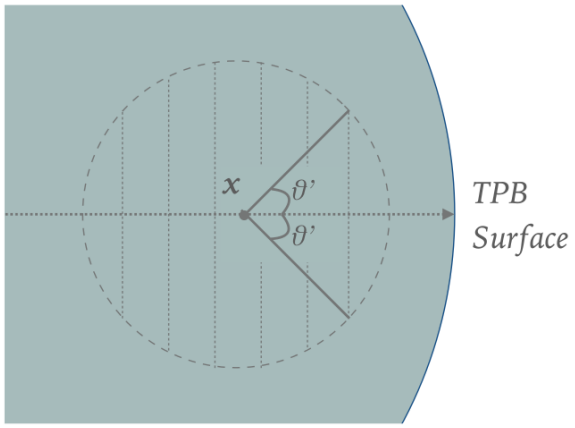

Figure 4.7: A schematic, not to scale, showing an example of the stripe orientation relative to the position vector $\vec{x}$ (vectors denoted in bold). The unit sphere is centred on the position vector $\vec{x}$ and stripe boundaries are circles with axes of symmetry parallel to $\vec{x}$. The circles are concentric on the point where $\vec{x}$ meets the TPB. Also shown is an example circle opening angle θ', defined such that $\cos(\theta') = 1$ refers to a direction parallel to the position vector $\vec{x}$.

$N_{\phi'}$ patches in it, bounded by circles at smaller and larger angles θ'_{small} and θ'_{large} relative to the unit position vector $\vec{x}$, the solid angle subtended by that stripe relative to $\vec{x}$ is given by:

$$N_{\phi'}\Omega_j = 2\pi(1-\cos(\theta'_{large})) - 2\pi(1-\cos(\theta'_{small})) = 2\pi(\cos(\theta'_{small}) - \cos(\theta'_{large})) \quad (4.9)$$

4.4.2 Computational Efficiency

The disadvantage of the UberShellFit solid angle calculation method is that it incurs a greater computational cost compared to the ShellFit method. The ShellFit method of calculating the solid angle weighted mean is performed with each minimisation step, and execution time scales linearly with the number of minimiser iterations. UberShellFit exploits the fact that ShellFit's two lookup tables are saved as analytic functions which can be evaluated for any position within the AV. The calculation of PE per photon for any given PMT and position can be performed and recorded in new lookup tables, which can depend on any positional variable.

For computational efficiency during event reconstruction the UberShellFit solid angle calculation is performed at the beginning of a RAT instance, before event processing begins. The mean PE per photon $\mu_i(\vec{x}, 1)$ is calculated for varying event radii $|\vec{x}|$, for

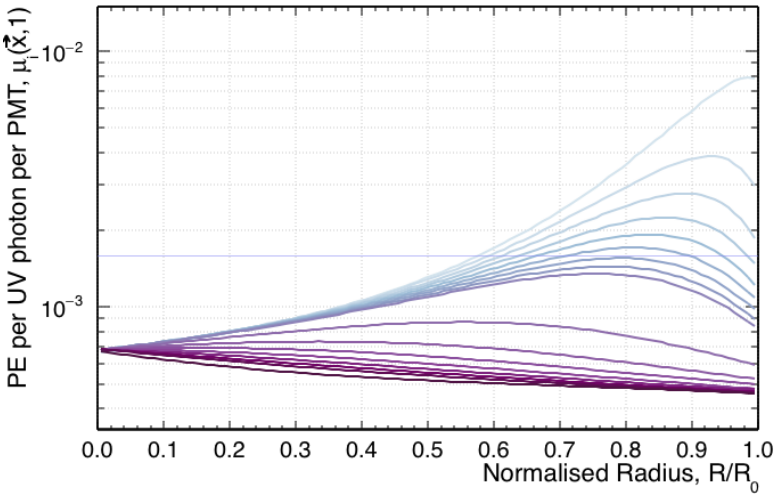

Figure 4.8: Number of PE observed per UV scintillation photon $\mu_i(\vec{x},1)$, vs event radius $R = \mid \vec{x} \mid$ normalised to the detector radius $R_0 = 851$ mm for varying $\cos(\theta_{ev,i})$ from $\cos(\theta_{ev,i}) = -1$ (lowest curve) to $\cos(\theta_{ev,i}) = 1$ (highest curve).

PMTs i at varying angles $\theta_{ev,i}$ from the event. The resulting $\mu_i(\vec{x},1)$ are saved as a set of splines as shown in Figure 4.8, which shows $\mu_i(\vec{x},1)$ against $\mid \vec{x} \mid$ for varying $-1 < \cos(\theta_{ev,i}) < 1$. Note that at low radii the $\mu_i(\vec{x},1)$ converge. For an event at the centre of the detector any set of TPB patches with equal solid angle is excited by the same amount of scintillation light, and so the PMTs see the same PE counts. For an event at high radius, as the PMT angle approaches $\cos(\theta_{ev,i}) = 1$ (the highest curve on the vertical axis), the difference in $\mu_i(\vec{x},1)$ with PMT-event angle increases. During event reconstruction, the calculation of $\mu_i(\vec{x},N_{UV})$ is reduced to the interpolation between 200 of the splines shown in Figure 4.8 at a fixed $\vec{x}$ for each PMT angle $\theta_{ev,i}$ from the event. The lookup table generation stage takes 10 minutes on a single CPU, making it useful for studies of the effects of the optical parameters on position reconstruction. The lookup tables can still be precomputed in a separate RAT instance and be saved to file, and loaded in reconstruction in future RAT instances. The reconstruction is a factor of 40 faster than ShellFit and a factor of 5.29 slower than MBLikelihood.

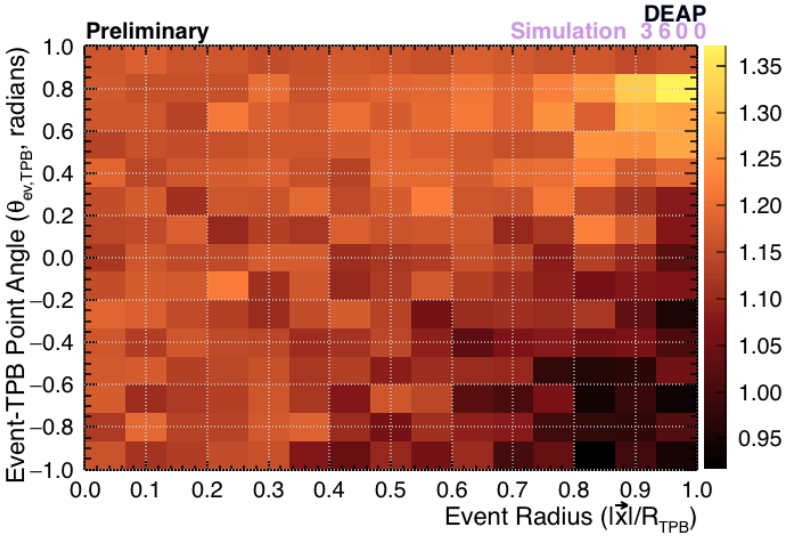

Figure 4.9: Number of photons re-emitted by TPB per incident UV photon, $W(\Omega,\vec{x})$, at a point Ω on the TPB surface. Shown against the radial co-ordinate $|\vec{x}|$ of the event and the deviation angle between the event position vector and the TPB re-emission position vector.

4.4.3 Reparametrisation

The final change that took place as part of the development of UberShellFit saw the re-parametrisation of the histogram of re-emitted photon per emitted UV photon $W(\Omega,\vec{x})$. A maximum likelihood fit of a surface to a 2D histogram maximises the product of Poisson terms comparing the fitted value to the population of each bin. Providing the fitting algorithm with a single bin in $|\vec{x}|$ for positions at radii smaller than 56 mm de-weights the low radius bins in the 2D surface fit compared to the 15 bins used for the outermost 56 mm, which dominate the fit. The histogram is re-parametrised from $|\vec{x}|$ and $|\vec{x}_{TPB}-\vec{x}|$ to $|\vec{x}|$ and $\theta_{ev,TPB} = |\vec{x}_{TPB}.\vec{x}| / (|\vec{x}_{TPB}||\vec{x}|)$. The new histogram is shown in Figure 4.9, which is used in the production of the splines shown in Figure 4.8. The difference between fit and histogram bin content is shown in Figure 4.10.

4.5 Time Reconstruction

This section discusses the construction of a time of flight model which describes the variation of observed pulse arrival times in PMTs with event position in the detector. The construction of a time based likelihood in addition to the existing charge-based likelihood

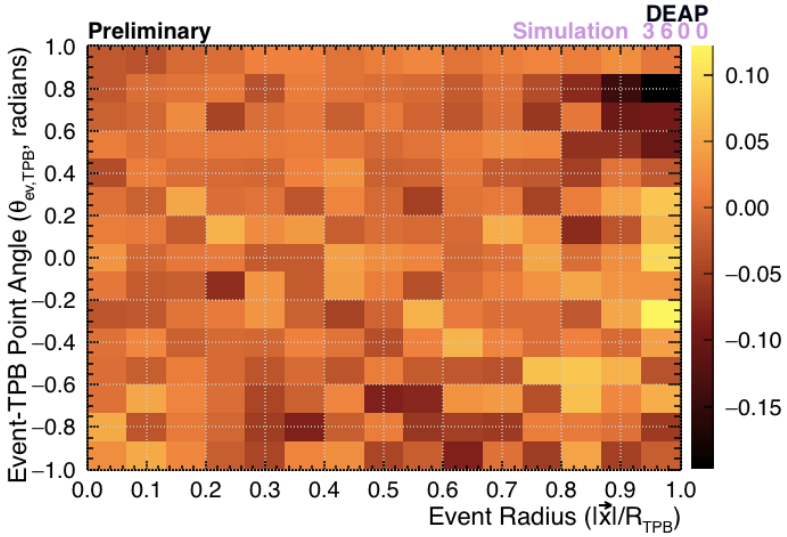

Figure 4.10: Difference between polynomial fit of $W(\Omega,\vec{x})$ and bin content from the histogram shown in Figure 4.9, using the same bin boundaries. Shown against the radial co-ordinate $|\vec{x}|$ of the event and the deviation angle between the event position vector and the TPB re-emission position vector.

is described. The model is then compared to the simulated data it models.

4.5.1 Position Dependence of Observed Time

The use of time information in position reconstruction is made possible by the use of pulse times measured in PMTs. A photon travelling along the diameter of the AV requires 6.34 ns to travel from surface to surface, whereas a photon travelling from the centre of the detector requires only 3.17 ns to travel to an AV surface. The arrival time distribution of photons at photocathodes at all PMTs for an instantaneous emission from a vertex at a given radius is shown in Figure 4.11. The distribution is recorded from a simulation of an instantaneous isotropic point source emitting light with the wavelength spectrum of argon scintillation. Time of flight t_{TOF} on the horizontal axis is shown relative to the time of light emission. As the event radial position from the centre of the AV increases the time of flight of the first photon to hit any PMT photocathode (the leading edge at early times in Figure 4.11) decreases, and the arrival time distribution widens to reflect higher time of flight to PMTs further away.

In Figure 4.12 the arrival time distribution for an event at the centre of the AV is

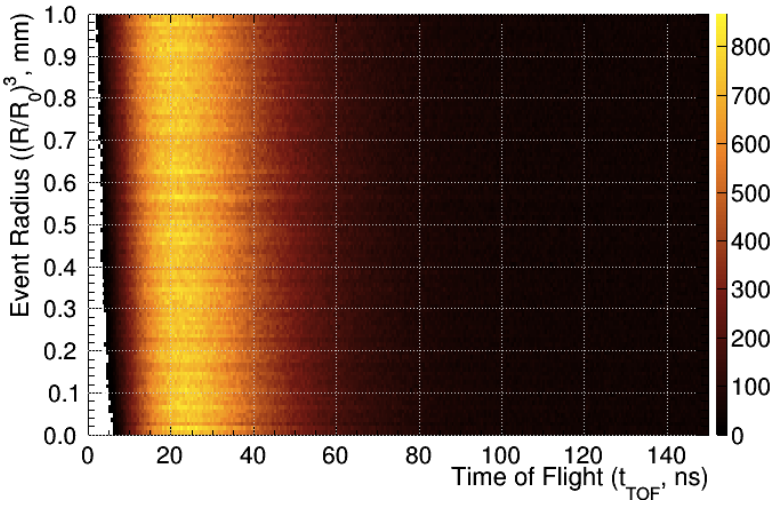

Figure 4.11: Radial co-ordinate $|\vec{x}|$ of the simulated event position vertex $\vec{x}$, vs time of flight t_{TOF} of photons from time of emission to time of arrival at a PMT photocathode. Colour axis: photons per histogram bin. Each simulated event is an instantaneous isotropic point source with the wavelength spectrum of argon scintillation.

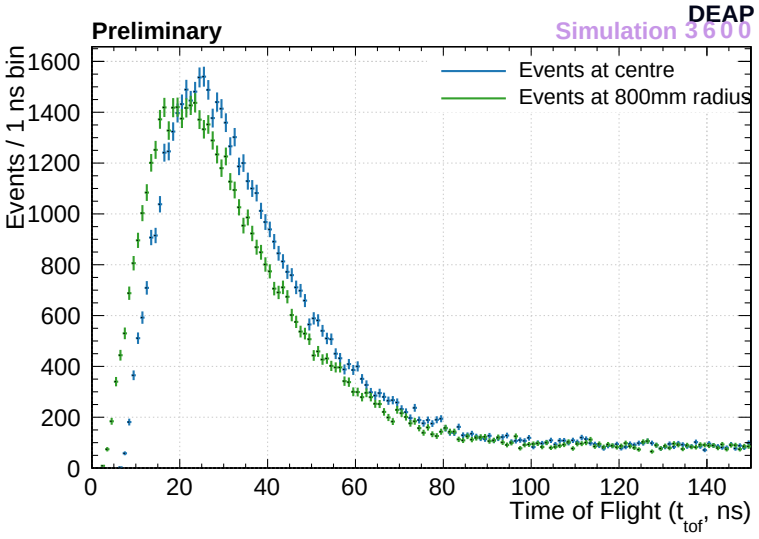

Figure 4.12: Probability of observing a time of flight t_{TOF}. Events located at the centre of the detector are shown in blue, and events located near the surface of the detector are shown in green. Each event is an instantaneous isotropic point source with the wavelength spectrum of argon scintillation.

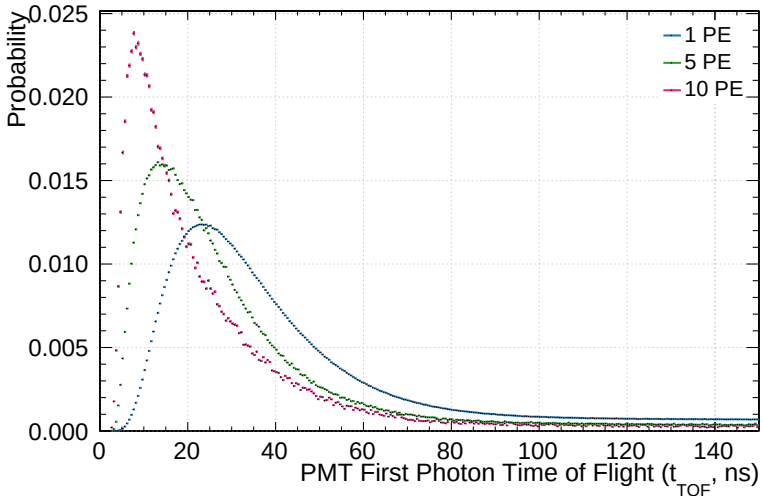

Figure 4.13: Probability of observing a time of flight t_{TOF} for the first photon observed in each PMT, for PMTs that observed 1PE (blue), 5PE (green), and 10PE (pink). Each event is an instantaneous isotropic point source with the wavelength spectrum of argon scintillation.

compared with that for an event at $|\vec{x}| = 800$ mm. In high radius events the distribution has a two peak structure, representing the addition of two arrival time distributions, with a faster time of flight peak for direct flight of photons to nearby PMTs and a slower peak dominated by high time of flight and reflections. In low radius events the distributions merge and produce a single distribution combining high time of flight and reflections.

The width of the distribution of the time of flight of the first photon to hit a given PMT is inversely proportional to the PE observed in that PMT, as shown for 1, 5 and 10 PE in Figure 4.13. Using a model relating the variation of the observed time distribution to position vertex parameters, vertex position is reconstructed from the time of each pulse observed in each PMT as follows.

4.5.2 The Timing Model

The light path of a scintillation photon in transit from an event in argon to a photocathode can be broken down into three stages, summarised in Figure 4.14. Firstly, scintillation photons are emitted at time $t_{emission}$ after energy deposition. Secondly, the photon travels from the event to the PMT over a time of flight $t_{TOF}(\vec{x})$, which depends on event position and is characterised in simulation. Lastly, the photocathode produces a photoelectron,

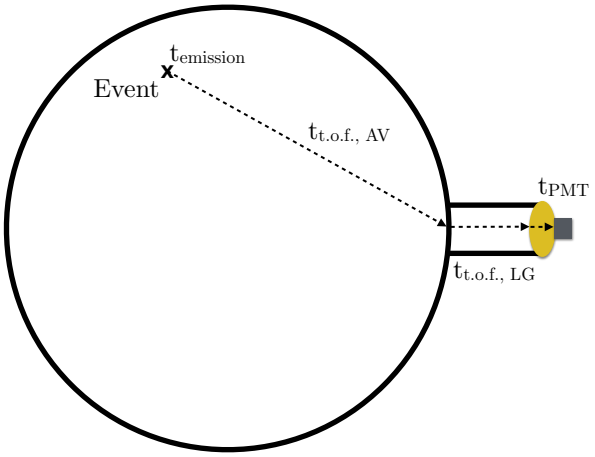

Figure 4.14: A summary of the time of flight from event to PMT. Note that in diagram notation, $t_{TOF} = t_{TOF,AV} + t_{TOF,LG} + t_{TOF,TPB}$, where $t_{TOF,TPB}$ is the time of flight in TPB, not shown.

which requires a transit time t_{PMT} from measurement to reach the first dynode in the PMT, cascade and produce a pulse. Each contribution is examined in turn in this subsection.

Scintillation Emission Time, $t_{emission}$

In liquid argon recoils, scintillation photons are emitted at a time $t_{emission}$ relative to the time of energy deposition, with a probability given by the sum of two exponential PDFs:

$$P(t_{emission}) = p\frac{1}{\tau_s}exp\left(\frac{-t_{emission}}{\tau_s}\right) + (1-p)\frac{1}{\tau_l}exp\left(\frac{-t_{emission}}{\tau_l}\right) \tag{4.10}$$

As implemented the contributions from short τ_s and long τ_l time constants are weighted by a probability parameter p describing the ratio of short to the late component, which varies with recoil hypothesis and energy. The scintillation emission timing is discussed in Section 1.5.3.

Time of Flight, t_{TOF}

The photon time of flight t_{TOF} from photon emission to PMT photocathode is measured in simulation using instantaneous, isotropic photon sources with the argon scintillation wavelength spectrum peaked at 128 nm. Photon arrival times at the photocathode are

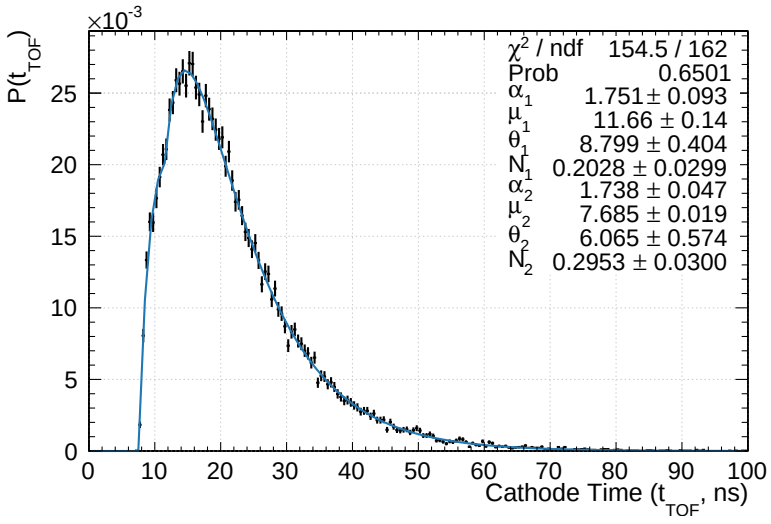

Figure 4.15: An example of a PMT photocathode arrival time PDF (Cathode Time) for an instantaneous, isotropic 128 nm photon source. The distribution is fitted using the weighted sum of two gamma distributions, with $\chi^2/n_{dof} < 1$.

described by the weighted sum of two gamma distributions:

$$P(t_{TOF}) = N_1 \frac{\theta_1^{-\alpha_1}}{\Gamma(\alpha_1)} (t_{TOF} - \chi_1)^{\alpha_1 - 1} e^{\left(-\frac{(t_{TOF}-\chi_1)}{\theta_1}\right)} + N_2 \frac{\theta_2^{-\alpha_2}}{\Gamma(\alpha_2)} (t_{TOF} - \chi_2)^{\alpha_2 - 1} e^{\left(-\frac{(t_{TOF}-\chi_2)}{\theta_2}\right)} \tag{4.11}$$

An example of a single PMT arrival time distribution fitted with the two gamma distribution model is shown in Figure 4.15. The shape parameters α_1, α_2 control the rising edge section before the peak of each gamma distribution; the exponential time constants θ_1, θ_2 control the falling exponential sections of each gamma distribution; and the offset parameters χ_1, χ_2 describe the first photon arrival time for each component. N_1, N_2 are normalisation parameters controlling the weighting of the two gamma distributions. The two gamma distribution model is normalised to unity under the curve after the weighted sum.

PMT Transit Times, t_{PMT}

The transit time from photocathode to the anode is described by the weighted sum of four separate PDFs. Each PDF describes the prompt, late, double and early pulse time distributions (neglecting noise and after pulses), as discussed in Section 2.3.6.

Prompt, late and double pulses assume that a photoelectron is produced at the photo-

cathode. The early contribution represents a probability that the photocathode is missed entirely and an incident photon strikes the first dynode. That is, p_{prompt}, p_{double} and p_{late} are independent of p_{early}, and $p_{prompt} + p_{late} + p_{double} = 1$. The transit time PDF is constructed as follows, where $P_i(t_{PMT})$ denotes a transit PDF for each type i and N is a normalisation constant:

$$P(t_{PMT}) = (1 - p_{early})P_{P,L,D}(t_{PMT}) + p_{early}P_{early} \tag{4.12}$$

$$\text{where } P_{P,L,D}(t_{PMT}) = \frac{1}{N}\left[p_{prompt}P_{prompt}(t_{PMT}) + p_{late}P_{late}(t_{PMT}) + p_{double}P_{double}(t_{PMT})\right]$$

SCB Convolution

As discussed in Section 2.6.1 PE produce a signal that is passed through signal conditioning boards (SCBs) to distribute the signal over more digitiser bins before they reach the digitisers. The effect on pulse timing is to convolve $P(t_{PMT})$ with an exponential model with constants $A = 1.0$ and $\tau_{SCB} = 4$ ns for SCB signal sent to a V1720:

$$P(t_{SCB}) = \frac{1}{A}\left(\frac{t_{SCB}}{\tau_{SCB}}\right)^2 \exp\left(\frac{-t_{SCB}}{\tau_{SCB}}\right) \tag{4.13}$$

Arrival Time, $\mathbf{t}(\tilde{\mathbf{x}})$

The observed arrival time is the result of the convolution of the PDFs governing each of the contributions described in the previous section, such that the PE arrival time probability is given by:

$$P_{arrival}(t(\vec{x})) = P(t_{emission}) * P(t_{TOF}(\vec{x})) * P(t_{PMT}) * P(t_{SCB}) \tag{4.14}$$

$$\text{where } t(\vec{x}) = t_{emission} + t_{TOF}(\vec{x}) + t_{PMT} + t_{SCB}$$

The dependence of the arrival time distribution $P_{arrival}(t(\vec{x})$ on position vertex $\vec{x}$ is assumed to be contained entirely in the position dependence of $P(t_{TOF}(\vec{x}))$, such that $P(t_{emission})$, $P(t_{SCB})$ and $P(t_{PMT})$ broaden the position dependent time of flight PDF in convolution.

4.5.3 Reconstruction Model

This subsection discusses the parametrisation of time of flight and its use in the construction of a time-based likelihood in position reconstruction. The combined UberShellFit and timing likelihood reconstruction is referred to as UberShellFit+Time.

Parametrising Position Dependent Time of Flight

The position variation is parametrised using a simulation of instantaneous, isotropic 128 nm photon sources at 20 positions of increasing radial co-ordinate from the centre of the AV, along lines in three perpendicular directions joining the centre of the AV to the AV walls. The PMT efficiencies are temporarily set to 100% to maximise light collection.

The time of flight distribution is recorded for each PMT for each position $\vec{x}$, and a weighted sum of two gamma distributions is fitted to each. From the two gamma distribution fits the shape parameters $\alpha_1,\ \alpha 2$ and $\beta_1,\ \beta 2$, time offset parameters $\chi_1,\ \chi_2$ and weighting parameters $N_1,\ N_2$ are plotted against $\vec{x}$ and $\cos(\theta_{ev,i})$. The angle $\theta_{ev,i}$ is the angle between the event position vector and the position vector of the centre of the PMT, shown in Figure 4.16. The resulting 2D parameter distributions are smoothed using a Kernel Density Estimation (KDE) routine and the result is shown for each parameter in Figures 4.17, 4.18, 4.19 and 4.20.

The parameter χ_1 is never higher than the 6.34 ns it takes for a photon to travel along the diameter of the detector, which suggests that the first gamma distribution corresponds to direct photon transit from event vertex to PMT. An exception is in the region $\cos(\theta_{ev,i}) \simeq -1,\ |\vec{x}|/R_0 \simeq 1$, where short time of flight from the opposite side of the detector from the PMT is not possible, and the distribution is de-weighted with a low N_1 parameter. The offset parameters χ have ranges that are offset from one another, with $\chi_1 < \chi_2$. An approximately constant large χ_2 controls a later distribution interpreted as non-direct light, and at high radius produces the offset double peak structure discussed in Section 4.5.1.

The θ parameter controls how quickly each gamma distribution exponentially decays after the peak. Generally $\theta_1 < \theta_2$ with exceptions at high radius and $\cos(\theta_{ev,i}) \simeq 1$, where

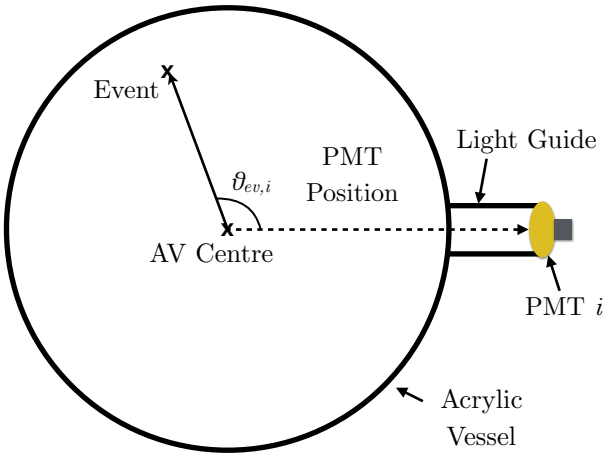

Figure 4.16: Schematic showing the angle $\theta_{ev,i}$ between event position vector and PMT position vector

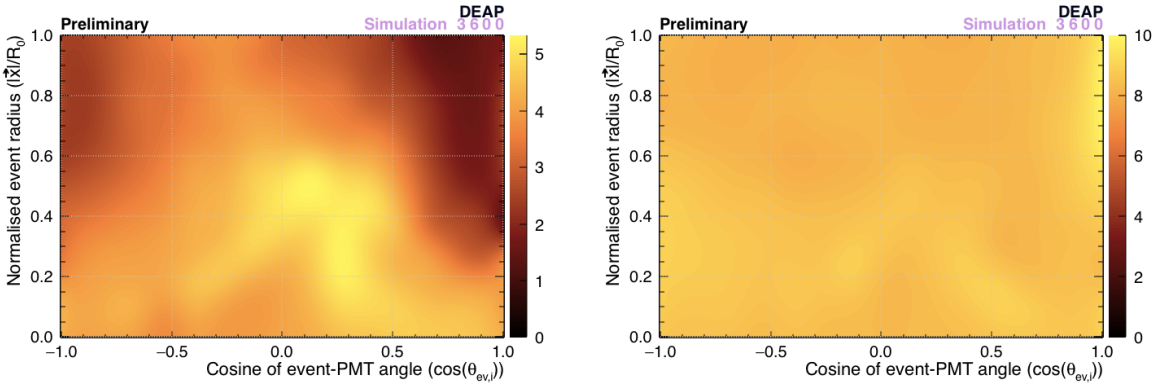

(a) χ_1 (b) χ_2

Figure 4.17: Time offset, χ (colour axis), plotted against event vertex radial co-ordinate (normalised to $R_0 = 851$ mm) and cosine of the angle $\theta_{ev,i}$ shown in Figure 4.16.

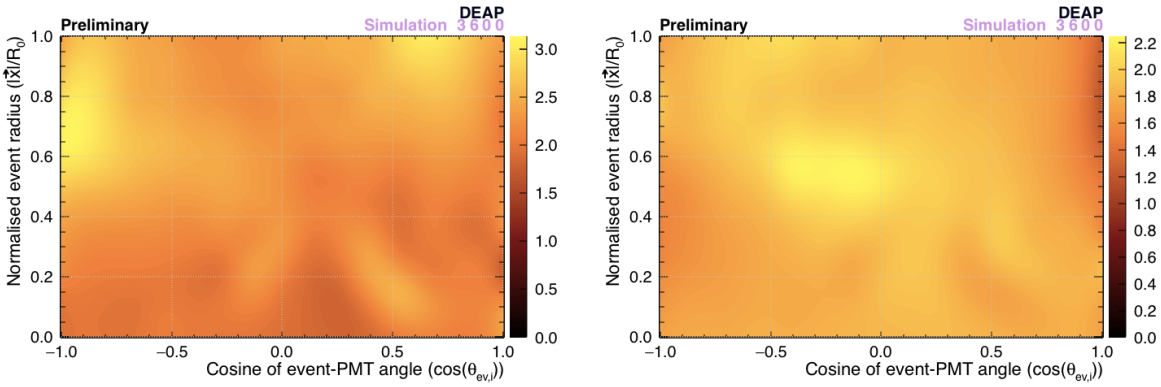

(a) α_1 (b) α_2

Figure 4.18: Polynomial parameter, α (colour axis), plotted against event vertex radial co-ordinate (normalised to $R_0 = 851$ mm) and cosine of the angle $\theta_{ev,i}$ shown in Figure 4.16.

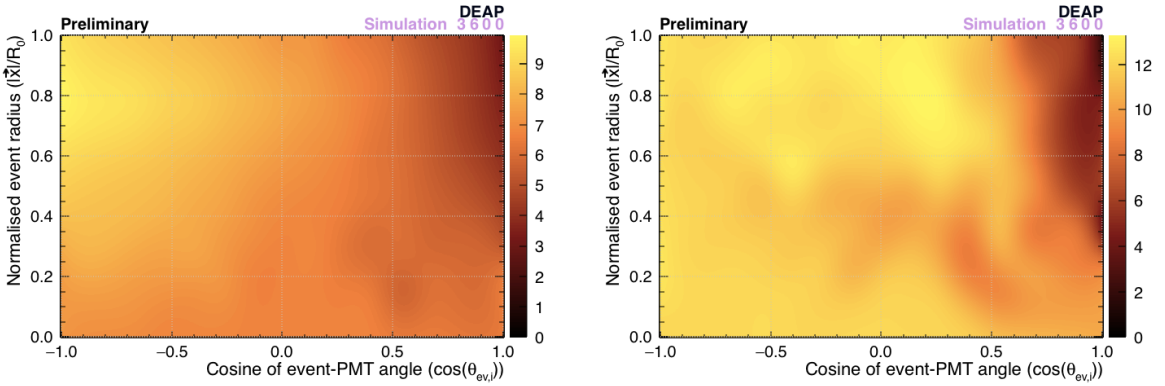

(a) θ_1 (b) θ_2

Figure 4.19: Exponential parameter, θ (colour axis), plotted against event vertex radial co-ordinate (normalised to $R_0 = 851$ mm) and cosine of the angle $\theta_{ev,i}$ shown in Figure 4.16.

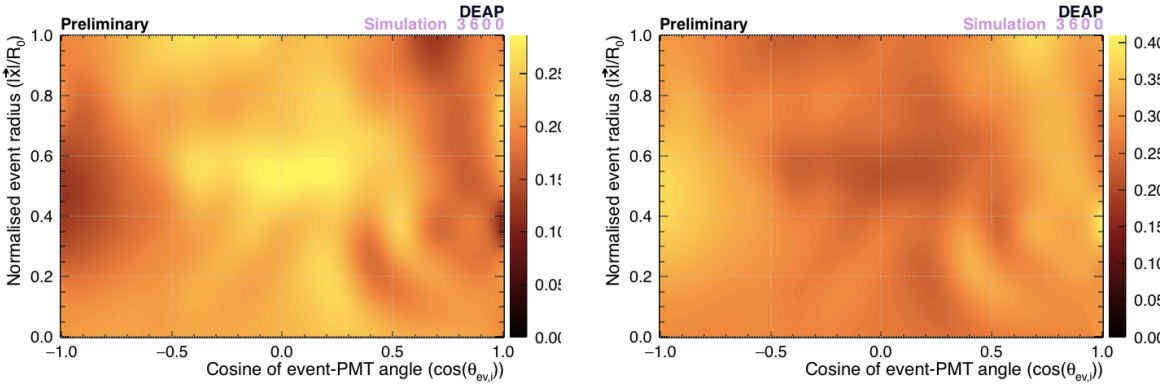

(a) N_1 (b) N_2

Figure 4.20: Normalisation weighting parameter, N (colour axis), plotted against event vertex radial co-ordinate (normalised to $R_0 = 851$ mm) and cosine of the angle $\theta_{ev,i}$ shown in Figure 4.16. The two gamma distribution model is normalised to unity under the curve after summation of the two gamma distributions.

$\theta_1 \simeq \theta_2$. Here the event is close to the PMT and time of flight is constrained to be short in both gamma distributions. The α_1 and α_2 parameters have small overlapping ranges, with $1.5 \lesssim \alpha_1 \lesssim 3$ and $1.2 \lesssim 2.2$, which indicates that the two gamma distribution shapes are similar. At intermediate distances from a PMT, in the region $0.4 < |\vec{x}|/R_0 < 0.7$, $0.5 < \cos(\theta_{ev,i}) < 0.5$ and at low radii $|\vec{x}|/R_0 < 0.3$, the two gamma distributions merge, with $N_1 \simeq N_2$, $\alpha_1 \simeq \alpha_2$ and the highest χ_1 values. This models the PMT observing non-direct light for events not near to, and off-axis from, the PMT.

Figure 4.21 shows the mean fit χ^2/n_{dof} for a given $\cos(\theta_{ev,i})$ and simulated radius normalised to $R_0 = 851$ mm. The best fits occur towards $\cos(\theta_{ev,i}) = -1$ and $|\vec{x}|/R_0 = 1$,

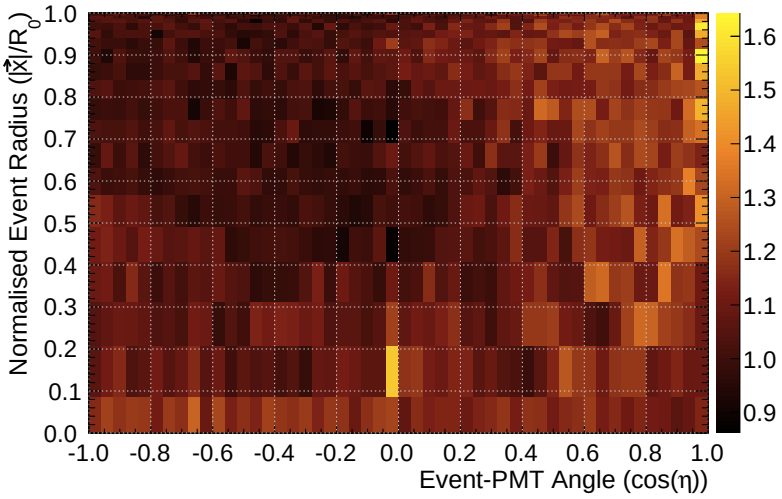

Figure 4.21: χ^2 per n_{dof} (colour axis), plotted against event vertex radial co-ordinate (normalised to $R_0 = 851$ mm) and cosine of the angle $\theta_{ev,i}$.

with a difference in χ^2/n_{dof} between the best and worst fits of approximately 0.7.

The complete table generation routine, from simulation to table generation, requires 5 hours running on 200 CPU cores in parallel. For reconstruction in UberShellFit the computational burden is reduced by generating lookup tables once using cluster computing, and importing the lookup tables later to process data multiple times.

Timing Likelihood

Only pulses close to the observation of the first pulse are used to reconstruct timing, as the earliest photons in the event are most likely to contain time-of-flight information that populates the rising edge of a cathode time distribution. Every photon to arrive at a PMT photocathode within the timing window defined in this section is used to construct the likelihood. The PDF for the cathode arrival time of the r^{th} photon $P_{r,i}(t_{TOF} \mid \vec{x}, n_{PE,i})$ in a PMT i depends on the number of PE $n_{PE,i}$ observed by that PMT, and is calculated from $P_i(t_{TOF} \mid \vec{x})$ as follows:

$$P_{r,i}(t_{TOF} \mid \vec{x}, n_{PE,i}) = P_i(t_{TOF} \mid \vec{x}) \times \left(\int_0^{t_{TOF}} P_i(t' \mid \vec{x}) dt' \right)^{r-1} \times \left(1 - \int_0^{t_{TOF}} P_i(t' \mid \vec{x}) dt' \right)^{n_{PE,i}-r} \tag{4.15}$$

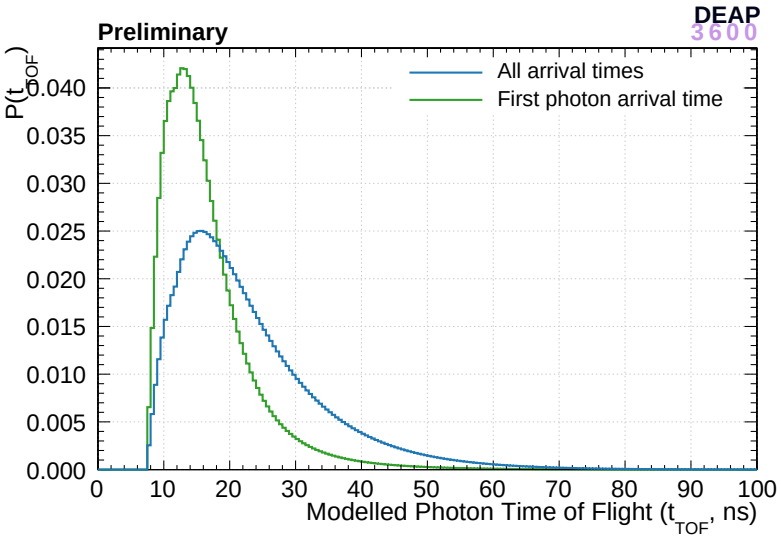

Figure 4.22: Single PMT arrival time PDFs showing modelled time of flight (t_{TOF}) to the PMT photocathode for every photon (blue) and first photon (green) in a PMT which observes 4 PE.

The above represents the product of three probabilities. The first is the probability that the r^{th} photon arrives at the cathode of PMT i at time t_{TOF}, given a hypothetical vertex position $\vec{x}$. The second is the probability that $r-1$ photons arrive before t_{TOF}, and the third is the probability that the remaining $n_{PE,i}-r$ photons occur after t_{TOF}.

An example of a photocathode first arrival time PDF (green) and its original photocathode arrival time PDF (blue) are shown in Figure 4.22. The domain of the first arrival time PDF largely occupies the same domain as the rising edge of its original arrival time PDF.

The r^{th} pulse time PDF including the effect of scintillation timing, PMT transit timing and SCB convolution is then produced by convolving the r^{th} arrival time PDF with the scintillation and PMT transit timing PDFs:

$$P_{r,i}(t(\vec{x})) = P(t_{emission}) * P_{r,i}(t_{TOF}(\vec{x})) * P(t_{PMT}) * P(t_{SCB}) \tag{4.16}$$

where $t(\vec{x}) = t_{emission} + t_{TOF}(\vec{x}) + t_{PMT} + t_{SCB}$. The time likelihood is calculated by evaluating the r^{th} arrival time PDF for each PMT at an observed pulse time in each PMT, and taking the product over all pulses in all PMTs:

$$\mathscr{L}_t(\vec{x}) = \prod_{i=1}^{N_{PMTs}} \prod_{r=1}^{N_{pulse,i}} P_{r,i}(t(\vec{x}) \mid \vec{x}, n_{SC,i}) \tag{4.17}$$

This is then substituted into the combined likelihood, and maximised as before:

$$\mathscr{L}_{Q+t}(\vec{x}, N_{UV}) = L_Q(\vec{x}, N_{UV})\mathscr{L}_t(\vec{x}) \tag{4.18}$$

Pulse times in data are related to times in the model by finding the left (early) edge of the histogram of pulse times for an event, binned in 80 ns bins. The left edge is found by searching the 240 ns range occupied by the selected bin, the bin before it and the bin after it, for the first observed pulse time. This 240 ns range also forms the timing window for the inclusion of pulse times in the likelihood. Pulse times are given by the peaks and sub-peaks found by the pulse finding algorithm. The earliest pulse time is assigned in the model to the time of the peak of the modelled distribution for that pulse in that PMT. All pulse times in the model are then relative to that earliest pulse time, and the earliest pulse is discarded from the likelihood such that it does not bias the reconstruction. A relative time offset factor is applied which is floated as a 5$^{\text{th}}$ parameter in the reconstruction and allows the reconstruction to adjust the earliest pulse time to correct for the earliest hit routine erroneously selecting a noise or early pulse.

Comparing Model to Simulation

The reconstructed timing model is compared to simulated arrival times at each stage of the convolution of cathode and post-transit arrival time PDFs which are available from simulation. Instantaneous isotropic 128 nm photon sources are simulated to model t_{TOF} and $t_{TOF} + t_{PMT}$, and 15 keV$_{ee}$ ^{39}Ar β^- decays are simulated to model $t_{TOF} + t_{PMT} + t_{emission}$. The time of flight PDF $P(t_{TOF})$ is compared to photocathode arrival times in simulation of instantaneous isotropic 128 nm photon sources in Figure 4.23, qualitatively indicating agreement in both rising edge and falling exponential between simulated data and the model reconstructing it. The convolution of the time of flight and PMT transit time PDFs $P(t_{TOF} + t_{PMT})$ is compared to arrival time at the end of a PMT dynode chain in simulation of 128 nm instantaneous photon sources in Figure 4.24, exhibiting qualitative agreement between simulated data and the model reconstructing it. Importantly the combination of double and late pulse features appear as a bump at 80-90 ns, as does a contribution

from early hits near 20 ns, as well as agreement at the rising edge, peak position and late contribution. The convolution with the scintillation time PDF $P(t_{TOF} + t_{PMT} + t_{emission})$ is compared to simulation of 15 keV$_{ee}$ ^{39}Ar events in Figure 4.25, using the appropriate $p_{short,\,long}$ for 15 keV$_{ee}$ electronic recoils. The simulated data agrees at the rising edge, peak position and short and long contributions to the argon scintillation time PDF.

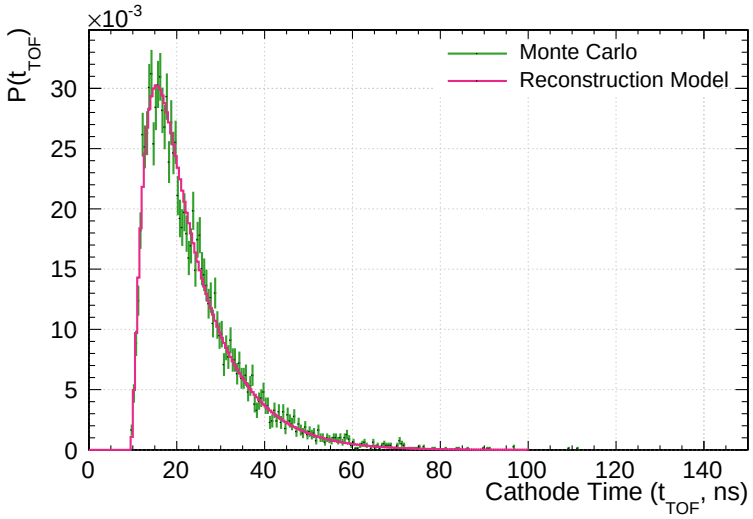

Figure 4.23: Photocathode arrival time PDF, comparing modelled time of flight (pink) to simulated photocathode time for simulated isotropic 128 nm photon sources (green)

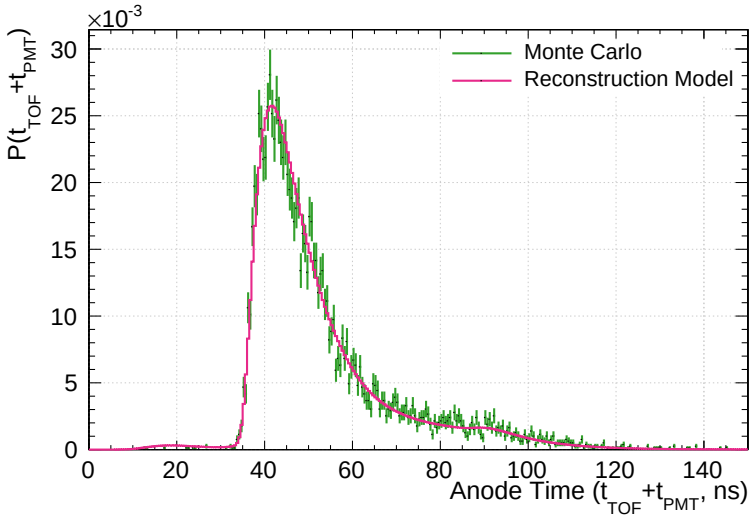

Figure 4.24: PMT anode arrival time PDF, comparing the model of the sum of time of flight and PMT transit time (pink) to simulated anode arrival time for simulated isotropic 128 nm photon sources (green)

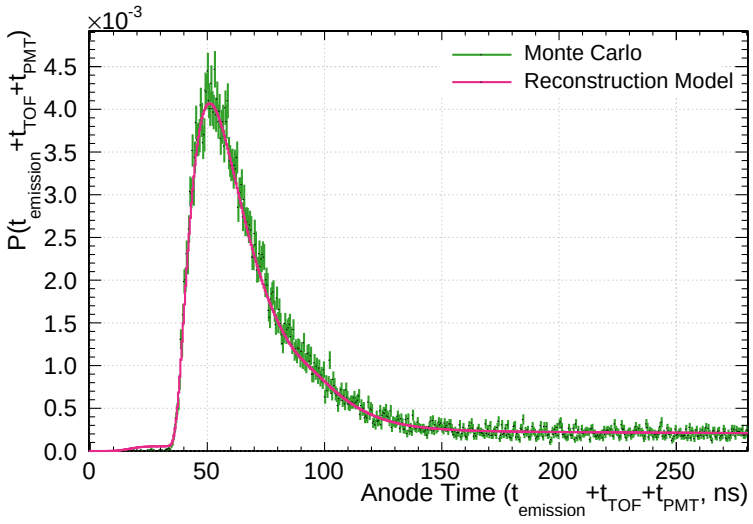

Figure 4.25: PMT anode arrival time PDF, comparing the model of the sum of scintillation emission time, time of flight and PMT transit time (pink) to simulated anode time for simulated ^{39}Ar β^- decays at 15 keV$_{ee}$ (green)

4.6 Performance

This section compares the performance of each of the algorithms discussed above on the reconstructed position distribution of ^{39}Ar decays, the reconstructed radial resolution and bias, and the reconstructed position distribution of alpha decay events originating at the detector surface.

4.6.1 ^{39}Ar

The intrinsic ^{39}Ar contamination is distributed uniformly throughout argon. As a result the event position distribution is flat in cubic radius $R^3 = \mid \vec{x} \mid^3$ at radii smaller than the elevation of the argon fill level above the equator. The same is true of a radius normalised to the AV radius $R_0 = 851$ mm. The blue curve in Figure 4.26 shows the distribution of normalised cubic radius of the simulated event vertex for 1 million ^{39}Ar β^- decays with the ^{39}Ar energy spectrum, distributed uniformly throughout argon. The simulated detector is filled to $z_{fill} = 551$ mm, which is within the error on the calculated in-situ final fill level, and the position distribution deviates downwards from flat beyond the fill level $(z_{fill}/R_0)^3 > 0.27$. The events have the energy spectrum for ^{39}Ar, and a loose energy region of interest cut is made on observed scintillation PE with afterpulsing removed,

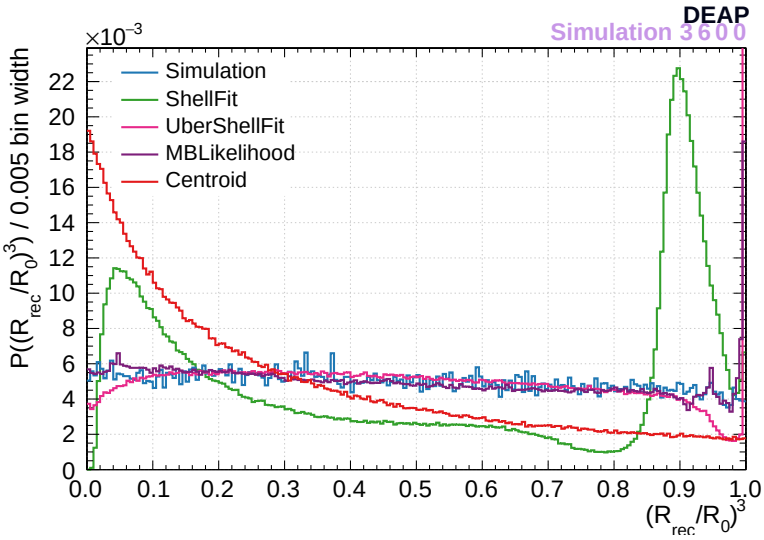

Figure 4.26: Probability of observing a reconstructed or simulated ^{39}Ar event at a radius $(R/R_0)^3$. A loose PE cut selects only those events which observed between 80 and 300 scintillation PE with afterpulsing removed. The blue distribution shows the simulated ^{39}Ar distribution after the cut. The reconstructed distribution for ShellFit is shown in green; UberShellFit is shown in pink; and MBLikelihood is shown in purple. The result of the centroid calculation is also shown in red.

leaving only those events with PE counts in the range $80 < n_{PE} < 300$.

Figure 4.26 also shows the reconstructed position distributions from the original ShellFit (green) and modified (pink) UberShellfit, alongside MBLikelihood (purple). The same histograms are shown as a ratio of reconstructed events per MC event in each bin in Figure 4.27. The blue line at ratio 1 represents exact agreement of the reconstruction with the simulation.

Qualitatively the differences between ShellFit and UberShellFit are noticeable at the lowest and highest radii, $(R/R_0)^3 < 0.2$ and $(R/R_0)^3 > 0.8$. At intermediate radii $0.2 < (R/R_0)^3 < 0.88$, UberShellFit produces a radial distribution which agrees with the simulated distribution more closely than ShellFit. The modification of the TPB solid angle mathematical model in UberShellFit alleviates the peak at high radius seen in the ShellFit distribution, and accounts for the increased uniformity. In the original ShellFit mathematical model the peak is produced by a false minimum in NLL near, but not at the surface, as NLL increases as the model fails close to the AV radius. A bias towards the centre of the detector is observed in the ShellFit distribution. The bias is caused by forcing the assumption that for an event at the centre of the detector all PMTs must see the same

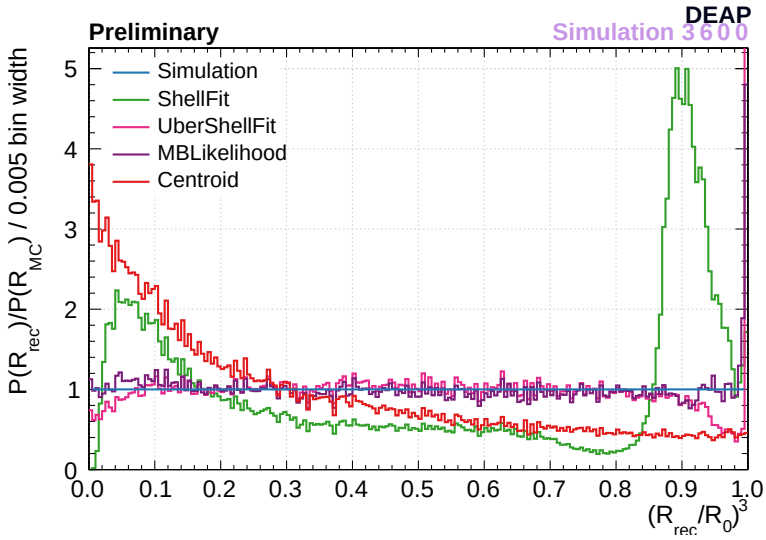

Figure 4.27: The ratio of reconstructed to simulated ^{39}Ar events in a given bin in radius $(R/R_0)^3$. A loose PE cut selects only those events which observed between 80 and 300 scintillation PE with afterpulsing removed. The blue line at ratio = 1 depicts the scenario where reconstruction matches simulation perfectly. The reconstructed distribution for ShellFit is shown in green; UberShellFit is shown in pink; and MBLikelihood is shown in purple. The result of the centroid calculation is also shown in red.

amount of light, and a single bin is used to record this information in the 2D re-emitted photon per UV photon histogram. The centroid calculation is also observed to be radially biased towards the centre of the detector across the range of detector radii. The power hyperparameter a in the centroid is not yet tuned and the standard value is suboptimal. For this reason the centroid calculation will not be featured in future studies in this chapter.

Both UberShellFit to MBLikelihood reproduce the simulated distribution to within statistical fluctuation at radii $(R/R_0)^3 > 0.06$. Below this radius the UberShellFit distribution deviates downwards relative to simulation to a maximum deviation of 38% from the simulated curve in the bin closest to $R = 0$ mm, limited by the coarse histogram binning and lower photon count used in its simulation compared to MBLikelihood. The same effect is also present at radii $(R/R_0)^3 > 0.9$, or $R > 821.6$ mm, with a maximum deviation of 65% at $(R/R_0)^3 = 0.9825$, or $R = 846.01$ mm.

MBLikelihood does not deviate at the same low and high radius ranges, but in those same ranges spikes are observed in the bins at $(R/R_0)^3 = 0.0475,\ 0.9475$ which persist using different bin widths. These spikes correspond to two of the twenty radial posi-

tions represented by each of the MBLikelihood lookup splines in $\theta_{ev,i}$. A cubic spline interpolation between the twenty lookup table radii is used to determine the predicted charge in each PMT, as discussed in Section 4.3. When the likelihood is evaluated during minimisation, for those twenty radii the predicted charge is not interpolated and a small local minimum in NLL is observed compared to interpolated values. The local minima can cause the reconstruction to return one of the twenty radii if the likelihood is calculated at or near one of those radii. Because the surface area of a sphere of a given radius increases with the square of the radius of the sphere, there are more possible positions in the detector at which this effect can occur for high radii than there are for low radii. Because UberShellFit stores continuous splines in radius and during reconstruction interpolates in angle between position vector and PMT $\theta_{ev,i}$, no such spiking is observed in the UberShellFit reconstructed ^{39}Ar distribution.

In ShellFit, UberShellFit and MBLikelihood a spike feature is observed in the bin closest to R_0, or $(R/R_0)^3 = 1$. The spike exists at R_0 in ShellFit and UberShellFit and $R =$ 850 mm in MBLikelihood and represents a failure mode in the reconstruction algorithm that is the result of the use of boundary conditions in minimisation. The reconstruction is given no information about the variation of charge in PMTs as a result of light sources outside of the AV. To counteract this limits and penalty functions are set which penalise reconstruction at $R \geq R_0$. For example, in UberShellFit and ShellFit a position at $R \geq R_0$ is penalised by returning a NLL contribution calculated according to the largest NLL thus far seen plus $exp((R-R_0)^2)$. This causes a discontinuity in the variation of NLL at positions with radial co-ordinate R_0. At the discontinuity Minuit is unable to calculate a derivative in NLL with respect to each spatial co-ordinate. The minimisation is terminated at the discontinuity and returns a position at radius R_0. For MBLikelihood the peak occupies wider range of radii than the UberShellFit peak, but its exact origin is currently under investigation.

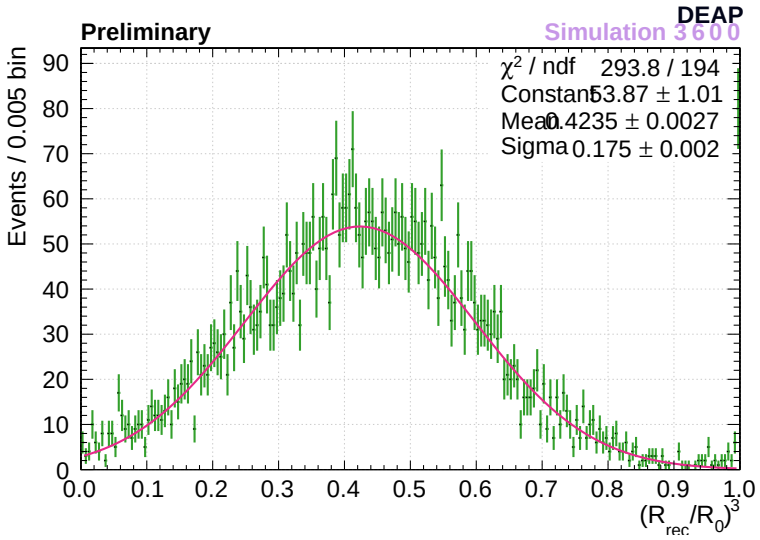

Figure 4.28: Number of events reconstructed per bin in $(R_{rec}/R_0)^3$, shown in green and the fit to a Gaussian, shown in pink, for $R_{MC} = 595.7$ mm.

4.6.2 Radial Resolution

Another measurement of the performance of a reconstruction algorithm comes from the study of radial bias and resolution. The radial resolution function is constructed by comparing reconstructed and simulated radial positions. The distribution of reconstructed radii R^3_{rec}, can be approximated by a Gaussian as shown for $R_{MC} = 595.7$ mm in the distribution of $(R_{rec}/R_0)^3$ in Figure 4.28. That is, $R^3_{rec} \sim \text{Gaus}(\mu_c, \sigma_c)$, where σ_c is the radial resolution in R^3_{rec}, and μ_c is the mean reconstructed cubic radius R^3_{rec}. The linear radial bias μ is then given by $\mu = \sqrt[3]{\mu_c} - R_{MC}$. Two linear radial resolutions in R_{rec} are given by $\sigma_\pm = \mid \sqrt[3]{\mu_c \pm \sigma_c} - \mu \mid$, where $\sigma_+ < \sigma_-$ because a constant difference in R^3_{rec} represents a smaller difference in linear R_{rec} at a larger values of R_{rec}. For example, take a difference $(R_{rec}/R_0)^3 - (R'_{rec}/R_0)^3 = 0.1$. At $(R_{rec}/R_0)^3 = 0.2$ and $(R'_{rec}/R_0)^3 = 0.1$ the difference $R_{rec} - R'_{rec} = 102.67$ mm. At $(R_{rec}/R_0)^3 = 0.3$ and $(R'_{rec}/R_0)^3 = 0.2$, the difference $R_{rec} - R'_{rec} = 72.02$ mm.

At lower radii the above approximation breaks down. In the range $(R_{rec}/R_0)^3 < 0.26$ the Gaussian distribution is truncated at $R_{rec} = 0$ as shown for $R_{MC} = 127.65$ mm in the distribution of $(R_{rec}/R_0)^3$ in Figure 4.29. The result is a Gaussian with an unphysical $\mu < 0$. Instead the distribution of linear R_{rec} is approximated by a Gaussian such that

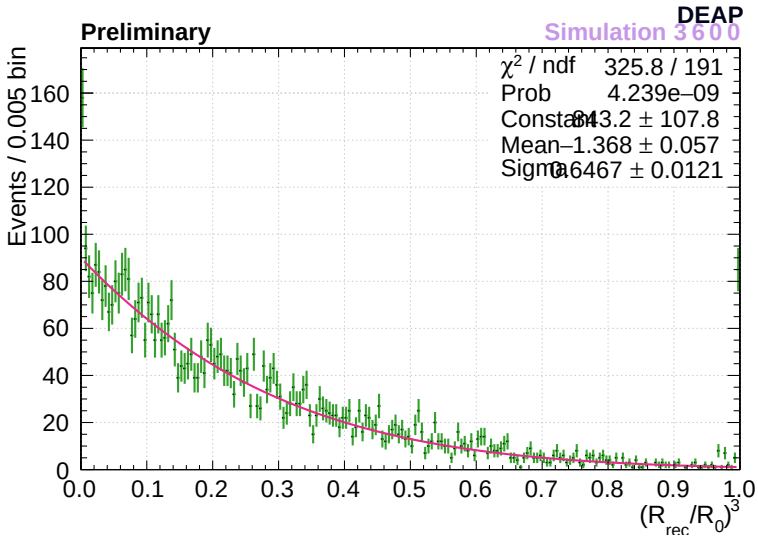

Figure 4.29: Number of events reconstructed per bin in $(R_{rec}/R_0)^3$, shown in green and the fit to a Gaussian, shown in pink, for $R_{MC} = 127.65$ mm. The Gaussian is a poor fit to the cubic radius distribution, which is truncated at $R_{rec} = 0$ and has an unphysical negative mean radius.

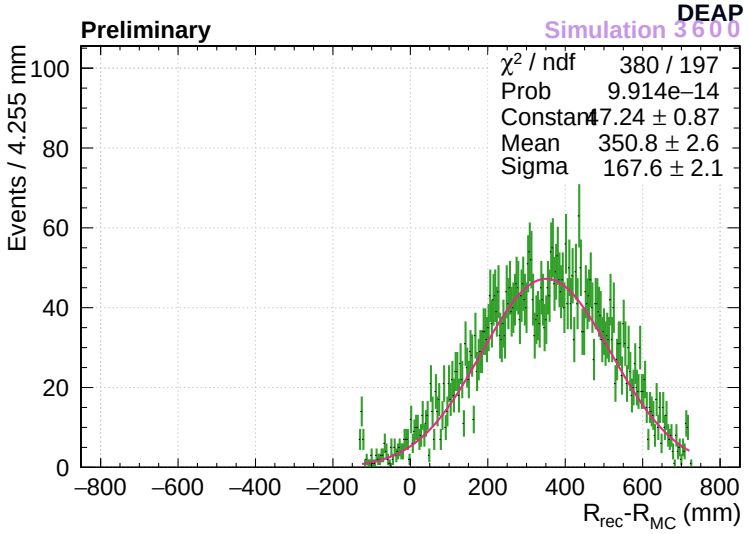

Figure 4.30: Number of events reconstructed per bin vs $(R_{rec} - R_{MC})$, shown in green and the fit to a Gaussian, shown in pink, for $R_{MC} = 127.65$ mm.

$R_{rec} \sim \text{Gaus}(\mu, \sigma)$, where μ is the linear radial bias and σ is the linear radial resolution.

For comparison, the fit to $R_{rec} - R_{MC}$ at $R_{MC} = 127.65$ mm is shown in Figure 4.30. At large radii, the fit to linear radius has asymmetric tails, as shown for $R_{MC} = 595.7$ mm in the distribution of $R_{rec} - R_{MC}$ in Figure 4.31. It was observed that for the shell at $R_{MC} = 553.15$ mm the Gaussian distribution and low radius tail in $(R_{rec}/R_0)^3$ are truncated at $> 2\sigma$ from the mean. $R_{MC,cutoff} = 553.15$ mm was chosen as a conservative lower radius

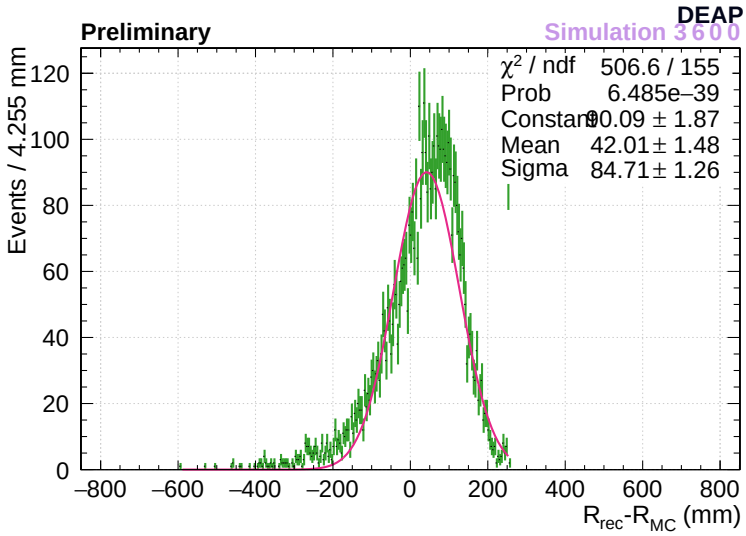

Figure 4.31: Number of events reconstructed per bin vs $(R_{rec} - R_{MC})$, shown in green and the fit to a Gaussian, shown in pink, for $R_{MC} = 595.7$ mm. The Gaussian is a poor fit to the event distribution which has asymmetric tails.

cut-off at and above which fits to the cubic radius are valid, and below which fits to the linear radius are valid.

To study the variation of radial resolution with radius, 12.5 keV$_{ee}$ events are generated in spherical shells at discrete radii which are uniformly distributed in radius, with 5000 events per shell. The distributions R_{rec} and R^3_{rec} are fitted with a Gaussian distribution for each shell. The best fit μ and σ are used from the fit to R_{rec} for $R_{MC} < R_{cutoff}$, and from the fit to R^3_{rec} for $R_{MC} > R_{cutoff}$. For the case of a fit to R^3_{rec} the vertical error bars are given by the difference in σ and μ produced by the uncertainty on the best fit μ_c and σ_c^+. In the linear case the vertical error bars are the uncertainty on the best fit μ and σ.

Figures 4.32 and 4.33 show μ and σ for ShellFit, UberShellFit, UberShellFit+Time, and MBLikelihood, vs the radii R_{MC} of the 20 shells on which events were generated. An outward radial bias $\mu > 0$ is observed in the entire range of R_{MC}, for all reconstruction algorithms. The outward radial bias is observed to decrease at increasing R_{MC}. MBLikelihood and UberShellFit+Time are compared with UberShellFit by calculating the ratio of μ and σ for each to μ_{USF} and σ_{USF} for UberShellFit. The ratios μ/μ_{USF} and σ/σ_{USF} are shown vs R_{MC} in Figures 4.34 and 4.35, where the pink line at ratio 1 represents perfect agreement with UberShellFit. Note that at $R_{MC} >= 723.35$ mm the UberShellFit bias

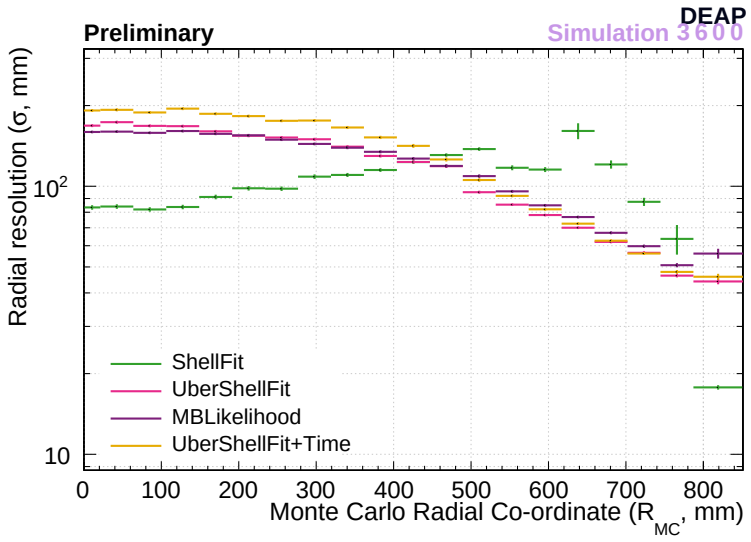

Figure 4.32: Radial resolution σ in mm for events simulated in 20 radial shells with radii R_{MC} distributed at equal spacing in radius between $R_{MC} = 0$ mm and $R_{MC} = 851$ mm. ShellFit is shown in green; UberShellFit is shown in pink; UberShellFit+Time is shown in yellow; and MBLikelihood is shown in purple.

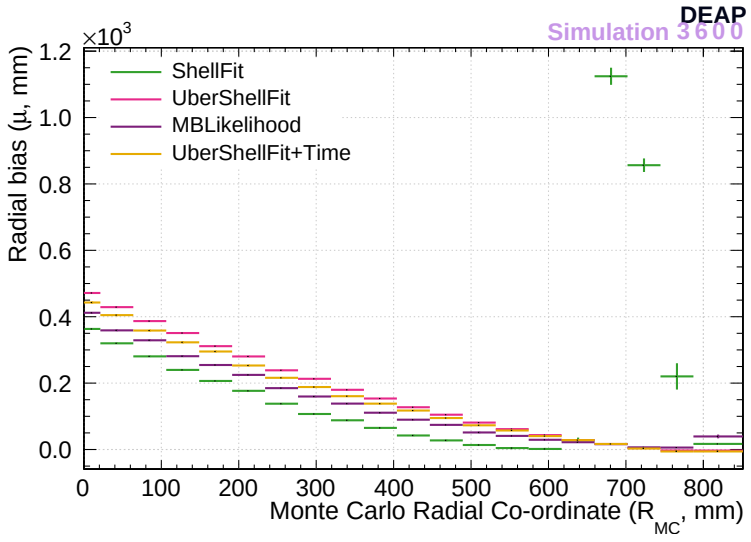

Figure 4.33: Radial bias μ in mm for events simulated in 20 radial shells with radii R_{MC} distributed at equal spacing in radius between $R_{MC} = 0$ mm and $R_{MC} = 851$ mm. ShellFit is shown in green; UberShellFit is shown in pink; UberShellFit+Time is shown in yellow; and MBLikelihood is shown in purple.

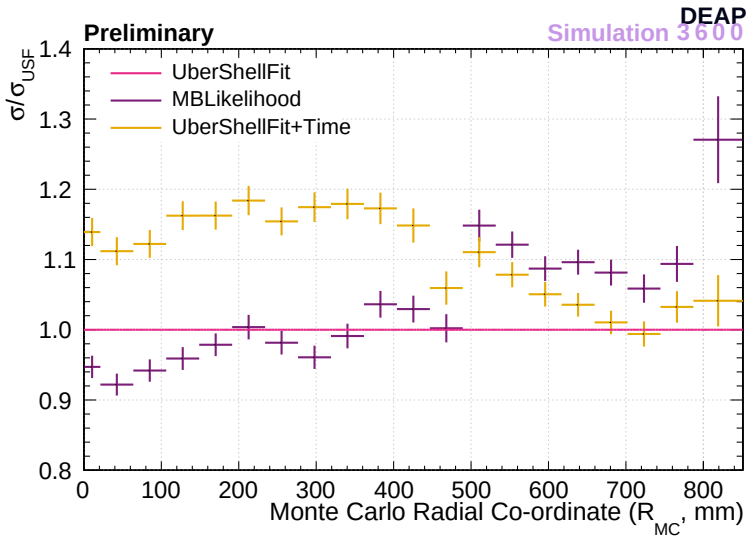

Figure 4.34: The ratio of radial resolution σ to UberShellFit radial resolution σ_{USF} for events simulated in 20 radial shells with radii R_{MC} distributed at equal spacing in radius between $R_{MC} = 0$ mm and $R_{MC} = 851$ mm. UberShellFit+Time is shown in yellow and MBLikelihood is shown in purple. The pink line $\sigma/\sigma_{USF} = 1$ represents perfect agreement between UberShellFit and another reconstruction algorithm.

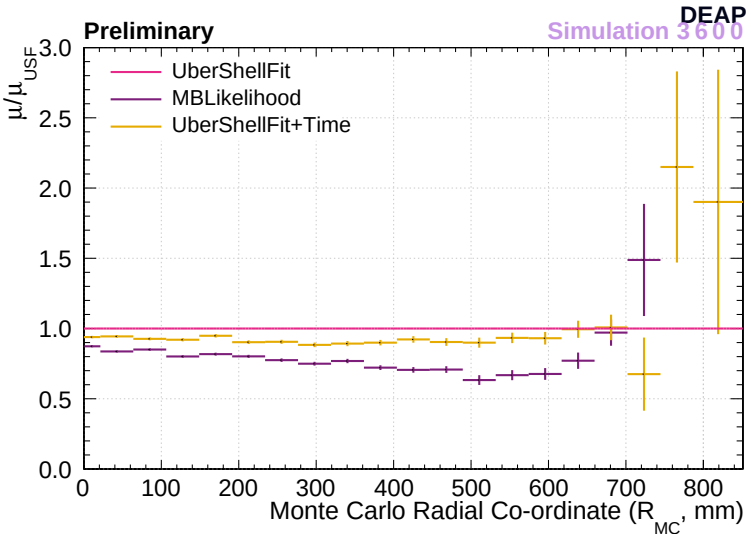

Figure 4.35: The ratio of radial bias μ to UberShellFit radial bias μ_{USF} for events simulated in 20 radial shells with radii R_{MC} distributed at equal spacing in radius between $R_{MC} = 0$ mm and $R_{MC} = 851$ mm. UberShellFit+Time is shown in yellow and MBLikelihood is shown in purple. The pink line $\mu/\mu_{USF} = 1$ represents perfect agreement between UberShellFit and another reconstruction algorithm.

μ_{USF} approaches zero and the ratio μ/μ_{USF} diverges.

The inward radial bias observed in the ShellFit ^{39}Ar distribution is visible at $R_{MC} <$ 600 mm, producing a lower outward radial bias than the other algorithms at the expense of ^{39}Ar uniformity. The high radius geometry feature causes events with R_{MC} near to R_0 to be biased towards the peak observed in the reconstructed ^{39}Ar distribution, which causes the Gaussian distribution to also become biased. The low and high radius biases cause the diverging values of μ at $R_{MC} > 600$ mm and increasing values of σ observed at increasing R_{MC} in Figures 4.32 and 4.33.

UberShellFit+Time exhibits a smaller outward radial bias compared to UberShellFit at $R_{MC} <= 638.25$ mm. The reduction in bias as a proportion of the UberShellFit value reaches a maximum of 11.7% for $R_{MC} = 297.85$ mm. The maximum such bias reduction in linear radius is observed in the R_{MC} bin closest to the centre of the detector, at 28.7 mm. At points in the range $R_{MC} > 638.25$, the UberShellFit and UberShellFit+Time bias curves converge, with less than a millimetre difference in μ at each point in R_{MC}. The addition of the timing offset parameter adds an extra fitted parameter. Given the position dependence of timing information the offset parameter has a non-zero correlation with x,y,z and increases the radial resolution across the range of R_{MC}. The increase in σ relative to UberShellFit reaches a maximum of 18.4% at $R_{MC} = 212.75$ mm. The net effect of adding timing information is a reconstruction algorithm which exhibits less bias away from the true value of R_{MC}, but as a trade-off exhibits increased uncertainty due to the necessity of fitting an extra parameter to align the model with the pulse times it reconstructs.

MBLikelihood exhibits less outward radial bias than UberShellFit at $R_{MC} <= 680.8$ mm. As a proportion of the UberShellFit bias the MBLikelihood bias decreases up to a maximum of 36.7% at $R_{MC} = 425.5$ mm. At $R_{MC} >= 765.9$ MBLikelihood is radially biased outwards compared to UberShellFit, due to the presence of the two spikes observed in that range in the MBLikelihood ^{39}Ar distribution. Relative to UberShellFit, the MBLikelihood radial resolution increases as R_{MC} increases. All but one R_{MC} point in $R <= 340.4$ mm have smaller resolutions than UberShellFit, up to a maximum reduction

of 7.8% of the UberShellFit resolution at $R_{MC} = 42$ mm. For all points at $R_{MC} > 340.4$, MBlikelihood exhibits larger resolutions than UberShellFit, up to a maximum increase of 27.1% of the UberShellFit resolution at $R_{MC} = 808.45$ mm.

4.6.3 Surface Alpha Reconstruction

Another measurement of the performance of each reconstruction algorithm is the probability that a surface background event will reconstruct within a fiducial sphere centred on the centre of the AV. A surface event is said to leak into the fiducial volume if it reconstructs within the fiducial radius, and the probability that it leaks is known as $P_{leak,fid}$ the fiducial leakage. Here the leakage is evaluated using for two fiducial radii currently being considered: 550 mm and 800 mm. From measured contamination level the largest contribution to the surface alpha background is the ^{210}Po decay in the TPB. Two million ^{210}Po decays are simulated in the TPB layer, and the result is reconstructed. An energy region of interest cut is made on observed scintillation PE with afterpulsing removed, accepting only those events which observed between 80 and 240 PE. $P_{leak,ROI} = 10.74\%$ of simulated events satisfy this energy region of interest cut. The fiducial leakage probability $P_{leak,fid}$ is then the proportion of simulated events which reconstruct in the region of interest and fiducial volume. The resulting reconstructed distributions are shown in Figure 4.36.

In the case of surface events the misreconstruction peak bin at $R_{rec} = R_0$ can be thought of as a correct result. Of the reconstructed position distributions shown MBLikelihood has the highest number of events at the AV radius, followed in descending order by UberShellFit, UberShellFit+Time and ShellFit. The MBLikelihood reconstructed radial distribution away from the peak resembles its high radius ^{39}Ar distribution, which has two peaks at $(R_{rec}/R_0^3) > 0.9$. The lower radius peak is located at $R_{rec} = 825.6$ mm, another of the twenty lookup table radii in MBLikelihood, and the wider high radius peak begins at $R_{rec}/R_0 > 0.975$. In this situation the anomalous high radius reconstruction plays in its favour, resulting in a factor 1.496 increased R_0 peak population containing 8.5×10^4 more events compared to UberShellFit. This contributes to a low fiducial leak-

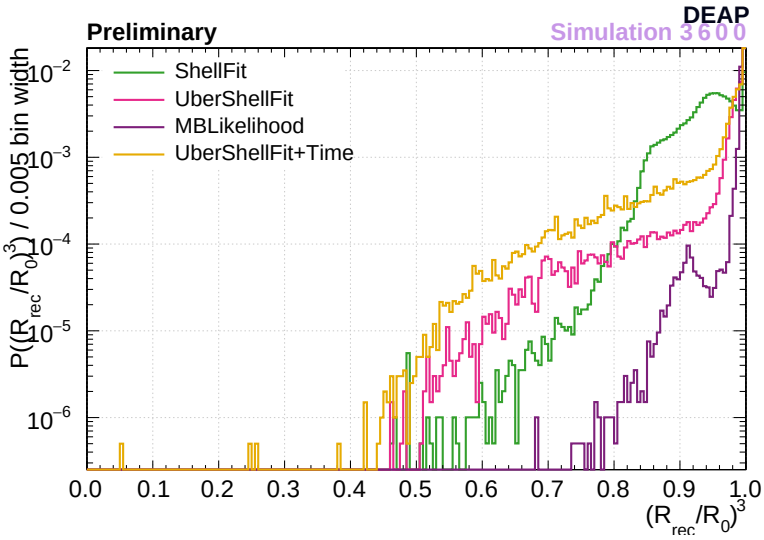

Figure 4.36: The distribution of cubic reconstructed radius $(R_{rec}/R_0)^3$ for 2 million ^{210}Po alpha decays simulated in the TPB layer. ShellFit is shown in green; UberShellFit is shown in pink; UberShellFit+Time is shown in yellow; and MBLikelihood is shown in purple.

age rate below 800 mm, at $P_{leak,fid} = 1.90 \times 10^{-5}$. Because UberShellFit reconstructs with a smaller $R_{rec} = R_0$ peak population than MBLikelihood, more events reconstruct at radii lower than the peak. The feature of the UberShellFit ^{39}Ar radial distribution observed at $(R/R_0)^3 > 0.9$ contributes to an inward bias of surface events. The product of these two effects is a fiducial leakage $P_{leak,fid} = 2.16 \times 10^{-3}$. The increased resolution and decreased outward radial bias of UberShellFit+Time contributes to a higher fiducial leakage $P_{leak,fid} = 7.76 \times 10^{-3}$. Both of the above are close to the nominal requirement $P_{leak,fid} = 1.3 \times 10^{-3}$, which assumes a 550 mm fiducial radius. From this study for an 80-240 PE ROI, a 777.12 mm fiducial radius would have UberShellFit satisfy the nominal leakage requirement. For a 550 mm fiducial radius only UberShellFit+Time exhibits any leakage at this statistical level with $P_{leak,fid} = 1.5 \times 10^{-6}$.

4.7 Conclusion

In this chapter the position reconstruction algorithms used in DEAP-3600 have been described. The position reconstruction algorithms have been benchmarked for consistency with the uniform ^{39}Ar distribution, radial resolution and bias, and performance on sur-

face ^{210}Po alpha events. The UberShellFit algorithm has been described, which produces a reconstructed ^{39}Ar distribution that is consistent with the simulated distribution at $0.06 < (R/R_0)^3 < 0.9$. A mechanism by which timing information can be included in position reconstruction has been described. UberShellFit+Time produces a less radially biased position reconstruction than UberShellFit, but the addition of a fitted time parameter increases its resolution through an additional uncertainty on a fitted time parameter in addition to three position parameters (and energy). This in turn increases its surface event leakage by a factor of 3.59. Time-based position reconstruction will gain position determination power as the next generation of larger detectors are constructed. As detectors are scaled up, the difference in light time of flight between an event at the centre of the detector and a surface event increases compared to recorded pulse time uncertainty.

The reconstruction algorithms each have their own strengths and weaknesses. The UberShellFit algorithm has the benefits of a smooth ^{39}Ar distribution and discrete failure mode. Its fast lookup table generation makes it a good candidate for studies exploring the effect of the variation of optical parameters on position reconstruction. Likewise UberShellFit reconstructs using over an order of magnitude less CPU time than ShellFit, and enables the use of a larger fiducial radius than in ShellFit. A larger fiducial radius increases sensitivity to WIMP signal, but introduces a higher ^{39}Ar background rate, which can be tackled with PSD. MBLikelihood has the best surface event leakage and an ^{39}Ar distribution which is more consistent with uniformity, and is faster than UberShellFit. MBlikelihood however exhibits unphysical spikes in its radial distribution throughout the range of detector radii (including in the fiducial volume) and has a failure mode that is distributed over more radii near R_0 than UberShellFit.

The above issues with each algorithm can be tackled by using position reconstruction in conjunction with other surface event identification techniques than only fiducialisation. An example is cutting on events with high F_{maxpe}, which must be positioned near to PMTs. In either case an understanding of the detector optical model is key to ensuring that a cut is made which is well understood, and consistent between simulation and data.

Chapter 5

Calibration

In this section, the UberShellFit position reconstruction algorithm is adapted for data taken with the laserball, and operated on data taken using the laserball and ^{22}Na calibration sources. Simulations of those sources are used to compare reconstruction of the simulated detector to reconstruction of in-situ data. The radial bias in data compared to simulation is discussed. The ^{39}Ar background is also used as a calibration source with which to discuss those parameters of the optical model which affect the radial bias in simulation and data in position reconstruction.

5.1 Optical Flask Calibration

The UberShellFit algorithm described in Chapter 4 considers the case of isotropic light from recoil events in liquid argon. Reconstructing laserball data required adaptation of the assumptions made about the event vertex to model the new optical source. The adaptation of UberShellFit to reconstruct the laserball data is described in this section. The adapted algorithm is used to reconstruct a simulation of the laserball and the in-situ laserball data. The performance on simulation and data are then compared to the known locations of the laserball.

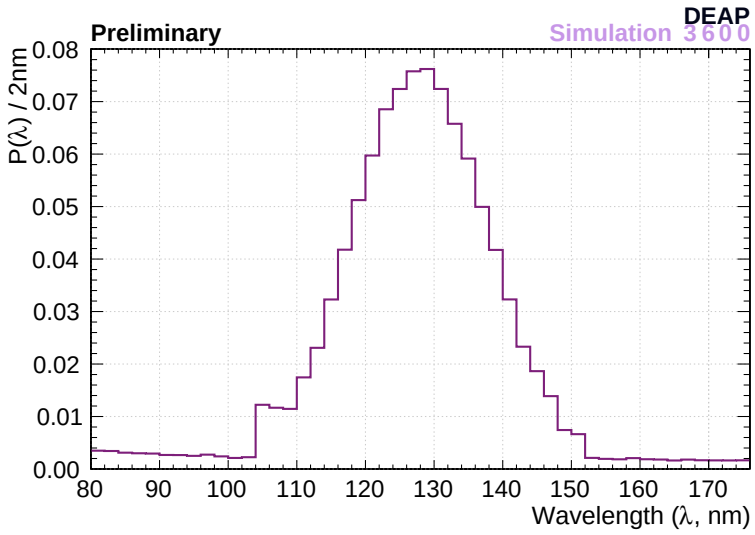

Figure 5.1: Argon scintillation wavelength spectrum, as recorded in simulation performed in each instance of ShellFit run during initialisation, before iterating over and reconstructing events.

5.1.1 Reconstruction Adaptation

Laser Head Wavelength Variation

In liquid argon scintillation the emission wavelength spectrum of a liquid argon recoil is approximately Gaussian, centred on λ =128 nm, shown in simulation in Figure 5.1. In measurements performed on the laserball using the 445 nm laser head by M. Kuzniak, the laserball emission wavelength spectrum was also approximately Gaussian, with a mean at λ =445 nm. The wavelength distributions in Figure 5.2 show the measured laserball wavelength distribution using a 445 nm laser head, and the same distribution translated to a mean of λ =375 nm. These laserball wavelength spectra are implemented instead of the argon scintillation wavelength spectrum in the simulation which is used to generate UberShellFit's lookup tables.

The modified wavelength spectrum also changes the ratio of the number of emitted photons to observed PE. In simulation of an isotropic point source with a singular wavelength distribution $P(\lambda) = \delta(\lambda - \lambda_{emit})$, the distribution of emitted photons per observed PE for λ_{emit} = 128 nm differs from λ_{emit} = 375 nm and λ_{emit} = 445 nm, as shown in Figure 5.3. In the simulation performed during initialisation, UberShellFit was adapted to calculate the mean PE per photon $\bar{n}_{PE/photon}$ using photons with the measured wave-

length spectra in Figure 5.2. The value of mean PE per photon observed from simulation is used in UberShellFit to seed the minimisation with an estimated value for the number of emitted photons from $N_{UV} = n_{PE,total} \times \bar{n}_{PE/photon}$ given the observed number of PE.

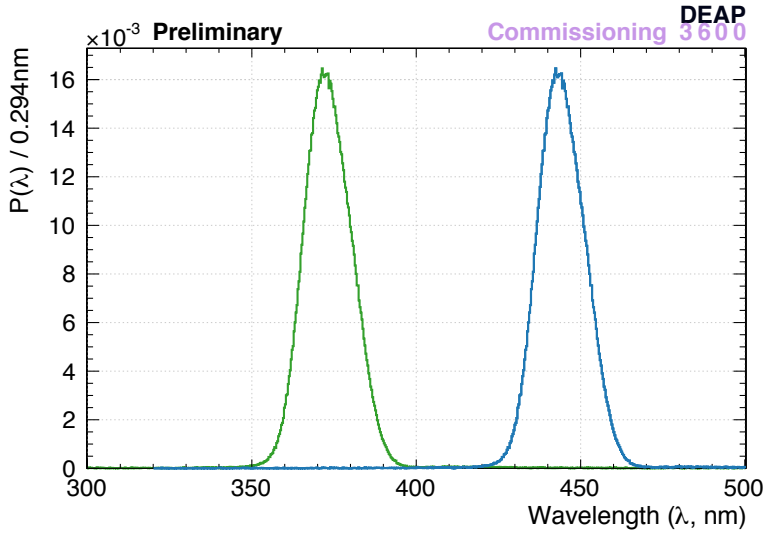

Figure 5.2: Laserball emission wavelength spectrum, as recorded by M. Kuzniak using the 445 nm laser head and extrapolated to 375 nm laser head, shown in blue and green respectively.

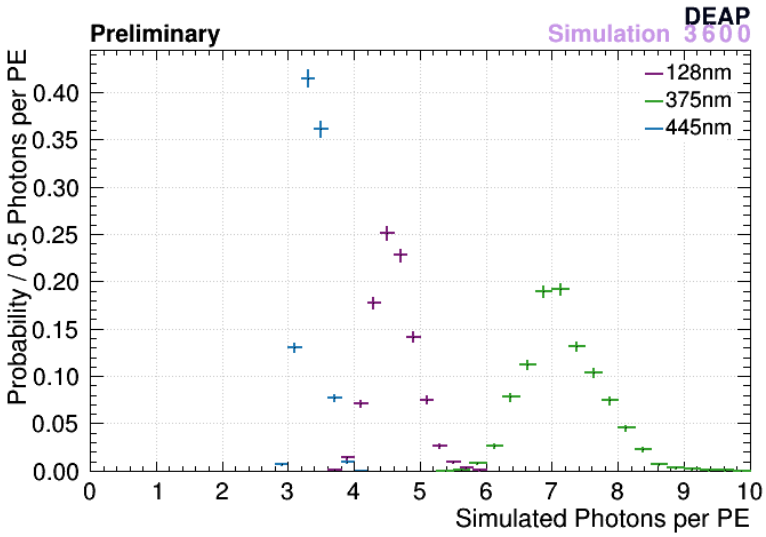

Figure 5.3: Simulated photons per PE for isotropic point sources with wavelength distributions $P(\lambda) = \delta(\lambda - \lambda_{emit})$, at the argon scintillation wavelength $\lambda_{emit} = 128nm$ in purple and at the laserball laser head wavelengths $\lambda_{emit} = 375nm$ in green and $\lambda_{emit} = 445nm$. Note that the lowest photon per PE values correspond to the highest yields of PE per photon.

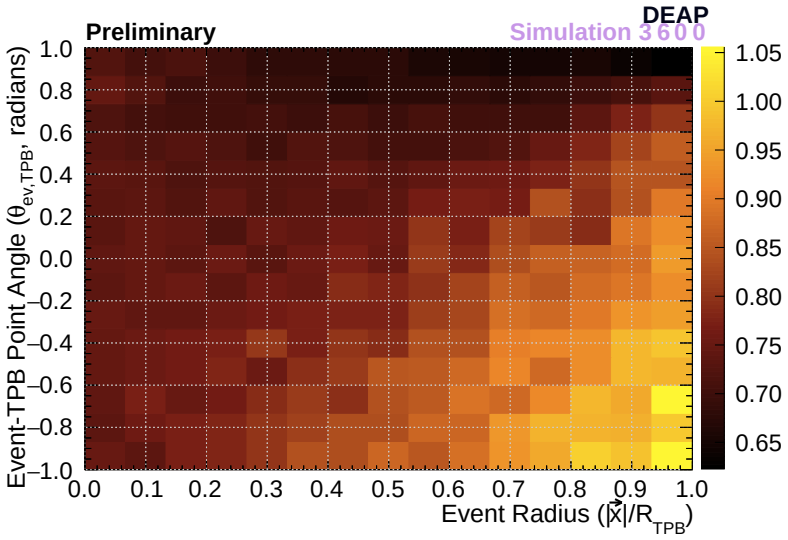

Figure 5.4: Number of photons re-emitted by TPB per incident UV photon, $W(\Omega,\vec{x})$ (colour axis), at any point Ω on the TPB surface. Shown against the radial co-ordinate $|\vec{x}|$ of the event and the deviation angle between the event position vector and the TPB re-emission position vector. Generated using the extrapolated 375 nm wavelength spectrum, analogously to Figure 4.9 in Section 4.4.3.

TPB Interaction

The standard UberShellFit reconstruction model also assumes that light emitted from the event vertex is absorbed by TPB, and light is re-emitted before reaching a PMT. This is violated by the wavelength dependence of the transmittance of TPB at incident wavelengths near the laserball wavelength spectra. The TPB transmittance increases between 375 nm and 445 nm, where at 375 nm all photons excite TPB and at 445 nm all photons are transmitted.

For incident light with the 375 nm wavelength spectrum, the proportion of TPB re-emission light produced per incident photon varies with event position relative to the TPB. A new $W(\Omega,\vec{x})$ lookup table is generated in simulation, analogously to the 128 nm argon excitation light case as shown in Figure 5.4. In simulation using the 445 nm wavelength spectrum in Figure 5.2, 99.5% of all photons that cross the TPB boundary are transmitted through TPB independent of position of the source relative to the TPB. Re-emission accounts for 0.05% of photons that produce PE in this case and the use of a lookup table is disregarded in favour of assuming a fixed effective 100% transmission probability. This is because 2000 PE would need to be observed in a single laserball

event for one re-emission PE to be observed, and a laserball event has a peak PE count at approximately 40 PE. In both cases, the PE production probability $H(\theta_i(\Omega))$ for a PMT i at an angle θ_i from a point Ω on the TPB varies with the incident light wavelength. The $H(\theta_i(\Omega))$ is also re-generated in an analogous fashion to the standard UberShellFit case, using laserball wavelength spectra. The resulting $H(\theta_i(\Omega))$ distributions are shown in Figures 5.5 and 5.6.

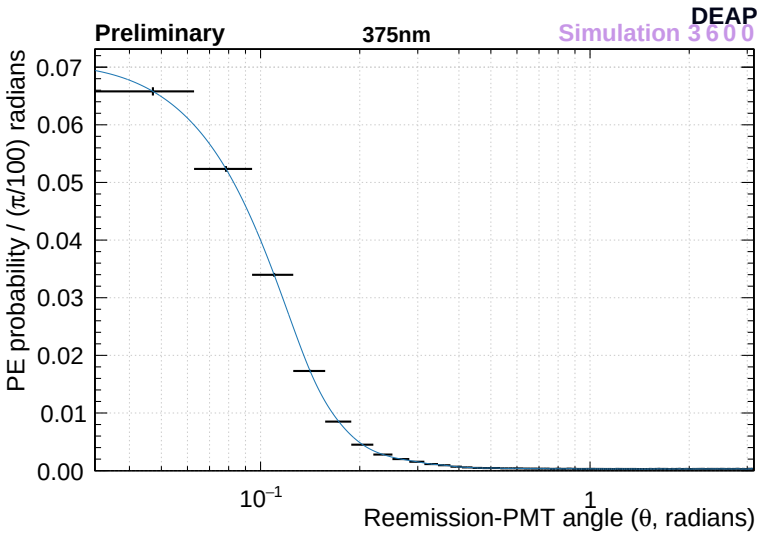

Figure 5.5: PE production probability $H(\theta_i(\Omega))$ at a re-emission angle θ. Generated using the extrapolated 375 nm wavelength spectrum, analogously to Figure 4.4 in Section 4.2.1.

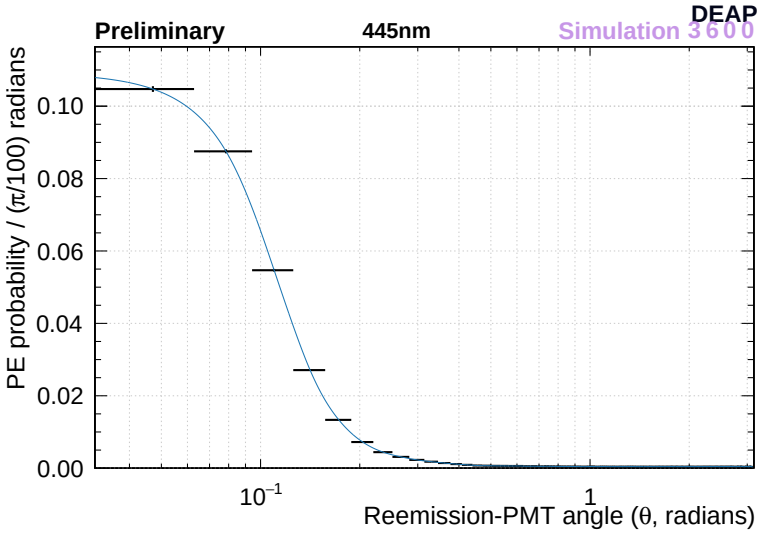

Figure 5.6: PE production probability $H(\theta_i(\Omega))$ at a re-emission angle θ. Generated using the measured 445 nm wavelength spectrum, analogously to Figure 4.4 in Section 4.2.1.

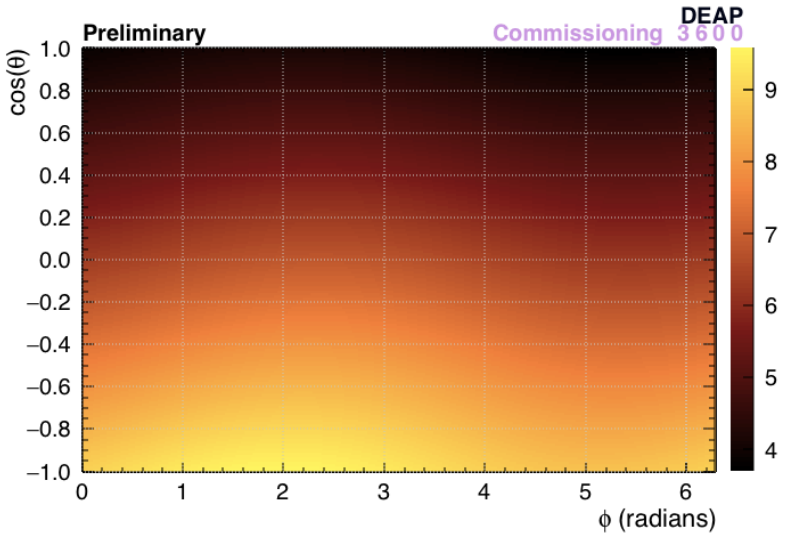

Figure 5.7: Occupancy (colour axis) observed in a PMT in direction θ_i, ϕ_i relative to the laserball surface. This map is produced using a fitting routine designed by N. Fatemighomi.

Source Anisotropy

The assumption of isotropy of the light source is violated by the anisotropy of emission from the laserball surface as observed in commissioning data. Figure 5.7 shows the $P_{hit}(\theta_i, \phi_i)$ of seeing $n_{PE} > 0$ in a PMT i in a given laserball event, oriented at angles θ_i and ϕ_i in a spherical co-ordinate system centred on the laserball. This probability is referred to as the 'occupancy'. The angle θ_i is the zenith angle centred on the laserball, such that $\theta_i = 0$ is parallel to the detector neck axis. The angle ϕ_i is defined as the azimuthal angle centred on the laserball, corrected by the laserball rotation angle ϕ_{LB}. When the laserball is rotated to $\phi_{LB} \neq 0$ the azimuthal angle of a PMT on the map in Figure 5.7 changes as $\phi_i \rightarrow \phi_i - \phi_{LB}$. The difference between the standard detector co-ordinate system $\theta_{pmt,i},\ \phi_{pmt,i}$ centred on the centre of the detector and the co-ordinate system $\theta_i,\ \phi_i$ is illustrated in Figure 5.8 for a translation of the laserball along the z axis. For a laserball in the centre of the detector with $\phi_{LB} = 0$, the angles $\theta_i = \theta_{pmt,i}$ and $\phi_i = \phi_{pmt,i}$.

The occupancy map shown in Figure 5.7 is produced in a multiple step routine designed by N. Fatemighomi. The routine begins by fitting the distribution of occupancy vs PMT ID with a straight line. An example of a fitted distribution of occupancy vs PMT ID for a 445 nm laserball dataset with the laserball located at the centre of the detector is

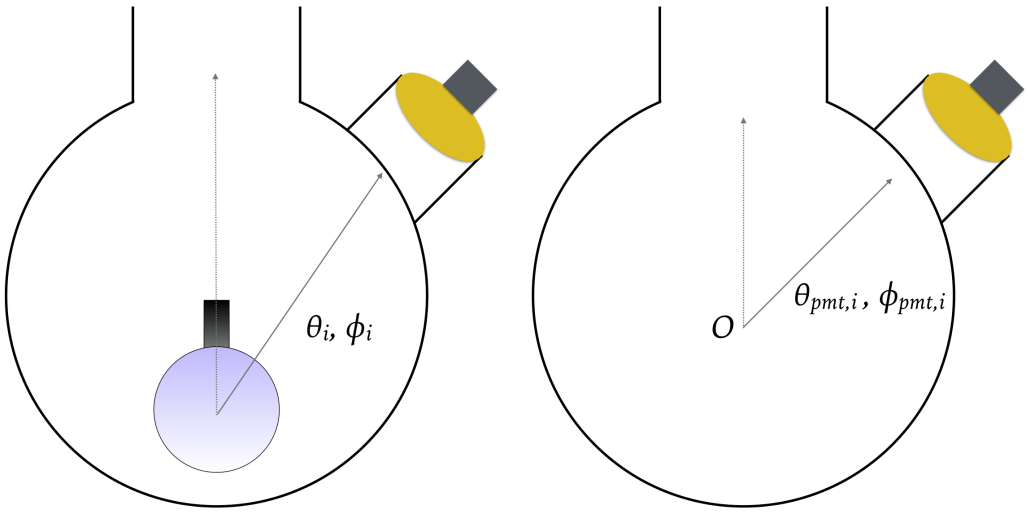

Figure 5.8: Schematic illustrating the difference between the position of a PMT θ_i, ϕ_i in a co-ordinate system centred on the laserball, and the position of a PMT $\theta_{pmt,i}$, $\phi_{pmt,i}$ in a co-ordinate system centred on the centre of the detector. The laserball is translated downwards relative to the centre of the detector. Laserball, AV and PMT dimensions are not to scale.

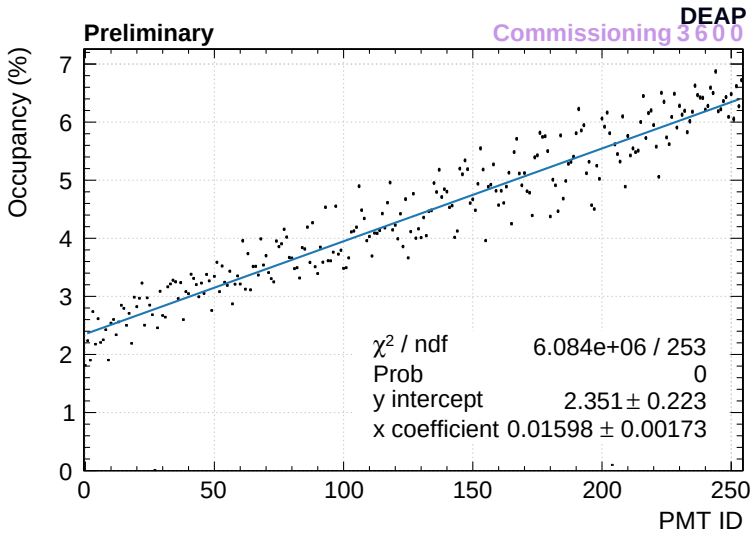

Figure 5.9: Hit occupancy, or fraction (in %) of events in which a PMT sees 1 or more PE, vs the PMT ID of that PE. A cut is made such that only PE observed within a window at ± 4 ns relative to the DTM trigger are considered. PMT IDs are arranged in order of vertical position, from the neck to the bottom of the detector with ascending PMT ID. The laserball is located at the centre of the detector, at a rotation $\phi_{LB} = 0$, and the laserball is illuminated using the 445 nm laser head. The distribution is fitted with a straight line, shown in blue.

shown in Figure 5.9. Note that for all laserball datasets PMT ID 204 was malfunctioning, represented by the very low point below the parameter box in Figure 5.9. PMT 204 is marked as malfunctioning and automatically omitted in subsequent analysis in this section. To isolate only direct light which has not reflected multiple times before producing PE, a timing cut is made to only accept PE detected within ± 4 ns of the trigger time, which is synchronised with the laser pulse generator. The occupancy does not account for PMTs with $n_{PE,i} > 1$, as the mean $n_{PE,i}$ for hit PMT in a 40 PE laserball event $\bar{n_{PE,i}} = 1$ and is dominated by Poisson fluctuations. Of those hit, 26.4% of PMTs see $n_{PE} > 1$, and 8.0% see $n_{PE} > 2$. The occupancy is also independent of light guide and PMT efficiencies $\{\varepsilon_i\}$. Efficiency variation is corrected for by dividing the occupancy in each PMT by the efficiency for that light guide and PMT.

The fitted occupancy is evaluated for each PMT ID, and the occupancies are mapped to PMT positions in spherical co-ordinates. The map is binned in ϕ_i and fitted with a sine function in $\cos(\theta_i)$ and the result is binned in $\cos(\theta_i)$ and fitted with a third degree polynomial in ϕ_i. The result is shown in Figure 5.7 for a 445 nm laser head. The laserball map shown uses occupancy distributions at multiple ϕ_{LB} rotations of the laserball and corrects for the rotation of the laserball. For this reason the non-uniformity is assumed to be an effect caused by the laserball surface, not the non-uniformity of the TPB surface or other detector component.

UberShellFit reconstructs by comparing a model of the total number of PE to the real total number of PE in each PMT, without a PE timing cut. The non-uniformity observed by the reconstruction is characterised using the same mapping procedure as the occupancy non-uniformity, but using the number of PE observed in each PMT, and without the ± 4 ns timing cut. The resulting occupancy distribution and map are shown for data taken using the 445 nm laser head in Figures 5.10 and 5.11. The straight line fit with PMTID has a higher gradient than the case using a timing cut, and a higher fitted minimum of 15.33%. The maximum deviation between fitted occupancy and observed occupancy is at around 20%.

The reconstruction model was adapted such that the set of predicted mean PE $\{\mu_i\}$

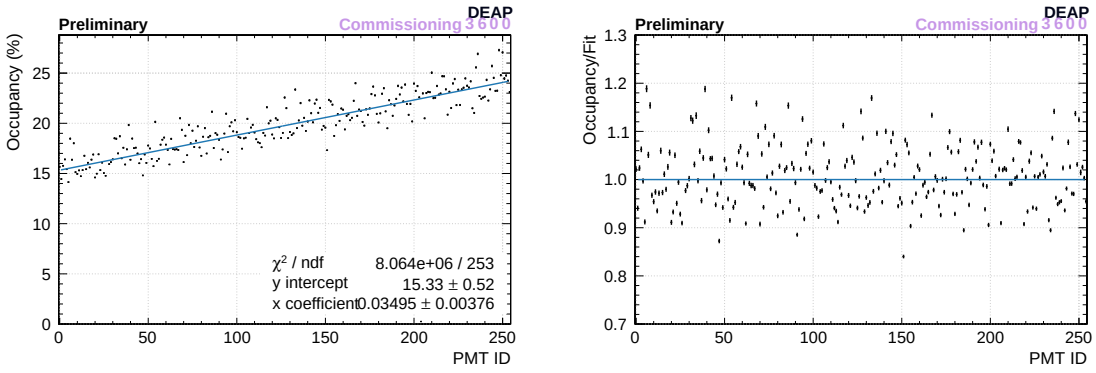

(a) Occupancy (b) Ratio of occupancy to fitted occupancy

Figure 5.10: PE occupancy, or PE per event per PMT, vs the PMT ID of that PE. No timing cut is applied. PMT IDs are arranged in order of vertical position, from the neck to the bottom of the detector with ascending PMT ID. The laserball is located at the centre of the detector, at a rotation $\phi_{LB} = 0$, and the laserball is illuminated using the 445 nm laser head. The distribution is fitted with a straight line in (a), shown in blue. The ratio of fitted occupancy to observed occupancy is shown in (b), where the blue line at ratio 1 represents perfect agreement between observed and fitted occupancy.

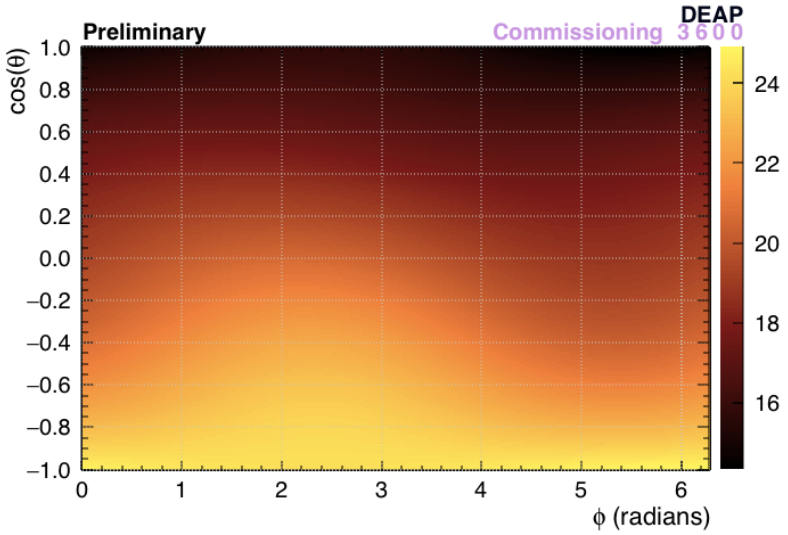

Figure 5.11: PE occupancy (colour axis) observed in a PMT in direction θ_i, ϕ_i relative to the laserball surface. No timing cut is applied. This map is produced using a fitting routine designed by N. Fatemighomi.

that are compared to detected PE counts are re-weighted according to the observed laserball non-uniformity. In the case of an event located at the centre of the detector emitting isotropic light, the probability that a PMT in a direction θ_i, ϕ_i observes $n_{PE,i} > 0$ is equal for every PMT, so $P_{hit}(\theta_i, \phi_i) = P_{hit}(\theta_k, \phi_k)$ for any i and k. In this case the probability that any PE observed in the event (for all PMTs) was observed in a PMT i in a direc-

tion θ_i, ϕ_i relative to the event vertex, for an isotropic event as usually considered by the reconstruction model, is:

$$I(\theta_i, \phi_i) = \frac{P_{hit}(\theta_i, \phi_i)}{\Sigma_i P_{hit}(\theta_i, \phi_i)} = \frac{P_{hit}(\theta_i, \phi_i)}{n_{PMTs} P_{hit}(\theta_i, \phi_i)} = 1/n_{PMTs} \tag{5.1}$$

For non-isotropic emission at the centre of the detector, $P_{hit}(\theta_i, \phi_i) \neq P_{hit}(\theta_k, \phi_k)$ for $i \neq k$, so that the probability that any PE observed is observed in a PMT i, in a direction θ_i, ϕ_i relative to the event vertex is given by the same ratio as in Equation 5.1:

$$N(\theta_i, \phi_i) = \frac{P_{hit}(\theta_i, \phi_i)}{\Sigma_i P_{hit}(\theta_i, \phi_i)} \tag{5.2}$$

The non-uniformity was modelled in reconstruction by adjusting each predicted mean PE μ_i by the ratio of the two weightings, $\mu_i \rightarrow \mu_i N(\theta_i, \phi_i)/I(\theta_i, \phi_i)$. For an event vertex away from the centre of the detector $|\vec{x}| \neq 0$, the solid angle weighting calculation in UberShellFit adjusts μ_i such that PE count variation due to position variation is modelled independently of the non-uniformity of the source.

5.1.2 Position Reconstruction of Commissioning Data

With the above adaptations implemented UberShellFit was used to reconstruct laserball data. UberShellFit was configured to reconstruct using PE counts from charge division, as Bayesian PE counting assumes a timing profile from scintillation in liquid argon. Table 5.1 summarises the properties of each commissioning dataset used in this analysis. The rotation angle is taken relative to a reference rotation angle at $\phi_{LB} = 0$. Only one high occupancy detector dataset exists, with a mean recorded PE count at 350 PE, far above the nominal energy region of interest of 120-240 PE for dark matter search data. Each low intensity dataset contains a factor 10^{-3} less data above 100 PE than the total number of recorded events.

For the dataset from run 11388 from Table 5.1, the laserball was deployed at the centre of the detector, and illuminated using the 445 nm laser head. The F_{prompt} discrimination parameter is plotted against observed PE from charge division in Figure 5.12. The majority of light is observed within the prompt window, and events are observed clustered

Run number	z Position (z, mm)	Wavelength (λ_{laser}, nm)	Relative Rotation (ϕ, degrees)	Mean Occupancy (%)
11388	0	445	90±7	5
11440	550	445	90±7	5
11415	-550	445	90±7	5
11391	0	375	90±7	5
11401	550	375	90±7	5
11433	-550	375	90±7	5

Table 5.1: A table summarising properties of six runs within the laserball dataset.

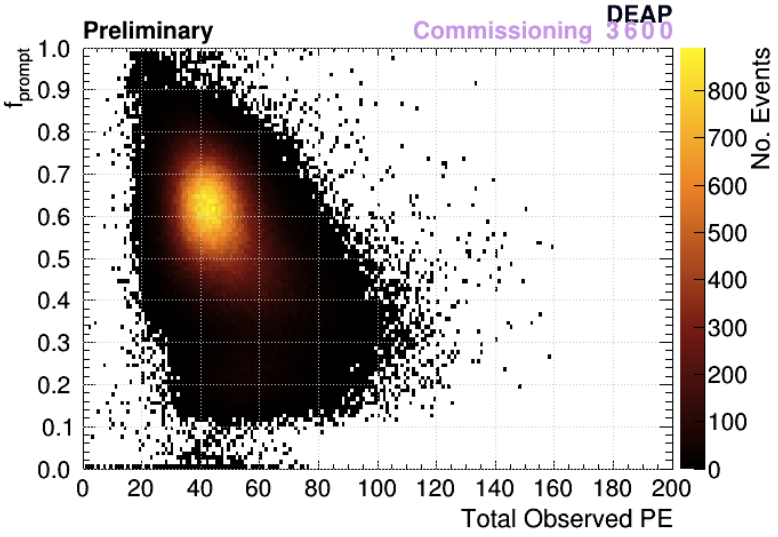

Figure 5.12: F_{prompt} plotted against the total observed PE from charge division. Colour axis is number of events per bin. The laserball is located at the centre of the detector, at a rotation of $\phi_{LB} = \pi/2$, and is illuminated using the 445 nm laser head.

around F_{prompt}=0.64. The low pulse intensity from the driver means the main population of events near n_{PE}=42. The main population in Figure 5.13 shows that the number of hit PMTs is distributed around n_{hit}=38.

The resulting reconstructed position distribution in cubic radius is shown in Figure 5.14. The reconstructed radius peaks at $R_{rec} = 0$. The high radius uniformity deviation feature of the UberShellFit ^{39}Ar cubic radial distribution (see yellow curve in Figure 5.28) is observed at $(R_{rec}/R_0)^3 > 0.7$. An excess of mis-reconstructed events at high reconstructed radius $(R_{rec}/R_0)^3 > 0.9$, is observed. This is caused by events having a low n_{PE} and low n_{hit} compared to the number of PMTs on the detector. A reconstruction based on PE counts which observes a low charge event is sensitive to an upward Poisson fluctuation in PE count, which moves the reconstructed position outwards. Excluding

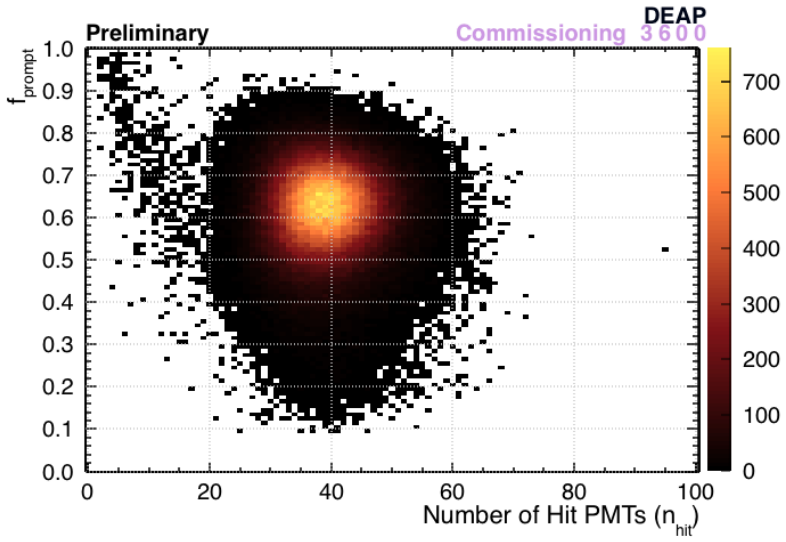

Figure 5.13: F_{prompt} plotted against the total observed PE from charge division. Colour axis is number of events per bin. The laserball is located at the centre of the detector, at a rotation of $\phi_{LB} = \pi/2$, and is illuminated using the 445 nm laser head.

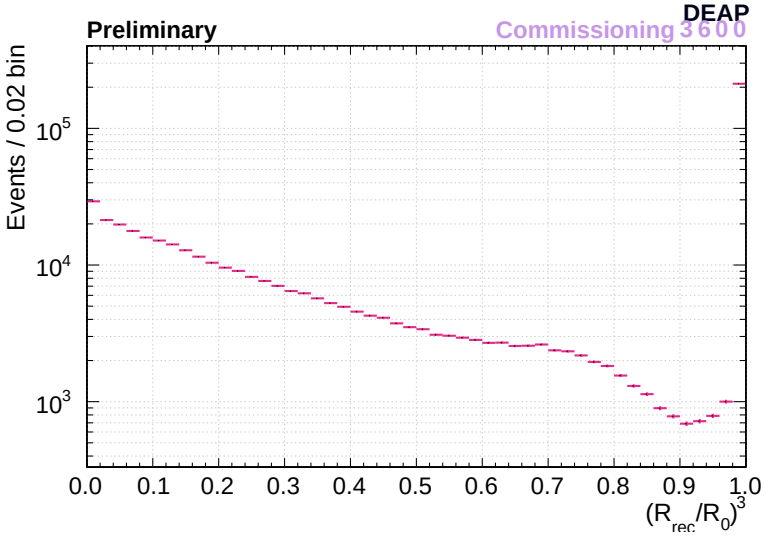

Figure 5.14: Reconstructed cubic radius distribution $(R/R_0)^3$, where $R_0 = 851$ mm is the AV-TPB boundary radius. The vertical axis is on a log scale. The laserball is located at the centre of the detector, at a rotation of $\phi_{LB} = \pi/2$, and is illuminated using the 445 nm laser head.

mis-reconstructed events with $R_{rec}/R_0 > 0.9$ leaves 41.6% of total reconstructed events.

Reconstructed position distributions in the x, y and z co-ordinates for data taken with the 445 nm and 375 nm laser heads in Table 5.1 are shown in Figures 5.15 to 5.17. When the laserball is located in the centre of the detector, reconstructed x, y and z co-ordinate distributions from data are observed to be approximately Gaussian in x, y and z, centred

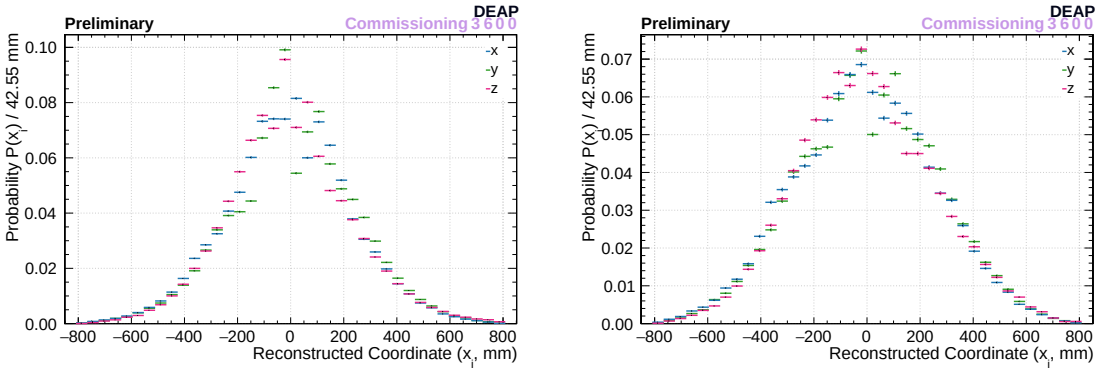

(a) 445 nm (b) 375 nm

Figure 5.15: Laserball data reconstructed co-ordinate distributions in x, y and z. The laserball is located at the centre of the detector, at a rotation of $\phi_{LB} = \pi/2$, and is illuminated using the 445 nm laser head in (a) and the 375 nm laser head in (b).

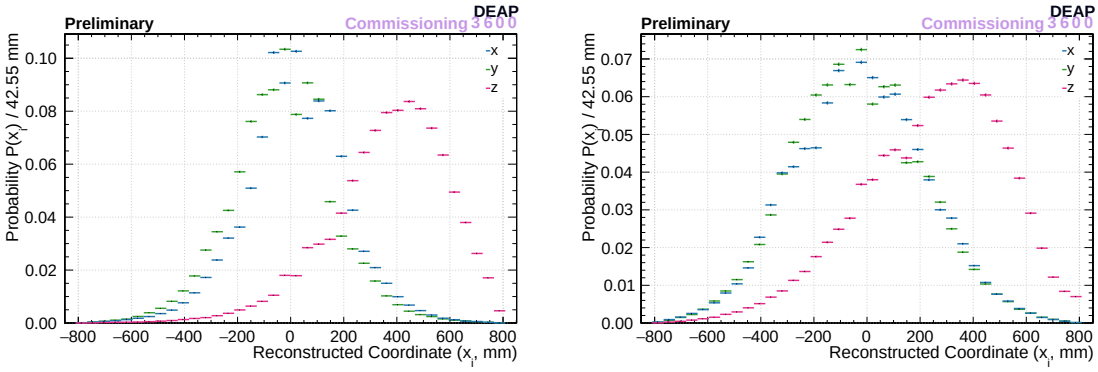

(a) 445 nm (b) 375 nm

Figure 5.16: Laserball data reconstructed co-ordinate distributions in x, y and z. The laserball is located 550 mm above the centre of the detector, at a rotation of $\phi_{LB} = \pi/2$, and is illuminated using the 445 nm laser head in (a) and the 375 nm laser head in (b).

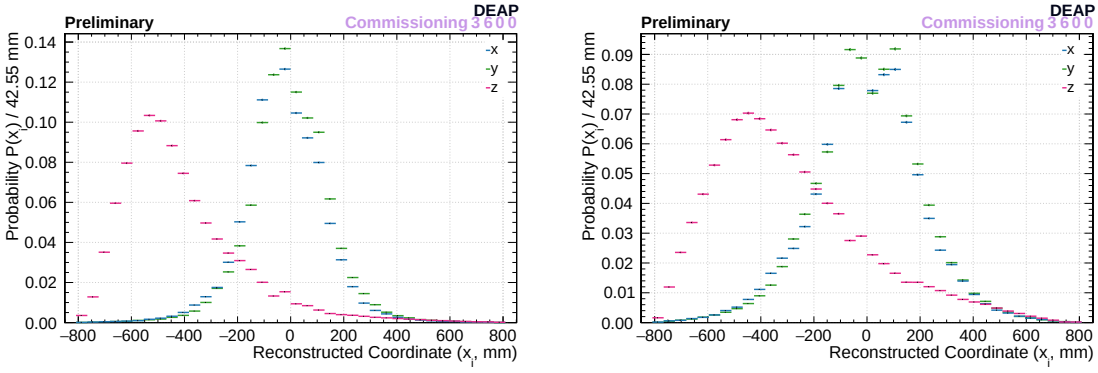

(a) 445 nm (b) 375 nm

Figure 5.17: Laserball data reconstructed co-ordinate distributions in x, y and z. The laserball is located 550 mm below the centre of the detector, at a rotation of $\phi_{LB} = \pi/2$, and is illuminated using the 445 nm laser head in (a) and the 375 nm laser head in (b).

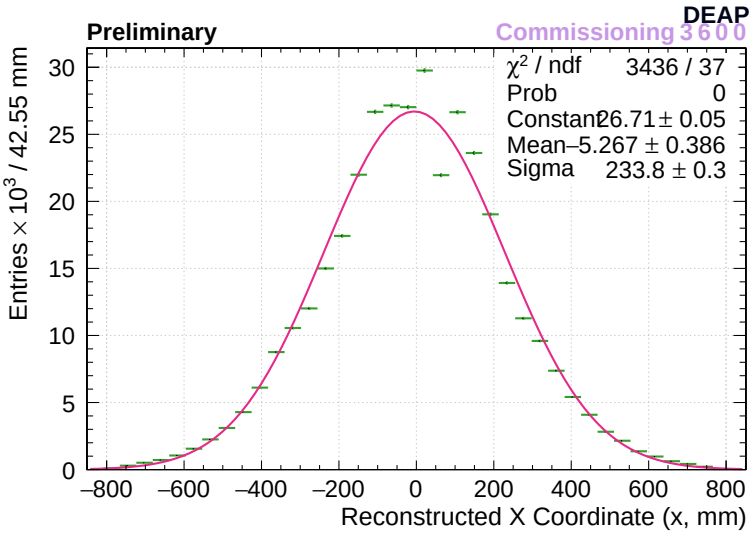

Figure 5.18: Reconstructed co-ordinate distribution in x for laserball data. The reconstructed distribution is fitted with a Gaussian. The laserball is located at the centre of the detector, at a rotation of $\phi_{LB} = \pi/2$, and is illuminated using the 445 nm laser head.

on the centre of the detector. In both the 375 nm and 445 nm cases the z distribution peaks at the centre of the detector. Figure 5.18 shows the x co-ordinate distribution for data with the laserball in the centre of the detector using the 445 nm laser head, fitted with a Gaussian with $\sigma = 233.8 \pm 0.3$ mm, $\mu = -5.267 \pm 0.386$ mm.

For every laserball position the reconstruction on 445 nm data outperforms the reconstruction on 375 nm data. The Gaussian tails for $z = 0$ are observed to be smaller in the 445 nm case. In the cases where the laserball is located at $z = \pm 550$ mm, the x and y Gaussian distributions have smaller σ values in the 445 nm case than the 375 nm case. For example, at $z = +550$ mm a Gaussian fit to the x distribution in the 445 nm case has $\sigma = 261.9 \pm 0.3$ mm, compared to $\sigma = 283.1 \pm 0.4$ mm in the 375 nm case. At $z = -550$ a Gaussian fit to the x distribution yields $\sigma = 191.9 \pm 0.2$ mm in the 445 nm case and $\sigma = 197.1 \pm 0.2$ mm in the 375 nm case.

At $z = +550$ mm the solid angle subtended by the neck opening with respect to the laserball position is larger than at $z = -550$ mm or $z = 0$. The model in UberShellFit assumes a uniform spherical detector, and the neck violates that assumption. The opaque metal neck clamp on the flask assembly is also the closest part of the laserball to the top-most PMTs. It is possible that the resulting shadowing and reflection is not fully included

in the adapted non-uniformity in the UberShellFit model. As a result, misreconstruction peaks are observed in the x and y distributions in both cases and the z distribution is biased inwards. The z distribution in the 445 nm case is peaked at a bin centred on $z = 446.8$ mm. In the 375 nm case the peak is observed at $z = 361.7$ mm. At $z = -550$ mm, the bottom of the laserball emits more light than the top of the laserball, and has opaque no component shadowing it. The higher intensity results in Gaussian distributions with smaller x and y as discussed previously and a more accurate z reconstruction. The 375 nm case exhibits two peaks at the laserball radius either side of $x, y = 0$. The peak of the z distribution in the 445 nm case is observed at $z = -531.9$ mm and in the 375 nm case the peak is observed at the bin centred on $z = -446.7$ mm. Every reconstructed z distribution is peaked either within the 54 mm laserball radius, or, with the exception of the 375 nm $z = +550$ case, within the combination of the laserball radius and a ± 50 mm uncertainty on the laserball elevation.

5.1.3 Position Reconstruction of Laserball Simulations

The laserball was simulated using a GEANT4 geometry of the laserball flask inside the detector using the real dimensions of the laserball as set out in Section 2.7.1. Outward-directed photons are randomly generated on the surface at positions with probabilities weighted by their values on the non-uniformity map shown in Figure 5.7, and omitting the neck of the PFA flask which is obstructed by the steel clamp. The laserball was simulated at elevations at of $z = 0$ mm and $z = \pm 550$ mm relative to the detector centre, as it was during deployment. The simulated DAQ captured every simulated event, analogous to the way that the real DTM was synchronised to the laserball pulse generator. At present, the simulations in this subsection use the same rotations as their analogues in the data listed in Table 5.1, and exhibit the same source intensity. The mapping routine is performed in the same way as for the analysis in the previous subsection, and the resulting non-uniformity maps are applied in reconstruction.

The x, y and z distributions corresponding to simulations of the laserball at $z = 0$ mm and $z = \pm 550$ mm are shown in Figures 5.19 to 5.21. As in data the deviation about the

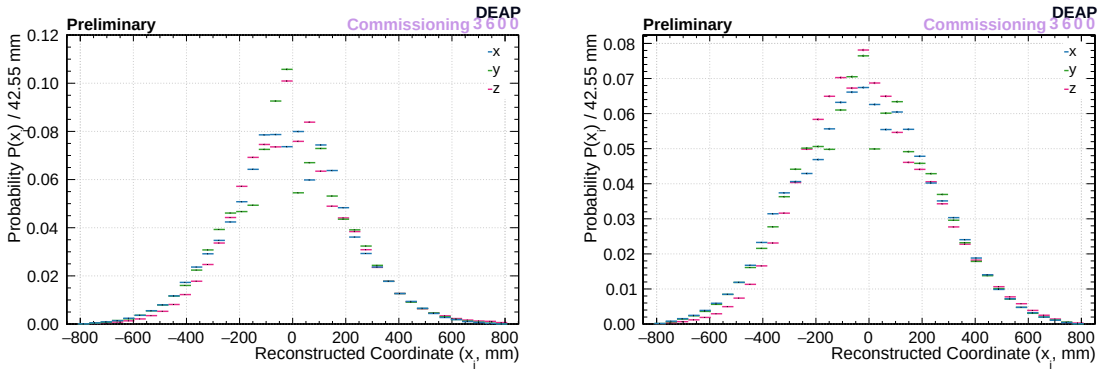

(a) 445 nm (b) 375 nm

Figure 5.19: Laserball simulation reconstructed co-ordinate distributions in x, y and z. The laserball is simulated at the centre of the detector, at a rotation of $\phi_{LB} = \pi/2$. The wavelength distribution from the 445 nm laser head is used in (a), and the distribution from the 375 nm laser head is used in (b).

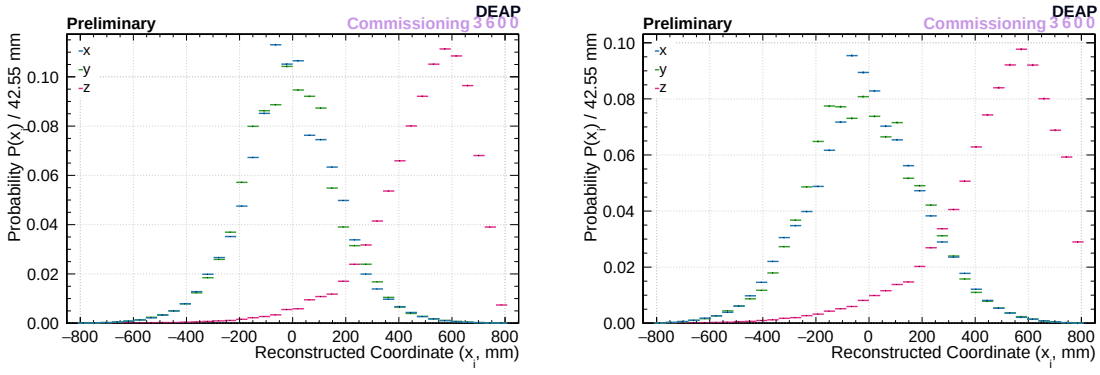

(a) 445 nm (b) 375 nm

Figure 5.20: Laserball simulation reconstructed co-ordinate distributions in x, y and z from simulation. The laserball is simulated 550 mm above the centre of the detector, at a rotation of $\phi_{LB} = \pi/2$. The wavelength distribution from the 445 nm laser head is used in (a), and the distribution from the 375 nm laser head is used in (b).

peak in each reconstructed position distribution decreases with increasing distance from the centre of the detector, with reconstruction of laserball simulation at $z = -550$ mm outperforming that at $z = 0$ and near the neck at $z = +550$ mm. In simulations with the laserball centre placed at $z = \pm 550$ mm, the z co-ordinate distribution peaks at the same bins in each laserball location, at a mean of 45.7 mm radially outwards from $R_{MC} = 550$ mm, within the laserball radius. In Section 4.6.2 an outward radial bias $\mu = +61.2$ mm is observed at $R_{MC} = 553.15$ mm for ^{39}Ar events which produce a mean 88.75 PE. For laserball events which produce a mean 42 PE, without using Bayesian PE counting, the bias at $R_{MC} = 550$ mm is 1.34 times greater than that observed in liquid argon events at

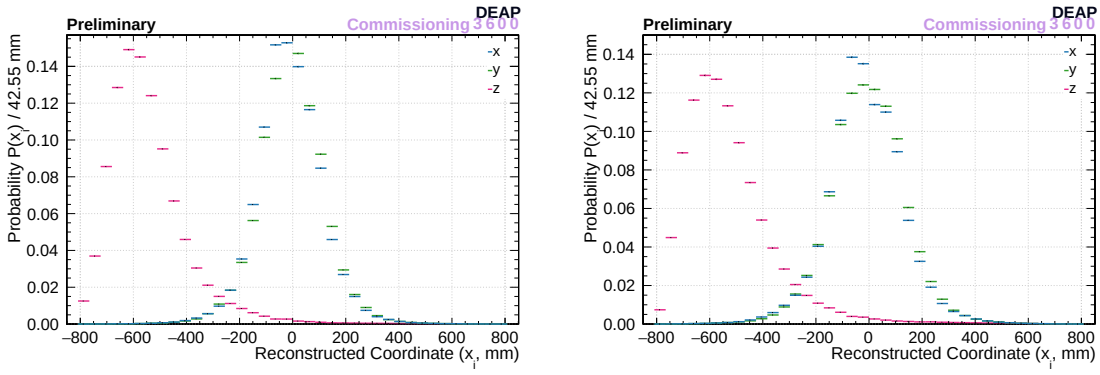

(a) 445 nm (b) 375 nm

Figure 5.21: Laserball simulation reconstructed co-ordinate distributions in x, y and z from simulation. The laserball is simulated 550 mm below the centre of the detector, at a rotation of $\phi_{LB} = \pi/2$. The wavelength distribution from the 445 nm laser head is used in (a), and the distribution from the 375 nm laser head is used in (b).

a mean 88.75 PE. The simulated distributions generally outperform the reconstruction of data in z position, as explored in the next subsection.

5.1.4 Comparison of Simulation to Data

Figures 5.22 through 5.24 compare reconstructed z distributions in data to those in simulation. In the $z = 0$ case, both the reconstructed position from data and simulation are centred on the centre of the detector, and for reconstructed positions at $z \pm 550$ mm the position distributions agree with the laserball position within the total uncertainty on the true laserball position. As mentioned in the previous subsections the reconstructed position distributions in data are biased radially inwards compared to those in simulation where the laserball is placed at $z = \pm 550$ mm. That the effect is radially inward irrespective of the proximity of the laserball to the neck suggests that the neck optics in simulation is not the cause of the discrepancy. That the effect is only observed away from the centre of the detector means that in data there is less light observed in PMTs nearest the laserball than predicted, and more light in PMTs furthest from the laserball. The magnitude of the non-uniformity in the z direction may be overestimated in the mapping routine for data.

Figure 5.25a shows the fitted occupancy plot from a simulation of the laserball at the centre of the using the 445 nm wavelength distribution. The distribution of the ratio of observed occupancy to fitted occupancy in simulation is shown in Figure 5.25b, where

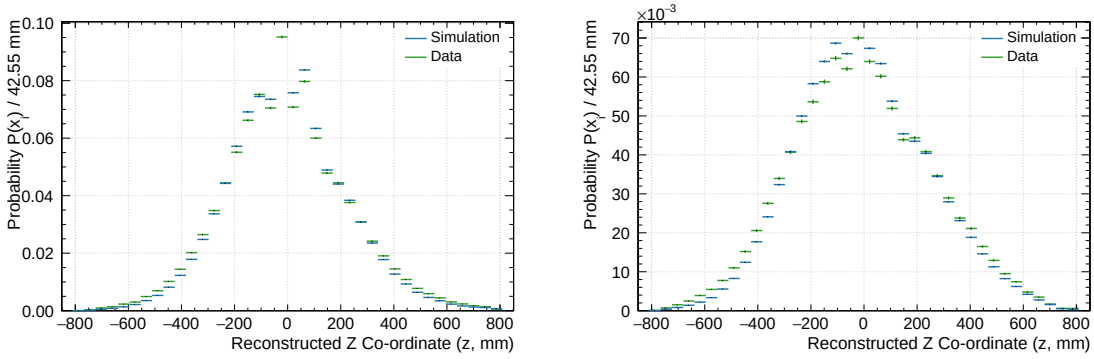

(a) 445 nm (b) 375 nm

Figure 5.22: Comparison of reconstructed z distributions from data and simulation. The laserball is located at the centre of the detector, at a rotation of $\phi_{LB} = \pi/2$. The simulated and real laserball are illuminated using the 445 nm laser head in (a), and the 375 nm laser head is used in (b).

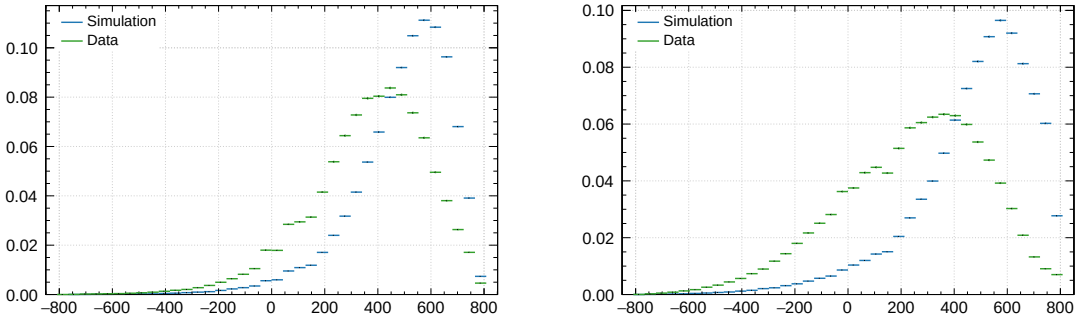

(a) 445 nm (b) 375 nm

Figure 5.23: Comparison of reconstructed z distributions from data and simulation. The laserball is located 550 mm above the centre of the detector, at a rotation of $\phi_{LB} = \pi/2$. The simulated and real laserball are illuminated using the 445 nm laser head in (a), and the 375 nm laser head is used in (b).

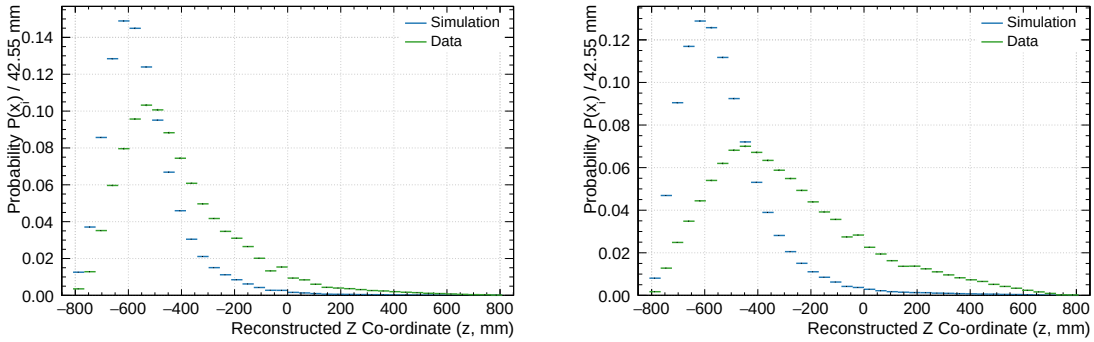

(a) 445 nm (b) 375 nm

Figure 5.24: Comparison of reconstructed z distributions from data and simulation. The laserball is located 550 mm below the centre of the detector, at a rotation of $\phi_{LB} = \pi/2$. The simulated and real laserball are illuminated using the 445 nm laser head in (a), and the 375 nm laser head is used in (b).

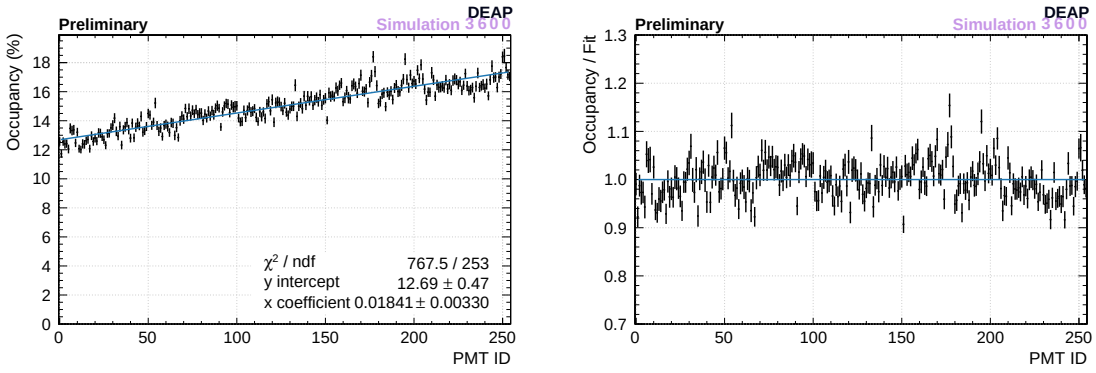

(a) Occupancy

(b) Ratio of occupancy to fitted occupancy

Figure 5.25: Simulated PE occupancy, or PE per event per PMT, vs the PMT ID of that PE. No timing cut is applied. PMT IDs are arranged in order of vertical position, from the neck to the bottom of the detector with increasing PMT ID. The laserball is simulated at the centre of the detector, at a rotation of $\phi_{LB} = 0$. The wavelength distribution from the 445 nm laser head is used. The distribution is fitted with a straight line in (a), shown in blue. The ratio of fitted occupancy to observed occupancy is shown in (b), where the blue line at ratio 1 represents perfect agreement between observed and fitted occupancy.

the blue line at ratio 1 represents an exact match between fitted and observed occupancy. Comparing this simulation with its analogue using data from the laserball in-situ in Figure 5.10b, the observed occupancy from simulation is more tightly distributed around the fit than in in-situ data, with fewer points outside of the range 0.9-1.1. This means the occupancy fit in simulation is more tightly constrained than in data, and an over-prediction of the non-uniformity in z can more easily occur in data than in simulation. Position reconstruction of the laserball is otherwise robust, reconstructing simulation to within one laserball radius of the true laserball centre and reconstructing data to within the combination of the laserball radius and the uncertainty on the real laserball position.

5.2 ^{39}Ar Radial Bias

In this section, the reconstructed cubic radial distribution of ^{39}Ar events in liquid argon from in-situ data is compared to the distribution from reconstruction of simulated ^{39}Ar events. In Chapter 3 the optical parameters which most affect the position reconstruction were explored, and this section continues to explore the effect that those parameters have on position reconstruction.

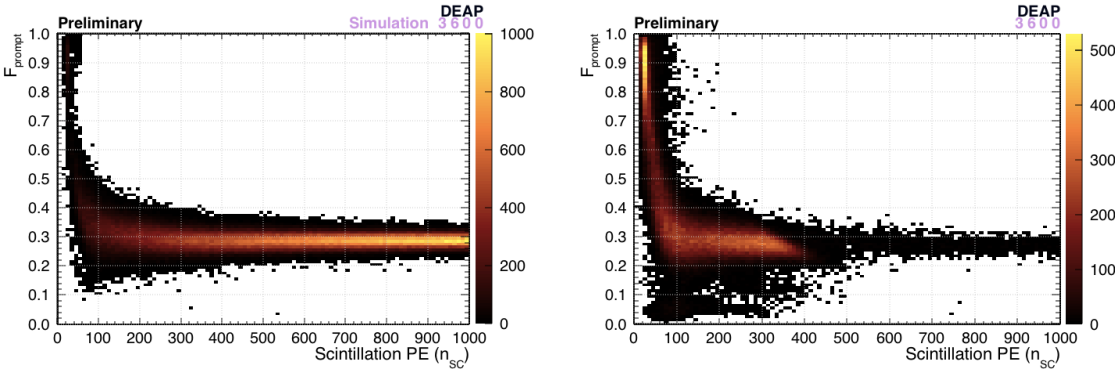

(a) Simulation (b) In-situ data

Figure 5.26: Comparison of the distribution of F_{prompt} vs n_{SC} in ^{39}Ar simulation and data. Colour axis is number of events per bin. The effect of the prescale is clearly visible at high n_{SC}.

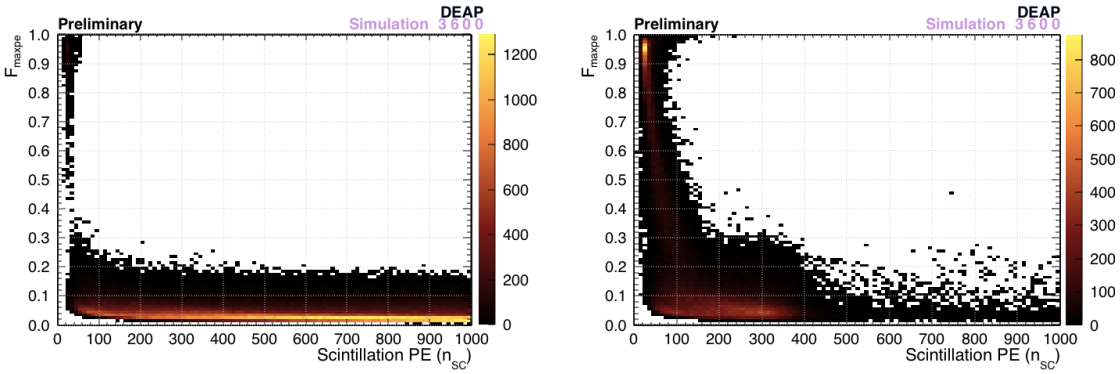

(a) Simulation (b) In-situ data

Figure 5.27: Comparison of the distribution of F_{maxpe} vs n_{SC} in ^{39}Ar simulation and data. Colour axis is number of events per bin.

The reconstruction was performed on data taken after the second fill, at the final argon fill level. The DTM was configured with the standard physics trigger settings listed in Section 3.1.3. The same simulation as was used in Section 4.6.1 is used here. One million ^{39}Ar decays were simulated uniformly distributed in liquid argon filled to $z = 551$ mm above the AV equator, and the physics trigger was used in the DAQ simulation. Figure 5.26 shows the distribution of F_{prompt} vs n_{SC} for the simulated and in-situ data, with the band around $F_{prompt} = 0.3$ corresponding to electronic recoils from ^{39}Ar. A stringent F_{prompt} cut is made to isolate events in the ^{39}Ar band at $0.2 < F_{prompt} < 0.4$. Figure 5.27 shows the distribution of F_{maxpe} vs n_{SC} for simulated and in-situ data. The high F_{maxpe} region at low n_{SC} is Cerenkov radiation in acrylic, and is removed with a stringent cut removing events with $F_{maxpe} > 0.15$. A loose energy region of interest cut is made

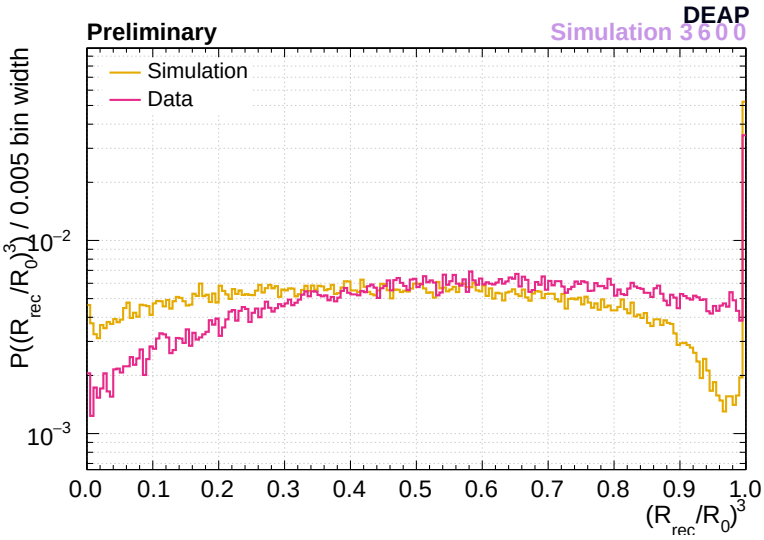

Figure 5.28: Reconstructed cubic radius $(R_{rec}/R_0)^3$ distributions, normalised to the event radius R_0, comparing simulated ^{39}Ar (yellow) to data (pink) in the electronic recoil band. A simulation-data bias is visible on comparing the two.

isolating events with $80 < n_{SC} < 300$, above which the DTM prescale acts to suppress the observed ^{39}Ar rate.

The reconstructed $(R_{rec}/R_0)^3$ distributions are compared for standard simulation (yellow) and in-situ data (pink) in Figure 5.28. The ratio of the probabilities that at an event will reconstruct in each bin is shown in Figure 5.29, where the yellow line at ratio 1 represents agreement between data and simulation. The misreconstruction peak at R_0 is smaller in reconstructed data than reconstructed simulation by 31% of the simulation peak size. An outward radial bias is observed in reconstruction of data compared to simulation, with the two distributions crossing over at $R_{rec} = 652$ mm. The bias is not observed in simulation because the same detector optical and physical properties are used in the simulation generating UberShellFit's tables and this simulation of ^{39}Ar events.

The optical and physical properties of the detector which most affect the ^{39}Ar reconstructed radius distribution are those of argon and TPB, as they are the first media in which light from scintillation and TPB re-emission light propagates. An optical effect which produces the observed radial distribution data using a charge-based reconstruction implies that in data more PE are observed in PMTs nearest to the event and less PE are observed in PMTs furthest from the event, than predicted in standard simulation. The

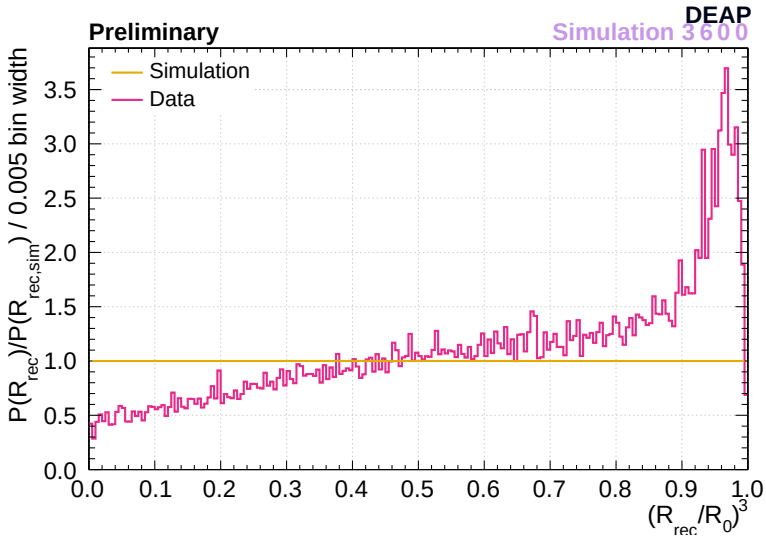

Figure 5.29: The ratio of the probability of an event reconstructing at a given cubic radius $(R_{rec}/R_0)^3$ in data (pink) to the probability in simulation, as compared in Figure 5.28. A ratio at unity represents perfect agreement.

effects of the following parameters are discussed, which produced the largest effects on reconstructed position during the investigation:

TPB scattering length As discussed previously in Chapter 3 the scattering length affects how PE are distributed amongst PMTs dependent on their distance from the source. A recent measurement of the scattering length in TPB by Stolp *et. al.* [143] is discussed in Section 3.3.2.

TPB thickness Affects the minimum distance that light emitted from TPB must propagate in order to leave the TPB layer. The larger the TPB thickness, the longer the average light path length is in the TPB layer, and the more frequently scattering occurs before leaving the TPB. In the simulation the TPB thickness is set at the measured thickness of 3 μm stated in Ref. [131].

Argon scattering length Rayleigh scattering changes the path a photon takes in the argon, which changes its point of incidence on the TPB, and consequently changes the PE count pattern seen across the PMTs. The Rayleigh scattering length of argon in simulation is disputed, as discussed in Section 3.3.1.

UberShellFit lookup tables are generated in advance using the standard simulation

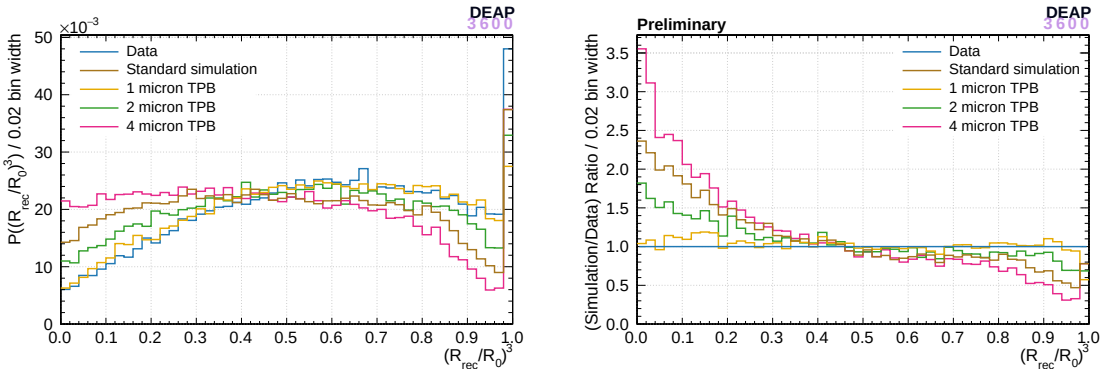

(a) Cubic radius distribution

(b) Ratio of modified to standard simulation

Figure 5.30: Reconstructed cubic radius $(R_{rec}/R_0)^3$ distributions, normalised to the event radius R_0, comparing the effects of changing the TPB thickness to 1, 2 and 4 μm, shown in (a) alongside the distribution from data. The distribution ratio of each modified simulation to the distribution from data is shown in (b). A ratio at unity represents perfect agreement.

optics. By making the same assumptions in reconstruction performed on simulation and adjusted simulation, the mismatch between simulation and data is modelled as the consequence of a mismatch between standard simulation parameters and adjusted parameters which occur in data. UberShellFit was operated using lookup tables generated with standard optics on simulations of 1M ^{39}Ar events in a detector filled with liquid argon to 551 mm above the AV equator with the same cuts as performed on in-situ data, stated above.

In each simulation one optical parameter is changed, and the resulting $(R_{rec}/R_0)^3$ distribution is compared to that from reconstructed data. The TPB thickness was changed to 1, 2 and 4 μm for the $(R_{rec}/R_0)^3$ distributions in Figure 5.30a. The ratio of the probabilities that at an event will reconstruct in each bin are shown in Figure 5.30b. As an example the TPB scattering length is changed to the Stolp value at 2.75 μm and the argon scattering length is changed to the Grace value at 57 ± 4 cm in Figure 5.31a, and the corresponding ratio plot is shown in Figure 5.31b. In each figure the distribution produced by the standard simulation is shown in brown.

The variation of TPB thickness affects the observed radial bias, such that the closer the ratio of the thickness to the scattering length is to unity, the more closely the reconstructed radial distribution replicates the distribution observed in data. This is due to the standard simulation over-predicting scattering in the TPB as seen in the discussion of scattering in TPB in Chapter 3. In the standard simulation this means that a TPB thickness of 1 μm

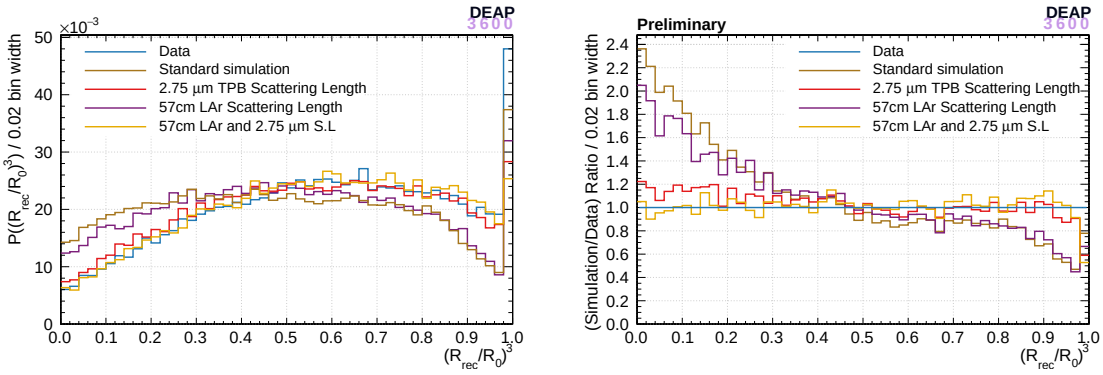

(a) Cubic radius distribution (b) Ratio of simulation to modified simulation

Figure 5.31: Reconstructed cubic radius $(R_{rec}/R_0)^3$ distributions, normalised to the event radius R_0, comparing the effects of changing the argon Rayleigh scattering length to the E. Grace measured value at 57 cm, changing the TPB scattering length to the value favoured by Stolp *et. al.* [143] and both changes at once, alongside the distribution from data. The distribution ratio of each modified simulation to the distribution from data is shown in (b). A ratio at unity represents perfect agreement.

is the thickness that most reproduces the distribution observed in data, which is ruled out by the measurement taken in-situ during TPB deposition [131]. The adjustment to a 1 μm thickness also appears to under-correct the radial distribution by up to a maximum of 10% at $(R_{rec}/R_0)^3 < 0.45$.

Changing the scattering length in TPB also affects the radial bias. The value favoured in Ref. [143] appears to produce a deviation from the data distribution by a maximum of 20% at $R_{rec} = 0$, and with a mismatch near R_0 that is consistent with the 1 μm thickness case. Changing the scattering length in liquid argon changes the distribution most at centre of the detector, where the mean path length of light from the event to the TPB is at its highest. Also shown in yellow in Figure 5.31 is the result of combining the argon scattering length measurement from E. Grace with the higher TPB scattering length from Stolp. The resulting agreement with data using the combination of argon and TPB scattering length changes outperforms the other individual changes at low and high radius.

The result of varying the TPB scattering length in the range estimated by Stolp is shown as a ratio plot in Figure 5.32. The least variation about the unit ratio line is observed for scattering lengths at ≥ 2.75 μm, including the bin nearest R_0 containing the mis-reconstructed events at R_0. No further variation was observed at higher TPB scattering

lengths.

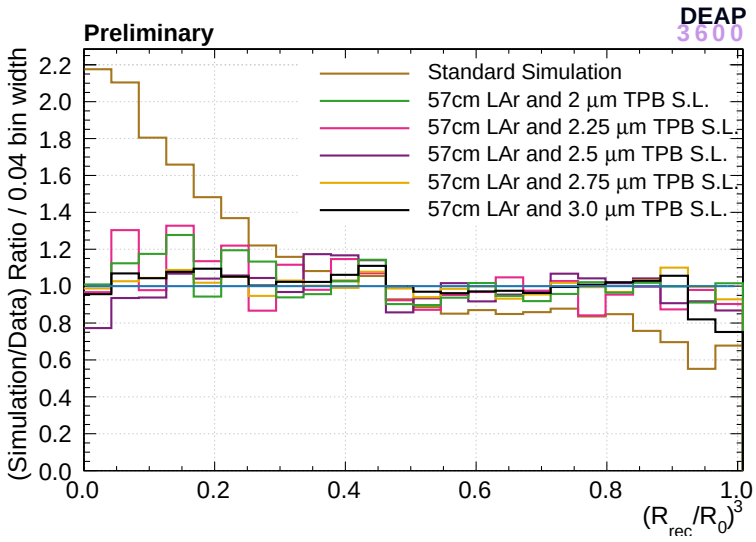

Figure 5.32: Comparing the agreement with data from the combination of the E. Grace measurement with the range of favoured TPB scattering lengths from the study by Stolp *et. al.* [143].

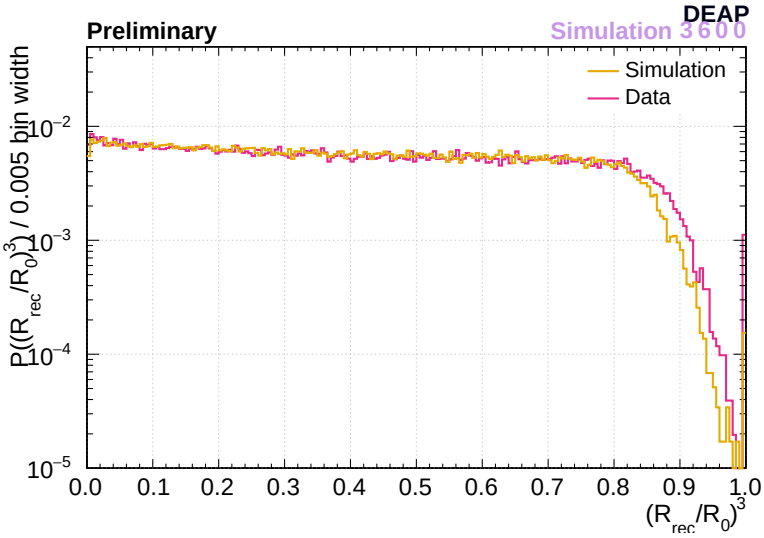

Figure 5.33: Demonstration of the effect of using the new optical model in Chapter 3 in lookup tables, reconstructing ^{39}Ar data and simulation also using the new optical model. Distributions are in reconstructed cubic radius $(R_{rec}/R_0)^3$, normalised to the event radius R_0, comparing simulated ^{39}Ar (yellow) to data (pink) in the electronic recoil band.

A new optical model including changes to the above optical parameters was discussed in Chapter 3. UberShellFit's lookup tables were regenerated using the updated model, and ^{39}Ar from data and an updated optical model simulation were reconstructed. The resulting cubic radial distributions are shown in Figure 5.33. The resulting distributions match to

within 10% of the simulation curve until $(R_{rec}/R_0)^3 > 0.8$, where the UberShellFit high radius effect from Figure 5.28 occurs. The new optical model more closely resembles the data in ^{39}Ar cubic radial distribution compared to the standard optical model.

5.3 ^{22}Na Source Calibration

The position reconstruction of the ^{22}Na gamma source is discussed in this section. Data taken during commissioning is compared to the results of Monte Carlo simulation. The effect of the adjustment to the optical model discussed in Chapter 3 is explored in reconstructed position as well as other variables.

5.3.1 Simulation

Light production from gamma interactions is expected to occur via electron excitation from Compton scattering and the photoelectric effect. The electrons can then produce more electrons through ionisation, produce light via scintillation in TPB and argon, and produce Cerenkov radiation in surrounding vessel acrylic. Identifying the argon scintillation and acrylic Cerenkov populations in simulation enables the identification of events with which to benchmark the position reconstruction.

One million ^{22}Na gamma decays were simulated with the source at the point where Cal F meets on the south point on the equator, calculated from measurement of the Cal F tube location during construction. The detector is simulated with the vessel containing liquid argon, filled to a 551 mm fill level, which is within the uncertainty on the calculated fill level as discussed in Chapter 2. The data taken with the source used a 16 μs long event window, in which an average 5.33 gamma decays may occur for a 333kBq source. The simulation features decays at 333kBq and uses 16 μs long event windows. In simulations with a single decay per event only 2% of single ^{22}Na decays result in enough observable light to trigger, and 10.6% of event windows observe a single light producing gamma interaction for a source simulated at the correct decay rate. The probability of observing two light producing gamma interactions in an event window is 0.4%, and even lower for more light producing gammas in an event window, so that triggered events are most

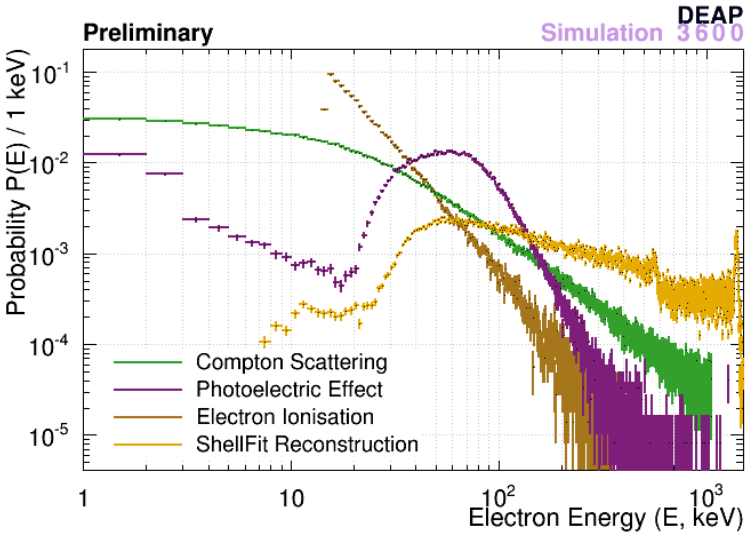

Figure 5.34: Energy spectra for the electrons produced in ^{22}Na gamma interactions in argon, showing the products of Compton scattering, the photoelectric effect, ionisation from other electrons, and the reconstructed energy of these events

frequently the result of a single light producing gamma.

Figure 5.34 shows simulated energy spectra for gamma interactions that occur within liquid argon, alongside their reconstructed energy spectra. Figure 5.35 shows the same energy spectra for gamma interactions in the surrounding detector acrylic, which can produce Cerenkov light. Also shown is the spectrum of reconstructed energies for the simulated data set. In the reconstructed data energies two peaks are visible corresponding to the 511 keV and full energy 1.27 MeV gammas. The same peaks are visible in the acrylic photoelectric spectrum and the full-energy peak is visible in the argon photoelectric spectrum. The peaks in photoelectron energy and reconstructed energy for interactions in argon coincide at 50 keV$_{ee}$. For the 7.1 PE/keV$_{ee}$ light yield that is standard in simulation, this corresponds to a peak at 350 PE. No such coincidence is observed in the acrylic, as only those electrons with enough kinetic energy to produce Cerenkov light are observed.

5.3.2 Cut motivation and simulation comparison

The source was simulated in Cal F at the southern-most point on the equator of the steel shell (which coincides with the equator of the AV). The DAQ was simulated using a

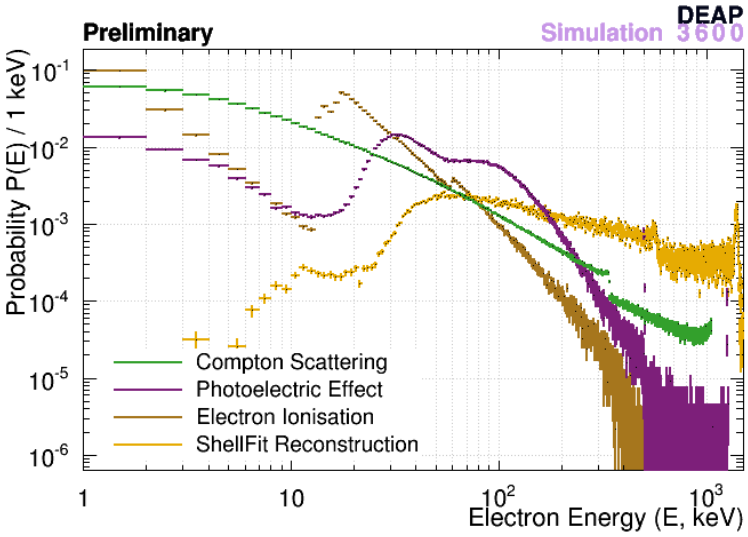

Figure 5.35: Energy spectra for gamma interactions in surrounding detector materials, showing the products of Compton scattering, the photoelectric effect, ionisation from other electrons, and the reconstructed energy of these events

trigger setting which requires the observation of n_{PE}>23 in a 144 ns window, in the configuration used during data taking in commissioning. For the data used in this analysis, the source is also located at the south point on the steel shell equator. In both simulation and data the fill level used is the final fill level after the second fill, simulated at 551 mm above the AV equator. A tagging analysis, designed by Franco La Zia and Pierre Gorel, is used to isolate ^{22}Na events where both tagging PMTs see scintillation from the two 511 keV gammas. The tagging requires that the two tagging PMTs each observe a pulse within 260 s of one another.

Figure 5.36 shows distributions of the PSD parameter F_{prompt}, for simulated data using the standard and modified optics discussed in Chapter 3, and real data with and without the tagging cut applied. Also shown is the F_{prompt} distribution from ^{39}Ar in the same detector configuration, cuts and trigger settings as the ^{22}Na simulations and data. In the absence of a strong neutron source the population of events observed in simulation at $F_{prompt} > 0.4$ corresponds to low PE Cerenkov radiation in the acrylic. Light produced in the acrylic has a shorter time of flight to its nearest PMT and as a result a greater prompt fraction than is usual for scintillation in argon. The population at $F_{prompt} < 0.12$ is present in simulations of the detector when it is filled entirely with gaseous argon, and corresponds

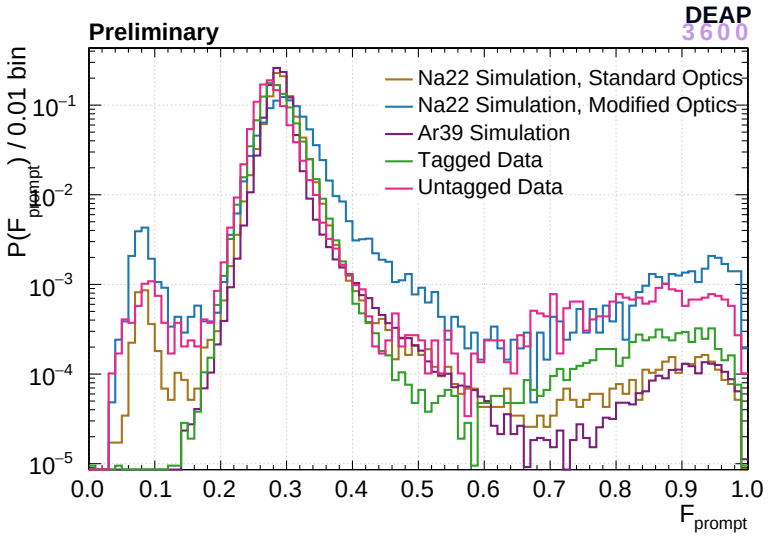

Figure 5.36: The distribution of F_{prompt} in a simulation of a 333kBq ^{22}Na source, using a 16μs event window, and the DAQ trigger configuration used in in-situ data, compared to in-situ data. Data corresponding to argon scintillation (blue), acrylic Cerenkov (green) and the mixture of the two (pink) is produced by requiring that simulation tracking information records interaction in the argon. The source (yellow) and background (brown) data correspond to events in real data where the source is and is not present in Cal F respectively.

to scintillation in the gas region in the volume above the liquid level. The remaining region contains the electronic recoil band, containing both the ^{22}Na photoelectric peak in argon, as well as the distribution from ^{39}Ar decays.

Figure 5.37 shows F_{maxpe} distributions for simulated data and real data with and without the tagging cut applied, as well as the same ^{39}Ar simulation. Cerenkov is observed at $F_{maxpe} > 0.4$, where the most charge is observed in the PMT of the light guide in or in front of which the Cerenkov light is generated. Together the F_{prompt} and F_{maxpe} regions stated above provide a way of selecting for and excluding Cerenkov events in the acrylic, as well as other surface event types, such as surface alphas scintillating in TPB and argon for which high charge is observed in the nearest PMTs. The effect of the tagging cut is remove the low $F_{maxpe} < 0.06$ peak which is observed in the untagged data. In this range in F_{maxpe} the peak in the untagged data coincides with the main peak from the ^{39}Ar simulation.

The main peak at $F_{prompt} = 0.3$ coincides with the tagged and untagged data in both the standard and modified variants of the simulation. For the simulation using standard

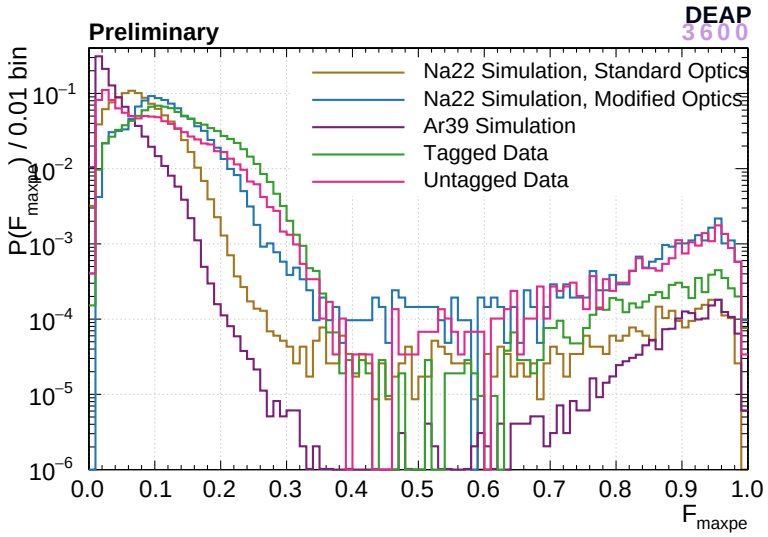

Figure 5.37: The distribution of F_{maxpe} in a simulation of a 333kBq ^{22}Na source, using a 16μs event window, and the DAQ trigger configuration used in in-situ data, compared to in-situ data. Data corresponding to argon scintillation (blue), acrylic Cerenkov (green) and the mixture of the two (pink) is produced by requiring that simulation tracking information records interaction in the argon. The source (yellow) and background (brown) data correspond to events in real data where the source is and is not present in Cal F respectively.

optics, the main peak of the F_{maxpe} distribution is observed at $F_{maxpe} = 0.07$, displaced by 0.03 from the peaks in tagged and untagged data at $F_{maxpe} = 0.1$. For the simulation with modified optics, the F_{maxpe} distribution peaks at $F_{maxpe} = 0.1$ and coincides with the peaks in tagged and untagged data.

Figure 5.38 shows the distribution of scintillation PE, n_{SC}, for simulation of the ^{22}Na source using both variants of the optical model and for tagged and untagged data. The n_{SC} distribution produced by a simulation using standard optics has a peak that coincides with the peak produced using modified optics. The peak in the n_{SC} distribution produced by either simulation also coincides with the tagged and untagged data at $n_{SC} = 300$ PE.

5.3.3 Reconstruction

The reconstructed position distribution from data are compared with those from both variants of the simulation. The cuts in F_{maxpe} and F_{prompt} specified in the previous subsection are used to select electronic recoils in argon, and the tagging cut is used to select only events which coincide with a ^{22}Na decay. Figure 5.39 shows the reconstructed $(R_{rec}/R_0)^3$

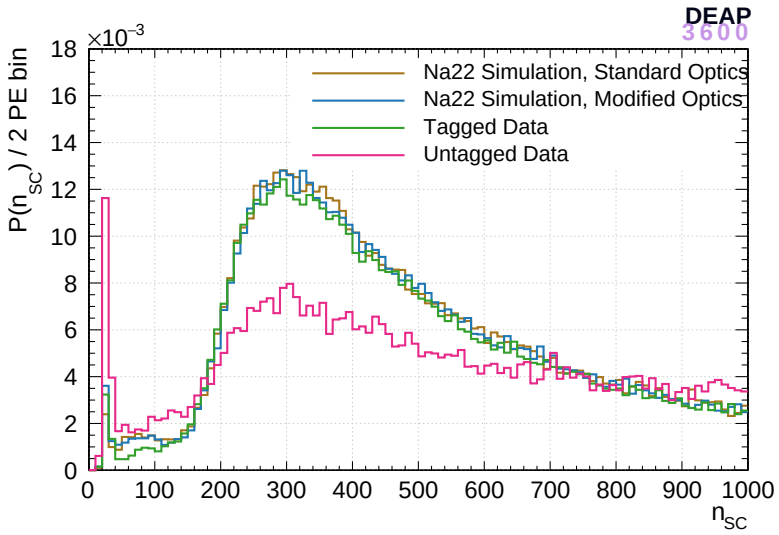

Figure 5.38: The distribution of scintillation PE n_{SC} in a simulation of a 333kBq ^{22}Na source, using a 16μs event window, and the DAQ trigger configuration used in in-situ data, compared to in-situ data. Data corresponding to argon scintillation (blue), acrylic Cerenkov (green) and the mixture of the two (pink) is produced by requiring that simulation tracking information records interaction in the argon. The source (yellow) and background (brown) data correspond to events in real data where the source is and is not present in Cal F respectively.

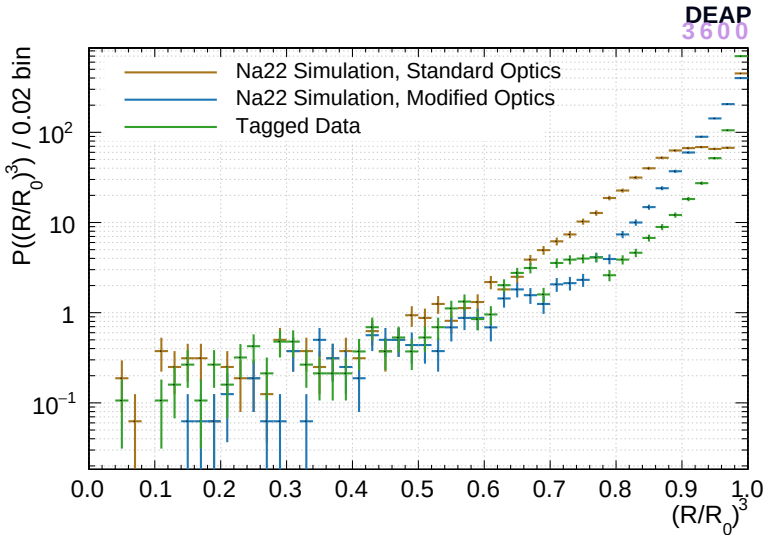

Figure 5.39: The reconstructed cubic radial distribution in a simulation of 1.27MeV gammas using the DAQ trigger configuration used in real data, compared to real data.

distributions that are produced using UberShellFit, using lookup tables which assume standard optical parameters, on the standard and modified simulation, and the tagged dataset.

As observed in the ^{39}Ar distribution the modified optics produces a pronounced difference in reconstructed radial bias which partially alleviates the difference between data and reconstruction. In this case the modified optics reproduces the main features of the data distribution, but fails to exhibit as much outward radial bias as the data. The data distribution has a greater proportion of its events reconstruct near R_0. The source of this remaining difference is thought to be a property of the acrylic, in which a gamma can scatter multiple times before reaching the argon. Properties of the acrylic that are under investigation are light-producing features of the acrylic optics, such as fluorescence or an increased Cerenkov yield in data compared to simulation. Other materials which are not considered in the discussion in Chapter 3 are also under investigation, such as the steel shell and outer component optics, which the gamma encounters as it propagates towards the detector. A simulated tagging system may also serve to alleviate some of the discrepancy.

5.4 Conclusion

In this chapter the position reconstruction algorithm UberShellFit was calibrated using data from three calibration sources. UberShellFit was adapted in order to be able to reconstruct data taken using the laserball. The wavelength distributions of the 375 nm and 445 nm laser heads were used in lookup table generation to model the propagation of light from the laserball source to the PMTs. A model of the non-uniformity of the laserball flask as observed in prompt PMT charges was adapted for the case of charge reconstruction using the total charge in each PMT. The effect of optical parameters on the position reconstruction was explored using ^{39}Ar β^- decays. In simulation the modification of the argon and TPB Rayleigh scattering lengths to those values obtained in recent measurement was observed to reconcile the difference in the cubic radial distribution between data and the standard simulation of ^{39}Ar. In addition the adjustment also reconciles the dis-

agreement observed in the variable F_{maxpe} in simulation and data using the ^{22}Na gamma source, but leaves some remaining bias between the reconstructed radial distributions of simulation and data.

Chapter 6

Dark Matter Search

In this chapter position reconstruction information is implemented in a preliminary dark matter search analysis. Dark matter search analyses commonly produce either: 1) a discovery claim at a given confidence level with a given a set of signal events, within a region in SD/SI WIMP-nucleon scattering cross section and mass (e.g. DAMA/LIBRA signal regions); or 2) a 90% C.L. exclusion region in WIMP SD/SI cross section and mass, given either a set of events comprised of background and signal, or zero events. For most search experiments at time of writing, including those discussed in Section 1.4, the common practice for a new dark matter search result for spin-independent interactions is the setting of a 90% C.L. upper limit on the SI WIMP-nucleon scattering cross section at a given WIMP mass (at smaller cross sections with increasing search sensitivity).

At time of writing, with the standard analysis cut flow described in Sections 3.2.2, 3.2.3 and 3.2.4, the PSD ROI cut and energy ROI of $80 < Q_{PE} < 240$ used in the first paper [3] analysis, 27 events are observed within the region of interest in 220 days of data, thought to be background events originating from scintillation in the neck and currently under further investigation. The events are shown against F_{prompt} and Q_{PE} in Figure 6.1.

Two methods for setting a 90% C.L. upper limit are described in this chapter, the Poisson method and the profile likelihood ratio. In the opening section of this chapter the Poisson method is used to explore the effect on a 90% C.L. upper limit of increasing the fiducial volume, lowering the PE threshold and observing a given number events in the search. A profile likelihood ratio analysis is then described which the author developed

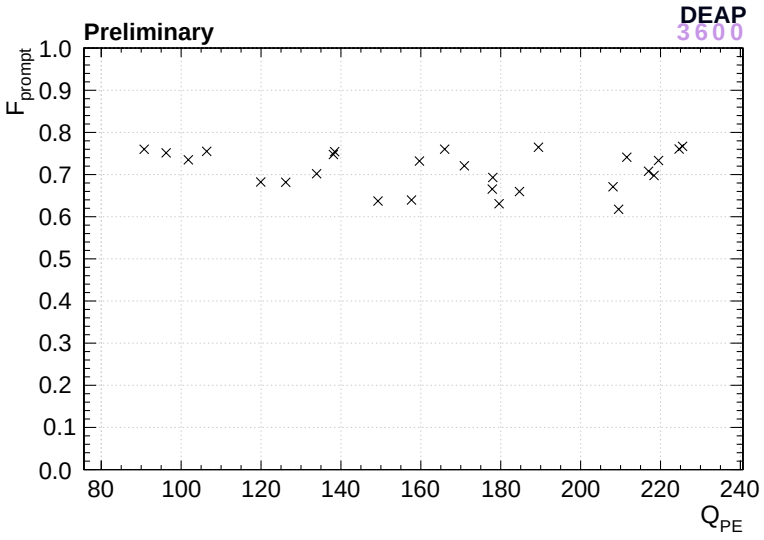

Figure 6.1: Scatter plot showing the distribution of 27 events in F_{prompt} and Q_{PE}, which pass the nominal cut flow from the first paper analysis. The events are thought to originate from a scintillation in the neck and are under investigation.

alongside Alistair Butcher and Shawn Westerdale, building on the progress set out in Ref. [140]. The remainder of the chapter focuses on the implementation of the reconstructed radius in the likelihood model, in addition to the observables Q_{PE} and F_{prompt}. Additionally the implementation of information about the surface alpha background is described, for which position reconstruction is particularly important. This chapter closes by calculating a preliminary 90% C.L. upper limit given the 27 event set, assuming 220 days of data and using the $80 < Q_{PE} < 240$ energy ROI, using the Poisson method and a profile likelihood ratio analysis.

6.1 Poisson Method

In this section, the Poisson method is used to explore the projected effects of fiducialisation, exposure and event observation on projected 90% C.L upper limits on the spin-independent WIMP-nucleon scattering cross section σ_{SI} as a function of WIMP mass m_χ. The Poisson method [149] is commonly used to set a 90% C.L. upper limit given the observation of a number of events in a search experiment. A standard set of assumptions set out in Sections 1.3 and 6.3.1 is commonly used such that different experimental results

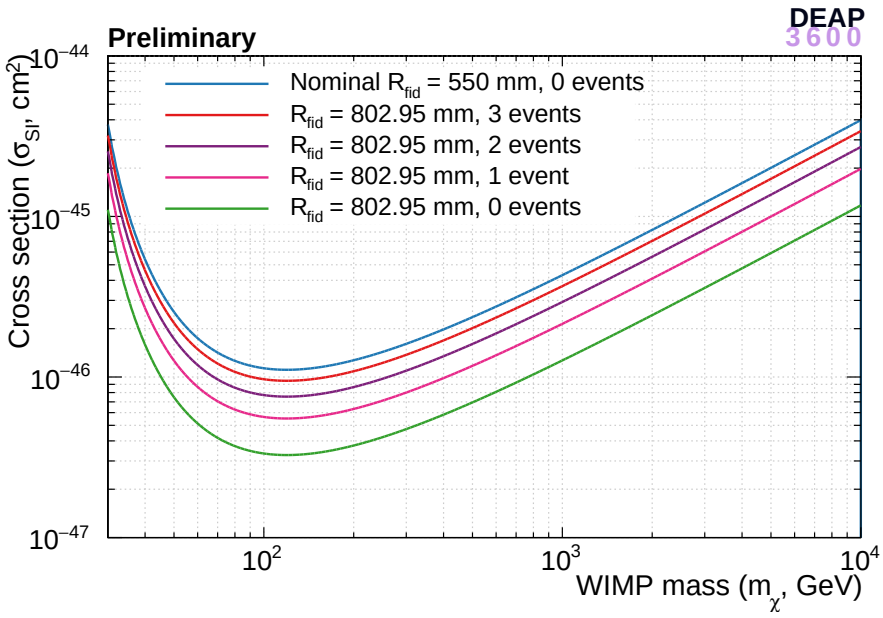

Figure 6.2: Zero event 90% C.L. upper limits on a spin-independent WIMP-nucleon scattering cross section vs WIMP mass, calculated using the Poisson method, using the original design specifications from the detector. For comparison, the same zero event limit with an 802.95 mm fiducial radius, and the 1, 2 and 3 event limits.

can be compared in the same m_χ and σ_{SI} parameter space given the same WIMP model. Following [149], to obtain a 90% C.L limit for an expected number of events μ (which is dependent on σ_{SI} and m_χ and the WIMP model being considered) and an observed number of events N, the μ is found which satisfies $1-\alpha(\mu)=0.9$, where $\alpha(\mu)$ is given by:

$$\alpha(\mu) = e^{-\mu}\sum_{m=0}^{N}\frac{\mu^m}{m!} \tag{6.1}$$

As an example the projected limit for DEAP-3600 assuming zero background events, calculated during the design phase, is shown in Figure 6.2. The limit assumes a light yield of 8 PE/keV$_{ee}$ and a 15-30 keV$_{ee}$ region of interest, which corresponds to 120-240 PE. The threshold was set according to the projected rejection capability of PSD at 50% nuclear recoil acceptance from the DEAP-1 PSD measurement [145]. The detector was originally designed to contain a spherical volume of liquid argon, and have a 1 tonne spherical fiducial mass with a 550 mm fiducial radius.

In Section 4.6.3 it was observed that the tolerable fiducial leakage for an ROI with a lower threshold of 80 PE (used in the DEAP-3600 first result) and a nominal 1.3×10^{-3}

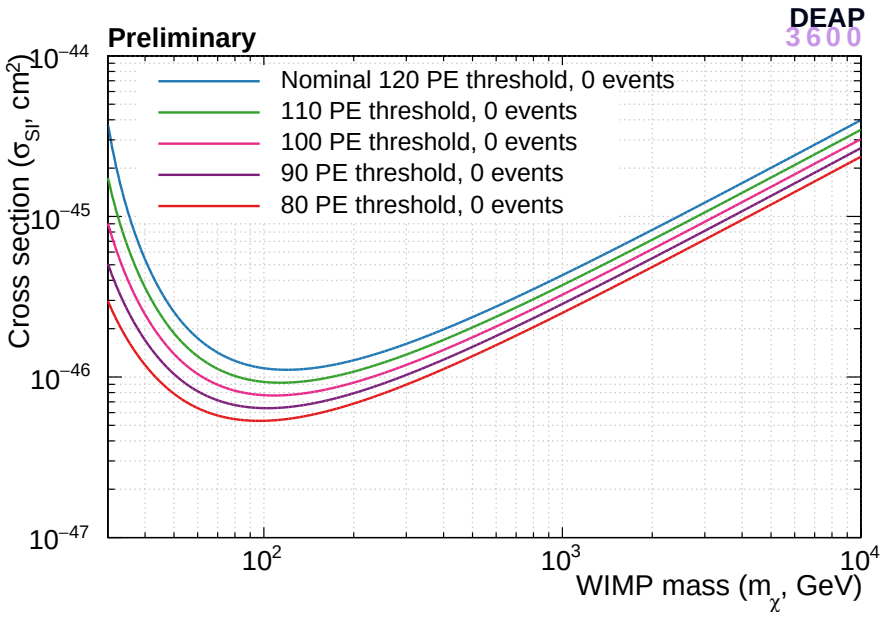

Figure 6.3: Zero event 90% C.L. upper limits on a spin-independent WIMP-nucleon scattering cross section vs WIMP mass, calculated using the Poisson method, using the original design specifications from the detector. Comparisons show the effect of lowering the PE threshold on the achieved sensitivity to lower scattering cross sections.

leakage fraction was satisfied in UberShellFit by a 777.12 mm fiducial radius cut. With the nominal threshold of 120 PE at a simulated light yield of 8 PE/keV$_{ee}$, the fiducial radius which satisfies the nominal leakage fraction increases to 802.95 mm. Assuming zero background events are introduced by the increase in ^{39}Ar events or other backgrounds observed within the fiducial volume, the relative change to the projected sensitivity is shown in Figure 6.2. The increase in target mass considered increases the exposure per unit time, which increases the expected number of events μ in Equation 6.1 and results in a lower limit in σ_{SI}.

In the non-zero event case the Poisson method does not discriminate between signal and background events in its observed number of events N. Violating the assumption that zero background events will be observed increases the number of events N in Equation 6.1. This effect reduces the magnitude of the increase in sensitivity from the increased exposure from a larger fiducial volume, as shown in Figure 6.2.

Another way in which the region of interest can be expanded is to lower the PE threshold, as shown in Figure 6.3 compared to the nominal limit, assuming no additional back-

ground events. The low energy region is where the electronic and nuclear recoil bands overlap so that lowering the energy threshold requires an improvement in PSD performance which improves band separation at lower energies. There is significant motivation to lower the threshold below the nominal due to the observation in the DEAP-3600 first result of improved PSD performance relative to the DEAP-1 measurement, which enabled the use of the 80 PE threshold [3].

In practice, however, in a search using a longer exposure which combines a larger fiducial radius and PE threshold reduction, background event rejection must be maintained. The ^{39}Ar background rate increases linearly with the fiducial volume, so any increase in fiducial volume must take into account PSD performance and the corresponding usable energy threshold. Likewise, surface event rejection must also be ensured when using a larger fiducial radius. These considerations will determine the usable fiducial volume and energy threshold used in future searches.

A limit setting method which successfully accounts for the presence of background events in the region of interest for a given dark matter search can counteract the resulting loss in sensitivity whilst enabling the expansion of the region of interest. The incorporation of the expected signal in a limit setting method can increase sensitivity in regions where backgrounds may be observed. Signal information features in limit setting methods such as the Maximum Gap/Optimum Interval method [150], and the Maximum Patch method [151], as well as the profile likelihood ratio method described in the next section.

6.2 Profile Likelihood Ratio Method

The profile likelihood ratio (PLR) method [152] is favoured by upper limit setting analyses from XENON-100 [153, 154] and LUX [71] as they are observed to outperform the Poisson and Maximum Gap methods in the presence of background events [149]. A preliminary framework was constructed for a PLR analysis of DEAP-3600 data in Ref. [140], which has been redeveloped extensively here in collaboration with the original author, Alistair Butcher, and Shawn Westerdale. In this section the PLR analysis is described, and the implementation of the reconstructed radius in signal and background

PDFs is described. The introduction of a surface alpha PDF is then discussed.

6.2.1 Hypothesis Testing

The profile likelihood ratio λ is defined as the ratio of two likelihoods. The numerator is the conditional likelihood of observing a fixed cross section σ which is being tested, given a set of nuisance parameters $\{\theta\}$. The nuisance parameters are defined as parameters of the models that are implemented as part of the likelihood, but are not known a priori and must be fitted from data. Maximisation of the conditional likelihood produces the conditional maximum likelihood estimators (MLEs) for the nuisance parameters $\{\hat{\hat{\theta}}\}$. The denominator is the unconditional likelihood of observing a cross section σ which is allowed to float in the likelihood alongside its nuisance parameters $\{\theta\}$. The maximisation of the unconditional likelihood produces unconditional MLEs $\hat{\sigma}$ and $\{\hat{\theta}\}$. The profile likelihood ratio λ is given by:

$$\begin{aligned}\lambda &= \frac{\max_{\text{fixed}\sigma}\mathscr{L}(\sigma;\{\theta\})}{\max\mathscr{L}(\sigma;\{\theta\})} \\ &= \frac{\mathscr{L}\left(\sigma;\{\hat{\hat{\theta}}\}\right)}{\mathscr{L}\left(\hat{\sigma};\{\hat{\theta}\}\right)}\end{aligned} \tag{6.2}$$

The test statistic q is defined in order to reduce the test statistic to one value. In the case of producing an upper limit exclusion curve the signal hypothesis H_σ for a test cross section σ is tested using:

$$q = \begin{cases} -2\ln(\lambda(\sigma)) & \hat{\sigma} < \sigma \\ 0 & \hat{\sigma} > \sigma \end{cases} \tag{6.3}$$

Higher q values indicate that the data tested is incompatible with the signal hypothesis. By only considering the case where $\hat{\sigma} < \sigma$, evidence which does not support the signal hypothesis is included but evidence which supports it is ignored. The p-value for this test statistic is constructed by considering $f(q \mid H_\sigma)$, the probability distribution function of q given the signal hypothesis H_σ. If theoretical observed datasets are generated at random by pseudo-experiments, which result in the test statistic q, the p-value used in the production of a confidence level is then given by the probability that a pseudo-experiment

observes a test statistic q larger than that produced for the observed dataset, q_{obs}. The production of pseudo-experiments is discussed in Section 6.5. The signal hypothesis H_σ is rejected if $p > 10\%$, or if $(1-p) < 90\%$, and p is given by:

$$p = \int_{q_{obs}}^{\infty} f(q \mid H_\sigma)\, dq \tag{6.4}$$

6.2.2 Likelihood Construction

The likelihood in the numerator and denominator is constructed in the same manner, and will be broken down into its seperate contributions and explained in turn. The complete likelihood can be described as a set of three terms:

$$\mathscr{L}(\sigma;\{\theta\}) = \mathscr{L}_{PDFs}(\sigma;\{\theta\}) \times \mathscr{L}_{constraint}(\{\theta\}) \times \mathscr{L}_{sideband}\{\theta\}) \tag{6.5}$$

The first term in the likelihood $\mathscr{L}_{PDFs}$ compares the number of events observed in an observed dataset N_{obs} with the expected number of events N_{exp} from the model PDFs implemented in the likelihood. The second term is an un-binned extended likelihood which includes information from three dimensional model PDFs $f_i(Q_{PE}, F_{prompt}, R_{rec})$ which describe the WIMP signal, ^{39}Ar background and surface α decay components of the expected number of events, as discussed in the next subsection. Each component i is expected to produce a number of expected events N_i. The un-binned likelihood is then given by:

$$\mathscr{L}_{PDFs}(\sigma;\{\theta\}) = \text{Pois}(N_{obs} \mid N_{exp}) \times \sum_{i=1}^{N_{PDFs}} \left(\frac{N_{exp,i}}{N_{exp}} f_i(Q_{PE}, F_{prompt}, R_{rec};\{\theta\}) \right) \tag{6.6}$$

For each included PDF there is associated with it a set of nuisance parameters which the PDF is dependent on. The nuisance parameters are constrained by a set of constraint PDFs which encode the probability of observing a value of each nuisance parameter given the information available about the parameter from measurement. The inclusion of constraint PDFs permits probable values and discourages unphysical and improbable ones. The constraint PDFs are included as:

$$\mathscr{L}_{constraint}(\{\theta\}) = \prod_{j=1}^{n_\theta} f(\theta_j) \tag{6.7}$$

Background and calibration source data can be used to further constrain the nuisance parameters, in PDFs known as side-bands. The ^{39}Ar side-band is constructed as a three-dimensional binned likelihood PDF in $Q_{PE}, F_{prompt}, R_{rec}$ constructed from detector data, using the cut flow set out in Chapter 3. The side-band term compares the expected number of events N_{exp} in each bin from side-band data to the number of events N_{pdf} from integrating the ^{39}Ar model PDF over the range of each bin. The side-band likelihood is given by the product of Poisson terms comparing N_{exp} and N_{pdf} for each of $N_{j,k,l}$ bins j,k,l in Q_{PE}, F_{prompt}, and R_{rec} in the side-band:

$$\mathscr{L}_{sideband}\{\theta\}) = \prod_{j=1}^{N_j}\prod_{k=1}^{N_k}\prod_{l=1}^{N_l} Pois(N_{pdf,j,k,l}|N_{exp,j,k,l}) \tag{6.8}$$

In practice the above results in computation of multiple empty side-bands where ^{39}Ar events are not expected. The ^{39}Ar side-band is evaluated in the electronic recoil band outside of the F_{prompt} region of interest, and within the energy ROI.

6.3 Model PDF Implementation

In this section, the construction of the WIMP, ^{39}Ar and alpha model PDFs are described in turn alongside their nuisance parameters. The (F_{prompt}, Q_{PE}) components and the additional radial component are described separately.

6.3.1 WIMP Model

The WIMP recoil energy spectrum is modelled as set out in Ref. [49] and Chapter 1. An Einasto [56] profile is assumed for the local dark matter density, and the Maxwellian WIMP velocity distribution is assumed. The escape velocity is constrained using the functional form produced by the RAVE survey in the blue curve in Figure 7 of [50], analogously to the implementation used by XENON-100 [153]. The median value is given by $v_{esc,med} = 544$ kms^{-1}, with a 90% C.L. upper and lower limit of $498 < v_{esc} < 608$ kms^{-1}. The WIMP observed PE spectrum is described by convolving the theoretical WIMP energy spectrum with a Gaussian PE response modelling both the detector light

yield (Gaussian mean) and energy resolution (Gaussian spread). The light yield is implemented using a quadratic function $E = A_1 + B_1 \cdot Q_{PE} + C_1 \cdot Q_{PE}^2$ from the DEAP-3600 first result [3]. The function was determined using an analytic fit relating the theoretical ^{39}Ar spectrum to the PE spectrum observed in data. Each parameter A, B and C is constrained by a Gaussian constraint term with mean set to the observed parameter value and spread set to the observed parameter error. The energy resolution is implemented as another quadratic function describing the variance $\sigma^2 = A_2 + B_2 \cdot Q_{PE} + C_2 \cdot Q_{PE}^2$. The PE count Q_{PE} from charge division is used in this analysis because the current model for light yield and energy resolution is dependent on Q_{PE}.

The quenching factor is modelled using the SCENE quenching factor measurement and uncertainties [116], handled analogously to the XENON-100 implementation [153]. The parameter which varies is the amount of deviation away from the measurement and towards the uncertainty on the measurement. The variation of the quenching factor is constrained as a Gaussian distribution centred on zero deviation, where 1σ from the mean moves the quenching factor to the uncertainty on the measurement. The F_{prompt} model from the DEAP-3600 first result paper is implemented as described in Section 3.2.3. The nuclear recoil mean F_{prompt} used in the paper analysis, adapted for F_{prompt} from SCENE and Regenfus *et. al.* in Ref. [155], is implemented with a Gaussian constraint which describes the deviation away from the measured F_{prompt} towards upper and lower errors in analogy to the quenching factor model. The mean F_{prompt} and upper and lower errors are shown in Figure 6.4. The result of the above is summarised in the as-implemented PDF of F_{prompt} vs Q_{PE} in Figure 6.5. The use of FFT convolution means that the colour axis is in arbitrary units, which is subsequently accounted for in the normalisation of the PDF during minimisation.

6.3.2 ^{39}Ar Model

The ^{39}Ar model shares the characterisation of light yield and PE resolution with the WIMP model, but the underlying distribution is characterised by the ^{39}Ar β^- energy spectrum. It shares light yield and PE spread parameters and constraints with the WIMP

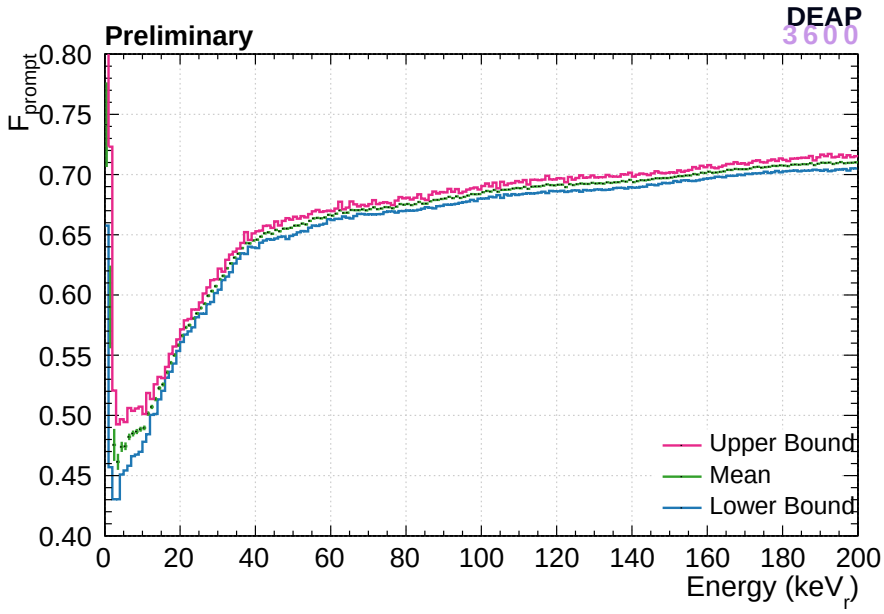

Figure 6.4: Mean and upper and lower error on F_{prompt} plotted vs Q_{PE}. Simulated and calculated by Shawn Westerdale for F_{prompt} for the DEAP-3600 first result, from data from SCENE and Regenfus *et. al.* [155].

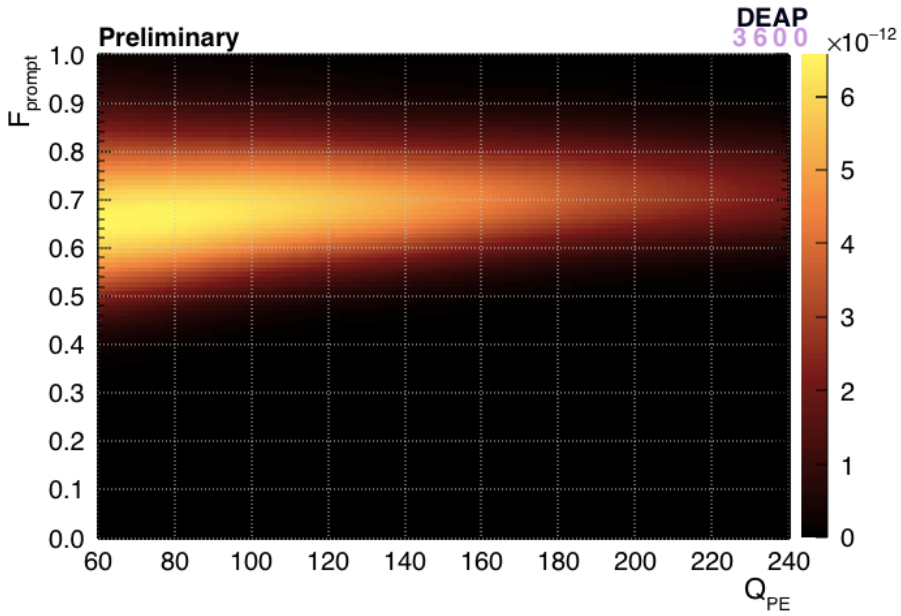

Figure 6.5: Projection of the WIMP PDF as implemented in the likelihood, in F_{prompt} vs Q_{PE}. The colour axis is in arbitrary units due to the use of FFT convolution, and the PDF is normalised internally in the algorithm.

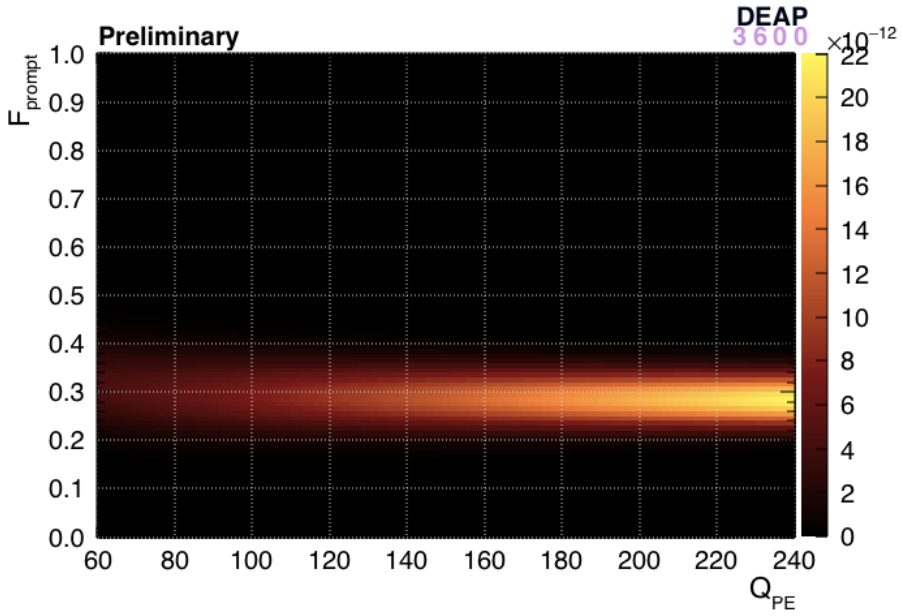

Figure 6.6: Projection of the ^{39}Ar PDF as implemented in the likelihood, in F_{prompt} vs Q_{PE}. The colour axis is in arbitrary units due to the use of FFT convolution, and the PDF is normalised internally in the algorithm.

PDF. The PE-dependent F_{prompt} distribution is implemented as the convolution of a Polya distribution and a Gaussian as described in Section 3.2.3. The Polya distribution mean and b parameters are implemented as in the DEAP-3600 first result paper [3], as is the Gaussian spread. The mean and b values are constrained by Gaussian constraint parameters controlling a scaling factor, where a scaling factor of 1 represents the measured value. The 1σ deviation from the Gaussian mean is set to the uncertainty on the mean that was observed from the analytic fit to the ^{39}Ar spectrum as described in the paper. The ^{39}Ar rate is varied by the $\pm 10\%$ uncertainty observed in Ref. [101], and constrained by a Gaussian with mean 1.01 Bq/kg and spread 0.1 Bq/kg. The result of the above is summarised in the PDF of F_{prompt} vs Q_{PE} in Figure 6.6, shown as implemented. Again, the use of FFT convolution means that the colour axis is in arbitrary units, accounted for in the normalisation of the PDF.

6.3.3 Radial Model

Like the ^{39}Ar background, WIMP scattering events are expected to be observed uniformly throughout the detector, because the WIMP scattering cross section is so small that it is

equally likely to scatter in any location in the detector. The radial component of the PDF is implemented identically for WIMPs and ^{39}Ar. The PDF is constructed from two components. The first is the expected probability that a scattering event will occur at a radius R_{real}, given from spherical geometry by:

$$f(R_{real}) = \frac{3}{R_0^3} R_{real}^2 \tag{6.9}$$

where R_0 is the radius of the AV. The distribution is normalised to unity when integrating over all radii from $R_{real} = 0$ to $R_{real} = R_0$. The fill level of the detector is neglected as the deviation from a uniform radial distribution produced by the fill level is negligible as discussed in Section 4.6.1. The second component is a PE and radius-dependent radial resolution function. This component is characterised by a Gaussian resolution function with PE and radius-dependent resolution $\sigma(R, PE)$ and bias $\mu(R, PE)$. The Gaussian parameters are obtained using the routine described in Section 4.6.2 for obtaining a radial resolution, from uniform ^{39}Ar simulation, using the physics trigger, binned in 20 bins in radius and 10 bins in Q_{PE} from 0-800 PE. A cubic polynomial is fitted to the variation of radial bias and resolution with $(R_{real}/R_0)^3$ in each energy bin. Typical examples of each fit for single energy bins are shown in Figures 6.7 and 6.8. The variation of each polynomial parameter with energy is then recorded and fitted with a quintic polynomial.

The reconstruction of a radial resolution or bias is simply the same procedure in reverse, where a cubic polynomial is constructed at a given energy and the radial PDF is reproduced using a Gaussian with parameters drawn from those cubic polynomials at the real radius being considered. To produce a PDF of reconstructed radius the PDF of R_{real} is convolved with the resolution function, whose bias and resolution are dependent on real radius. The resulting variation in reconstructed radial distribution with energy is shown in Figure 6.9. The radial bias and resolution are each varied in the likelihood with a linear scaling factor, such that a factor 1 reproduces the fitted bias or resolution.

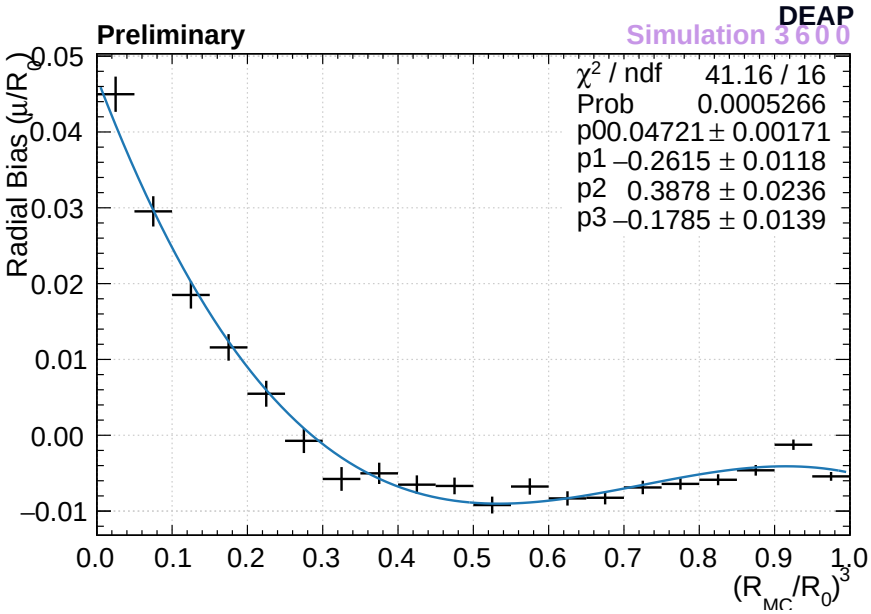

Figure 6.7: The variation of the observed radial bias μ normalised to the AV radius R_0, with the true cubic radius of the event $(R_{MC}/R_0)^3$. The distribution is fitted with a cubic polynomial.

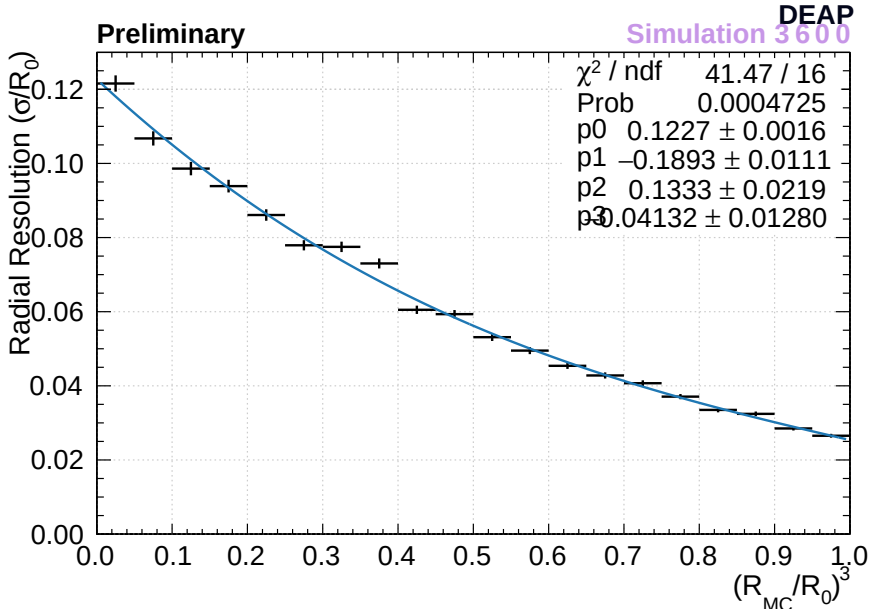

Figure 6.8: The variation of the observed radial resolution σ normalised to the AV radius R_0, with the true cubic radius of the event $(R_{MC}/R_0)^3$. The distribution is fitted with a cubic polynomial.

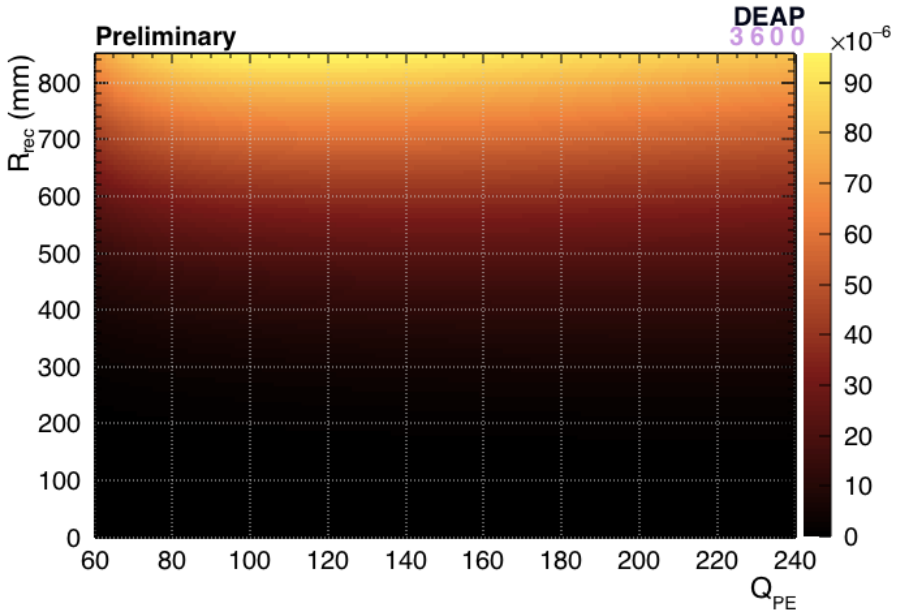

Figure 6.9: A projection of the ^{39}Ar PDF in observed reconstructed radius R_{rec} and Q_{PE}, as implemented in the likelihood. The colour axis is in arbitrary units due to the use of FFT convolution, and the PDF is normalised internally in the algorithm.

6.3.4 Alpha Model

The alpha background model is described by three components, corresponding to the three sources of surface alpha background events as described in Section 2.2.2, which are the TPB bulk and AV bulk, and plated out radon daughters on the TPB surface. 7 million surface alpha background events were simulated for each alpha location, with the DAQ simulated using the physics trigger and using the standard cut flow. The light yield of alpha scintillation in the TPB is lower than that in the argon, which means that the dominant contribution to events observed in a low energy region of interest are characterised by the path length of the alpha in TPB. As a result it was observed that the best fits to PDFs in Q_{PE}, F_{prompt} and reconstructed radius were invariant with the energy of the incident alpha, but not with alpha location of origin, and the contributions from each alpha in the ^{238}U and ^{232}Th decay chains could be treated equivalently within their chains. A three component model was constructed corresponding to the three classes of surface alpha location of origin. The fractional contribution of each location is given by the ratio of the alpha rate from that location to the total predicted alpha rate in all three locations, using

values for the predicted alpha rates from in Table 2.1 in Section 2.2.2.

The PE distributions of each component are described in the $50 < Q_{PE} < 600$ range by the sum of three exponential distributions as follows:

$$f(Q_{PE}) = \sum_{i=1}^{3} \frac{C_i}{A_i} exp\left(\frac{-(Q_{PE} - B_i)}{A_i}\right) \tag{6.10}$$

where A_i, B_i and C_i are parameters floated in the fit. An example of the resulting fit is shown in Figure 6.10 for the TPB bulk. Beyond this QPE range, the DAQ trigger acts to truncate the distribution at low PE and the full TPB energy deposition peak is observed at higher PE. The F_{prompt} distribution in the same Q_{PE} range was fitted with a Gaussian distribution, an example of which is shown for the TPB surface in Figure 6.11. An alpha from the AV bulk could scatter in the acrylic multiple times before emerging and scintillating in TPB and argon at low energies. As a result two peaks in the acrylic F_{prompt} model were observed, shown and fitted in Figure 6.12. The TPB peak is the larger of the two peaks, as scintillation in TPB occurs more frequently than in argon for alphas originating in the AV, as the argon is further from the AV surface. Finally the radial distributions from each alpha location component in the $50 < Q_{PE} < 600$ range were parametrised using the sum of three half-Gaussian distributions as follows below, and an example of the resulting fit is shown in Figure 6.13.

$$F(R_{rec}) = \sum_{i=1}^{3} \frac{N_i}{\sigma_i} \left(\frac{2}{\pi}\right)^{\frac{1}{2}} exp\left(-\frac{(R_{rec} - \mu_i)^2}{2\sigma_i^2}\right) \tag{6.11}$$

The parameters of the Q_{PE} distribution are simply called in the fit, and not varied. Instead the energy scale is varied in conjunction with the WIMP and ^{39}Ar PDFs. The variation of F_{prompt} mean and spread with Q_{PE}, including the parameters for the double Gaussian distribution for the AV bulk, are fitted with quartic polynomials to within χ^2/N_{dof}<1.5. The alpha rate is varied by a nominal $\pm 1\%$ during the development of the PLR analysis, based on the uncertainty on the acrylic surface ^{210}Po background in the DEAP-3600 first result [3]. The alpha rate is constrained by a Gaussian term which acts as a scale factor with mean value 1 corresponding to the nominal rate, and a spread set to

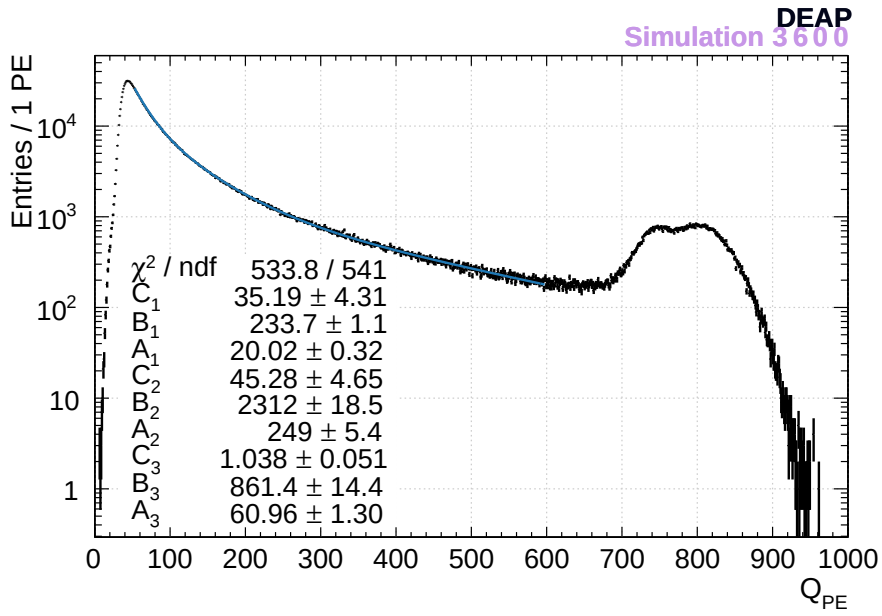

Figure 6.10: The distribution of observed Q_{PE} for simulated ^{210}Po alphas emitted from the TPB bulk. The distribution is fitted with a three-component exponential which is implemented in the likelihood. The full energy deposition peak in TPB is observed above the fitted QPE range of $50 < Q_{PE} < 600$, and the DAQ trigger condition truncates the distribution below it.

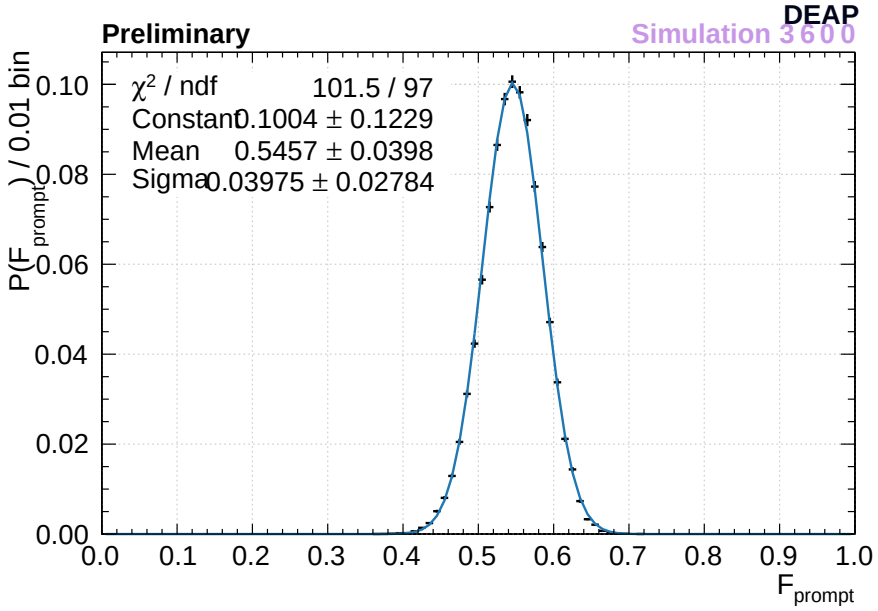

Figure 6.11: The distribution of F_{prompt} observed from simulation of ^{210}Po alphas emitted from the TPB surface. The distribution is fitted with a Gaussian distribution which is implemented in the likelihood.

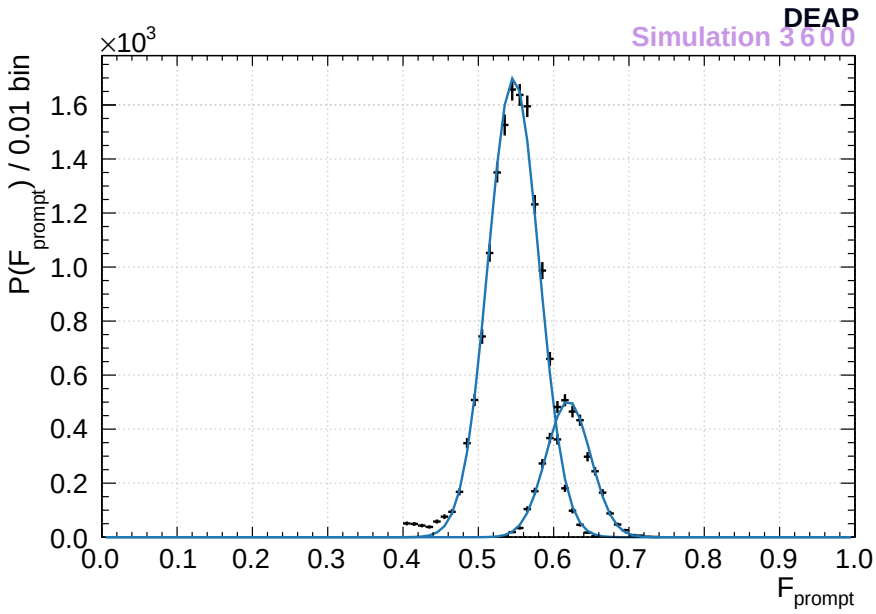

Figure 6.12: The two-component distribution of F_{prompt} observed from simulation of ^{210}Po alphas emitted from the AV inner 80 μm. The distribution is fitted with two Gaussian distributions separately, which are implemented in the likelihood.

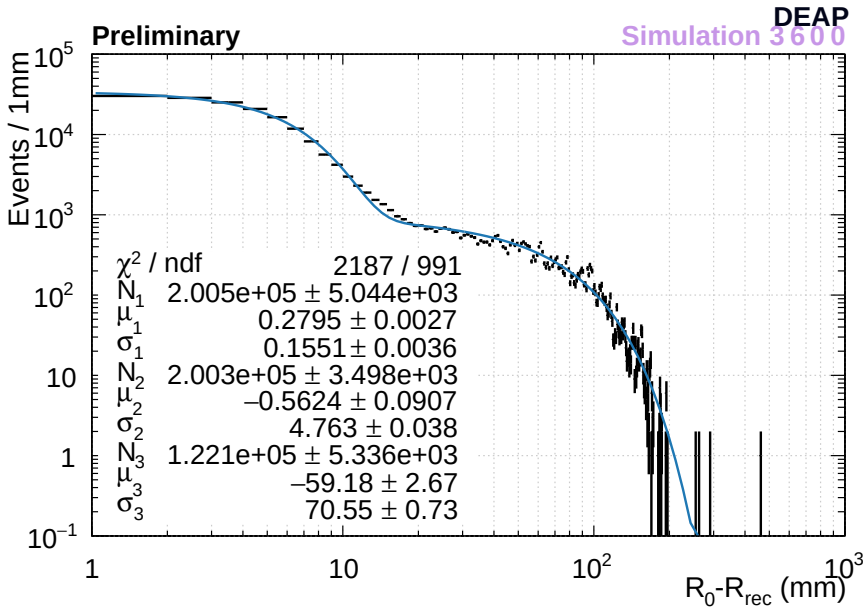

Figure 6.13: The distribution of reconstructed radius, plotted as the radial distance inward from the AV boundary, $R_0 - R_{rec}$, for simulated ^{210}Po alphas emitted from the AV inner 80 μm. The distribution is fitted with a weighted sum of three half-Gaussian distributions, which is implemented in the likelihood.

the nominal 1%. The F_{prompt} mean and spread are also varied by scale factors and constrained by Gaussian terms with a nominal 10% spread. The bias and resolution terms of the half-Gaussian distributions are varied using the same scaling factors as the Gaussian resolution functions in the WIMP and ^{39}Ar PDFs.

6.4 Operation

The full likelihood model is dependent on 20 nuisance parameters which are tabulated in Table 6.1 alongside their constraints. The likelihood is implemented as a custom function in Minuit2, and minimised using the MIGRAD method. Pseudo-experiments are generated by randomly drawing nuisance parameters distributed according to the constraint PDFs, calculating the expected number of events from integrating each PDF inside the chosen ROI, and drawing an event count from a Poisson distribution given the expected number of events. The chosen number of events from each source are generated as sets of observables F_{prompt}, Q_{PE} and R_{rec}, drawn randomly according to the model PDF for the relevant source. The unconditional and conditional likelihood maximisations are performed for each pseudo-experiment and a q distribution is generated over many pseudo-experiments. Using the distribution of q-values for a given σ and m_χ, the p-value is found and the 90% C.L. upper limit on the cross section is that test cross section for which $(1-p) < 90\%$. The process is repeated on several discrete masses and to produce a curve for consistency with other methods the upper limit cross section is interpolated between the masses.

6.4.1 Consistency checks

The implementation of the likelihood was validated by checking that a known result was obtained by the minimisation in certain configurations of the likelihood. The PDF and nuisance parameter implementation is validated first. Following this the addition of sidebands is validated by verifying that the nuisance parameters are constrained by the sideband to correct values.

For a large number of events ($\sim$ 1000 or greater) per pseudo-experiment, without a

Nuisance parameter	Constraint
WIMP F_{prompt} Polya mean ‡	Gaus(0, 1)
WIMP F_{prompt} Polya b parameter †	Gaus(0, 0.005317)
WIMP F_{prompt} Gaussian σ †	Gaus(0, 0.01478)
^{39}Ar F_{prompt} Polya mean †	Gaus(0, 0.03)
^{39}Ar F_{prompt} Polya b parameter†	Gaus(0, 0.005317)
^{39}Ar F_{prompt} Gaussian σ †	Gaus(0, 0.01478)
^{39}Ar event rate	Gaus(1.01, 0.1) (Bq/kg)
Quenching factor ‡	Gaus(0, 1)
LY constant A	Gaus(1.15, 0.5)
LY linear B	Gaus(0.121, 0.004)
LY quadratic C	Gaus(1.32×10^{-6}, 7.0×10^{-8})
PE resolution constant A	Gaus(0, 0.01)
PE resolution linear B	Gaus(1.185, 0.01886)
PE resolution quadratic C	Gaus(0, 0.01)
Alpha F_{prompt} mean scale factor	Gaus(1, 0,1)
Alpha F_{prompt} Gaussian σ scale factor	Gaus(1, 0.1)
Alpha rate scale factor	Gaus(1, 0.01)
Radial bias scale factor	Gaus(1, 0.2)
Radial resolution scale factor	Gaus(1, 0.05)
Escape velocity	RAVE parametrisation, See Ref. [50], $498 < v_{esc} < 608$ kms^{-1}, $v_{esc,median} = 544$ kms^{-1}

Table 6.1: Summary of nuisance parameters and their constraint forms and parametrisation. A parameter with no symbol is constrained by a PDF of its value. A † denotes a parameter whose constraint encodes the amount of deviation from the measured value. A ‡ denotes a parameter whose constraint encodes the (positive or negative) number of measurement errors away from measurement that the parameter can be.

side-band in the likelihood to constrain the nuisance parameters, the minimisation must be able to reproduce the distribution of nuisance parameters from which the pseudo-experiment generation step samples. This verifies that the minimisation can fit the nuisance parameters correctly. The number of events per pseudo-experiment and associated long computational time requires that each parameter be tested in turn, using only its PDF. For each test an element of the constraint PDF was deliberately changed such that minimisation failure or bias towards nominal values could be spotted immediately. For example, the error on the WIMP light yield linear coefficient B was changed by 25% to 0.003 in Figure 6.14. The distribution is fitted with a Gaussian, the parameters of which reproduce the Gaussian parameters of the sampled nuisance parameter distribution.

The ^{39}Ar side-band is sampled from data taken after the second fill using the physics trigger in DAQ and applying the standard cut flow. The implementation of the side-

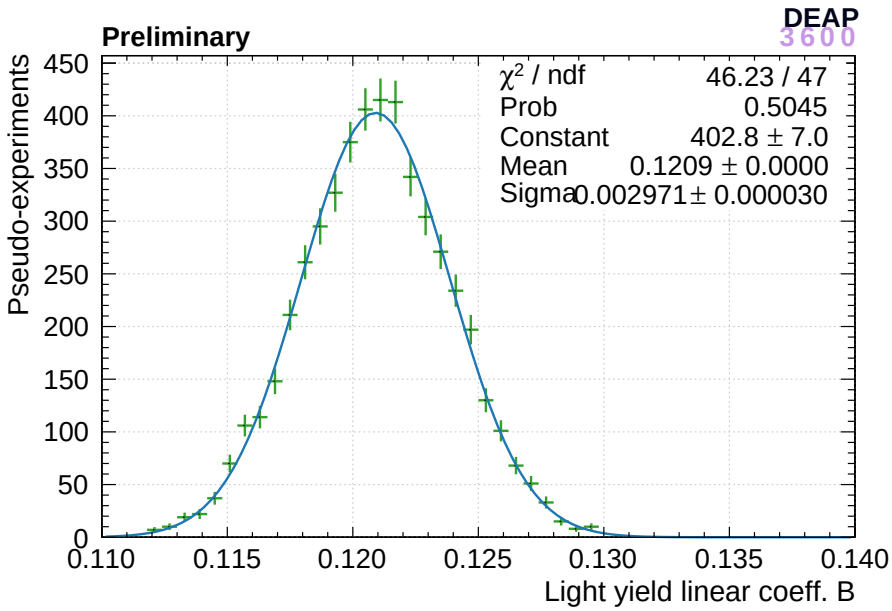

Figure 6.14: Fitted light yield linear coefficient B distribution for 5000 pseudo-experiments generated and fitted using only the ^{39}Ar PDF and constraint terms. Only the B parameter is floated in the minimisation.

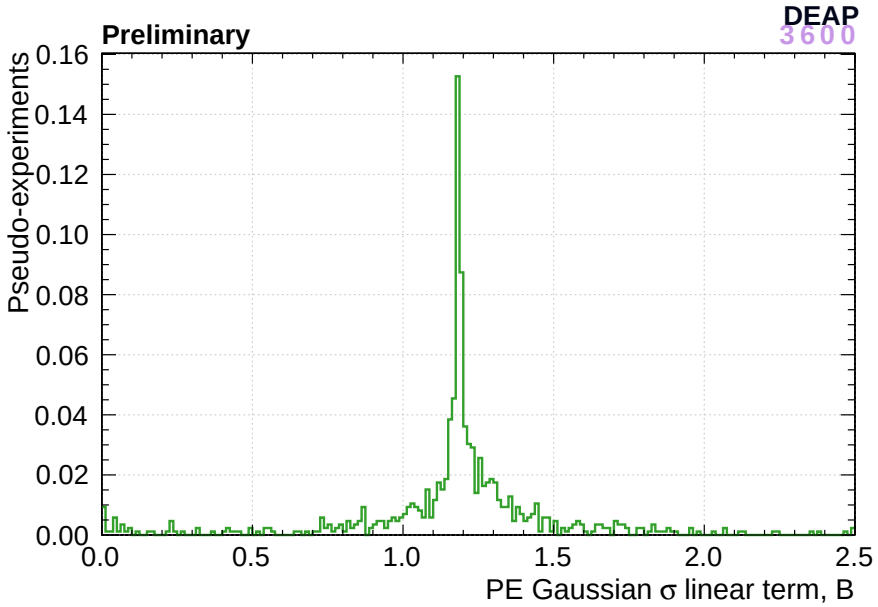

Figure 6.15: Fitted linear PE resolution coefficient B distribution for 1000 pseudo-experiments generated and fitted with the full likelihood model, including the ^{39}Ar side-band from data. Every nuisance parameter is floated in the minimisation.

band was verified by ensuring the parameters of the parts of the model derived from data are constrained compared to their nuisance parameters, and constrained to correct values. 1000 pseudo-experiments were generated and fitted, every nuisance parameter was floated in the minimisation and the full likelihood model with data side-band was implemented. An example of the resulting nuisance parameter distribution for the linear PE resolution coefficient B is shown in Figure 6.15. The distribution is strongly peaked at the correct value $B = 1.185$. Another version of this consistency check was performed where the ^{39}Ar model PDF implemented in the likelihood was integrated over each side-band bin in order to construct an artificial side-band. The artificial side-band was generated with single ^{39}Ar nuisance parameters offset from the nominal, and 1000 pseudo-experiments were generated and fitted using only the ^{39}Ar model PDF and side-band. The minimisation was able to reproduce the offset nuisance parameters to within <1% of each parameter.

6.5 Limit Calculation

In this section the 90% C.L. upper limit on the WIMP cross section is calculated using the profile likelihood ratio analysis. The 27 event dataset is used which assumes 220 days of data and an $80 < Q_{PE} < 240$ PE energy ROI. A fiducial radius cut $R_{rec} < 800$ mm is made, and the $80 < Q_{PE} < 240$ energy ROI is used for consistency with the 220 day dataset. The F_{prompt} ROI cut was defined for a given PE by finding the lower F_{prompt} value that for maximises $\sqrt{s/(s+b)}$, where s is the expected number of signal events and b is the expected number of background events from integrating the PDFs. The resulting lower limit on F_{prompt} is shown in blue in Figure 6.16. The 27 events are all within this ROI and no further events are admitted by using this ROI.

A set of 5 WIMP masses at 10 GeV intervals was chosen to sample the region around the minimum of the nominal zero event distribution, at 100 GeV. For each mass and test cross section, 5000 pseudo-experiments were generated. The 90% C.L. upper limit on the SI WIMP-nucleon scattering cross-section was calculated using the PLR analysis for an observation of the 27 events in the data set. The limit at each selected mass is shown as a set of crosses in Figure 6.17. The purple line in Figure 6.17 is the 90%

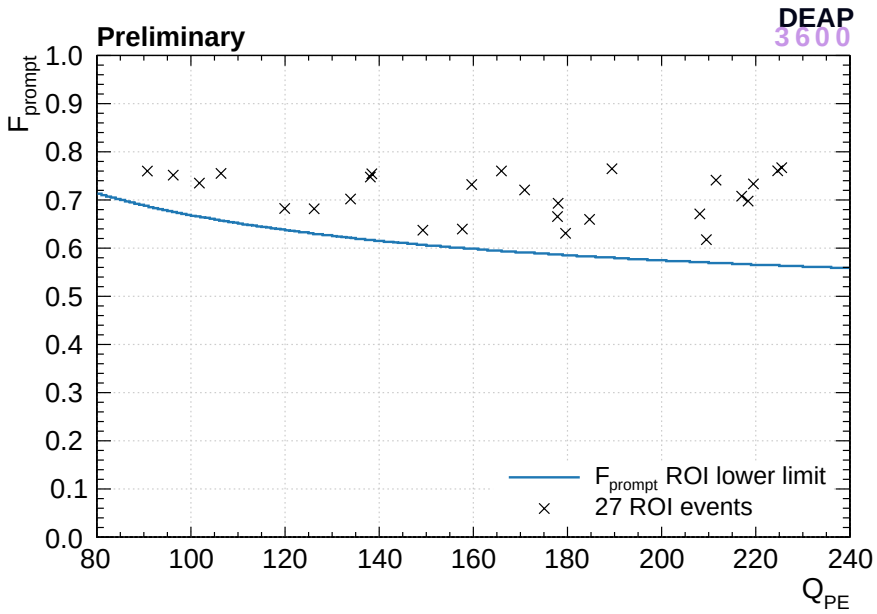

Figure 6.16: The variation of the ROI lower boundary in F_{prompt} with Q_{PE}, together with a scatter plot showing the distribution of the 27 events in F_{prompt} and Q_{PE} from Figure 6.1. The boundary in F_{prompt} is chosen by choosing the value which maximises $s/(s+b)^{1/2}$, and does not exclude any of the 27 events.

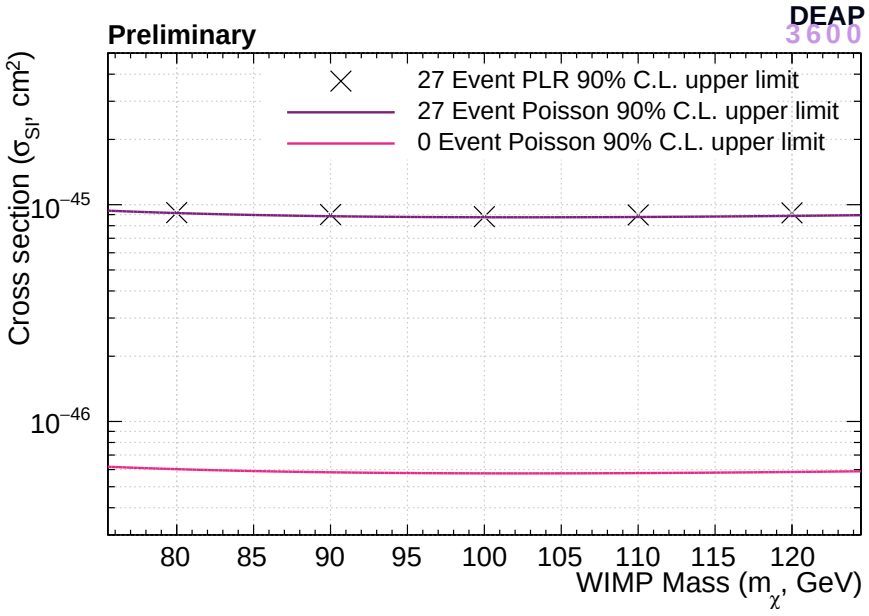

Figure 6.17: Preliminary 90% C.L. upper limits on the spin-independent WIMP-nucleon scattering cross section. Grey crosses are obtained from a profile likelihood ratio analysis using a dataset containing 27 events which reconstruct in the ROI. The pink line is obtained using the Poisson method assuming zero background events, and the purple line is obtained using the Poisson method assuming 27 events.

C.L. upper limit calculated using the Poisson method for 27 observed events. Here the same WIMP and detector response models and ROI are used in the PLR analysis and the Poisson method. The error on each PLR upper limit cross section is 1.5% of the point's cross section, and is not shown. All of the points produced by the PLR analysis agree with the Poisson method limit within 3%, with three points agreeing within 1.5%. Also shown in Figure 6.17 is the 90% C.L. upper limit calculated using the Poisson method for zero observed events. Each upper limit cross section from the Poisson method and PLR analysis falls above the zero event Poisson limit by greater than an order of magnitude due to the presence of observed events. Future versions of this preliminary analysis will sample a wider and more finely separated range of masses and cross sections and use more pseudo-experiments to constrain the error on the PLR cross section.

6.6 Conclusion

A detailed model for the reconstructed radial event position was included in a profile likelihood ratio analysis. The position reconstruction algorithm used allows for an increase in the fiducial volume to 802.95 mm, assuming that the nominal light yield and energy ROI from the design specification of the experiment applies and that no additional background events are seen in the energy and PSD ROI. The increased exposure from an increased fiducial volume yields an order of magnitude difference in the minimum 90% C.L. upper limit on the SI cross section. Reconstructed radial position information was used to construct PDFs and account for the presence of surface alpha events at a given radius. With a fiducial radius of 800 mm and an 80 PE threshold, a preliminary PLR analysis was performed on a data set containing 27 events which reconstruct in the ROI. This returned a 90% C.L. upper limit which is consistent with the 27 event Poisson limit for the same model and higher than the zero event Poisson limit. The origin of the 27 events is currently being investigated. These events are thought to be background events and are under investigation. Current simulation studies suggest that they originate from scintillation in thin films of argon on neck apparatus nearest the AV.

The preliminary analysis presented here uses only the ^{39}Ar side-band to constrain

nuisance parameters pertaining to the ^{39}Ar background and considers only sources of two backgrounds. As the PLR analysis is developed further the likelihood model will be improved by including background PDFs which characterise the neutron nuclear recoil background. The nuclear recoil model nuisance parameters will be constrained with a side-band PDF constructed using AmBe neutron source calibration data. An additional constraint on the electronic recoil nuisance parameters will come from a side-band PDF constructed from ^{22}Na gamma source calibration data. Likewise, the use of bayesian single PE counting will enable greater rejection of electronic recoils whilst allowing the PE threshold to be lowered. Additional considerations will be made to include the effect of the DAQ trigger efficiency in the low Q_{PE} region, enabling the expansion of the ROI in the profile likelihood analysis without compromising on model PDF realism compared to detector data.

As DEAP-3600 continues to take data towards its full exposure, ongoing work to characterise backgrounds and calibration sources will reduce the uncertainty in nuisance parameter prior PDFs in the signal and background models. Ongoing modelling of backgrounds from alpha and ^{39}Ar scintillation in the neck may characterise the source of the current 27 events allowing the exclusion of as many as possible as background events, whilst incorporating them as a background PDF in a profile likelihood analysis. As work continues on improving realism in the optical and material model in simulation, the position reconstruction and other event reconstruction variables will continue to become more consistent between simulation and data. With a simulation using data, position reconstruction alongside other analysis techniques will continue to be crucial for identifying and rejecting surface and neck background events and maintaining a large fiducial volume and exposure.

Bibliography

1. Planck Collaboration *et al.* Planck 2015 results. XIII. Cosmological parameters. *Astron. Astrophys.* **594,** A13 (2016).
2. Amaudruz, P.-A. *et al. DEAP-3600 Dark Matter Search* in *Proceedings of the 37th International Conference on High Energy Physics (ICHEP 2014) Valencia, July 2-9, 2014* **273-275** (June 2016), 340–346.
3. Amaudruz, P.-A. *et al.* First results from the DEAP-3600 dark matter search with argon at SNOLAB. *ArXiv e-prints* (July 2017).
4. Rubin, V. C. & Ford, W. K. Jr. Rotation of the Andromeda Nebula from a Spectroscopic Survey of Emission Regions. *Astrophys.J* **159,** 379 (Feb. 1970).
5. Begeman, K. G., Broeils, A. H. & Sanders, R. H. Extended rotation curves of spiral galaxies - Dark haloes and modified dynamics. *MNRAS* **249,** 523–537 (Apr. 1991).
6. Rubin, V. C., Burstein, D., Ford, W. K. Jr. & Thonnard, N. Rotation velocities of 16 SA galaxies and a comparison of Sa, Sb, and SC rotation properties. *Astrophys.J* **289,** 81–98 (Feb. 1985).
7. Salucci, P. & Persic, M. *Dark Halos around Galaxies* in *Proceedings, Dark and Visible Matter in Galaxies and Cosmological Implications* (eds Persic, M. & Salucci, P.) **117** (1997), 1.
8. Sofue, Y. & Rubin, V. Rotation curves of spiral galaxies. *Ann. Rev. Astron. Astrophys.* **39,** 137–174 (2001).
9. Zwicky, F. On the Masses of Nebulae and of Clusters of Nebulae. *Astrophys.J* **86,** 217 (Oct. 1937).
10. Tyson, J. A., Kochanski, G. P. & Dell'Antonio, I. P. Detailed Mass Map of CL 0024+1654 from Strong Lensing. *Astrophys. J. Lett.* **498,** 107 (1998).
11. Milgrom, M. A modification of the Newtonian dynamics as a possible alternative to the hidden mass hypothesis. *Astrophys.J* **270,** 365–370 (July 1983).
12. Begeman, K. G., Broeils, A. H. & Sanders, R. H. Extended rotation curves of spiral galaxies - Dark haloes and modified dynamics. *MNRAS* **249,** 523–537 (Apr. 1991).
13. Sanders, R. H. & McGaugh, S. S. Modified Newtonian dynamics as an alternative to dark matter. *Ann. Rev. Astron. Astrophys.* **40,** 263–317 (2002).
14. Bertone, G. *et al. Particle Dark Matter: Observations, Models and Searches* (ed Bertone, G.) (Cambridge Univ. Press, Cambridge, 2010).
15. Clowe, D. *et al.* A direct empirical proof of the existence of dark matter. *Astrophys.J* **648,** 109–113 (2006).

16. Barrena, R. *et al.* The dynamical status of the cluster of galaxies 1E0657-56. *Astron. Astrophys.* **386,** 816 (2002).

17. Harvey, D. *et al.* The non-gravitational interactions of dark matter in colliding galaxy clusters. *Science* **347,** 1462–1465 (2015).

18. Markevitch, M. *Chandra observation of the most interesting cluster in the universe* in *Proceedings of the X-ray Universe* (ed Wilson, A.) **604** (Sept. 2005), 723.

19. Bennett, C. L. *et al.* Nine-year Wilkinson Microwave Anisotropy Probe (WMAP) Observations: Final Maps and Results. *Astrophys. J. Suppl.* **208,** 20 (Oct. 2013).

20. Planck Collaboration *et al.* Planck 2015 results. I. Overview of products and scientific results. *Astron. Astrophys.* **594,** A1 (Sept. 2016).

21. Hu, W. *Lecture Notes on CMB Theory: From Nucleosynthesis to Recombination* (2008).

22. Iocco, F. *et al.* Primordial Nucleosynthesis: from precision cosmology to fundamental physics. *Phys. Rept.* **472,** 1–76 (2009).

23. Aver, E., Olive, K. A., Porter, R. L. & Skillman, E. D. The primordial helium abundance from updated emissivities. *JCAP* **1311,** 17 (2013).

24. Cooke, R. *et al.* Precision measures of the primordial abundance of deuterium. *Astrophys.J* **781,** 31 (2014).

25. Baker, C. A. *et al.* An Improved experimental limit on the electric dipole moment of the neutron. *Phys. Rev. Lett.* **97,** 131801 (13 Sept. 2006).

26. Peccei, R. D. & Quinn, H. R. Constraints Imposed by CP Conservation in the Presence of Instantons. *Phys. Rev. D.* **16,** 1791–1797 (1977).

27. Peccei, R. D. & Quinn, H. R. CP Conservation in the Presence of Instantons. *Phys. Rev. Lett.* **38,** 1440–1443 (1977).

28. Primakoff, H. Photo-Production of Neutral Mesons in Nuclear Electric Fields and the Mean Life of the Neutral Meson. *Phys. Rev.* **81,** 899–899 (5 Mar. 1951).

29. Dine, M., Fischler, W. & Srednicki, M. A simple solution to the strong CP problem with a harmless axion. *Phys. Lett. B* **104,** 199 –202 (1981).

30. Shifman, M. A., Vainshtein, A. I. & Zakharov, V. I. Can Confinement Ensure Natural CP Invariance of Strong Interactions? *Nucl. Phys. B* **166,** 493–506 (1980).

31. Peccei, R. D. The Strong CP problem and axions. *Lect. Notes Phys.* **741,** 3–17 (2008).

32. Asztalos, S. J. *et al.* SQUID-Based Microwave Cavity Search for Dark-Matter Axions. *Phys. Rev. Lett.* **104,** 041301 (4 Jan. 2010).

33. Hagmann, C., Sikivie, P., Sullivan, N. S. & Tanner, D. B. Results from a search for cosmic axions. *Phys. Rev. D.* **42,** 1297–1300 (4 Aug. 1990).

34. DePanfilis, S. *et al.* Limits on the abundance and coupling of cosmic axions at $4.5 < m_a < 5.0\ \mu$eV. *Phys. Rev. Lett.* **59,** 839–842 (7 Aug. 1987).

35. Wuensch, W. U. *et al.* Results of a laboratory search for cosmic axions and other weakly coupled light particles. *Phys. Rev. D.* **40,** 3153–3167 (10 Nov. 1989).

36. Brubaker, B. M. *et al.* First results from a microwave cavity axion search at 24 μeV. *Phys. Rev. Lett.* **118,** 061302 (Feb. 2017).

37. McAllister, B. T. *et al.* The ORGAN Experiment: An axion haloscope above 15 GHz. *Phys. Dark Univ.* **18,** 67–72 (2017).

38. Tanabashi, M. *et al.* Review of Particle Physics. *Phys. Rev. D.* **98,** 030001 (2018).
39. Ayala, A. *et al.* Revisiting the Bound on Axion-Photon Coupling from Globular Clusters. *Phys. Rev. Lett.* **113,** 191302 (19 Nov. 2014).
40. Payez, A. *et al.* Revisiting the SN1987A gamma-ray limit on ultralight axion-like particles. *JCAP* **2,** 6 (Feb. 2015).
41. Ajello, M. *et al.* Search for Spectral Irregularities due to Photon-Axionlike-Particle Oscillations with the Fermi Large Area Telescope. *Phys. Rev. Lett.* **116,** 161101 (16 Apr. 2016).
42. Abramowski, A. *et al.* Constraints on axionlike particles with H.E.S.S. from the irregularity of the PKS 2155 − 304 energy spectrum. *Phys. Rev. D.* **88,** 102003 (10 Nov. 2013).
43. Haber, H. E. & Kane, G. L. The search for supersymmetry: Probing physics beyond the standard model. *Phys. Rept.* **117,** 75 –263 (1985).
44. Jungman, G., Kamionkowski, M. & Griest, K. Supersymmetric dark matter. *Phys. Rept.* **267,** 195–373 (1996).
45. Ackermann, M. *et al.* The Fermi Galactic Center GeV Excess and Implications for Dark Matter. *Astrophys.J* **840,** 43 (May 2017).
46. De Boer, W., Gebauer, I., Neumann, A. & Biermann, P. L. An alternative Explanation for the Fermi GeV Gamma-Ray Excess. *ArXiv e-prints* (2016).
47. Calore, F., Cholis, I. & Weniger, C. Background model systematics for the Fermi GeV excess. *JCAP* **2015,** 038 (Mar. 2015).
48. Lowette, S. Accelerator searches for new physics in the context of dark matter. *J. Phys. Conf. Ser.* **718,** 022011 (2016).
49. Lewin, J. D. & Smith, P. F. Review of mathematics, numerical factors, and corrections for dark matter experiments based on elastic nuclear recoil. *Astropart. Phys.* **6,** 87 –112 (1996).
50. Smith, M. C. *et al.* The RAVE Survey: Constraining the Local Galactic Escape Speed. *MNRAS* **379,** 755–772 (2007).
51. Kerr, F. J. & Lynden-Bell, D. Review of galactic constants. *MNRAS* **221,** 1023–1038 (Aug. 1986).
52. McMillan, P. J. & Binney, J. J. The uncertainty in Galactic parameters. *MNRAS* **402,** 934 (2010).
53. Schönrich, R., Binney, J. & Dehnen, W. Local kinematics and the local standard of rest. *MNRAS* **403,** 1829 (2010).
54. Green, A. M. Astrophysical uncertainties on direct detection experiments. *Mod. Phys. Lett.* **A27,** 1230004 (2012).
55. Navarro, J. F., Frenk, C. S. & White, S. D. M. The Structure of cold dark matter halos. *Astrophys.J* **462,** 563–575 (1996).
56. Graham, A. W. *et al.* Empirical Models for Dark Matter Halos. II. Inner profile slopes, dynamical profiles, and ρ/σ^3. *Astron. J.* **132,** 2701–2710 (2006).
57. Catena, R. & Ullio, P. A novel determination of the local dark matter density. *JCAP* **1008,** 004 (2010).
58. Helm, R. H. Inelastic and Elastic Scattering of 187-Mev Electrons from Selected Even-Even Nuclei. *Phys. Rev.* **104,** 1466–1475 (1956).

59. Caldwell Jr., T. S. *Searching for Dark Matter with Single Phase Liquid Argon* PhD thesis (University of Pennsylvania, 2015).
60. Mei, D.-M. & Hime, A. Muon-induced background study for underground laboratories. *Phys. Rev. D.* **73,** 053004 (5 Mar. 2006).
61. Monroe, J. & Fisher, P. Neutrino Backgrounds to Dark Matter Searches. *Phys. Rev. D.* **76,** 033007 (2007).
62. Gütlein, A. *et al.* Solar and atmospheric neutrinos: Background sources for the direct dark matter search. *Astropart. Phys.* **34,** 90–96 (Sept. 2010).
63. Strigari, L. E. Neutrino Coherent Scattering Rates at Direct Dark Matter Detectors. *New J. Phys.* **11,** 105011 (2009).
64. Bernabei, R. *et al.* Final model independent result of DAMA/LIBRA-phase1. *Eur. Phys. J. C* **73,** 2648 (Dec. 2013).
65. Bernabei, R. *et al.* First results from DAMA/LIBRA and the combined results with DAMA/NaI. *Eur. Phys. J. C* **56,** 333 (Aug. 2008).
66. Bernabei, R. *et al.* The DAMA/LIBRA apparatus. *Nucl. Instrum. Methods Phys. Res. A* **592,** 297–315 (July 2008).
67. Ueshima, K. *et al.* Scintillation-only Based Pulse Shape Discrimination for Nuclear and Electron Recoils in Liquid Xenon. *Nucl. Instrum. Methods Phys. Res. A* **659,** 161–168 (Dec. 2011).
68. XMASS Collaboration *et al.* Direct dark matter search by annual modulation in XMASS-I. *Phys. Lett. B* **759,** 272–276 (Nov. 2016).
69. Szydagis, M. *The Present and Future of Searching for Dark Matter with LUX and LZ* in *Proceedings of the 38th International Conference on High Energy Physics (ICHEP 2016) Chicago, IL, USA, August 3-10, 2016* (Nov. 2016).
70. Akerib, D. S. *et al.* Improved Limits on Scattering of Weakly Interacting Massive Particles from Reanalysis of 2013 LUX Data. *Phys. Rev. Lett.* **116,** 161301 (Apr. 2016).
71. Akerib, D. S. *et al.* Results from a search for dark matter in the complete LUX exposure. *Phys. Rev. Lett.* **118,** 021303 (Jan. 2017).
72. Aprile, E. *et al.* Physics reach of the XENON1T dark matter experiment. *JCAP* **4,** 027 (Apr. 2016).
73. Aalseth, C. E. *et al.* Search for An Annual Modulation in Three Years of CoGeNT Dark Matter Detector Data. *ArXiv e-prints* (Jan. 2014).
74. Marrodán Undagoitia, T. & Rauch, L. Dark matter direct-detection experiments. *J. Phys. G* **43,** 013001 (2016).
75. Aalseth, C. E. *et al.* Results from a Search for Light-Mass Dark Matter with a P-type Point Contact Germanium Detector. *Phys. Rev. Lett.* **106,** 131301 (Apr. 2011).
76. Davis, J. H., McCabe, C. & Boehm, C. Quantifying the evidence for Dark Matter in CoGeNT data. *JCAP* **1408,** 014 (2014).
77. Liu, S. K. *et al.* Limits on light WIMPs with a germanium detector at 177 eVee threshold at the China Jinping Underground Laboratory. *Phys. Rev. D.* **90,** 032003 (Aug. 2014).
78. Yue, Q. *et al.* Limits on light WIMPs from the CDEX-1 experiment with a p-type point-contact germanium detector at the China Jingping Underground Laboratory. *Phys. Rev. D.* **90,** 091701 (Nov. 2014).

79. Angloher, G. *et al.* Results on light dark matter particles with a low-threshold CRESST-II detector. *Eur. Phys. J. C* **76,** 25 (Jan. 2016).

80. Angloher, G. *et al.* Results from 730 kg days of the CRESST-II Dark Matter search. *Eur. Phys. J. C* **72,** 1971 (Apr. 2012).

81. Armengaud, E. *et al.* Constraints on low-mass WIMPs from the EDELWEISS-III dark matter search. *JCAP* **5,** 019 (May 2016).

82. Archambault, S. *et al.* Constraints on Low-Mass WIMP Interactions on ^{19}F from PICASSO. *Phys. Lett. B* **711,** 153–161 (May 2012).

83. Behnke, E. *et al.* First dark matter search results from a 4-kg CF_3I bubble chamber operated in a deep underground site. *Phys. Rev. D.* **86.** [Erratum: Phys. Rev.D90,no.7,079902(2014)], 052001 (2012).

84. Barnabé-Heider, M. *et al.* Response of superheated droplet detectors of the PICASSO dark matter search experiment. *Nucl. Instrum. Methods Phys. Res. A* **555,** 184–204 (Dec. 2005).

85. Menendez, J., Gazit, D. & Schwenk, A. Spin-dependent WIMP scattering off nuclei. *Phys. Rev. D.* **86,** 103511 (2012).

86. Amole, C. *et al.* Dark Matter Search Results from the PICO-60 C_3F_8 Bubble Chamber. *Phys. Rev. Lett.* **118,** 251301 (June 2017).

87. Grothaus, P., Fairbairn, M. & Monroe, J. Directional Dark Matter Detection Beyond the Neutrino Bound. *Phys. Rev. D.* **90,** 055018 (2014).

88. Santos, D. *et al.* MIMAC: MIcro-tpc MAtrix of Chambers for dark matter directional detection. *J. Phys. Conf. Ser.* **469,** 012002 (Dec. 2013).

89. Daw, E. *et al.* Spin-Dependent Limits from the DRIFT-IId Directional Dark Matter Detector. *ArXiv e-prints* (Oct. 2010).

90. Battat, J. B. R. *et al.* First background-free limit from a directional dark matter experiment: results from a fully fiducialised DRIFT detector. *Phys. Dark Univ.* **9,** 1–7 (Sept. 2015).

91. Couturier, C. *et al. Directional detection of Dark Matter with the MIcro-tpc MAtrix of Chambers* in *Proceedings, 51st Rencontres de Moriond, Cosmology session: La Thuile, Italy* (Mar. 2016), 165–170.

92. Nakamura, K. *et al.* Direction-sensitive dark matter search with gaseous tracking detector NEWAGE-0.3b'. *Progr. Theor. Exp. Phys.* **2015,** 043F01 (2015).

93. Deaconu, C. *et al. Track Reconstruction Progress from the DMTPC Directional Dark Matter Experiment* in *Proceedings of the 13th International Conference on Topics in Astroparticle and Underground Physics (TAUP 2013)* **61** (2015), 39 –44.

94. Leyton, M. & the DMTPC Collaboration. Directional dark matter detection with the DMTPC m^3 experiment. *J. Phys. Conf. Ser.* **718,** 042035 (2016).

95. Mayet, F. *et al.* A review of the discovery reach of directional Dark Matter detection. *Phys. Rept.* **627,** 1–49 (Apr. 2016).

96. Battat, J. B. R. *et al.* First background-free limit from a directional dark matter experiment: results from a fully fiducialised DRIFT detector. *Phys. Dark Univ.* **9,** 1–7 (Sept. 2015).

97. Lemmon, E., McLinden, M. & Friend, D. *Thermophysical Properties of Fluid Systems* <http://webbook.nist.gov> (National Institute of Standards and Technology, Gaithersburg MD, June 2009).

98. Hitachi, A. *et al.* Effect of ionization density on the time dependence of luminescence from liquid argon and xenon. *Phys. Rev. B.* **27,** 5279–5285 (9 May 1983).

99. Hwang, S.-C., Lein, R. D. & Morgan, D. A. In *Kirk-Othmer Encyclopedia of Chemical Technology* (John Wiley & Sons, Inc., 2005).

100. Doke, T. *et al.* Absolute Scintillation Yields in Liquid Argon and Xenon for Various Particles. *JJAP Pt. 1* **41,** 1538–1545 (Mar. 2002).

101. Benetti, P. *et al.* Measurement of the specific activity of ar-39 in natural argon. *Nucl. Instrum. Methods Phys. Res. A* **574,** 83–88 (Apr. 2007).

102. The LZ Collaboration *et al.* LUX-ZEPLIN (LZ) Conceptual Design Report. *ArXiv e-prints* (Sept. 2015).

103. Bolozdynya, A. I. *et al.* A chromatographic system for removal of radioactive ^{85}Kr from xenon. *Nucl. Instrum. Methods Phys. Res. A* **579,** 50–53 (Aug. 2007).

104. Lindhard, J, Scharff, M. & Schiott, H. E. Range concepts and heavy ion ranges (Notes on atomic collisions, II.) *Mat. Fys. Medd. Dan. Vid. Selsk* **33,** 1–42 (1963).

105. Kubota, S, Hishida, M & Raun, J. Evidence for a triplet state of the self-trapped exciton states in liquid argon, krypton and xenon. *J. Phys. Condens. Matter* **11,** 2645 (1978).

106. Nikkel, J. A., Hasty, R., Lippincott, W. H. & McKinsey, D. N. Scintillation of liquid neon from electronic and nuclear recoils. *Astropart. Phys.* **29,** 161–166 (2008).

107. McKinsey, D. *et al.* Radiative decay of the metastable He 2 (a 3 Σ u+) molecule in liquid helium. *Phys. Rev. A.* **59,** 200 (1999).

108. Lippincott, W. H. *et al.* Scintillation time dependence and pulse shape discrimination in liquid argon. *Phys. Rev. C.* **78.** [Erratum: Phys. Rev.C81,039901(2010)], 035801 (2008).

109. Agnes, P. *et al.* Results from the first use of low radioactivity argon in a dark matter search. *Phys. Rev. D.* **93.** [Addendum: Phys. Rev.D95,no.6,069901(2017)], 081101 (Apr. 2016).

110. Kubota, S. *et al.* Recombination luminescence in liquid argon and in liquid xenon. *Phys. Rev. B.* **17,** 2762–2765 (6 Mar. 1978).

111. Chepel, V. & Araujo, H. Liquid noble gas detectors for low energy particle physics. *JINST* **8,** R04001 (2013).

112. Lenardo, B. *et al.* A Global Analysis of Light and Charge Yields in Liquid Xenon. *IEEE Trans. Nucl. Sci.* **62,** 3387–3396 (2015).

113. Birks, J. B. Scintillations from Organic Crystals: Specific Fluorescence and Relative Response to Different Radiations. *Proc. Phys. Soc. Section A* **64,** 874 (1951).

114. Mei, D. M., Yin, Z. B., Stonehill, L. C. & Hime, A. A Model of Nuclear Recoil Scintillation Efficiency in Noble Liquids. *Astropart. Phys.* **30,** 12–17 (2008).

115. Gastler, D. *et al.* Measurement of scintillation efficiency for nuclear recoils in liquid argon. *Phys. Rev. C.* **85,** 065811 (2012).

116. Cao, H. *et al.* Measurement of Scintillation and Ionization Yield and Scintillation Pulse Shape from Nuclear Recoils in Liquid Argon. *Phys. Rev. D.* **91,** 092007 (May 2015).

117. Hitachi, A., Doke, T. & Mozumder, A. Luminescence quenching in liquid argon under charged-particle impact: Relative scintillation yield at different linear energy transfers. *Phys. Rev. B.* **46,** 11463–11470 (18 Nov. 1992).

118. Mozumder, A. Free-ion yield in liquid argon at low-LET. *Chem. Phys. Lett.* **238,** 143 –148 (1995).

119. Mozumder, A. Free-ion yield and electron-ion recombination rate in liquid xenon. *Chem. Phys. Lett.* **245,** 359 –363 (1995).

120. Acciarri, R. *et al.* Effects of Nitrogen contamination in liquid Argon. *JINST* **5,** 6003 (June 2010).

121. Acciarri, R. *et al.* Oxygen contamination in liquid Argon: combined effects on ionization electron charge and scintillation light. *JINST* **5,** 5003 (May 2010).

122. Ziegler, J. F., Ziegler, M. D. & Biersack, J. P. SRIM - The stopping and range of ions in matter. *Nucl. Instrum. Methods Phys. Res. B* **268,** 1818–1823 (June 2010).

123. Amaudruz, P.-A. *et al.* Radon backgrounds in the DEAP-1 liquid argon based Dark Matter detector. *Astropart. Phys.* **62,** 178–194 (Mar. 2015).

124. Pollmann, T., Boulay, M. & Kuźniak, M. Scintillation of thin tetraphenyl butadiene films under alpha particle excitation. *Nucl. Instrum. Methods Phys. Res. A* **635,** 127–130 (Apr. 2011).

125. Westerdale, S. *In situ measurement of the neutron background rate* DEAP-3600 Technical Report 11 (Carleton University, 2017).

126. Vásquez-Jáuregai, E. *Neutron backgrounds in DEAP-3600: simulations* DEAP-3600 Technical Report 8 (National Autonomous University of Mexico, 2017).

127. Cai, B., Boulay, M., Kuzniak, M. & Skensved, P. *Neutron backgrounds in DEAP-3600* DEAP-3600 Technical Report 2 (Queen's University, 2011).

128. Golovko, V. V., Kuzniak., M., Boulay, M. G. & Skensved, P. *Testing Cast Acrylic for Light Guide for DEAP-3600 Experiment* DEAP-3600 Technical report (Queen's University, Aug. 2010).

129. Cai, B. *The DEAP-3600 Dark Matter Experiment* in *Proceedings, Meeting of the APS Division of Particles and Fields (DPF 2015) Ann Arbor, Michigan, USA, August 4-8, 2015* (2015).

130. Gehman, V. M. *et al.* Fluorescence Efficiency and Visible Re-emission Spectrum of Tetraphenyl Butadiene Films at Extreme Ultraviolet Wavelengths. *Nucl. Instrum. Methods Phys. Res. A* **654,** 116–121 (2011).

131. Broerman, B. *et al.* Application of the TPB Wavelength Shifter to the DEAP-3600 Spherical Acrylic Vessel Inner Surface. *JINST* **12,** P04017 (Apr. 2017).

132. Amaudruz, P.-A. *et al.* In-situ characterization methods for the Hamamatsu R5912 photomultiplier tubes used in the DEAP-3600 experiment. *ArXiv e-prints* (2017).

133. *Sigma-Aldrich Co. L.L.C.: Silicone Oil 1000 cSt Catalogue Entry and Specification Sheet* http://www.sigmaaldrich.com/catalog/product/aldrich/378399. 2014.

134. Bugel, L. *et al.* Demonstration of a lightguide detector for liquid argon TPCs. *Nucl. Instrum. Methods Phys. Res. A* **640,** 69–75 (June 2011).

135. *Hamamatsu Photonics: Borosilicate Glass Specification* 2008.

136. Caldwell, T, Seibert, S & Jaditz, S. Characterization of the R5912-02 MOD photomultiplier tube at cryogenic temperatures. *JINST* **8,** C09004 (2013).

137. Chubar, O., Elleaume, P. & Chavanne, J. A three-dimensional magnetostatics computer code for insertion devices. *J. Synchrotron Radiat.* **5,** 481–484 (May 1998).

138. Elleaume, P., Chubar, O. & Chavanne, J. *Computing 3D magnetic fields from insertion devices* in *Proceedings of the 1997 Particle Accelerator Conference* **3** (May 1997), 3509–3511.

139. Mastbaum, A. *RAT Github Page* <https://github.com/rat-pac> (2014).

140. Butcher, A. J. *Searching for dark matter with DEAP-3600* PhD thesis (Royal Holloway, University of London, 2015).

141. E. Grace, A. Butcher, J. Monroe, and J. A. Nikkel. Index of refraction, Rayleigh scattering length, and Sellmeier coefficients in solid and liquid argon and xenon. *Nucl. Instrum. Methods Phys. Res. A* **867,** 204–208 (2017).

142. Sinnock, A. C. & Smith, B. L. Refractive Indices of the Condensed Inert Gases. *Phys. Rev.* **181,** 1297–1307 (3 May 1969).

143. Stolp, D. *et al.* An estimation of photon scattering length in tetraphenyl-butadiene. *JINST* **11,** C03025 (2016).

144. Akashi-Ronquest, M. *et al.* Improving photoelectron counting and particle identification in scintillation detectors with Bayesian techniques. *Astropart. Phys.* **65,** 40–54 (May 2015).

145. Amaudruz, P.-A. *et al.* Measurement of the scintillation time spectra and pulse-shape discrimination of low-energy β and nuclear recoils in liquid argon with DEAP-1. *Astropart. Phys.* **85,** 1–23 (2016).

146. Seidel, G. M., Lanou, R. E. & Yao, W. Rayleigh scattering in rare gas liquids. *Nucl. Instrum. Methods Phys. Res. A* **489,** 189–194 (2002).

147. Ishida, N. *et al.* Attenuation length measurements of scintillation light in liquid rare gases and their mixtures using an improved reflection suppresser. *Nucl. Instrum. Methods Phys. Res. A* **384,** 380 –386 (23 Jan. 1997).

148. ArDM Collaboration *et al.* Measurement of the attenuation length of argon scintillation light in the ArDM LAr TPC. *Astropart. Phys.* **97,** 186–196 (Nov. 2016).

149. Billard, J., Mayet, F. & Santos, D. Exclusion limits from data of directional Dark Matter detectors. *Phys. Rev. D.* **82,** 055011 (2010).

150. Yellin, S. Finding an upper limit in the presence of an unknown background. *Phys. Rev. D.* **66** (Aug. 2002).

151. Henderson, S., Monroe, J. & Fisher, P. The Maximum Patch Method for Directional Dark Matter Detection. *Phys. Rev. D.* **78,** 015020 (2008).

152. Cowan, G., Cranmer, K., Gross, E. & Vitells, O. Asymptotic formulae for likelihood-based tests of new physics. *Eur. Phys. J. C* **71.** [Erratum: Eur. Phys. J.C73,2501(2013)], 1554 (2011).

153. Aprile, E. *et al.* Likelihood Approach to the First Dark Matter Results from XENON100. *Phys. Rev. D.* **84,** 052003 (Sept. 2011).

154. Aprile, E. *et al.* Dark Matter Results from 225 Live Days of XENON100 Data. *Phys. Rev. Lett.* **109,** 181301 (Nov. 2012).

155. Regenfus, C *et al.* Study of nuclear recoils in liquid argon with monoenergetic neutrons. *J. Phys. Conf. Ser.* **375,** 012019 (2012).